A multi-physics simulation approach to Investigating the underlying mechanisms of Low-Speed Pre-Ignition

Adnan Mahmood

Submitted for the degree of

Doctorate of Philosophy (Ph.D.)

In

Mechanical Engineering

I, Adnan Mahmood confirm that the work presented in this thesis is my own. Where information has been derived from other sources, I confirm that this has been indicated in the thesis.

_____

Acknowledgements

I would like to take this opportunity to thank all those that have enabled me to complete my PhD.

First and foremost, I thank God, it is only through your blessings and will that this has been possible.

I am very thankful to my supervisors; Paul Hellier and Nicos Ladommatos for all their exceptional support, guidance and teaching. A special thanks to Radomir Slavchov, your guidance and advice has been invaluable.

A big thanks to BP, and various employees for their support. To mention a few; Tim Yates, Chris Bannister, Gordon Lamb, Nikos Diamantonis and Chris Smith.

I am very appreciative of the support provided by Convergent Science. In particular, the support provided by Pietro Scienza has been invaluable. Thank you also to Gamma technologies for their help.

I thank my parents for all their support and hard work, for always encouraging me to aim high and achieve my ambitions. I am very indebted to my wife who has always encouraged and supported me, you are my backbone.

Abstract

As part of the effort to improve thermal efficiency, engines are being significantly downsized. A common issue in gasoline engines which limits thermal efficiency and is further exacerbated by downsizing, is low speed pre-ignition (LSPI). This thesis uses a Multiphysics approach, initially using a validated 1D engine performance model of a GTDI engine, to define realistic boundary conditions. A strong emphasis on validating each simulation methodology as much as possible is maintained at each stage.

A hydrodynamic model of the ring-liner and Lagrangian CFD model are used to investigate the impact of engine oil fluid properties on the mass of oil transported from the crevice volume to the combustion chamber. A heat transfer and evaporation model of a single droplet inside an engine environment was developed for alkanes of chain lengths representing the extremes of the chain lengths present in engine oil. It was found the droplet generally evaporates at a crank angle which is close to the point where LSPI is observed. The hydrocarbon study ends with a CFD constant volume simulation to understand why engine oil like hydrocarbons ignite in rig tests but not in an engine.

This research then proceeds to develop a single particle detergent model in an engine environment, to initially understand why ignition occurs when a calcium Ca based detergent is present but not in the case of a magnesium Mg detergent. It was found from simulation that the common theory of calcium oxide CaO resulting from thermal degradation from the previous cycle then reacting with Carbon dioxide CO_2 late in the compression stroke is unlikely. There is a stronger case for the CaO particle causing ignition as it is present in fresh engine oil sprayed onto the liner. As predicted by the hydrocarbon evaporation model the oil will cover and protect the CaO particle until late in the compression stroke when the oil will evaporate, exposing the CaO particle to CO_2.

Impact statement

From the literature survey that was carried out, this seems to be the first time such an extensive numerical exercise that examines the chemical equilibrium and heat release under actual in-cylinder conditions in relation to LSPI has been carried out. The difference in chemical reaction behaviour between Mg and Ca has been simulated and explained. The impact of factors such as particle size and burned gas fraction on the ignition timing was also investigated to much extent. The capability developed in this thesis allowed us to evaluate the plausibility of a CaO particle remaining from the previous engine cycle. This theory was deemed questionable, the new theory combining the behaviour of the hydrocarbon components and detergent reaction is a novel addition to this field.

The single particle approach has proven to be successful. It was possibly to understand the thermodynamic behaviour of a detergent within realistic engine conditions. This meant it was possible to tightly control local boundary conditions and thus understand sensitivity, rather than decipher a stochastic system.

Similarly, the thesis explains why engine oil like hydrocarbon ignition was observed on rig tests but not on engines.

Finding a solution for the LSPI problem will have a profound impact on future mobility. For hybrid vehicles, calibrators would have access to all the low speed-high load region that is currently being avoided, a region that could provide good BSFC. If the sectors move towards gaseous fuels, LSPI will be the major limitation to thermal efficiency because of the low minimum energy for combustion.

Figures and Tables

6

15

Nomenclature

Acronyms:

Atdc	After top dead centre
BSFC	Brake specific fuel consumption
BTdc	Before top dead centre
CFD	Computational fluid dynamics
CI	Compression ignition
DI	Direct injection
FEA	Finite element analysis
GTDI	Gasoline turbocharged direct injection
HD	Hydrodynamic
HC	Hydrocarbon
LSPI	Low speed pre-ignition
MD	Molecular dynamics
MON	Motor octane number
PFI	Port fuel injection
SI	Spark ignition
SMD	Sauter mean diameter
RON	Research octane number

VOF   Volume of fluid

Symbols:

U	total fluid velocity	(m/s)
S	momentum source due to body force	(kg m/s)
i	internal energy	(J)
φ	viscous dissipation	(J)
$C_{D,sphere}$	drag coefficient of a perfect sphere	
y	droplet distortion	
ω_{RT}	growth rate	
k_{RT}	wave number	
ρ_l	liquid density	(kg/m^3)
μ_l	liquid dynamic viscosity	(Pa s)
$\bar{C}_{eq}$	equilibrium concentration	(mol/m^3)
$H(T)$	Henry constant	
y_{eq}	gas volume fractions at equilibrium	
y_t	gas volume fractions at time t	
P	pressure	(Pa)
τ	time constant.	
R	universal gas constant	(J/K/mol)
$\dot{m}$	mass flow rate	(kg/s)
ω	angular velocity	(rad/s)
r	radial distance	(m)

17

I	second moment of inertia	(m^4)
k	turbulent kinetic energy	(m^2/s^2)
	rate constant	$(1/s)$
	equilibrium constant	
A	Area	(m^2)
	Pre-exponential factor	
h_c	convective heat transfer coefficient	$(W/(m^2K))$
B	cylinder bore size	(m)
R	rate of change of droplet radius	(m/s)
D	mass diffusivity of vapour	(m^2/s)
ρ	density	(kg/m^3)
r	droplet radius	
μ	viscosity	$(Pa\ s)$
T	temperature	(K)
H, h	enthalpy	(J/mol)
G	Gibbs free energy	(J/mol)
S	Entropy	(J/K)
$T\_{(end,p)}$	End temperature of previous time step	(K)
K	thermal diffusivity	(m^2/s)
P_{vap}	vapour pressure	(Pa)
T_{vap}	vapour temperature	(K)
H_{vap}	Latent heat of vapourisation	(J/g)
T_{cyl}	cylinder gas temperature	(K)

T_{wb}	wet bulb temperature	(K)
Q_react	energy released by reaction	(J)
m_part	particle mass	
Cp_part	particle specific heat capacity	(J/(kg K))
SA_part	particle surface area	(m^2)
time_react	reaction time	(s)
Lt	thermal diffusion length	(m)
T_{gas}	global average gas temperature	(K)

CONTENTS

21

23

24

1. Background and Motivation

1.1. Introduction to Internal combustion engines and operation

Internal combustion engines (ICE) are a prominent provision of mechanical energy in our everyday lives. Utilised in transport, power generation or machinery operation. As suggested by the name, ICE are powered by exothermic, high power density, combustion events. As liquid fuels have a very high specific enthalpy change of oxidation, the ICE has been preferred. Gasoline, gaseous fuels and Diesel fuels provide a means by which chemical energy can be stored and released, under the correct conditions just using only oxygen in air at high pressure and temperature.

Over time it has been understood that the optimal conditions and method to initiate oxidation for the two predominant fuels (Diesel and Gasoline) are different, as are their subsequent combustion characteristic during energy release. This understanding has seen unique engine design and engine control strategies developed for optimal performance, in the case of each fuel type [27]. The performance characteristics and the specific benefits each option offers have determined their respective areas of application [27][69][101]. For example, the need to operate at high loads and low speeds has made the Diesel engine suitable for power generation and heavy-duty vehicles Diesel engines can offer good thermal efficiency approaching peak torque, a high torque at low speeds because of the high cylinder pressures but require a very high level of boost at higher engine speeds. A Diesel

26

engine will also offer good thermal efficiency at part load engine. On the other hand, they make up most of the passenger vehicle population. As a particularly high toque is not required at low speed, a gasoline engine can provide good transient response, often without even requiring a turbocharger (lower AFR required), it also offers good thermal efficiency at high load, and mid-high speed. A gasoline engine also allows an engine to reach a greater speed range with a boosted engine in particular as it can sustain an elevated torque over a broader speed range, Gasoline engines require a lower compression ratio then Diesel engines and therefore require low inertia components that do need to withstand such high pressures, assisting in transient response[102].

Direct Injection (DI) engines [101] have a high pressure injector that injects fuel directly into the combustion chamber late in the compression stroke for Diesel engines and close to the beginning of the intake stroke for gasoline engines. In both cases, fuel droplets will immediately experience primary and secondary droplet breakup, fuel evaporation and mixing with air. For Diesel engines, the combustion can be split into two phases: pre-burn and diffusion burn. The pre-burn is the kinetically limited phase that will ignite the mixed fuel once a sufficient local enthalpy has been reached. Ignition will take place as a series of micro-ignition events across the mixed region. Following ignition, as the injector continues to introduce liquid fuel into the chamber at high momentum the combustion process will be diffusion limited, and with the high enthalpy of the mixture following heat release, the rate of reaction will instead

27

be limited by the rate of air entrained by the fuel jet. For Gasoline engines, the DI serves the purpose of quenching the charge and therefore allowing for a higher density, increasing turbulence and ram effects by contributing to the charge momentum. It also reduces the fuel lost to wall wetting and 'puddling' in the ports like PFI (port fuel injection). The purpose of the injection so early in the engine cycle is to allow ample time for fuel phase change and mixing so that a homogeneous mixture is present by the time of ignition. The extent to which this is achieved will impact the efficiency of the combustion as well as emissions. This is different to stratified charge injection when fuel is injected at specified timings to initiate heat release at optimal points but only allows a short period for fuel-air mixing.

1.2. Engine efficiency, combustion processes & Implications of abnormal combustion

Approximately 40-50% of the energy released from combustion in an IC engine is lost to exhaust gas heat, mechanical friction losses and energy associated with gas transport into and out of the combustion chamber [101]. Therefore, the efficiency and characteristics of a combustion event are important to understand and optimise. There are various reasons that should motivate one to pay attention to combustion behaviour. Amongst these factors are; the need to reduce the fuel consumption for the operator, legal and ethical requirement to reduce emissions and reduce damage to engine components.

In a practical engine, there are various factors that contribute to the nature and efficiency of the combustion [27] event(s) including component selection/design, engine control and calibration and fluids present in the combustion chamber.

One such undesired and abnormal modes of operation is Knock [32], which results by autoignition of the unburned end gas zone. For an SI engine the primary flame front will propagate from the ignition point, increasing the temperature of the unburned zone ahead of it by heat transfer, compression due to a hotter burned zone expanding, compression of the gas by the piston (if knock occurs before Tdc) and potentially radiation from the flame itself. Knock in an SI engine can also occur due to pre-ignition. Where a micro-ignition event takes place before the spark event; often the pre-ignition is able to heat the end gas to the extent that it propagates into a larger auto ignition event known as Mega Knock [101].

There are other factors that contribute to the heating of the end gas zone. One of these factors is compression ratio. A recent trend for improved power density and thermal efficiency is through higher compression ratio with the addition of increased boost pressure. An example of an investigation into the benefits of such design changes was carried out by Smith et al[33], where variable compression ratio performance data was acquired by Sloan laboratory. Compression ratios of 10 to 13 were compared, the AFR was stoichiometric and the spark timing was retarded from MBT (maximum brake torque) timing to avoid Knock. Average improvements of 5.1% brake efficiency, 4.6% gross indicated efficiency (pressure-volume integral of compression and expansion strokes only) and 4.5% for net indicated efficiency (pressure-volume integral over all 4 strokes) were observed by increasing compression ratio. Obviously, the brake efficiency will account for the friction loss as well as pump loads etc.

29

Low speed pre-ignition (LSPI) has come to greater prominence in recent times as engines are downsized to improve thermal efficiency, the prevalence of which has been exacerbated by the dominance of DI technology. GTDI engines have high compression ratios for improved mixing and thermal efficiency; they also have higher gas density due to boosting which means more work done during compression. This results in higher initial enthalpy upon ignition, improving the burn speed and efficiency of combustion. Unfortunately, the improvements also mean the higher mixture enthalpy before ignition makes the mixture more vulnerable to pre-ignition.

There are several mechanisms that have been proposed to explain the propensity of Low speed Pre-ignition event. Some of the main hypothesis will be investigated as part of this thesis; these will include chemical mechanisms, impact of a directly injecting fuels spray, fuel composition, lubricant properties and phase change relative to engine operating conditions.

The nature of LSPI and Knock combustion can be very damaging to the engine components, however more concerning is that combustion phasing precision is lost, especially in the case of LSPI when combustion will initiate earlier than the calibrated spark timing. LSPI is also far more difficult to mitigate, unlike knock which can be reduced by retarding the timing. Retarding spark timing simply allows the pre-ignition points more time to react and transfer heat to the surrounding mixture. In most cases advancing the

30

spark timing is not possible at the low speeds where LSPI occurs, as the spark timing will be at the knock limit or MBT.

Although LSPI is associated with GTDI engines, previous combustion mechanism research associated with Diesel CI and HCCI engines is extremely relevant as they rely upon a controlled autoignition event. HCCI engines exist for both Diesel and Gasoline applications; they involve injecting fuel very early and relying upon compression to achieve the enthalpy of combustion. The early injection allows ample time for good mixing and to achieve SI like emissions, with CI thermal efficiency. Although ideal for steady state operation HCCI engines are challenged for transient operation, as changing fuel temperature, charge temperature and compression ratio are the only ways of controlling ignition timing. The major challenge is being able to vary the mentioned control parameters quickly enough and accurately for a conventional vehicle. However, HCCI could potentially be an ideal solution for series hybrid technology, which involves steady state engine operation.

Understanding LSPI physical mechanisms and the factors that affect them is a multi-faceted challenge; it involves mass transfer under engine boundary conditions, heat transfer, phase change and chemical reactions. Although, macro level behaviour (cylinder pressure/apparent heat release) can be achieved using several engine testing techniques (that will be discussed later), it is extremely difficult to decouple all contributors and assess their sensitivity with physical testing. A simulation environment allows us to investigate the

31

contribution of different sub-models and the impact of various boundary conditions. A range of techniques will be investigated and utilised in this thesis ranging from component dynamics and deformation to computational fluid dynamics; in 0D, 1D, 2D and 3D domains.

In 2018 the intergovernmental panel on climate change (IPCC) provided a stern warning to the world, concluding that the world must reduce its emissions to net zero in order to have any hope of limiting the temperature increase due to global warming to 1.5°C higher than pre-industrial times. Not taking action will have detrimental consequences on sea levels, flooding and droughts. Prior to this 196 parties adopted the Paris agreement in 2016. The members set themselves that target of limiting the temperature increase to less than 2°C compared to pre-industrial times. Members will try to reach a global peak in greenhouse gases as soon as possible, allowing for the possibility of being globally carbon neutral by mid-century. The transport has since embarked on an accelerated green technology initiative and a variety of propulsion technologies have found their way to the common market, such as; hybrid vehicles (various architectures), battery powered electric vehicles, H2 fuel cell cars and H2 combustion engine cars. However, there are practicality challenges associated with each and the internal combustion engine remains the most popular choice in the short term. Be it in the form of a solely ICE vehicles, hybrid vehicles or just serving as a range extender. For this reason, it is crucial the efficiency of the IC engine is improved and thus so is its carbon footprint. As mentioned, downsizing the engine will improve thermal efficiency

due to a higher worked density of the air-fuel charge, and possibly a lowed FMEP because of the lower displacement. However, the highly stressed end gas will result in knock and megaknock events that will retard the spark timing and increase BSFC. In order for an engine to achieve its fastest transient response, it must have the ability to achieve maximum torque at each engine speed. The 1500-2000 rpm maximum torque region of engine operation is where LSPI occurs. It is also very difficult to modify the torque curve to avoid the LSPI region without compromising boost recovery and transient response for speeds that pass through this region.

1.3. Aims and objectives of this study

This thesis aims to use simulation to prove or disprove the predominant conjecture offered by publication regarding the causes and mechanism regarding LSPI, by assessing their plausibility using a combination of simulation techniques. The major contribution of this thesis will be the physics-based reasoning and substantiation behind each theory of LSPI, and conclusions as to which theory of impact of hydrocarbons and detergents, is most corroborated, whether theories can be combined and whether the findings give rise to a new theory.

In-order to achieve the overarching aim described above the following will be investigated and researched.

33

From literature survey:

- Understand the characteristic behaviour of LSPI and its consequences
- Research the factors that impact LSPI, suppress it or exacerbate it
- Understand the various approaches taken to test for LSPI, detect it and quantify it
- Assess the explanations offered for the cause of LSPI in literature, and the amount of supporting evidence
- From the literature review deduce the most plausible steps leading up to LSPI, even if the paths split and there is more than one path than can proceed.
- Research the modelling techniques that could be used to simulate each step of the proposed path(s).

Technical Investigation

- Develop the simulation capability to investigate each aspect contributing to LSPI individually with sensitivity analysis within expected variation of inputs
- Assessment of impact of fuels and lubricant selection, in terms of transport, evaporation and reactions
- Investigate contribution of detergent selection to LSPI
- Assessment of impact of fuels
- Investigate any solutions offered in literature to mitigate LSPI
- Understand the nature of LSPI heat release and propagation

We will revisit these objectives and the aim in the conclusions section and assess to what extent the study, research and findings address each one.

1.4. Thesis structure

The thesis has thus far provided a background to the LSPI problem within engines provided some context to terms that are commonly used regarding this topic and its consequences. The remainder of the thesis will focus on information that is currently available in literature; simulation capability will be developed to investigate the predominant theories for LSPI mechanisms providing physics-based substantiation.

An overview of the thesis structure is provided below:

- Chapter 2: Literature survey on how test methodologies and simulation are used to understand combustion and autoignition. Relevant engine fundamentals are provided, and knowledge gaps identified.
- Chapter 4: An overview of all the simulation techniques that could be useful in understanding LSPI. Not all of these methodologies will be used in the simulation study.
- Chapter 5: Summary of the proposed stages that lead to LSPI based on literature survey and 1D combustion model used for boundary conditions
- Chapter 6: Hydrodynamic modelling of ring-liner contact, and impact of viscosity on oil transported from crevice volume
- Chapter 7: Simulating a single hydrocarbon droplet in and engine environment. Including heat transfer, phase change and ignition.
- Chapter 8: Modelling of detergent particles in an engine environment, including heat transfer and reactions.
- Chapter 9: Impact of fuel selection, water injection and nature of reaction propagation
- Chapter 10: Final conclusions and future work

2. Background theory and Literature Review

The first part of the literature survey contains research that equips us with fundamental knowledge of engine behaviour that is required to appreciate the findings from technical publications focusing on LSPI. A review of studies considering LSPI follows and will be divided into; a section for experimental research, a section for research that attempts to arrive at fundamental mechanisms of pre-ignition and sensitivities relating to its behaviour. Following this the gaps in knowledge will be summarised, as well as implications for the future. The section will be concluded with a plan of how the gaps in knowledge can be addressed, this will set the thesis.

2.1. Abnormal Combustion in SI engines

Autoignition [32] is a combustion event that occurs when an air-combustible mixture reaches an enthalpy state to result in a highly energy exothermic reaction without a spark source. CI engines are dependent upon autoignition for their operation and compression ratio has to be high to provide the elevated initial enthalpy. However, for SI engines the autoignition is not part of the 'planned' ignition provided by the spark plug but does occur and often results in Knock. This is a distinct sound that can be heard particularly when accelerating a SI engine and is a result of the shock wave that is created during autoignition of the air-fuel mixture ahead of the advancing flame front. As both this type of autoignition occurring in the end gas and LSPI qualify as autoignition events, the scenario described above will be called end gas autoigntion and the spontaneous ignition for LSPI will just be referred to as Pre-ignition.

36

As demonstrated in figure 1(a), the propagating flame front of an SI engine heats the unburned zone of the fuel-air mixture by conduction, convection, and radiation. Simultaneously the piston compresses the mixture, further increasing its enthalpy, the burned zone is also expanding and compressing the unburned zone. If the temperature of the unburned zone is high enough autoignition will occur close to the flame front interface. Occurring here because of the thermal gradient between the flame front and the cylinder wall. The fast expansion of the autoignition point initiates a supersonic shock wave, interference between the shock wave and the primary flame front, and the reciprocating travel of the wave across the bore is what creates the characteristic knocking sound (as shown in Figure 1(b)) [27][69].

(a)   (b)
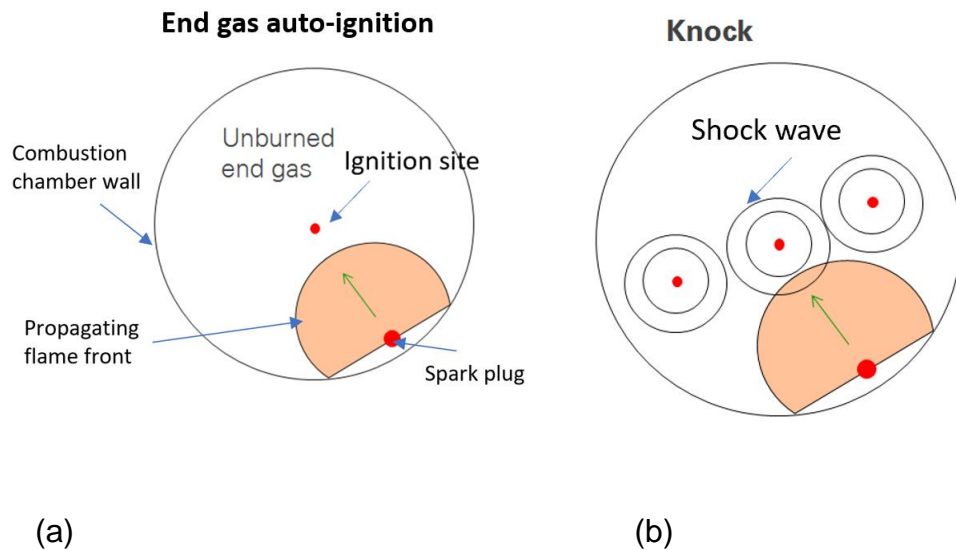
Figure 1 - Illustration of (a) Initial autoignition in unburned zone (b) Knock caused by autoignition and flame front interference

Knock [69] can severely affect thermal efficiency, emissions and damage components due to the high pressure and high temperature detonation event. The turbulent flame speed of the primary flame front will determine the time available for heat transfer into the unburned zone before it is engulfed by the flame. In the event an autoignition does occur the speed of the flame front will also determine the time available for the detonation to propagate. For this reason, Knock is highly sensitive to the level of turbulent kinetic energy, and thus is more of a problem at low engine speeds than high. On most engines knock is overcome by retarding spark timing once the Knock sensor has detected an event. By retarding the spark timing later in the compression stroke of the engine [67], the flame propagates within an environment that has a lower enthalpy because the amount of compressive work done on an ignited gas is reduced, in turn reducing the propensity of knock. Other ways include using cooled exhaust gas recirculation (EGR) to cool the mixture with a higher specific heat capacity and dilute the oxygen in the unburned zone, reducing intercooler exit temperatures so the initial unburned temperature is lower, enrich charge mixture so that the extra fuel quenches the unburned zone also reducing head and water jacket temperature. Occasionally a leaner mixture can also reduce knock tendency as a reduction in fuel concentration will reduce the rate of reaction, and there is a relatively high mass of excess air that can absorb any heat release to keep end gas temperature low. However, such solutions are not always successful as they result in a slower burn rate, allowing for more time to heat the end gas zone. Some more rare solutions include water injection and variable compression ratio. However, countering the possible measures to reduce knock are the compromise in thermal or

38

brake efficiency. Retarding the spark timing away from the engines maximum brake torque timing (MBT) will transfer less energy to the piston and will retain more energy as enthalpy in the exhaust gas. Quenching the charge mixture will also reduce the thermal efficiency of the combustion event. DI can also help cool mixture due to latent heat transfer from charge gas during evaporation and thus reduce knock. Internal EGR (Exhaust gas recirculation) from burned gas residuals increase knock as they are very hot, but cooled EGR can reduce knock as the oxygen dilution and increase in specific heat capacity dominates.

Compression ratio is a key specification in the design of engines. It is calculated by dividing the total swept volume of the piston by the remaining cylinder volume when the piston is in its Tdc position. A high compression ratio improves Otto efficiency [69] (heat energy due to combustion + heat rejection to water jacket/heat energy due to combustion). It should be noted that heat energy due to combustion will have a positive convention as it is heat energy created within the system, and heat rejection will have a negative convention as it is heat energy leaving the system. However, a high compression ratio does also make the engine more prone to knock as the piston is doing more work on the fuel-air mixture, increasing the end gas temperature.

LSPI is an autoignition event that occurs before the spark ignition [70]. As mentioned, the source of LSPI is an area of active discussion, but a micro-

ignition takes place due to a droplet, particle, or hot spot early in the compression stroke. Depending on the energy intensity and the proximity to the spark event the LSPI may act as a precursor to 'megaknock', or just an LSPI event. If a LSPI event provides sufficient pre-heating to the unburned gas, the main flame front will propagate with an elevated end gas temperature which increases the propensity to Knock. Even a single megaknock event can potentially destroy an engine. Solely an LSPI event without progress to a Knock event, is less damaging immediately but can result in substantial surface damage if repeated regularly, as it is a locally high temperature and high-pressure event.

Figures 2(a) and (b) illustrate how LSPI can either just be a very early autoignition or it can transfer heat to the unburned zone and create knock.

LSPI normally occurs at low speed (1000rev/min – 2000rev/min) under wide open throttle (WOT) conditions. Reasons as to why it happens at low speed will be discussed later in the thesis. It is also most common with boosted engines because a higher state of enthalpy is available for the autoignition reactions to occur. Retarding the timing actually further promotes LSPI as it is not affected by the intensity of the primary flame front (it does not exist at the time of LSPI autoignition), and so retarding the timing just provides more time and energy to the thermodynamic system to propagate the autoignition event, prior to primary ignition.
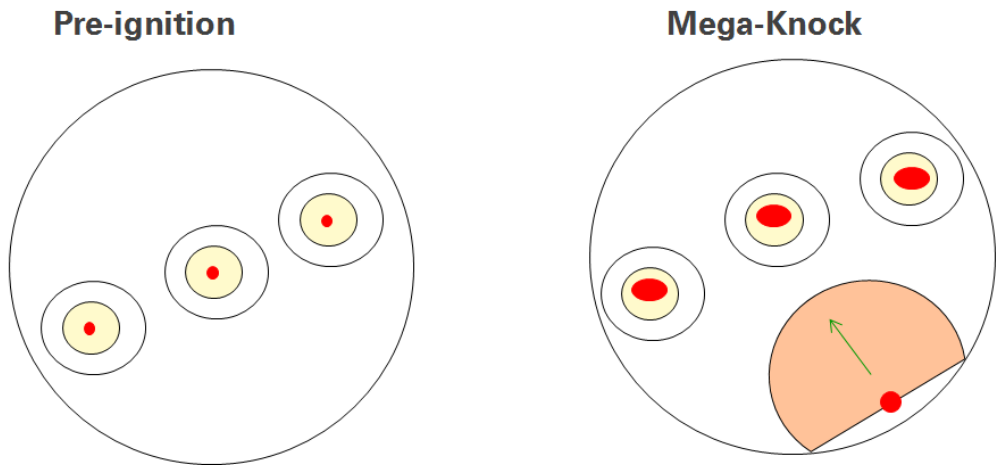
Figure 2 - Illustration of (a) LSPI event (b) An LSPI event which results in Megaknock

MegaKnock can be extremely destructive as described in Passsow et al [57]. Generally, the location of the MegaKnock event will determine if it will result in a component failure. The main components that are impacted include piston (land and ring groove), piston rings and conrod. The piston and rings fail mainly due to fatigue failure, caused by high and local cycling of stress. The rings generally experience chipping due to high pressure, high temperature local LSPI events taking place. Chipping or spalling (surface or subsurface fatigue failure of running surfaces, causing cranks and breaking of material) of the ring coating can cause high blowby (high oil consumption), but the change in roughness could damage the cylinder liner. Specific coatings are being investigated for the affected surfaces in order to reduce damage due to LSPI, this adds cost to the price of vehicles.

2.2. Deflagration, Detonation and Transition

Spark ignition combustion (SI) which commonly uses fossil gasoline as a fuel, relies on a small spark created between two electrodes to initiate combustion. SI combustion can take place under stoichiometric conditions, as the initial flame kernel is sufficient to energise the mixture and increase collision rates to propagate a flame front. Therefore, SI engines often do not require a turbocharger for low power density engines but do require for the air flow to be throttled at part-load increasing the parasitic loss due to pumping. SI combustion is more structured in terms of ignition site and flame propagation, with the 'plug gap' between the electrodes defining the initial flame kernel size. The flame is initially in laminar phase where the flame speed is dependent upon fuel properties, local air-fuel concentration and local enthalpy only. Although turbulence does not impact the flame speed in this phase, it will crinkle the flame front. If the flame does become substantially unstructured, the diffusion of thermal energy becomes spatially intermittent, and the flame can disintegrate. Once the flame stretch is large enough it will be impacted by turbulence and will enter the turbulent flame phase, where reaction/collision rate and thus flame speed is determined by the turbulent kinetic energy adjacent to the flame front. Once again, the timing of the spark event can be controlled to gain maximum thermal efficiency, control emissions and influence exhaust conditions.

A self-sustaining flame propagation can be divided into two categories [31][32]; detonation and deflagration. Both are exothermic reaction fronts propagating through a fuel air mixture. The main difference in their behaviour is their speed of propagation, a deflagration is subsonic (slower than the speed of sound of the air-fuel mixture) and a detonation is equal to or faster than the speed of sound.

A detonation is initiated by a fast heat release at a point in the mixture, this causes a rapid expansion of combustion products which causes a rapid

compression in the gas mixture adjacent to it. This sets up a supersonic pressure wave that will propagate a reaction front due to the increase in enthalpy due to compression and the heat produced by the previous reaction zone.

A deflagration occurs when the combustion process is initiated by a slower heat release, which does not cause a rapid compression, but the heat release is sufficient to ignite the mixture adjacent to the reaction zone. A reaction front will propagate due to thermal diffusion but also due to the release of active radicals from the reaction front.

When the volume of the mixture is constrained by a vessel for example, what begins as a deflagration can transition to a detonation if the unburned gas zone reaches a critical state due to expansion of the burned gases compressing the unburned zone and heat from the reaction front.

It is important to remember an autoignition event can result in both a detonation and deflagration, depending on the ate of heat release. An autoignition take place as a gradual heating process accumulates a high concentration of unstable species, the concentration is also impacted by the constant changing volume, once a critical concentration at an appropriate temperature has been achieved a spontaneous reaction will take place. Even an induced ignition (an ignition initiated by a local high temperature spot, such as spark ignition), begins as a local autoignition that does not create a shock wave, but the heat release is sufficient to create a propagating reaction front driven by thermal and mass diffusion/transport. The reason why some autoignition events create shock waves and others do not is because, the heat release and reaction pathways can be quite different in an induced ignition event. During a detonating autoignition event the temperature of the mixture is normally relatively low and thus a higher number of metastable radicals can be accumulated over a period of time without initiating

43

subsequent reactions. An induced ignition is a very fast event, the mixture is raised to a very high temperature locally, the concentration of intermediate species is very low, and the rate of reaction is mostly influence by the elevated temperature. An induced ignition is defined by its minimum ignition energy.

One should note that just because a particular end gas temperature provides autoignition for a particular engine, the autoignition temperature will change if solely the turbulence is increased. For a higher level of turbulence if the same end gas temperature is attained but at a later stage in the engine cycle (different crank angle), then the combustion volume would also be different to the low turbulence case, as will the concentration in the end gas and thus the rate of reaction is different. Meaning the autoignition temperature has changed.

2.2.1. **Flame types – Laminar, Turbulent and Diffusion**

There are various types of flame propagation, three of the common types that are most relevant to engine operation will be covered in this section [31][32][27].

Laminar flame – This flame exists during the early stages of combustion as the kernel is developed due to a local heat source and will remain as a small portion of the reaction front. The propagation is nominally at a constant velocity. The size of the laminar portion is much smaller than the turbulent length scale inside an engine, and so is not impacted by air motion so much. The only time it may be impacted by turbulence is during the early kernel, when high velocity flow strains and thus crinkles the flame front, slightly increasing flame area. If the flow into the reaction zone is so high that the rate of convective heat extraction is greater than the rate of heat release, this my

44

lead to flame extinction. The laminar flame speed is mostly dependant upon fuel properties, local concentration and temperature.

Turbulent flame – Once the flame is of a certain size the turbulence effects dominate. The level of turbulence will determine the rate at which air is provided to the reaction front and thus determine the propagation speed.

Diffusion flame – This is when a plume of fuel is introduced to air, normally at high velocity. The plume entrains air, mixes and evaporates due to the heating provided. The rate of heat release will be determined by the rate at which the fuel can evaporate from the plume, diffuse into the air and react.

2.3. Standard testing for Abnormal combustion and quantification

There is a long heritage of testing associated with conventional Knock and compression ignition, and standard ways of quantifying ignition quality have been established [27].

For Diesel fuels the most common quantity is 'Cetane number'. The Cetane test involves using a standard Cooperative Fuel Research (CFR) CI engine, running it at a standard condition, and increasing the compression ratio until the ignition delay (time between fuel injection and initial heat release) is 2.407ms. The Cetane number is calculated by assessing which mixture of Hexadecane and heptamethylnonane that would produce the same ignition performance. The Cetane number of Hexadecane is 100 and that of heptamethylnonane 15, from the matched composition a volume averaged Cetane number can be calculated. Unlike Octane number the higher the Cetane number the shorter the ignition delay.

The quantification of Knock behaviour in SI engines also uses a traditional CFR engine, comprising of a carburettor, a knock sensor and once again

45

variable compression ratio. There are two quantities; called Research octane number (RON) and Motor octane number (MON). The running conditions for each can be found in the table below.

RON	MON
Inlet temperature = 52 degC	Inlet temperature = 142 degC
Inlet Pressure = 10atm	Inlet Pressure = 1atm
Engine speed = 600rev/min	Engine speed = 900rev/min
Spark advance = 13 deg bTDC	Spark advance = 19-26 deg bTDC (variable)
AFR (variable for max Knock)	AFR (variable for max Knock)

Table 1 - Comparison between RON and MON testing

The compression ratio is varied between 3-30 until Knock is detected. The results are scaled between those of Heptane (ON = 0) and IsoOctane (ON=100).

2.4. Scavenging and burned gas residuals

An engine consists of intake valves allowing in fresh air and exhaust valves for burned gas to exit. Many engines use VVT (variable valve timing) to optimise the timing of the opening to achieve maximum volumetric efficiency. The volumetric efficiency is the ratio between the actual mass inside cylinder (calculated from mass flow during intake stroke) and the theoretical mass that would be contained if the density of air inside cylinder was equal to a reference density (often based on manifold pressure and temp) [27]. In the case of a Miller cycle engine, a later opening of the exhaust valve allow for a larger effective expansion ratio i.e. the expansion work done on the piston until the exhaust valve opens and reduces the cylinder pressure. However,

this also means the intake valve will open later, but this loss in flow is compensated by a turbocharger or supercharger.

During the exhaust valve closing (EVC) and intake valve opening (IVO) there is a period called the overlap period when all valves are open to different extents. It is highly desirable to get maximum scavenging during the overlap period. When the intake pressure is higher than the cylinder pressure and cylinder pressure is higher than the exhaust pressure, burned gas residuals in the cylinder will be transported out of the cylinder, this is called scavenging [69]. The greater the difference in pressure, the more efficient the scavenging. Because pressure waves are created between the compressor/turbine and intake/exhaust valves. The valve timings should be set to avoid periods when the exhaust pressure is higher than cylinder pressure to avoid reverse flow. Similarly, the intake valve period to capture a peak in intake pressure.
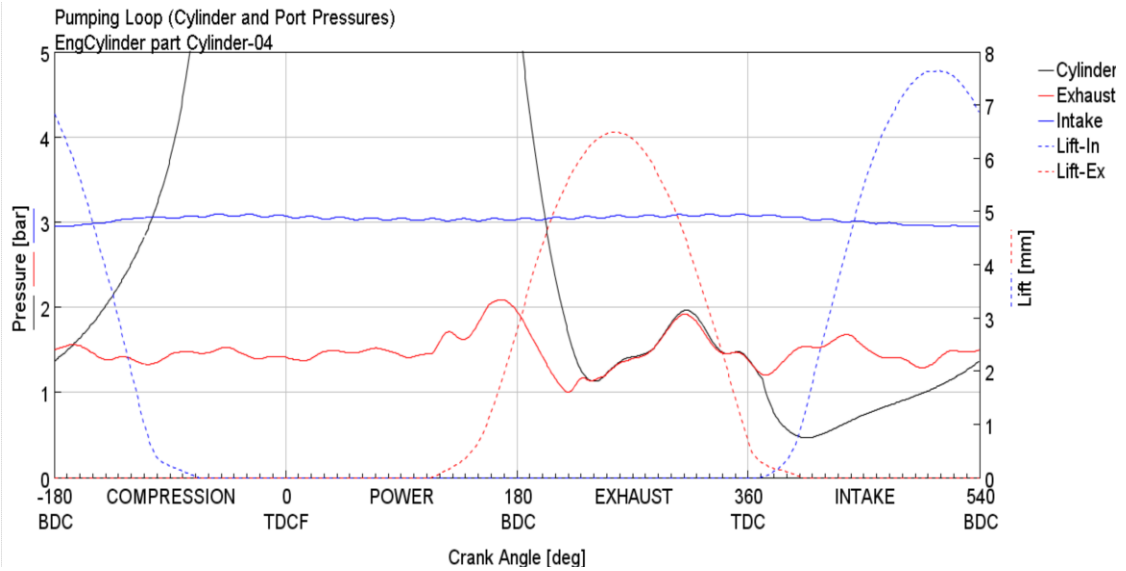
(a)
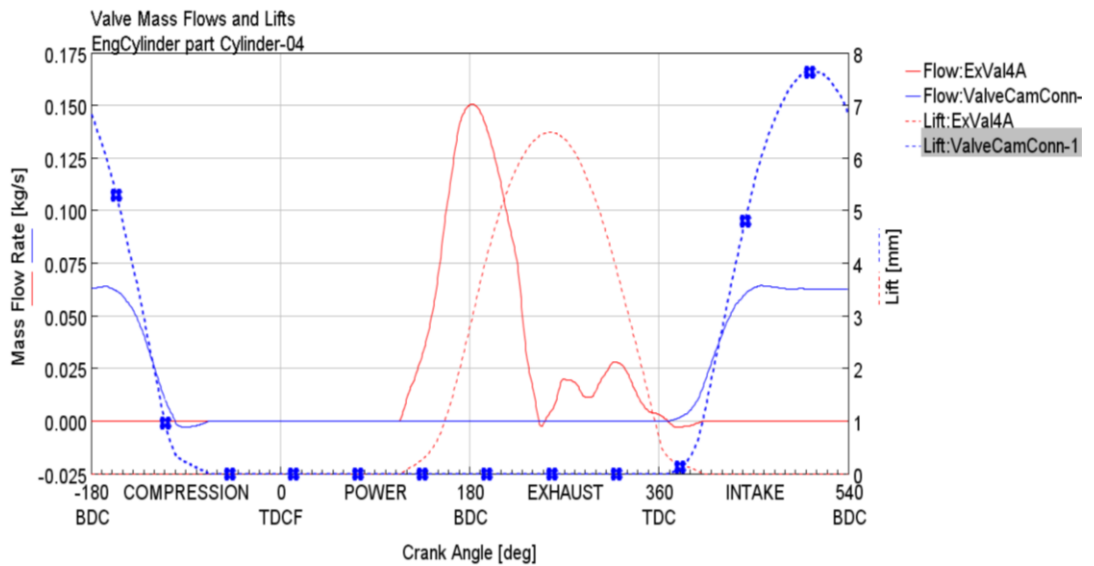
(b)

Figure 3 - (a) Pumping plot of single cylinder engine operating at 5000rpm WOT (b) mass flow plot of single cylinder engine operating at 5000rpm

Figure 3 shows an example of engine gas dynamics for a single cylinder engine (from the SC1 engine that will be simulated later in the thesis). The intake pressure profile is more stable than a normal engine because there is no interference from adjacent cylinders, but also because an electrical compressor is used with a very large plenum to dampen anu oscillations.

Although the intake pressure is quite high it offers limited scavenging because the overlap period is so small for this condition. However, what can be observed is that cylinder pressure drops below the exhaust pressure during overlap, and some negative (reverse) flow is observed from the exhaust valves.

2.5. Pistons and blowby

A piston is made up of several components, each one plays a key role in assuring the primary mover is functioning and protected. A description of the main parts is provided below [69]. A detailed schematic of the piston assembly is also provided in Figure 11 (b):

Piston bowl – This is the part of the piston that interacts with the gases inside the combustion chamber. It is designed to order the air motion and fuel spray in the desired direction. It will also have recesses designed to avoid a collision with intake and exhaust valves.

Piston skirt – The skirt is the part of the piston that is in contact with the liner. It keeps the piston aligned within the cylinder throughout its motion. It is often coated with a slightly rough material to hold oil and improve lubrication.

1st Compression ring – This assures no gas from the combustion chamber escapes into the crankcase.

2nd Compression ring - This is a reinforcement ring to prevent any gas that escapes past the first compression ring does not travel any further. It also assists in wiping off any excess oil on the down strokes.

Oil control ring – These are situated at the bottom of the piston and control the amount of oil available for lubrication, they wipe of excess oil but also spread oil evenly around the circumference of the bore.

Piston grooves – These are recessed regions that hold the piston rings. They can be problematic as pistons rings expand and move during the engine cycle; it becomes possible for gases to escape from the groove region.

Gudgeon pin – Connects the piston to the connecting rod. It provides a pivot as well as a bearing surface for the two members to rotate relative to one another.

Despite measures to avoid it taking place, in most cases some gas does manage to escape from the combustion chamber into the crankcase, this gas is known as blowby[27]. The gas is then ventilated via the breather back into the intake (closed circuit breather). Chowdhury et al [60] completed a multi-dimensional simulation to understand gas flow past the piston rings during an engine cycle. The study shows there is significant circumferential flow between the rings, this gas is pressurised and forced towards the combustion chamber during the expansion stroke.

2.6. Standard viscosity measurements for lubricant oils and Lubricant composition

Lubricants play a key role in assuring engine health and are the only protection between frictional components. Lubricants not only protect surfaces from wear and pitting but can also often reduce the losses associated with sliding contact [27].

A lubricant comprises of several components in order to allow it to carry out its function:

Base Oil – This is the main component the lubricant consists of. It is the main hydrocarbon source, obtained from distillation. The API (American Petroleum Institute) divide base stock oils into five groups depending on which crude oil they are refined from and whether they are synthetic. Each one of the groups will have a different range of saturates, Sulphur and Viscosity Index (explained later).

Detergents – These are metal base soaps that are used to neutralise harmful acids present in the engine.

Magnesium and Calcium based detergents are the commonly used in the automotive sector.

Dispersants – These are hydrocarbon chains with a highly polar functional group. The role of the dispersant is to distribute contaminants within the lubricant. One of the main parameters used to evaluate a detergent is the Total Base Number (TBN). This is a measure of the detergents ability to neutralise acids, also called basicity. Basicity is quantified in KOH/g, meaning the amount of equivalent Potassium Hydroxide per gram of oil. W. van Dam et al [59] shows that you require a mixture of both Mg and Ca detergents to start with and sustain a high TBN. It is suggested the Ca neutralises a broader range of acids, so allows for a high initial TBN but is consumed quickly as it forms salts in neutralisation. The Mg detergent neutralises a narrower range of acids, and thus helps sustain a high TBN.

51

Anti-Wear – This forms a 'tribofilm' layer on the surface of metal components, a sacrificial layer that prevents metal to metal contact.

Viscosity modifier – Changes the viscosity of the lubricant within a specific temperature range.

Antioxidant - Because of the elevated temperatures and pressures observed within an engine, the hydrocarbons within the oil can oxidise to form deposits. Antioxidants are used to starve the lubricant of oxygen.

Viscosity is a key fluid parameter for lubricants as it is a measure of the fluid's resistance to shear. It will determine the force required to move two sliding surfaces relative to another, film thickness and generally the nature of fluid flow. Because the contribution of the lubricant in promoting LSPI will be investigated it is important to understand viscosity as it will be a dominant factor in its transport.

Oils are normally given a SAE grade of the form XWYY [66]. The number before of the W is an indication of the oil viscosity under cold temperatures, cold cranking and cold pumping conditions, and the number after is a rating for its viscosity warmer temperatures (100degC for low shear rate and 150degC for high shear rate).

Another commonly used value is the viscosity index [66][65]. This value assumes the KV (kinematic viscosity) of lubricants at 100C is similar and compares the KV at 38degC in a standardised way. The difference in kinematic viscosity between the oil of interest and a high and low quality reference oil are calculated. The low reference is divided by the high reference difference to calculate a % VI.

Because an engine environment can get very hot, and the frictional conjunctions provide very high shear rates, the High temperature High shear viscosity (HTHS) becomes of utmost importance. To measure the HTHS, the fluid is introduced into a rotary ultra-high shear viscometer at 130degC. The viscometer has concentric surfaces, meaning the shear rate can easily be measured from the rotational speed. The viscometer measures the torque, allowing for the shear stress to be measured. Finally, the HTHS viscosity can be calculated.

2.7. Generic Hydrocarbon combustion process

Initiation – Disassociation of C-H bonds and to a lesser extent C-C binds forming alkyl groups.

C-C bonds break at high temperature

Propagation – Formation of metastable peroxyl radicals and peroxides. Rate determining step (ignition delay). Negative temperature coefficient

Degenerative chain branching – Predominantly the decomposition of peroxides to form radicals or stable molecules (small heat release).
- Low temp: requires free radicals
- Hight temp: nonradical decomposition

Termination – Destruction of radicals to form stable combustion products. Large heat release

Zeldovich – Nox reactions. Pathway very dependant upon temperature

Figure 4 – Generic phases of Hydrocarbon combustion

The generic hydrocarbon oxidation and heat release process can be seen in the flow diagram above [27][32]. The process begins with the disassociation of C-H bonds and C-C bonds at higher temperatures. Following initiation, is a

53

step that ultimately determines the ignition delay of the combustion process, this is essentially a stage that involves accumulating metastable radicals until a critical concentration is attained. Once the concentration of peroxyl radicals and peroxides is high enough the degenerative chain branching process will begin, this involves the decomposition of peroxides into more unstable radicals or stable combustion products, there may be a small heat release at this stage. Degenerative branching of peroxides creates OH(hydroxile radicals) or decomposes to oxidise and give a small heat release (CO_2, CO and H_2O).

Finally, the combustion process concludes with the termination and destruction of free radicals into stable combustion products, producing a large heat release. The Zeldovich reactions help model the creation of NO/NO_2 combustion products, which are a harmful emission.

During propagations, alkanes such N-heptane demonstrate a negative temperature coefficient (rate of reaction reduces with increasing temperature). The NTC occurs because the formation of HO2 radicals becomes more dominant than the peroxide radical production and isomerisation reactions. HO2 radicals are more stable and their propagation reactions are less exothermic than peroxide. Thus, the rate of reaction reduces with temperature until higher temperatures when the formation of peroxides begins to dominate again.

2.8. Experimental investigation of LSPI

Several technical papers have found experimentally that the addition of a Calcium based detergent in engine oil increases the propensity of LSPI, to the extent to it is unanimously agreed upon despite there not being a robust theory to explain the mechanism behind the combustion event. One of the

most persuasive explanations for a Calcium initiated combustion event was offered by Moriyoshi [19] following tests conducted on a 4-cylinder turbocharged production engine (GTDI). To extend the testing an additional supercharger (powered by a motor) was added to the engine configuration. This would allow then engine to run at higher boost pressures, increasing the testing domain to higher levels of in cylinder enthalpy. The engine was held at 1750 rev/min, boost pressure was 190 kPa, AFR was 14.5 and fuel injection was as per the engine map. This condition was chosen because preliminary testing had confirmed it yielded the highest level of LSPI. The engine was held at this condition for three 30minute durations with a cool down and warm up in between. The fuel used was the domestic high-octane Japanese gasoline (RON 100). An endoscope was attached to the cylinder head in such a way that the gas volume could be viewed from a side position as the piston heads towards TDC. A high-speed digital camera was also used to capture images of the LSPI events. A fluorescent imaging technique was also used to identify lubricant oil droplets inside the cylinder.One of the aspects that were investigated in this study was the impact of coolant temperature. It was found a lower coolant temperature significantly increased the number of LSPI events. The explanation offered was that the cooler cylinder liner temperature condenses more of the fuel that impinges on the wall, causing dilution of the oil film, the resulting reduction in viscosity mean more of the oil is introduced into the combustion chamber as the piston moves upwards. With regards to the effect of injection timing it was found there was an optimal timing of 120 deg ATDC which provided the lowest level of LSPI, the LSPI frequency increased as the timing was advanced or retarded relative to this point. Pre-

ignition was mostly observed around the exit of the piston crevice volume. It was observed the pre-ignition was initiated by hot particles attached to the wall and detached, there were also signs of the oil droplet itself acting as the heat source. The visual description of the autoignition event was with the origin being a glowing particle followed by flame propagation. The LSPI events consistently developed into knock events. An interesting finding was that a ring of a luminous flame was observed around the crevice volume even after the main combustion event, toward the latter stages of the expansion stroke. This autoignited ring is thought to be a mixture of fuel and lubricant. A Ca free oil was tested on a single cylinder engine and as expected no LSPI events were measured. The mechanism proposed is; $CaCO_3$ particle thermally degrades to CaO particle during the expansion and exhaust strokes, it then cools during the intake and compression strokes during which it cools and reacts with the available CO_2 to for $CaCO_3$ again. However, the formation of $CaCO_3$ is an exothermic process and thus is potentially a source for pre-ignition. A study was completed to predict the autoignition of a CaO particle under constant temperature and pressure for varying particle size and equivalence ratio of the IsoOctane-air mixture. It was found the ignition delay reduced with increasing particle size and with a richer air-fuel mixture.

Kuboyama et al [44] investigated LSPI using a production GTDI engine that was modified to allow for an endoscope to view pre-ignition events. Light induced fluorescent imaging and direct photography was achieved by a fast imaging camera through the endoscope.Various hot particles and deposits could be

observed in the combustion volume during the compression stroke, for cycles with LSPI. A luminous flame was also observed near the crevice area during the exhaust stroke. From this it was inferred the oil-fuel mixture could burn under low Oxygen conditions, and the hot particles that cause LSPI are the remnants of oil combustion during the expansion stroke. The crevice volume is cooler, and the flame is quenched before entering it, so it can undergo slow combustion before being exposed to the main burning/burned volume. Most of the pre-ignition events were observed close to the crevice volume, and they were rarely sequential, very stochastic. It is proposed this specific engine may have low LSPI frequency because of efficient scavenging, as it is suspected LSPI is initiated by residual deposits from the combustion event remaining in the cylinder. With this engine these our scavenged from the cylinder.

LSPI has been an area that engine designers have struggled with for quite some time. It has generally been found that any hardware modification that resulted in a reduction in LSPI had other draw backs. For example, increasing ring tension also increases friction. Increasing the crevice volume will reduce the compression ratio and increase the inactive volume of the combustion chamber. It has been suggested the solution is one of a combined effort of engine and oil design. For this reason, Mounce et al [45] summarises a sequence IX test that will be added to the ILSAF GF-6 test for automotive lubricants. A design-of-experiments was carried out to establish the engine running conditions that were most prone to LSPI. LSPI events were identified using cylinder pressure data. Following this, the LSPI causing conditions were

run using various lubricants to see if a test could be devised to differentiate between lubricants.A statistical average is calculated for the 'normal' condition peak pressure and the mean MFB2 was established. An abnormal combustion event is one that has a peak pressure that is in excess of the normal by a minimum of a predefined standard deviation or a MFB2 that is less than a defined standard deviation of the average.A steady state condition of 1750rpm and 17bar produced the most LSPI. Increasing the intake temperature and oil temperature increased LSPI frequency.

Impact of the age of oil and age of engine on LSPI is investigated by Michlberger et al [46]. The level of LSPI was monitored for engine-dynomometer testing as well as vehicle testing on roads. For phase 1; a GM 2.0L GTDI engine was tested on a dyno, the engine was brand new. A cycle comprising of a series of steady state points; all high load with engine speed varying between mid-speed and low speed, this test was repeated 4 times, and conducted to establish the level of LSPI. Following this, an ageing cycle was completed, these points were taken from a WLTC. The ageing cycle was repeated 100 times and the LSPI evaluation cycle was repeated following every 100 cycles of the ageing cycle. After the engine had completed a total of 11250 simulated vehicle miles, the oil was replaced with fresh oil and the LSPI evaluation test was run to assess the impact of engine age on LSPI. The engine was then installed into a Buick Regal and driven on roads for a total of 65000miles, whilst adhering to the oil spec and oil drain intervals in the handbook. The engine remained instrumented to identify LSPI events. Finally,

the engine was removed from the vehicle and placed on a dyno again, the LSPI evaluation tests were repeated using old oil from the road test and fresh oil, with what is now a much-aged engine.During simulated cycling, the number of LSPI events initially went up and then later went down. Overall, LSPI events for low and high speeds reduce with engine age. Although the age of oil did not impact the number of LSPI events, fresh oil increased the proportion of single LSPI events (separated by 3 or more normal cycles). As the engine ages the number of LSPI events demonstrating an elevated peak pressure increases, as does the number of cycles showing both an elevated temperature and an early MFB02 angle increases.

The study of Welling et al [48] looks at the impact of 'contaminants' on LSPI propensity. Testing was conducted on a Ford Sigma Zetec engine. Although the engine is naturally aspirated, and port injected. It has a particularly high compression ratio of 11:1. One of the cylinders was modified to allow for a DI injector that can be used to inject contaminants and the spark plug was inactive so that the only heat release that could be detected was from autoignition.No trend was observed between PI frequency and API (American Petroleum Institute lubricant groups) categorisation. For groups I-IV the higher group number corresponds to lower levels of aromatic content. A petrochemical diester was found to reduce PI substantially. Generally, the base stocks with the longest ignition delay provided the least PI events. The calculated ignition index correlated with the PI frequency, with the highest index providing the higher PI.

The impact of oil formulation on LSPI has been investigated in several publications. However, another curiosity has always been as to whether the nature of the impact of lubricants on LSPI changes with both engine and oil ageing. The physical and chemical state of the oil will change over time as will the condition of the engine as parts wear, debris is created, and surfaces covered with combustion products. Swarts et al [50] carried out an extensive study investigating the impact of ageing under conditions that would exacerbate LSPI. The testing used multiple installations of the GM LHU Ecotec engine (2.0L). A relatively modern GTDI engine. The engines were adequately instrumented, including in-cylinder pressure measurement. Care was taken during oil change to assure minimal carry-over, followed by an engine health check to detect any drift in performance. The P3 test cycle was employed for each of the test cases. A simple test that consists of 24 segments of 2000rev/min at high load. The steady state spark timing was retarded and AFR made leaner to increase the propensity of LSPI.Health checks were performed at regular intervals throughout the cycle to assure the results were not compromised due to changes in engine performance. The final 25000 cycles were analysed for LSPI. To define an LSPI event a criteria was used that mean any event with a peak cylinder pressure beyond a define standard deviation from the mean, and a MF2% (crank angle at which 2% of the fuel is burned) less than a defined deviation from the mean, was counted as an event. Two baseline oils and several candidate oils were used. The baseline oils very similar in their formulation; synthetic oils with more than 2000ppm of calcium and almost no Magnesium. The fuel remained the same

for all the test cases.The overall conclusion was of this paper was that despite using separate engines, differing lubricants and running tests in a consistent was, insufficient evidence of any trend due to ageing could be extracted from the data. LSPI mechanisms continued to be extremely stochastic throughout the life of the engine. Results even varied when exactly the same test was repeated for the same lubricant.It is deemed that extra care is required to examine the engine components variation, engine build and test bed setup from one test case to another. To extract meaningful results advanced statistical analysis is required to interoperate the disperate nature of the data but also correct for any segment repeats or additional health checks that may be required on specific engine, to allow for a fair comparison between cases. Although in this case all test were conducted on a single type of engine, there is nothing to suggest that similar behaviour would not be observed on any other GTDI engine, or that LSPI would be any more orderly in the field.

LSPI is possibly not just limited to gasoline engines. Konigsson [51] investigated the impact of LSPI on CNG (compressed natural gas)-DDF (Diesel dual fuel) engines as part of his PhD thesis. Although the purpose of the thesis was to investigate combustion behaviour of such an engine in totality, inevitably LSPI and knock (autoignition) will play a major role. The thesis predominantly investigates a port injected DDF engine. Methane is injected into the intake manifold and mixed with air during the intake and compression strokes. A micro-pilot injection of Diesel is introduced late in the compression stroke to initiate combustion. It is thought the approach

potentially offers the thermal efficiency benefits of a Diesel engine, due to being a compression ignition process, but emissions similar to an Otto engine as the flame will be propagating. DDF engines allow for a leaner mixture, so the part load pumping losses normally associated with Otto engine is less significant. The Diesel must have a high Cetane number to assure a precise and fast ignition (small ignition delay). A single cylinder Scania lab engine was used for the experiment. It is a 2L displacement. The gas injectors were placed in the runners and fed by a high-pressure common rail system. Pure Methane was used for most of the experiments. Although for the pre-ignition tests a Biogas was used (97% Methane, 3%CO_2), as well as two gas blends of Methane number; 70 and 80 were used. The Methane number is a quantity very similar to the Octane number for Gasoline and represent the fuels resilience to autoignition when tested using an industry standard engine. For the ignition fuel a Petroleum Diesel with 10% RME (repressed methyl ester). A range of lubricants were used for the LSPI investigation, all with varying viscosities and Calcium content. To gain some appreciation of in cylinder temperature the injector was instrumented with a thermocouple. To assess the likelihood of local hotspots giving rise to LSPI in a controlled manner, two glow plugs were placed in the head accompanied with a thermocouple. A feedback loop would control the current to the slow plugs to achieve the desired surface temperature.The LSPI tests were conducted at 1400rev/min, at IMEP points between 12-22bar.The results show that Knock onset load due to pre-ignition is not impacted by the Methane number of the fuel, generally speaking mega-knock always occurred at 15bar IMEP. Although the average knock amplitude increased for lower Methane number fuels. Knock amplitude

62

with and without LSPI events were compared. The difference below 18bar IMEP was minimal. However, the knock amplitude grew substantially for the LSPI cases above 18bar IMEP. In this case the LSPI is the limiting factor preventing the engine from reaching elevated torque, as conventional knock can be mitigated by retarding the timing whereas it will just give more time for oxidation reactions for LSPI events. Oscillations also occur due to the detonation of micro-pilot injection. Meaning that the knock oscillation measured is a superposition of the oscillation due to knock and what remains of the ignition shock wave. When the maximum torque curves achieved by the various gas fuels are compared against the Scania production Diesel, the torque at all speeds are lower. Although, as expected the higher Methane number fuels allow the engine to achieve higher torque. Even with a Methane number of 100 the maximum torque achieved is approximately 5bar IMEP less than the Diesel engine. The factor limiting this technology can almost entirely be attributed to LSPI activity.When the LSPI testing was 800rev/min, 1225rev/min and 1600rev/min no increase in the number of events was seen at 1600rev/min with increasing load. At the lower speeds however, the number of LSPI events increased with IMEP. The number of events at 1225rev/min were higher than the number observed at 800rev/min. A small calibration parameter study was carried out and compared to the results obtained from the base calibration at 1225rev/min. A large difference was seen when the intake manifold temperature was increased, the number of LSPI events increased and the engine was unable to achieve an IMEP above around 14bar. This is expected as it will increase the temperature during compression, making early oxidation reactions more likely. Increasing the

63

external EGR helped to reduce the number of events by diluting oxygen concentration in the air. Late CA50 helps reduce the temperature of the end gas but has a detrimental impact on thermal efficiency, as well as allowing more time for the LSPI process. The exhaust valves are a prime suspect for components that could provide a hot surface to provoke LSPI. LSPI experiments were compared between a standard valve and Sodium cooled valve. A Sodium cooled valve is one which has its hollow interior filled with Sodium. The Sodium melts and then evaporates at the hot face of the valve, it then rises to the top/cooler end of the valve and dissipates heat to the cooler face. This causes the Sodium to condense and return to the bottom/hot side again. The cycle continues. A Sodium cooled generally has a surface temperature that is about 100degC lower than a conventional valve. At 21bar IMEP the number of events for the standard valve increased. Similarly, a supplementary experiment involved controlling the glow plug temperature, another source of local heating. Again, there was no obvious correlation between glow plug surface temperature and LSPI events. The various lubricants showed mixed results. There was some indication that Calcium content had an impact on LSPI, but it seems viscosity had a more affect. Interestingly a lower viscosity demonstrated a lesser susceptibility to LSPI. Oil viscosities varied between 5W30-15W40.

Although LSPI is predominantly a lubricant formulation problem, studies have shown that fuel selection can have a profound impact on LSPI propensity. One of these studies is kar et al [53], in which they carried out extensive

64

experimentation with different combinations of fuels and lubricants to measure LSPI mitigation performance. In addition, they quantified the potential benefit to BMEP as a result of LSPI reduction. Fuel selection has an implication on all emissions, but in particular particulate matter, both particulate matter and particular number were measured in this study. Particulate number is the total number of particles per unit volume of exhaust gas and the particulate mass is the total mass of particles per unit volume of exhaust gas. A 4 cylinder, 2L, GTDI engine with external (cooled) EGR was used for this investigation. The positive crankcase ventilation (PCV) was disabled, and crankcase gases were vented through the oil filler cap. The air inlet conditions were very carefully controlled, coolant temperature was controlled using an external heat exchanger, and an additional oil cooler was added for the oil system. For most cases the cooled EGR was not used, and spark timing was constant for a given speed-load point for all experiments. To detect LSPI, once again the MFB2% was used to measure SOC. A mean SOC was calculated for the non-pre-ignition cycles, and the initial detection for LSPI was defined as any cycle that has a SOC less than 5 standard deviations from the mean. A subsequent stage of filtering involves analysing the cylinder pressure at spark timing. If the SOC is less than 5sd than the mean and the pressure at spark timing exceeds a pre-defined threshold, the event is finally counted as LSPI. The first tested involved running the engine at a steady state speed load point for 160000 cycles, followed by engine health checks and an oil system flush. Following a trial of various low speed, high load conditions it was found the running condition of 1500rev/min, 21bar BMEP and Oil, coolant temperatures of 80C and an intake temperature of 30C were found to provide the highest epm

65

(events per million cycles). A second test procedure consisted of four lots of 80000 cycles at 1500 rev/min. The load was increased by 1 bar BMEP for each portion of 80000 cycles. All the lubricants selected were of 5W-30 viscosity grade, similar HTHS, similar viscosity index and the same viscosity modifier. The difference between the lubricants was the concentration of detergency, commercial solutions for low LSPI and the concentration of friction modifier often thought to suppress LSPI. For all tests, LSPI increased with low engine speeds, higher loads, high intake temperature and cooler coolant temperature. The tests showed that LSPI has a high dependency on lubricant formulation. The dominant contributor being Calcium detergent concentration. LSPI events increases with increasing Calcium presence. Magnesium detergents only provided a small suppression of LSPI. It was concluded that although friction modifiers do help reduce LSPI, they should not be considered a primary route because of the composition restrictions placed by the industry. Based on the findings an optimal lubricant was developed. This lubricant drastically reduced LSPI events and expanded the engine's low speed, high load operation envelope. Fuel selection also impacts LSPI propensity. Fuels with a high molecular mass, have high boiling points and are thus more susceptible to wall wetting and oil dilution. This could reduce the viscosity of the wall film and have a higher chance of escaping into the combustion zone. For the engine conditions that were run, a high aromatic content in the fuel resulted in high LSPI, high particulate mass and high particulate number. Interestingly, a close correlation was observed between LSPI events and an increase in PM (particulate matter) emissions. A spike in PM emissions consistently followed a LSPI event.

As mentioned in the introduction, downsizing has been the dominant strategy car manufacturers have employed to improve power density and thermal efficiency. The extreme levels of downsizing were investigated by Turner et al [34] using a JLR naturally aspirated 5.0L V8 engine. The aim of the project was to show that the engine could be downsized using advanced engine technology to achieve the same torque curve as the original NA (naturally aspirated) engine, whilst contributing substantially to the target 35% CO_2 reduction at the tailpipe for a New European Drive Cycle (NEDC). The original engine was baselined in terms of fuel consumption and maximum torque. The engine was then substantially modified, initially fitted with an air handling unit to behave like an advanced charging system. The engine was tested in simulated supercharged mode when the correct pressure and temperature for various conditions was provided at the intake; the values were based on a 1D engine simulation. The brake load that would have been required of the engine to power the supercharger was also calculated by simulation and imposed using the dyno. For the turbocharger case the predicted pressure and temperature from the 1D simulation was used and an active valve was used to simulate the back pressure from the turbine. The engine was also tested with an actual turbocharger later. Various other changes were made to the intake port geometry, the valvetrain design shifting lift profiles and phasing, advanced engine management system (EMS), PFI and DI injection modes. This study found that the chosen engine was able to produce a reduction in fuel consumption in the order of 23% relative to the original baseline with a displacement reduction of 60% (5L to 2L). This shows that downsizing still has margin for fuel consumption reduction, and any improvements that can be

67

made to knock mitigation allowing for spark advance will further assist fuel economy.

2.9. Existing theories and Mechanistic models of LSPI found in literature

As a result of the experimental and observation-based findings in the literature survey so far, there are several theories that are alluded to or one could deduce from, as to the mechanisms that lead to LSPI. In this section we will cover two of the most prominent theories that exist in literature. The two subsections will cover autoignition due to hydrocarbon components of the lubricant, autoignition due to detergents present in the lubricant and finally the impact of fuels selection. Although most current theories suggest it is deemed necessary for the lubricant to initiate the ignition, the fuel selection can play a role promoting the ignition process.

2.9.1. LSPI initiation due to the reaction of lubricant hydrocarbons

Dahnz et al [17] and Palaveev et al [18] established that an oil droplet can auto ignite and act a source of ignition if the droplets hydrocarbons are similar to that of Hexadecane and N-Heptane. Following on from this Mitsuaki Ohtmo et al [16] completed a set of experiments using a rapid compression and expansion machine (RCEM) to understand the factors that impact the autoignition propensity of an oil droplet. The RCEM consisted of an optical window and a high-speed camera, when the autoignition was not visible the UV light emitted was measured. A single oil droplet was introduced into the

68

chamber using an injector that has been modified to allow for control over droplet diameter. A heat pipe was used to control the temperature of the droplet. The compression chamber will contain a pre-mixed air- Gasoline fuel mixture. When the droplet reached a wall before autoigniting the droplet was captured and suspended at the top of the chamber using Tungsten wires, this was to assure the ignition measurements were not corrupted due to quenching from the wall and the whole droplet was exposed to the fuel-air mixture. A compression speed representative of 1200rpm engine operation was selected and the piston was held at its top-dead-centre (tdc) position for 5ms. This is an attempt to create conditions that cause the oil droplet to ignite before the fuel-air mixture. The 5ms limit is a measure to protect hardware as a rapid increase in pressure will be observed in the event the fuel-air mixture is ignited. It was found the ignition delay was shorter as the droplet diameter was reduced (varied between 60-500µm). This suggests the reactions are phase change limited; and the heat transfer and rate of evaporation is what determines the ignition time. A large molecule has higher thermal capacitance and thus takes longer to heat up, resulting on slower evaporation. The oil needs to be in a vapour state to ignite, as vapour has a higher enthalpy. The higher energy state allows for more collisions with reactive species, collisions of a higher momentum and the dispersed nature of a gas allow more access to molecules. Similarly, a higher initial droplet temperature means the droplet requires less energy transfer from the surroundings to achieve a given evaporation rate, it was observed higher droplet temperatures also reduced ignition time. The experiments were conducted using two different hydrocarbons: N-dodecane and N-hexadecane, with N-dodecane having a

69

lower boiling point and lower cetane number. N-dodecane was found to have the shorter ignition delay, despite having a slower ignition process in its gaseous state (lower Cetane value), this once again confirmed the dominance of the evaporation phase. It was observed an initial ignition took place in the cloud of vapour surrounding the droplet, which provided energy for a second ignition that originated at the droplet liquid-vapour interface and proceeded through the whole droplet. The two ignition events were sufficient to ignite the fuel-air mixture in the chamber and initiate a propagating flame front. Higher droplet temperatures also increased the probability of vapour ignition, most likely due to the higher concentration of vapour. The experiments were repeated using fuels of various MON numbers (MON 100-130) for the premixed air-fuel mixture. It was noticed the increasing MON number did reduce the probability of vapour ignition, suggesting this is a problem that is coupled between fuels and lubricants. However, a very high difference in ignition probability was observed when the mixture was diluted using an inert gas by 10% and 20%, the probability reduced from 0.8 to 0.2 for a MON 100 fuel. This means diluting the air with a gas such as EGR (cooled) can reduce reactive species collision rate to such an extent that vapour ignition is almost mitigated.

Distaso et al [49] attempted to simulate the hydrocarbon reaction aspect of lubricants and the subsequent impact on pre-ignition using a 3D CFD approach. Hexadecane with a reduced reaction mechanism scheme was used to represent the lubricant. Fluid property and ignition delay data of

70

Hexadecane were found to agree with that of a lubricant. The surrogate ignition fuel was represented by Iso-Octane. The reduced mechanism comprising of what were deemed to be the most influential reactions were used for a 0D combustion simulation of a uniformly mixed control volume. The time-based pressure rise was compared to a simulation comprising of a full reaction mechanism. A good agreement was found. A CFD based autoignition simulation of an oil droplet was to be developed and validated against IQT (Ignition Quality Tester) tests that were conducted for an oil droplet by kuti et al. A lagrangian scheme was used to model the fuel spray and a Eularian scheme for the gas phase. For combustion modelling a Sage chemical kinetics solver was used with adaptive zoning, which puts continuum cells into bins of temperature and equivalence ratio then calculates a solution for each bin. This allows for a more time efficient solution. The IQT test is a bench device that is used to measure the ignition delay time of common hydrocarbons. In particular it is used to recreate conditions that are representative of the end gas of a DISI engine. It consists of a control volume with external (electrical) temperature control, and a known mass of combustible is injected from one side into the gaseous phase. The composition of the Hexadecane-IsoOctane based fuel was as per the experiment carried out by Kuti et al. The procedure was in alignment with the standard ASTM D6890-08. The IQT equipment is 0.213L in volume and consists of a large combustion chamber with a narrow end tube. As with the Kuti et al experiment, the purpose of the simulation is to assess how and if the presence of Hexadecane reduces the TID (total ignition delay) time of IsoOctane. Kuti et al created conditions like those typically found close to

71

ignition in a GTDI engine, and the similar conditions were simulated in this case. This was an initial pressure of 15bar and temperatures 730, 770, 800 and 833K. 83mg of fuel was injected into the combustion chamber. The TID values were calculated using the gradient method (using the derivative of the pressure profile to establish start and end of ignition). When fuel is initially injected into a gaseous phase the pressure drops as the liquid quenches the mixture and then cools it further as the fuel evaporates. In and engine the temperature will eventually 'recover' due to compression of the mixture, in this case the recovery is due to external heating. A tangent is drawn at the point when the pressure returns to that at the soi (start of injection). A second tangent is drawn at the maximum derivative point during the thermal runaway phase (steep change in pressure). The point at which these two tangents intersect is considered the ignition point, and the duration between soi and the ignition point is the TID time. It was found the reduced 'gaslube' mechanism of Hexadecane, representing the lubricant provide TID results that are in good agreement with test data. It was found even very small amounts of lubricant can hugely reduce increase the ignition propensity of IsoOctane. Under the pressure and temperature conditions mentioned above; 1% increase in volume of the lubricant reduces the TID by 15%, a 10% increase in lubricant volume can reduce the TID by 54%. An exponential curve can be fitted to the reduction in TID time against percentage volume of lubricant present. The ignition delay period prior to the rapid thermal runaway phase is divided into two phases; the physical ignition delay (PID) and the chemical ignition delay (CID). The PID is the period from the soi to the point of maximum reduction in pressure, also called the point of inflection (poi). This is the period when the

72

fuel is breaking up, evaporating, and diffusing. The CID phase is the period when the early stage/slow reactions are taking place and is measured from the poi to ignition point calculated from the two tangents. It was found the PID was mainly responsible for the reduction in TID when the lubricant was added to Iso-Octane. Meaning the fast evaporation was the cause of the eventual rapid heat release rather than the impact of chemical species interacting between the two fluids. It is difficult to establish why the addition of Hexadecane makes the IsoOctane evaporate faster, but we can speculate the and energetic buffer is created between the IsoOctane molecules, reducing their intermolecular forces and thus making it more volatile. However, this behaviour was only observed at high temperature. At lower temperatures, the reduction in PID with increasing Hexadecane volume was far less pronounced. In fact, the difference became smaller at higher percentage volume. It is well known that IsoOctane combustion takes place in predominantly 2 stages at high temperature and predominantly 3 phases at low temperature. With increasing quantity of Hexadecane the intermediate phase became less present. Reducing the combustion phases to 2 phases at low temperature and almost 1 phase at higher temperatures. The paper suggests the early-stage reactions which involve hydrogen peroxide and isomerization reactions are the most dependant upon fuel chemistry and ultimately determine low temperature heat release (LTHR). Hexadecane has a high Cetane number making it suitable for a short ignition delay. The longer and more flexible chain also increases the likelihood of a Hexadecane molecule interacting with an oxygen atom. An initial small release will give rise to a faster rate of

73

evaporation of both the Hexadecane and Iso-Octane, resulting in a much shorter TID.

2.9.2. **LSPI initiation due to Ca detergent present within the lubricant**

The research conducted by Moriyoshi et al [43] is closely related to the work completed in this thesis. The study uses experimental and simulation data to help understand the root causes of LSPI in highly boosted engines. The Initial assessment involved the simulation of a static particle in a controlled gaseous CFD domain. The gaseous domain consists of an air-fuel mixture, consisting of reduced chemical kinetics to establish the point of autoignition. Gas temperature was varied between 700K-800, Gas velocity 0-2m/s, gas pressure 2-4Mpa, gas excess ratio 0.6-1.4, deposit temperature 800-1200K, deposit diameter 100-600 micrometres. The particle is assumed to be a spherical body of known heat transfer properties, the body transfers heat under convection abiding by Fourier's unsteady heat transfer. The temperature distribution across the particle is calculated using the heat transferred to the convective environment, conductivity and thermal capacitance of the particle. It was found the autoignition delay reduced with increasing gas temperature, reduced with increasing pressure, reduced with increasing particle temperature, increased with excess air ratio and increased with smaller particle size. A simple 1D heat transfer calculation was set up to predict the unsteady heat transfer temperature for a layer of deposit on top of the metal liner, using the heat equation and an estimation of the htc (heat transfer coefficient) to the gaseous environment. Various parameters such as

deposit conductivity, specific heat capacity, density and deposit thickness were varied. As the thickness of the deposit is increased the maximum wall temperature also increases due to an increase in thermal resistance. As the specific heat capacity is increased the maximum particle temperature is reduced and the rate of cooling of the particle during the expansion stroke is reduced. The maximum temperature increases with increasing particle size due to the increased heat flux area. However, the larger particles take longer to cool down during the expansion stroke when the heat flux from the particle is lower. The transport of oil into the combustion chamber was simulated by assuming an oil film on the piston land and defining piston acceleration. It was found as the initial oil film thickness was increased the time required for the oil to move from the top land to the main piston face is reduced; this is because the ratio between the inertial forces and surface retention forces is higher for thicker films. The simulation was conducted by imposing an acceleration of piston motion on the entire domain. The impingement on other surfaces was not captured. As the surface tension of the film is increased the time required for the film to be transported to the main face of the piston, this is because the surface retention forces have to be overcome before the film can be deformed and sheared in transport. An oil droplet was assumed to be N-heptane (too short of a C chain length to represent lubricant oil). A static droplet in an Isooctane-air mixture, static air, thermal diffusion across the domain ignored, gas assumed to be incompressible. As gas temperature is increased the ignition delay is reduced. As the initial droplet temperature is increased the ignition delay is reduced. As gas pressure is increased the ignition delay is reduced. The excess air ratio only impacts ignition delay for droplets at lower

75

initial temperatures. This is because the reaction of hotter droplets is dominated by energetics rather than concentration. For cooler droplets, the collision rate is impacted by concentration to a greater extent. The ignition delay increases with higher excess air ratio - leaner mixture means the local concentration of fuel reduces. As the droplet diameter is increased the ignition delay increased, the adjective diffusion due to turbulence impacts the local concentration and this is not accounted for. A plot of the equilibrium temperature and $P(CO_2)$ at which a reaction is provided but not applied to an engine scenario. In the analysis a particle of constant temperature is immersed in a constant temperature and pressure environment. Ignition delay reduced with higher equivalence ratio (richer) and ignition delay also reduced with increasing particle size.

A possible solution suggested as an attempt to overcome the calcium promoted LSPI issue is to displace some or all of the Calcium detergent in lubricants with a Magnesium based detergent. This is not a favoured option for formulators as Magneium does not have the ability to neutralise a diverse type of acids like Calcium or provide the same level of deposit control. Calcium also allows for more options when formulating. Elliott et al [52] investigated a possible solution to this dilemma by trialling additives that would allow for the use of Calcium as a detergent whilst suppressing its nature to cause LSPI. The baseline case was a full Calcium formulation (around 2200ppm), this is a formulation that would normally fail the Sequence IX test. The formulation includes all the usual additives that an automotive

lubricant would comprise of anti-wear additive such as ZDDP, dispersant, friction modifiers, antioxidants and viscosity modifiers. Overall, most concentrations stayed constant for all cases. The Sequence IX test was used to assess the ability of the formulation iterations to suppress LSPI. As mentioned above the Sequence IX is an industry standard test that uses a Ford EcoBoost engine and operates at 1750rev/min and 269Nm torque. LSPI events are detected by either an early combustion (before spark), or peak pressures above the average. The onset of combustion is defined as the crank angle at which 2% of the fuel is burned (MFB02). This is the criteria that was used to measure an early combustion. In order to qualify as an LSPI event, the event must meet both criteria; an early MFB02 and a peak cylinder pressure that exceeds a defined threshold. It was found many Zirconium components helped to reduce LSPI, irrespective of the type of compound. These were formulated with Calcium. Not only was the frequency of LSPI events reduced by increasing the Zirconium concentration but the severity of the events was also lessened. Cobalt did assist in minimising the number of LSPI events by suppressing Calcium ignition, but the efficiency of suppression depends completely on the type of ligand. A ligand is an ion or functional group that binds to a central metal atom (donating electrons) to form a complex. Zinc compounds were tested and demonstrated an ability to mitigate LSPI. This was despite the absence of phosphorous. As phosphorous is a flame retardant it can often help reduce autoigniton. However, stringent limits for Phosphorous limits are being put into place for lubricant specifications, because of the detrimental effect it can have on the catalytic converter. For this reason, Zinc compounds could be an attractive

77

solution for the automotive sector. This has historically been a problem when trying to add ZDDP, as experiments have shown it helps suppress the pre-ignition activity of Calcium, but Phosphorous limitation due to its detrimental impact on exhaust catalyst performance, has been an antagonistic towards adding it at elevated concentrations. In addition to additives that suppress the undesired behaviour of Calcium, potential replacements as detergents were also investigated. Potassium demonstrated signs of promised, and significantly reduced LSPI events when used in similar concentrations to Calcium. With Lithium on the other hand, no reduction in LSPI events was observed, but the severity of the events (measured by peak pressure) was less. When a detergent was formulated consisting of a combination of Calcium and Lithium a marked improvement was achieved compared to solely a Calcium or Lithium detergent. Most of the experiments show an improvement from using solely a Calcium based detergent or LSPI propensity like it. Calcium is the most problematic detergent but the most effective detergent from the information that is currently available. This study is suggesting that there may be an alternative approach to the default solution that involves reducing the Calcium content and displacing it with Magnesium. This is a viable solution for LSPI but not quite an optimal solution for lubricant detergency. Several of the formulations could be used individually or on combination to overcome LSPI if their lubricant detergency performance can be proven to be on par with Calcium.

The action of Calcium detergents causing LSPI has been corroborated by several papers. Kocsis et al [54] conducted similar experiments. A 2L GM Ecotec engine was used, Haltermann EEE was the fuel used and a commercially available 5W-30 oil was the baseline candidate. The test consists of 6 segments; the first two are identical and are high load, higher speed (around 2000rpm), and there is an idle period at the same speed between the two segments, what follows are another two identical segments at lower speed (around 1300rpm) and lower load, once again with an idle period in between. The cycle ends with the final set of identical segments returning to the high speed, high load conditions. Once again MFB02 and the peak cylinder pressure were used to identify LSPI events. A large Matrix DOE of lubricants were tested for their ability to influence LSPI. The DOE consisted of varying levels of ZDDP, Calcium Sulfonate and Molybdenum. A separate DOE was completed to assess the sensitivity to Magnesium vs Calcium detergents, lubricant volatility, and base stock selection. As in previous studies, increasing the concentration of Calcium increases the number of LSPI events. However, the suppression of LSPI due to Zinc and Molybdenum additives was only seen at high concentrations of Calcium. Displacing the Calcium detergent with Magnesium also reduced the LSPI events. The paper does mention the mechanism as to why the two detergents render different results is unclear. Volatility and viscosity were both shown to make a very subtle difference to LSPI.

Singh et al [55] attempted to establish the mechanism behind LSPI by using an AVL single cylinder engine. The engine allows for a better control over a conventional engine, as it uses a compressor with a plenum to attenuate any pulsation, the single cylinder means the manifold pressure during valve opening is more stable as there is no pulsations from adjacent cylinders causing interference. The engine was run at 2000rpm, high load. It was found that residuals play a dominant role in causing LSPI, meaning that the behaviour of the previous engine cycle influences the level of LSPI in the current cycle. Residuals were varied by increasing the back pressure, whilst maintaining a constant fuel and air flow. Both LSPI and mega knock events increased with increasing back pressure. For the following experiment the mass flow of fuel and air were kept constant whilst varying the back pressure. However, the manifold pressure required to achieve the same mass flow rate will vary as the back pressure impacts the scavenging efficiency (the more efficiently the engine scavenges the better the fresh air volumetric efficiency and the lower the residuals). For this reason, the intake temperature was adjusted to maintain a constant intake manifold pressure. Pre-ignition counts increased the LSPI events, despite the lower back pressure providing better scavenging. Finally injecting water late in the exhaust stroke was excellent in washing out residuals and resulted in a reduction in LSPI events.

Singh et al completed another study [56] using the same single cylinder AVL engine, and similar running conditions but this time injecting a fluid late in the compression stroke, in addition to the main injection during the intake stroke.

The hope was that the secondary injection will help suppress LSPI events either by cooling the fuel-air mixture or by chemistry. Methanol, Ethanol, water and Gasoline were the secondary fluids tested. Methanol, Ethanol and Gasoline all increased the COV (coefficient of variance of the IMEP) and reduced the mean IMEP, if injected late in the compression stroke and in large quantities. Water was the most effective at reducing LSPI as it can be injected late in the compression stroke without increasing COV. Being able to inject late is key, as the latent heat cooling of the gas (due to phase change of the secondary fluid) take place close to the LSPI timing.

2.9.3. Impact of Fuel properties on LSPI

LSPI is an ignition event of which the source is disputed, and the possibilities have been researched in previous sections. It goes without saying that the propagation medium is the gasoline fuel-air mixture, this section will investigate how the fuel that is use impacts the likelihood of observing LSPI.

A 1.6L Ford Ecoboost DI engine was converted to a single cylinder engine by deactivating two of the cylinders [47]. The LSPI assessment was made for each setup by holding the engine at 2000rev/min and then cycling the engine

continuously between low and high load. The peak load was higher for the EEE fuel than the 70 RON fuel. The CA50 was kept constant for each test case, by varying the spark timing. Four fuels were tested in total; the EEE fuel, a 70 RON low volatility, 70 RON high volatility and a 70RON high volatility with 6.5% vol. CH_3NO_2. The injector was positioned in various orientations on the head to change the fuel spray wall impingement, the change in static pressure at the sump was used to estimate the fuel in oil during each high load phase of the cycle. Ignition delay predictions of the four fuels were predicted using ChemKin reactor model. The Ignition Quality Tester (IQT) is a constant volume, enclosed combustion chamber, that comprises of an injector and cartridge heaters to control the volume. Typically, pressure is measured during the ignition event. As expected, If the kinetic state of the fuel-air mixture (temperature and concentration) is similar to that of high a low load then the correlation in autoignition behaviour is similar between test and chemical kinetics simulation. If the Spray targeting is such that the wall impingement is increased, an increase in SPI is observed, due to a higher transport of fluid from the top ring region. At low load the quantity of Calcium detergent present in the lubricant had no bearing on the SPI count. However, a trend of increasing SPI with Calcium content was observed when the load was increased from 13bar IMEP to 16bar IMEP. Unburned fuel present in the crevice and top ring zone of the engine create nitric and nitrous acids that can make the fuel present more prone to SPI, and from this work it is found to be lubricant initiated SPI that is triggered when CH_3NO_2 is mixed with fuel, the SPI is found to occur even at low load. The impact of additives was investigated, it was found the impact on PI (pre-ignition) frequency was

82

related more to the impact on kinematic viscosity and density rather than any chemical kinetic effects. The PI frequency increased with both KV and density. Naphta is very similar to the heavy ends of Gasoline. Heavy Naphta was added to lubricant base stock in varying concentrations. It was found the addition of Naphta generally reduced PI frequency, but at low concentrations there is a small increase in frequency is seen up to 6% Naphta concentration with Non-ignitive base stock and a reduction is seen with ignitable base stock. The fact that PI events are reducing with increasing Naphta concentration suggests the flow rate in not sufficient to feed the crevice volume and influence the droplet detachment. In this case the dilution is most likely just impacting the phase change and ignition delay. No explicit correlation is claimed in this paper between fuel volatility and LSPI.

However, it is known from the extensive testing done by Abhishek et al [53] that fuels with heavier molecular components (high boiling points) result in increased wall wetting and oil dilution, in turn giving rise to LSPI as they have a higher probability of escaping from the crevice volume in liquid form and entraining oil droplets too.

2.10. Summary of literature survey

The key findings from the literature survey are outlined in Chapter 2.9, but for the readers convenience, some selected points are summarized below:

- The causes of LSPI are not well understood. Some explanations are offered but mostly conjecture, little numerical substantiation is provided.

- LSPI is a very stochastic and non-repeatable

- Lubricant Hydrocarbon autoignition is observed on a RCM, but not so much on engines

- LSPI is triggered by Ca based detergents but not Mg based detergents

- Miyosh et Al [43] suggests LSPI is due to the $CaCO_3$ thermally degrading to CaO, which later reacts with CO_2 in an exothermic manner.

- The amount of burned gas residuals present in the cylinder increases the number of LSPI events

- LSPI is impacted by fuel selection, and more prominent in GTDI engines.

- LSPI can be reduced by water injection

- Increasing viscosity of engine oil can reduce LSPI, very high viscosity will increase LSPI.

- Lower coolant temperatures can increase LSPI

- LSPI is the biggest limitation to thermal efficiency on CNG engines

- LSPI can result in MegaKnock which can not only impact thermal efficiency but also be destructive

- The reason why LSPI occurs at the knee point of the torque curve [46] is because that is when the highest level of burned gas residuals is observed. The highly pressurized charge assures a high work rate and thus high temperatures during compression. However, the engine speed is low, meaning the mass flow is relatively low compared to higher speed, full load conditions. Lower momentum inlet air means less of the residuals are scavenged, resulting in a higher mass being retained in the cylinder during the compression stroke. In some cases the lower engine speed means a lower turbulent flame speed, meaning the spark timing may need to be retarded to avoid Knock. This allows more time for LSPI to occur.

3. Knowledge Gaps from Literature summary & Future implications

3.1. Knowledge gaps in literature

Many researchers provide details of the outcome and findings of their experimentation regarding LSPI, but do not explore delving into the physical-chemical explanation as to why the behaviour occurs. Usually when a scientific explanation is given, it is usually conjecture and absent of mathematical solutions that provide substantiation.

Of the literature survey that was carried out, the main paper that attempts to reconcile experimental observation with scientific calculations is Moriyoshi et al [43]. Conceptually the aspects investigated in [14] are the same as some of those investigated in this thesis, but we will now discuss how the approach taken in this publication is a productive first step but has several opportunities for improvement and further development.

For the oil transport investigation, the oil film was assumed to initially accumulate on the piston land, but in reality, the oil film is sprayed onto the liner surface initially, meaning the oil will be scraped by the top ring and accumulated in the crevice volume. This study simulates the motion of oil droplets from the initial state of wall attachment. The film thickness is also not uniform along the length of the liner, as the ring-liner boundary conditions change at each position. The oil remaining on the liner will be the Elasto-hydrodynamic film remaining during the intake stroke.

85

Oil comprises mainly of long chain hydrocarbons, the evaporation behaviour of hydrocarbons of differing chain lengths should be investigated and its impact on the rate of vaporisation thought the compression stroke. This is particularly important, as the mechanism that causes autoignition due to reaction of hydrocarbons is a phase change limited process, whereas Moriyoshi et al [43] assumes a static gaseous environment. In addition, the publication [43] assumes the droplet is static, no thermal diffusion across gaseous domain and the gas is incompressible. It was thought all these simplifications could have a significant impact on the results and thus the neglected factors were accounted for in this thesis.

In the case of investigating the Calcium and Magnesium reactions; no comparison is made with Magnesium in publication [43]. The conditions simulated are steady state and the transient boundary conditions of the engine cycle are not captured. The particle equilibrium stability as function of changes in temperature and CO2 concentration throughout the engine cycle are not accounted for, as the equilibrium condition is not established for each stage of engine operation. The unsteady convective heat transfer impact on the particle during engine operation was neglected, as well as the impact of particle size on convection. This all means the moment in time the reaction is likely to occur, correspondingly the CO2 diffusion rate and equilibrium temperature cannot be calculated.

An interesting behavioural attribute of LSPI is its stochastic nature. Although LSPI has a much higher probability of occurring under certain conditions, it is very difficult to achieve repeatability with LSPI tests, even for the same condition. This means that LSPI only occurs when more than one event/activity must take place at specific times. These is no explicit explanation for the stochastic nature to date. However, contributors such as EGR are mentioned, and could be prone to cycle-to-cycle variation in quantity and mixture uniformity. It is also important to understand exactly why EGR gives rise to LSPI.

Literature suggest the LSPI is a combined phenomenon associated with lubricant selection, fuel selection as well as engine design and performance. Once again, literature offer speculation as to e how each one contributes but lacks numerical corroboration. The nature of LSPI heat release is also not well understood. It is unclear as to whether it is a slow heat release such as a micro-deflagration or a local detonation that occurs.

Another source of confusion is why lubricant hydrocarbon autoignition (often represented by Hexadecane) is observed in RCM and IQT bench tests but LSPI in an engine is mostly influenced by detergent selection.

From the literature survey it was concluded that the number of aspects that contribute to LSPI are several, and simulation techniques must be used to

gain significant insight. LSPI also seems to be sensitive to aspects of engine behaviour that vary from cycle to cycle. For LSPI to be problematic it also needs to occur within a specific time frame. Several of the behaviours that need to be investigated take place at very small time and length scales and therefore it is very difficult to observe and gain insight using testing. With testing it is very difficult to study the sensitivity to specific inputs whereas each input can be isolated and defined precisely in a simulation domain.

3.2. Future implications of LSPI

It is suspected a solution for LSPI will probably require a combined effort from engine developers, fuel formulators and lubricant formulators. However, it is very difficult to cure a problem that one does not understand the behaviour of or the physics and chemistry that govern it. It is hoped the research from this thesis will provide insights each facet can build upon, as well as a simulation approach that allows for each specialism to synergise.

Most hybrid vehicles spend a lot of their time in series mode. Series mode is when the engine is being used like a generator to charge the battery, which powers a motor that propels the vehicle. The series condition is normally a low speed, high load condition which avoids the LSPI region. If a remedy for LSPI was found, the engine could generate at an even lower speed, high load. The lower speed will result in lower friction losses and thus improved fuel consumption.

It was seen that LSPI was biggest limitation with CNG engines because of the higher ignitability of fuel-air moisture. If CNG was to be considered as a low PM solution in the future, resolving the LSPI issue would make is a more appealing solution. Any other gaseous fuel that may be considered in the future is likely to have similar limitations, due to a low minimum ignition energy.

4. Literature review on Simulation Techniques potentially useful for modelling LSPI

4.1. Simulation methodologies

Following the conclusion that simulation will be the best approach to gain further insight into LSPI behaviour and the mechanisms that lead up to it. This is a Multiphysics problem involving, mechanics, thermodynamics, chemistry, fluid dynamics and mass transfer. Hence, it is necessary to research various methodologies that offer capability in each one of these facets. This section will take an in depth investigate the simulation methodologies that will assist in the simulation of all stage in Figure 6. Techniques will be selected based on their ability to account for science in sufficient detail as well as their computational expense. It is possible additional code may need to develop in addition to the techniques readily available and investigated in this section. Because the limitations, flexibility and functionality offered by each technique need to be understood in detail, this section will be highly theoretical, attempting to understand methodology from first principal formulation.

4.1.1. Introduction into computational fluid dynamics

As all the thermodynamic work done in an engine originates in the fluid phase, in the form of hydrocarbons (fuel and oil) and air, it is crucial the behaviour of the reacting fluids is captured accurately. Computational fluid dynamics (CFD) is a technique that allows us to calculate transport, thermodynamic and chemical behaviour of a fluid in motion through a defined geometry, in space and time domains. The space domains can be 1D, 2D or 3D and time domain can be steady, quasi steady or unsteady.

4.1.1.1. Fluid transport equations and turbulence modelling, RANS, DNS and LES

All types of CFD modelling, irrespective of whether it is 3D, 1D, steady or unsteady involve solving the Navier-Stokes equations. These are a set of equations that simulate fluid dynamics by conserving mass, momentum and energy. The equations are non-linear and need to be solved iteratively by discretising the fluid domain. Several methodologies are used to discretise the problems such as; Finite Element Analysis, Finite volume method and Finite difference method [41] [40].

Continuity (mass conservation):

$$\frac{\partial p}{\partial t} + div(\rho U) = 0 \quad \text{[eqn 1]}$$

Where; U is the total fluid velocity

Momentum is conserved including viscous forces, inertia and pressure:

$$\frac{\partial(\rho u)}{\partial t} + div(\rho u U) = -\frac{\partial p}{\partial x} + div(\mu \, grad \, u) + S_{Mx} \qquad \text{(X direction) [eqn 2]}$$

$$\frac{\partial(\rho v)}{\partial t} + div(\rho v U) = -\frac{\partial p}{\partial y} + div(\mu \, grad \, v) + S_{My} \qquad \text{(Y direction) [eqn 3]}$$

91

$$\frac{\partial(\rho w)}{\partial t} + div(\rho w U) = -\frac{\partial p}{\partial z} + div(\mu \ grad \ w) + S_{Mz} \qquad \text{(Z direction)} \quad \text{[eqn 4]}$$

Where; S is the momentum source due to body force

Energy is conserved including thermal energy, kinetic, work done by surface forces and viscous dissipation :

$$\frac{\partial(\rho i)}{\partial t} + div(\rho i U) = -p \ divU + div(k \ gradT) + \varphi + S_i \quad \text{[eqn 5]}$$

Where, i is internal energy and φ is viscous dissipation

Many fluid systems will consist of flow regimes that are turbulent. Turbulent flow by its very nature is extremely stochastic and multi-dimensional. Obviously, simulating effects such as eddie formation and breakdown, flow separation and reversal is extremely computationally expensive when direct numerical simulation is employed. For this reason, the Navier-Stoke equations are decomposed using Reynolds averaging, often referred to as Reynolds-Averaged-Navier-Stokes (RANS), i.e. the velocity in a given direction can be divided into a mean velocity and a fluctuating component.

Two commonly used turbulence models that are based on RANS decomposition are the K-ω and K-ε models. The K-ε represents turbulence due to diffusion and convection by k, the turbulent kinetic energy and ε is the

turbulent dissipation rate. The eddy viscosity in the K- ε model is quite simply the product of the velocity scale and length scale. In the case of the K-ω model, a turbulence frequency term is added to the calculation of the length scale.

The K-ω model is ideal for low Reynolds number internal flows, as it does not require wall damping functions for solutions close to the wall. However, the model is less suitable for free stream conditions such as external aerodynamics.

Depending on the nature of the fluid dynamics problem being solved, the resulting partial differential equations (pde) can take the form of; Elliptic, Parabolic and Hyperbolic.

Elliptic – Used for equilibrium problems or viscous steady state flow, only contains special derivatives and no temporal derivative.

Parabolic – Contains a first order temporal term and thus requires a time-marching scheme. Suitable for unsteady problems that are highly diffusive i.e. highly viscous or large amounts of heat transfer.

Hyperbolic – Contains a second order temporal term, meaning it also requires a time marching scheme. Generally used for supersonic flow where energy dissipation is negligible.

Unsteady solutions can be explicit; when the time derivative is based on data known about the current time step and previous time step, or they can be

implicit; when the solution is based on data known about the derivative between the current time step and the following timestep.

RANS solvers are a very efficient and versatile method of computing turbulence, but the assumption at all points is that each eddy is isotropic and impact the bulk from in similar ways. This assumption is fine when eddy lengths are small, larger eddies however can be very anisotropic. Their shape, size, energy dissipation and energy transfer to/from the bulk fluid due to viscous diffusion will be geometry and boundary condition dependant. Hence, it becomes necessary larger, more energetic eddies in more detail. Large Eddy Simulation (LES) schemes apply special filtering to the fluid domain. A cut off length is defined above which all eddies are resolved using a filtered form of Navier-Stokes's equations. However, numerical sub-grid stresses (SGS) are formed due to the smaller eddies not being resolved, and the need to account for in even a compact way the interaction between large, resolved eddies and smaller unresolved ones. The SGS are an additional stress term added to the momentum equation. SGS can be computed by creating a decomposition variable that sums the special variations of the resolved and unresolved eddies.

When the instantaneous form of the Navier-Stokes equation is used, with instantaneous velocities (rather than the Reynolds decomposed version), assuming the fluid is incompressible to begin with (density is always constant for first time step), a set of four closed form equations with four unknowns are attained (three velocities and pressure). The solution can then transition to the compressible form of transport equations. If a very fine is used, with a very small time-step, eddies of all sizes can be captured as well as the smallest and fastest fluctuations. This method is known as Direct numerical simulation (DNS). It is very detailed and accurate but very computationally expensive.

4.1.2. **Eularian and Langrangian CFD modelling of multiphase systems**

Two main approaches are taken to simulate the behaviour of fluids in a CFD domain, depending on the nature of the flow entities. In many cases, as will be the case in this study, both techniques are used in conjunction with one another[41] [40].

Lagrangian: This is when the fluid domain is separated into particles. Each particle is tracked as it moves through the continuum, and the transport properties are conserved for each. The behaviour and properties of the particle are a function of its position, time and the instantaneous boundary conditions. This approach is commonly used to understand the behaviour of droplets and particles.

Eularian: For this approach the flow domain is separated into finite volumes. The flow at the boundaries of each finite volume as well as the flow from within the volume is represented by special and temporal differential equations. This is the most popular approach that is used for general fluid flow. The Eularian approach can be used to simulate the motion of smaller entities of fluid using the Volume of fluid model (VOF).

4.2. Droplet modelling

The chosen droplet sub-models accounting for the various aspects of droplet behaviour will be covered in this section, and a brief background will be provided into the Eulerian VOF model which was not used, rather a Lagrangian Rayleigh-Taylor approach was utilised. Droplets are influenced by their momentum, their energy state, density, viscosity, surface tension which determines their breakup and coalescence. Depending on the environment within which the droplet resides the manner and extent to which each one of these factors impact behaviour will vary.

95

4.2.1. **Droplet transport – Lagrangian method**

Droplet acceleration is calculated using Newton's second law of motion. The resultant force acting on the droplet is calculated by the vector sum of the inertia, body and drag forces. The resultant force and mass of the droplet can then be used to calculate acceleration.

The drag force exerted on liquid parcels will be dependent upon their surface area and drag coefficient (related to leading geometry) whilst deforming.

The Taylor Analogy Breakup (TAB) [1] model takes a very interesting approach to understanding droplets. TAB assumes the droplet is a continuously excited entity that is trying to expand and extract in a sinusoidal manner, equation 6 is the classic single degree of freedom mass spring equation. The surface tension is analogous to spring stiffness, the viscous forces to damping and drag is analogous to the external excitation force (eqn 6 –9).

$$m\ddot{x} = F - kx - d\dot{x} \qquad \text{[eqn 6]}$$

$$\frac{F}{m} = C_f \frac{\rho_g U^2}{\rho_l r^3} \qquad \text{[eqn 7]}$$

$$\frac{k}{m} = C_k \frac{\sigma}{\rho_l r} \qquad \text{[eqn 8]}$$

$$\frac{d}{m} = C_d \frac{\mu_l}{\rho_l r} \qquad \text{[eqn 9]}$$

96

Where; F = Force, k = stiffness, d = damping coefficient, x = displacement, ρ_g = density of gas, ρ_l = density of liquid, μ_l = droplet viscosity, U= relative velocity of droplet, r = droplet radius, σ = droplet surface tension

The displacement calculation from the mass-spring model represents the maximum displaced point of the distorted droplet from the undisturbed state (spherical). An expression for droplet distortion acceleration can be developed, assuming the local gas velocity (mean and fluctuating component) and boundary conditions do not change for that time step, by calculating the second integral of the distortion acceleration to get displacement (eqn 10 – 11). The spring model displacement term can be non-dimensionalised ($y = \frac{x}{C_c} r$)

$$\ddot{y} = \frac{C_f}{\rho_l r} \frac{\rho_g}{\rho_l} \frac{u^2}{r^2} - \frac{C_k \sigma}{\rho_l r^3} y - \frac{C_d \mu_l}{\rho_l r^2} \dot{y} \qquad \text{[eqn 10]}$$

$$y(t) = \frac{C_f}{C_k C_b} We + e^{\frac{-t}{t_d}} \left[\left(y_0 - \frac{C_f}{C_k C_b} We \right) \cos \omega t + \frac{1}{\omega} \left(\dot{y}_0 + \frac{y_0 - \frac{C_f}{C_k C_b} We}{t_d} \right) \sin \omega t \right]$$

[eqn 11]

We – drop Weber number

The drag coefficient of a perfect sphere and that of a perfect disc can be obtained from testing, and thus a linear relationship between the distortion parameter and drag coefficient can be developed as can be seen in equation 12 [2].

$$C_D = C_{D,sphere} (1 + 2.632 y) \qquad \text{[eqn 12]}$$

97

$C_{D,sphere}$ is the drag coefficient of a perfect sphere

y is the droplet distortion (y=0 for a perfect sphere and y=1 for perfectly flat disc)

$C_{D,sphere}$ is the drag coefficient associated with a perfect sphere which will change as a function of Reynolds number [2].

Finally drag force can be calculated by using the equation of motion shown in equation 3.2.1.8[2].

$$F = ma = \rho_l V \frac{d^2 \bar{x}}{dt^2} = C_D A_f \rho_g W^2 / 2 \qquad \text{[eqn 13]}$$

Where W is the velocity of the gas relative to the droplet.

The Rayleigh-Taylor is a model that accounts for part of the mechanism, which is responsible for droplet breakup, Rayleigh-Taylor instability is thought to occur within the droplet when it is rapidly decelerated due to drag force, causing RT waves to be generated at the surface of the droplet.

Jospeh et al [4] conducted a set of experiments where a series of viscous/viscoelastic droplets were introduced inside a shock tube, in a region behind the air shock wave at varying We and Re numbers, and recorded images of the breakup regimes. They were able to witness Bag, Bag-Stamen and R-T waves in the catastrophic regime at high We numbers (higher tendency to breakup). It was noted viscosity had to be accounted for when comparing a predicted critical wavelength and associated growth rate, the

critical wavelength is the one with the greatest growth rate. The growth rate was calculated using equation 14 [4].

$$n = -k^2 \frac{\mu_2 + \mu_1}{\rho_2 + \rho_1} \pm \left[k \frac{\rho_2 - \rho_2}{\rho_2 + \rho_1} g - \frac{k^3 \gamma}{\rho_2 + \rho_1} + k^4 \left(\frac{\mu_2 + \mu_1}{\rho_2 + \rho_1} \right)^2 \right]^{\frac{1}{2}} \quad \text{[eqn 14]}$$

The wave growth rate for a given wavenumber (cycles per unif distance) is given by the following equation [9]:

$$\omega_{RT} = -k_{RT}^2 \left(\frac{\mu_l + \mu_g}{\rho_l + \rho_g} \right) + \sqrt{ k_{RT} \left(\frac{\rho_l - \rho_g}{\rho_l + \rho_g} \right) a - \frac{k_{RT}^3 \sigma}{\rho_l + \rho_g} + k_{RT}^4 \left(\frac{\mu_l + \mu_g}{\rho_l + \rho_g} \right)^2 } \quad \text{[eqn 15]}$$

Where ω_{RT} is the growth rate for k_{RT} wave number, ρ_l and μ_l are the liquid phase density and viscosity of the droplet, ρ_g and μ_g are the gas phase density of the medium the droplet is travelling within and σ is the droplet surface tension. The wavenumber corresponding to the largest growth rate can be found iteratively by using a bisection method. If the fastest growing wavelength (WL = $2\pi/k_{RT}$) is smaller than the droplet diameter then it is assumed that wavelength is growing on the droplet surface. When the wavelength has been growing for a time period defined by the time constant divided by the growth rate, the droplet is deemed to have broken up due to the RT mechanism. The droplet size resulting from the break up is calculated by multiplying the fastest growing wavelength by a constant.

Kelvin-Helmholtz is another Lagrangian breakup model that is commonly used for engine simulation. However, this is associated with the instability caused to a column jet of fluid from its leading droplet impingement as it interfaces

99

with the gaseous domain. It models how droplets are removed from the nose of the jet, more suitable for modelling injector jet flow.

4.2.2. **Volume of fluid (VOF) model**

A volume of fluid scheme can be Langrangian or Eulerian [61]. It is a multiphase scheme that can predict the deformation, stress and breakup of the free surface between a liquid phase and gaseous domain. Some schemes require for the user to define a slip velocity between the two phases others will use a function. Diffusion across the free surface between the two phases is also accounted for. This could be diffusion due to evaporation of the liquid phase or dissolution of the gaseous phase into the liquid phase. Dissolution diffusion is normally modelled by using the Henry constant to calculate the equilibrium once nitration of air at a specified temperature and pressure. The molar diffusion can be estimated using a time constant.

$$\bar{C}_{eq} = \frac{H(T)}{P} \quad \text{[eqn 16]}$$

$$\frac{dy}{dt} = \frac{y_{eq} - y_t}{\tau} \quad \text{[eqn 17]}$$

Where; $\bar{C}_{eq}$ is the equilibrium concentration, $H(T)$ is the Henry constant which changes as a function of temperature, y_{eq} and y_t are gas volume fractions at equilibrium and time t, P is pressure and τ is the time constant. At a sub-grid level the fluid properties used for conservation equations are a volume fraction average of the two phases. The deformation and movement is calculated by conserving the liquid volume fraction ratio (ψ). The conservation equation can be seen below.

$$\frac{\partial \psi}{\partial t} + U \nabla \psi = 0 \quad \text{[eqn 18]}$$

U is the velocity vector

4.2.3. **1D Gas dynamics modelling**

1D gas dynamics models are commonly used to simulate an entire engine system, from intake to exhaust. It solves the Navier-stokes equation is the predominant direction of flow and makes simplistic assumptions of the other two axis. The models are relatively inexpensive, and thus allow for several iterations and optimisations. 0D models are used for volumes, that contain, charge and discharge fluid.

High level 1D engine modelling function:

- Intake and exhaust boundary conditions can be set to any pressure, temperature and composition

- Flow geometry is discretised into control volumes, and a 1D solution of Navier-Stoke is achieved for compressible and incompressible fluids (conservation of mass, energy and momentum).

- Model corrects pressure losses due to irregular cross section, bends, tapers.

- Conservation of species is accounted for

- There are no turbulence models in 1D CFD but expansion losses (due to formation of eddies, in turn inducing heat by internal and surface friction and compression) are accounted for in an empirical manner.

- Wall surface friction losses are accounted for (empirical)

- Thermal boundary conditions can be applied at each component (can be detailed accounting for external and internal htc as well as thermal conductivity of material).

- Can develop temperature related chemical mechanisms in ducts (sometimes used for EGR specie correction in EGR path, and reactions in after-treatment ducts)

Navier-Stokes can be solved using two methods:

Explicit method:

- Uses derivative from current time-step

- The solution of the previous time-step yields an energy, momentum, and mass derivative (as they must be conserved) that can be integrated over the current time-step

- Density can be calculated as the mass and volume of each discrete element is known

- Then temperature, mass flow and pressure can be forward calculated for the current time step using an iterative approach

- Appropriate for unsteady and high resolution solutions.

Implicit method:

- Uses the pre-derivative for the next time-step

- Iteratively solving a non-linear system of algebraic equations for all the discrete volumes at once

- Appropriate for scenarios when high frequency pressure fluctuations are not of importance, large time-steps.

- This model is better for phase transition

Defining intake and exhaust ports:

One of the methods of simulating charge motion of gas inside the cylinder is described in Morel et al [8]:

- Define geometry (Reference diameter, Valve lash)

- Define Lift profiles

- Define Valve timing

- Look up table (vs. L/D)

    - Forward and reverse discharge coefficients

    - Forward and reverse swirl ration (Torque based)

    - Forward and reverse tumble ration (Torque based)

- Mass flow rates are corrected for choked conditions (Above Mach 1 flow is only effected by upstream pressure – impact on speed of sound at throat)

- All parameters can be optimised using a PID controller

- Variable geometry of ports can be captured

- Thermal conditions of ports can be accounted for

- 'Fuel puddling' is a common issue in PFI engines. The fuel deposition, evaporation, entrainment, and liquid fuel transport by shear forces are modelled.

The in-cylinder flow model (0D)

- The cylinder is broken into the following regions [25]:

- Squish region

- Region above cup lip

- Piston cup region.

- The axial velocity component can be calculated from the piston velocity relative to the cylinder wall.

- Radial flow component due to squish can be calculated for each time-step using empirical approximations offered by Heywood [27]

- These velocities are used in the heat transfer model.

- Single zone turbulence and tumble models- solve the turbulence kinetic energy equation and the turbulence dissipation rate equation. The turbulence length scale is also calculated.

- The turbulence values are used in predictive combustion models and heat transfer model.

- A scavenging model is available particularly for 2-stroke engines (otherwise residual gases are assumed to be homogeneously mixed)

- For mass flow associated with swirl motion; an angular momentum conservation equation can be used to calculate the rate of change of momentum (=force or torque) [25];

$$\left(I_j \dot{\omega_j}\right) = \sum \dot{m}_{ij}\, \dot{\omega}_{ij} r_{ij}^2 + \sum \rho\, U_{dif}\left(\omega_i - \omega_j\right) \int r^2\, dA + \dot{m}_{intake} + M_{intake(1)} - \dot{m}_{exhaust}\omega_j r_{j(1)}^2 - \frac{1}{2}\rho \int C_f r^3 \omega_j\, dA \qquad \text{[eqn 19]}$$

j is the region being solved for, i is the adjoining region, $\dot{m}$ is mass flow rate, ω is the angular velocity, r is the radial distance from the centre of the piston, C_f is the skin friction coefficient, I is the second moment of inertia, U_{dif} is the diffusion velocity, r_{ij}^2 is the ratio between second moment of inertia and

104

mass, M_{intake} is the mass flow based on the isentropic velocity. Note: (1) – for squish volume and cup volume only.

Similarly, the turbulence model is a reduced version of the k-ε model that is solved for the zones, the equations for the change in mass product turbulent kinetic energy and turbulent dissipation can be seen below;

$$\left(m_j \dot{k}_j\right) = \sum \dot{m}_{ij}\, k_{ij} + \sum \rho\, U_{dif}\left(k_i - k_j\right)A + m_j s_k + \dot{m}_{intake} k_{intake(1)} - \dot{m}_{exhaust} k_{j(1)} - \dot{m}_{injection} k_{injection(2)} + \dot{m}_{sq} k_{sq(2)} \quad \text{[eqn 20]}$$

Where k is the turbulent kinetic energy, ε is the turbulent dissipation, A is area, k_{sq} is the route-mean-square value of the turbulent kinetic energy associated with the flow from the squish volume to the cup volume. Note: (2) – for cup volume and region above cup lip.

$$\left(m_j \dot{\varepsilon}_j\right) = \sum \dot{m}_{ij}\, \varepsilon_{ij} + \sum \rho\, U_{dif}\left(\varepsilon_i - \varepsilon_j\right)A + m_j s_\varepsilon + \dot{m}_{intake} \varepsilon_{intake(1)} - \dot{m}_{exhaust} \varepsilon_{j(1)} - \dot{m}_{injection} k_{injection(2)} + \dot{m}_{sq} k_{sq(2)} + k_j^2 / L_j^2 \quad \text{[eqn 21]}$$

Where; L is dissipation length.

s_k is the source term for turbulence generation and s_ε the source term form turbulent dissipation. There are a subset of equations that allow us to calculate source terms using pressure, turbulent viscosity, density and strain field parameters.

105

The ode equations above will be integrated for each zone will be integrated, the assumption is that the turbulent kinetic energy and dissipation rate are constant throughout a zone.

The in-cylinder heat transfer models

It is important to remember that there is a large amount of heat transfer through the wall of the cylinder liner and combustion dome in the head, especially when a coolant is within close proximity of the gas zone. The heat flux will be dependent upon the heat transfer coefficient and temperature of the gas. GT offers various models that allow for the calculation if Nusselt number throughout the engine cycle. If the thermal conductivity of the gas and characteristic length are known the htc can be calculated (as Nusselt = htc x characteristic length/thermal conductivity).

Convective heat transfer models offered in GT:

– WoschniClassic [27]: Classic Woschni formulas for mean piston speed, Nu number, pressure, temperature. This correlation was developed from dimensional analysis.

$$h_c = 3.26 B^{0.2} \, P^{0.8} \, T^{-0.55} \, w^{0.8} \quad \text{[eqn 22]}$$

Where; h_c is the convective heat transfer coefficient, B is the cylinder bore size, T is the gas temperature and w is the mean gas velocity.

– Flow: The in cylinder turbulence model is used to derive a local velocity and thus a corresponding heat transfer coefficient (Using Colburn analogy)

– WoschniHuber [163]: Heat transfer model developed by; K. Huber, G. Woschni, and K.Zeilinger (accounts for swirl and in cylinder turbulence)

106

- Hohenberg [164]: Heat transfer model developed by G.F. Hohenberg. Generally more accurate for DI Diesel engines.

- Hgprofile: Heat transfer coefficients mapped from 3D CFD analysis.

4.3. Evaporation modelling

The Frossling [4] and Chiang [162] models account evaporation in terms of mass diffusion due to a concentration gradient at a given temperature, and thus the resulting reduction in droplet diameter, this is diffusion that occurs when the vapour pressure of the droplet is below the surrounding gas pressure. Once the vapour pressure exceeds the surrounding gas pressure i.e. boiling/bubble formation occurs a boiling model is required. The formulation for the Frossling scheme can be seen below. The Chiang is very similar but uses a scaling factor, it also provides a Nusselt number (heat transfer due to convection/conduction). The Sherwood number is a ratio of mass transfer due to convection/mass transfer due to diffusion.

Droplet radius change:

$$R = \frac{\rho_{air} D_{air}(\widetilde{T})}{2\rho_d \, r} \frac{Y_1^* - Y_1}{1 - Y_1^*} \, Sh_d \quad \text{[eqn 23]}$$

Transport inputs to radius change function:

$$Sh_d = \left(2 + 0.6 Re_d^{\frac{1}{2}} Sc_d^{\frac{1}{3}}\right) \frac{\ln(1 + B_d)}{B_d} \quad \text{[eqn 24]}$$

$$Re_d = 2\rho \frac{|u + u' - v| r(\widetilde{T})}{\mu_{air}} \quad \text{[eqn 25]}$$

$$Sc_d = \frac{\mu_{air}(\widetilde{T})}{\rho_{air} D_{air}(\widetilde{T})} \quad \text{[eqn 26]}$$

107

Thermal and phase inputs:

$$B_d = \frac{Y_1^* - Y_1}{1 - Y_1^*} \quad \text{[eqn 27]}$$

$$(\widetilde{T}) = \frac{T_{gas} - T_{drop}}{3} \quad \text{[eqn 28]}$$

Where;

R = rate of change of droplet radius

$\rho_{air} D_{air}(\widetilde{T})$ = mass diffusivity of vapour in air

ρ = density of gas

r = initial droplet radius

u = local mean gas velocity

u' = turbulent gas velocity

v = droplet velocity

μ = viscosity

Y_1 = vapour fraction within droplet

Y_1^* = Vapour fraction at droplet surface

T = temperature

Other equations for mass transfer from a liquid to gaseous domain have been developed based in kinetic energy solutions, such as the equation below [62]:

$$\int_0^t N_A \, dt = 2c_i \sqrt{\frac{D_{AB} t}{\pi}} + \frac{c_i D_{AB}}{k_i} \left[erfc \left(k_i \sqrt{\frac{t}{D_{AB}}} \right) * \exp\left(\frac{k_i^2 t}{D_{AB}} \right) - 1 \right] \quad \text{[eqn 29]}$$

108

Where; N_A is Molar flux of solute, D_{AB} is the diffusion coefficient, c_i is gas concentration and k_i is the coefficient of mass flux (ratio of molar mass flux/potential driving force).

4.4. Combustion modelling and species prediction

This section will cover 1D and 3D domain combustion simulation. For both dimensional approaches we will discuss reaction flame combustion (such as SI), diffusion combustion (such as CI) and autoignition (in theory CI combustion is also an autoignition event but for convenience this thesis will be referring to knock and LSPI when autoignition is mentioned). CI combustion is discussed because its mechanisms are very similar to that of autoignition, despite being of different energy, mass and space scales. As both processes are generally diffusion limited and rely upon the local concentration and enthalpy of the mixture to be sufficient to ignite, for both autoignition and CI combustion the enthalpy source is the work done on the fluid and heat transfer rather than a spark source.

4.4.1. Flame propagation prediction for Spark ignited combustion

With the exception of the quantity of burned gas residuals and the enthalpy associated with them, the characteristics of the actual combustion event itself does not influence LSPI too much, as LSPI occurs before the spark event. However, as has been discussed earlier the LSPI event is often what promotes MegaKnock by pre-heating the unburned gas, for this reason it important for us to understand the nature of the speed of propagation of the LSPI event, and so it will be investigated late in the thesis.

4.4.1.1. Two zone combustion models

Two zone combustion models are generally used for SI combustion, whereas single zone for HCCI and multizone for CI. The zones for a two zone model can quite simply be split into burned and unburned. The temperature,

pressure, composition and velocity of each zone can be calculated on a timestep basis. Below is a summary of the aspects a 2 zone combustion models can account for and how they are used:

- Conservation of chemical species is maintained in the combustion process. The concentration of each species is dependent upon combustion temperature, pressure and Equivalence ratio.

- The energy change in each zone can be calculated by the time integral of heat released due to combustion, work done by the piston and heat transfer to the walls, allowing for pressure and temperature to be calculated.

- Wiebe functions [69] – Imposed burn rate based on duration, timing and shape. Wiebe functions are different for SI and DI (to allow for ignition delay and combustion tail differences in burn shape).

- Sequential and concatenated Wiebe function for multi-shot injection

- The model can potentially be made semi-predictive by modifying Wiebe function as a result of other parameters (e.g. mass flow, turbulence).

- Total fuel quantity burned will be corrected for rich mixtures

- Burn rate can be reverse calculated from cylinder pressure, approximate trapping ratio, intake temperature/composition and injection/spark timing. This will be discussed in more detail in the next chapter

- TPA analysis – Instantaneous pressure data for intake, cylinder and exhaust is provided. In addition, intake temp/composition (including EGR) and injection/spark timing are also provided. A burn profile, trapping ratio, trapped residuals and trapped air/fuel can be calculated based on the boundary conditions and the resulting mass flow rate. The model will iterate the burn profile until the predicted pressure and temperatures converge with the boundary data.

- The TPA can be repeated for several cycles

The Energy state equations for burned and unburned zones are solved separately [26]. These are based on the First law of Thermodynamics and the gaseous equation of state.

Unburned Zone (Used for onset of combustion)

$$\frac{d(m_u e_u)}{dt} = -P\frac{dV_u}{dt} - Q_u + \left[\frac{dm_f}{dt}h_f + \frac{dm_a}{dt}h_a\right] + \frac{dm_{f,i}}{dt}h_{f,i} \quad \text{[eqn 30]}$$

m_u = Unburned zone mass $m_f = fuel\, mass$ m_a = air mass $m_{f,i}$ = injected fuel mass

e_u = Unburned zone energy P = Cylinder pressure V_u = Unburned zone volume

Q_u = Unburned zone heat transfer rate h_f = enthalpy of fuel mass h_a=enthalpy of air mass

$h_{f,i}$= enthalpy of injected fuel mass

Burned Zone (Used for exhaust conditions)

$$\frac{d(m_b e_b)}{dt} = -P\frac{dV_b}{dt} - Q_b - \left[\frac{d(m_f)}{dt}h_f + \frac{d(m_a)}{dt}h_a\right] \quad \text{[eqn 31]}$$

'b' denotes the equivalent burned zone parameters

The rate at which mass is transferred from unburned to burned is determined by the combustion model

4.4.1.2. 1D CFD predictive combustion modelling

In 1D engine performance simulation there are predominantly two main methods of accounting for the combustion; predictive combustion and pre-defined combustion. As explained earlier the pre-defined combustion is characterised using a Wiebe function, an exponential function that defines the start of combustion and the fraction of the total fuel burned as a function of crank angle. The predictive combustion models predict the burn rate as a function of other parameters such as air flow rate, gas residuals, gas temperature, piston speed, turbulence and composition. For spark ignition combustion a predictive flame speed model is used. A commonly used flame speed model is summarised below.

- This is a model that calculates the laminar and turbulent flame velocities as a function of the instantaneous in cylinder boundary conditions and is based on Morel et al [8]. This model:

    - Assumes homogeneous charge (even if DI)

    - Accounts for cylinder geometry, spark location(s), spark timing, charge motion, charge composition and fuel properties to calculate the burn rate.

    - Assumes a spherically propagating flame front originating from the spark position

- The mass entrained into the flame front and burn rate are governed by:

$$\frac{dM_e}{dt} = \rho_u A_e (S_T + S_L) \quad \text{[eqn 32]}$$

$$\frac{dM_b}{dt} = \frac{(M_e - M_b)}{\tau} \quad \text{[eqn 33]}$$

$$\tau = \frac{\lambda}{S_L} \quad \text{[eqn 34]}$$

112

Where;

M_e = entrained mass of unburned mixture

t   = time

ρ_u = Unburned density

A_e = Surface area of flame periphery (modelled as a spherical section)

S_T = turbulent flame speed (impacts entrainment)

S_L = laminar flame speed

M_b = burned mass

τ = time constant

λ = Taylor micro-length scale

S_T and S_L come from empirical relationships that were derived from testing. The relationships use values at a reference condition, temperature and pressure ratios, dilution level, flame radius, turbulent length scales, turbulence intensity (can use flow model or be imposed).

$$S_L^\alpha = S_{L0}^\beta \left(\frac{T_u}{T_0}\right)^b \left(\frac{P}{P_0}\right)(1 - aF_d) \quad \text{[eqn 35]}$$

where S_{L0} is the laminar flame speed as a function of equivalence ratio at the reference pressure and temperature (T_e, P_e), T_u is the instantaneous unburned gas temperature, P is the instantaneous cylinder pressure, and F_d is the diluent volume fraction (residuals), T_e is a reference temperature (298

K), P_e is a reference pressure (1 atm), α and β are constants that vary as a function of equivalence ratio.

$$S_T = C_s U' \left(1 - \frac{1}{\left(1+\frac{C_k R_f^2}{L_t^2}\right)} \right) \quad \text{[eqn 36]}$$

where U' is turbulence intensity, L_t is turbulent length scale, R_f is the flame radius, C_s and C_k are constants.

The laminar flame speed dominates rate of entrainment at the onset of combustion, but during the latter stages when the flame has a larger surface area the turbulent flame speed dominates.

4.4.1.3. 3D Combustion modelling of Pre-mixed fluids

Pre-mixed models assume the fuel and oxidant are homogeneously mixed and at a temperature that does not allow oxidation reactions prior to ignition. The source being the spark elevates the local temperature above the activation energy of the oxidation reactions. A stable burned phase (in chemical equilibrium) and unburned phase is produced as a result of the flame front. One of the most popular formulations used for pre-mixed combustion is the G equation formulation. Flame propagation occurs because of entrainment of mass into the thin reaction zone where small scale turbulence is most influential, and the thicker corrugated flamelet zone consisting of larger turbulent length scales. During the initial stages of combustion, the thickness of the turbulent brush will be zero and only consist of a thin reaction zone for laminar propagation. The turbulent brush will then increase in thickness as the flame front proceeds. Because of the variation of

114

the turbulent brush thickness, and its impact on the formulation below, both the early (predominantly laminar) and latter (predominantly turbulent) phases of combustion can be accounted for.

$$\langle\rho\rangle\frac{\partial\tilde{G}}{\partial t} + \langle\rho\rangle\nabla\tilde{G}\cdot\tilde{\vec{u}} = \langle\rho\rangle D_t' \tilde{k}|\nabla\tilde{G}| + (\rho\,\widetilde{S_T})|\nabla\tilde{G}| \quad \text{[eqn 37]}$$

$$\langle\rho\rangle\frac{\partial\widetilde{G''^2}}{\partial t} + \langle\rho\rangle\nabla\widetilde{G''^2}\cdot\tilde{\vec{u}} = \nabla\cdot\left(\langle\rho\rangle D_t \nabla\widetilde{G''^2}\right) + 2\langle\rho\rangle D_t\left(\nabla\tilde{G}\right)^2 - C_s\langle\rho\rangle\,\widetilde{G''^2}\frac{\varepsilon}{k} \quad \text{[eqn 38]}$$

Where $\langle\rho\rangle$ is the burned gas density, $\tilde{G}$ is the mean G value (man flame front position), $\widetilde{G''^2}$ is the flame front positional variation due to turbulence (equal to square of turbulent flame thickness), ρ is the unburned density, $\tilde{\vec{u}}$ is the mean gas velocity of the cell, D_t' is the turbulent diffusivity, D_t is the standard diffusivity under equilibrium conditions, S_T is the turbulent flame speed, ε is the turbulent dissipation, k is the turbulent kinetic energy, C_s is a constant, ∇ represents a special derivative.

The value of G will establish if the cell with the space domain consists of gas that is unburned, burned or within the flame zone:

G<0 Unburned

G>0 Burned

115

G=0 Flame

The global equations above are coupled with a system of equations that allow for the calculation of inputs such as turbulent flame thickness, standard and turbulent diffusivity, laminar and turbulent flame speeds as well as turbulent flow terms from the gas dynamics model.

4.4.2. **Autoignition and Compression ignition combustion**

The Diesel combustion process bears some resemblance to the LSPI process at much lower penetration velocity. As with Diesel a droplet is introduced to the combustion chamber, only difference is that it does not undergo break up due to high velocity exit at the nozzle and then high levels of drag in the turbulent environment due to the very high penetration velocity. The oil droplet is sheared and deformed in the crevice volume and then stressed to a much lower extent by the gaseous environment. The droplet will then need to evaporate, diffuse and react. Obviously, the LSPI scenario will not have a diffusion burn phase originating from a plume.

4.4.2.1. Multi-Zone combustion models

The multizone model described below is that which is based on Takuo Yoshizaket al [22] and T Morel et al [23], particularly suitable for CI combustion.

- Higher resolution DI combustion model for Diesel engines

- The injected fuel is divided into 5 radial zones in each direction from the centre of the spray. The axial zones are several and dependant on the spray characteristics.

- Each zone contains subzones representing:

    - Liquid fuel

    - Unburned vapour fuel and entrained air

    - Burned gases

- The model tracks fuel from an injected liquid plume, as the fluid moves into the cylinder it entrains air and evaporates (function of pressure and temperature) – forming the unburned subzone.

- A conservation of momentum calculation takes place, as the air is entrained into the fuel the mass increases and thus the velocity decreases.

- The rate of entrainment increases as you move further out from the centre of the plume (higher swirl velocity), thus the velocity of the mixed fluid packet and penetration also decrease (lower momentum).

- Fuel proceeds as a jet column until it breaks up into droplets

- The diffusion limited case is governed by the velocity of the droplets relative to the velocity of air. The velocity will decay exponentially (with time). The time-constant will be dependent upon the calculated droplet diameter and droplet velocity.

- The ignition delay only allows combustion for equivalence ratios below a rich limit.

- If the equivalence ratio is above the rich limit, it is assumed there is no combustion

- The reciprocal of the ignition time constant is integrated and the onset of combustion is assumed when the integral equals 1.

- The time-constants are an exponential function based on pressure, temperature, activation temperature, equivalence ratio and dilution.

- There is a similar exponential function for the kinetics limited combustion model, based on the same parameters.

- The smaller of the kinetics limitation or the fuel vapour available within the sub zone will be used for the rate of combustion.

- Also has multishot allowance

An illustration of the multizone simulation process can be found below:

Injection — Jet Velocity — f (discharge coeff, pressure/mass , density)

Break up — Time to break up / Sauter diameter — f (nozzle size, jet velocity, density)

Penetration — Penetration distance (after breakup) — f (penetration during jet phase, jet velocity, time, time to breakup, swirl ratio, RPM – for absolute swirl torque)

Air entrainment — Mass of air entrained into fuel zone:
- Entrainment before ignition
- Entrainment after combustion
- Entrainment after impingement with piston bowl (loss of momentum and mass in gas zone)

— f (EGR mass, Injection event properties, mass of fuel in injection zone, penetration velocity)

Evaporation — Mass based evaporation rate, droplets get smaller.
- Diffusion limited evaporation – dependant upon the velocity of fuel droplets relative to the velocity of air. The velocity will decay exponentially with a relation to the Sauter diameter.
- Boiling limited evaporation – based on pressure and temperature of unburned zone

— f (Saturation temp, pressure, temp, droplet velocity, Sauter diameter, air velocity)

Ignition delay — Ignition delay time.
- Only calculated for equivalence ratio below 3 (otherwise assumed there is no combustion.
- Delay for each unburned subzone is calculated.
- The integrated reciprocal of the ignition time constant is a function of equivalence ratio, pressure, temperature, EGR, Fuel Cetane

— f (Pressure, temperature, EGR, Cetane number of fuel)

Combustion — Fuel burn rate:
- Can handle both mixing/diffusion limited and kinetics limited combustion.
- Will account for premixed combustion and diffusion burn.
- It will burn the lower of the vapour fuel available in each subzone or the kinetics limited amount.
- The kinetics limited amount is based on equivalence ratio, pressure and temperature
- Each subzone will be calculated individually.
- No combustion assumed for equivalence ratio above 3.
- The amount of air & fuel transferred to the burned zone is proportional to the AFR of the unburned zone.

— f (Pressure, temperature, EGR, fuel properties, equivalence ratio in subzone, vapour fraction in sub zone)

Figure 5 – Process diagram for a phenomenological multizone combustion model

119

Although this model cannot be used for the autoignition of an oil droplet that escaped from the piston crevice volume as the velocity scale is different, the breakup mechanisms differ and because of the absence of a plume. Nevertheless, it can provide a methodology by which localised autoignition can be simulated very quickly within a 0d domain. It can potentially be simulated as a single parcel that contains a liquid droplet that is of a Sauter mean radius of the droplet population. Air entrainment-controlled combustion is irrelevant because the droplet velocity or the mass of fuel will not be sufficient to entrain much air due to wake effects or momentum diffusion. However, kinetically limited or evaporation limited combustion such as the pre-burn phase of CI combustion is very applicable. An empirical function that calculates the rate of evaporation in the parcel as a function of air pressure and temperature can be established. The mass of liquid fuel, fuel vapour, air mass and Sauter mean diameter can be calculated as a function of time. Momentum can be conserved as the fuel vapourises and air diffuses into the parcel (velocity will reduce due to increasing mass). Similar to the multi zone CI combustion model empirical relationships can also be determined for the fraction of fuel vapour that will ignite based on the air temperature and fuel vapour to air ratio.

4.4.2.2. Phenomological Autoignition models

Phenomenological models are commonly used in 0D combustion models to predict the onset of autoignition. Autoignition will take place in the end gas zone when the following condition is satisfied [27]:

$$\int_{t=0}^{t_i} \frac{dt}{\tau} = 1 \quad \text{[eqn 39]}$$

120

Where; τ is the induction time and the time integral of $1/\tau$ can be calculated throughout the simulation. Various empirical equations exist for the calculation of the induction time integral for different hydrocarbons and at differing levels of accuracy. In most cases the induction time calculation will take the form [27]:

$$\tau = Ap^{-n}e^{\frac{B}{T}} \quad \text{[eqn 40]}$$

Where; T is temperature and A, n, B are fitting constants

The Douaud and Eyzat [159] equation is commonly used for gasoline engine because it can account for fuels of varying Octane rating by inputting the octane number itself. The equation is as follows [27]:

$$\tau = 17.68 \left(\frac{ON}{100}\right)^{3.402} p^{-1.7} e^{\frac{3800}{T}} \quad \text{[eqn 41]}$$

Where; p is the absolute pressure, T is temperature and ON the octane number of the fuel

Empirical models that are commonly used to predict engine knock:

- Models are developed by fitting an Arrhenius function to measured autoignition timing and pressure/heat relate data, over appropriate conditions,

121

- All models are empirical and do not model the super-sonic pressure wave created after auto-ignition.

- These models account for the increase in heat transfer you get due to turbulence, and the difference in total heat transfer to the unburned gas zone from the burned zone.

- All models monitor the state of the unburned end gas close to the flame front

- The model creates a temperature gradient between the unburned gas adjacent to the flame front and the cylinder walls.

- Knock frequency is calculated based on the speed of sound at the air density in the cylinder at the onset of Knock and the time taken for the shock wave to travel across the bore and back again.

  - Model assumes all fuel is burned in the timestep after knock onset. A corresponding peak in pressure is observed.

  - More detailed reaction mechanism functions can be developed for unburned zone – This will change burn rate using an exponential relationship based on pressure, temperature and composition of unburned zone.

Common empirical models for predicting the Onset of Knock:

- Douaud and Eyzat [159]:

  – In theory can be used to predict autoignition pre-spark event and used to model Knock (post spark) by monitoring the state of the unburned gas mixture

  – This is the simplest Knock model and only uses the Fuel Octane number as an input

- Onset of Knock is when induction time integral is equal to1

- Induction time is a function of RPM, pressure, temperature, Fuel Octane number and specific coefficients.

- Franzke [160]:

  - Franzke built upon the D&E's function but also included a reference condition that is defined by; induction time integral, burn duration and crank angle.

  - Specific set of coefficients

- Worret [161]:

  - Worret built upon Franzke's model and selected more advanced angles to define the burn duration for the reference point.

  - Worret also accounted for AFR

  - Specific set of coefficients

- Knock models using Chemical kinetics relationships specified by the user (Arrhenius functions and activation energy) can be used. The enthalpy change in each reaction will quantify heat release.

- The reaction relationships can be input directly or referenced to a ChemKin file

Generic autoignition models:

These are autignition models that are not necessarily developed specifically for prediction of knock inside engines and can be applied to any detonation scenario, so long as the assumptions made by the model of the thermodynamic system do not invalidate the scenario that is being analysed.

- Semenov's function for explosions [32]
    - o Assumes a spatially homogeneous system (pressure, temperature and composition)
    - o The combustion event is represented as a single step, first order reaction
    - o Assumes the reactant consumption/rate of reaction is low at the initial stages
    - o Heat transfer is based on Newton's law of heat i.e. for a given external heat transfer coefficient the heat flux from a system will be proportional to the temperature differential between the system and the surroundings
    - o The temperature of the system is calculated based on the state that results from the difference between heat created and that lost to the surroundings
    - o Based on the difference between heat loss and heat creation the system can be in stable (heat loss dominates), unstable (heat creation dominates and further accelerates the rate of reaction) or metastable (small changes in temperature can cause it to deviate between stable and unstable).
    - o According to the Semenov model the temperature derivative can be calculated using the following equation:

$$\rho \, C_p \frac{dT}{dt} = P - L = \left(h_F - h_p\right)\rho \, A \, e^{\frac{-E}{RT}} - \gamma \, S \, (T - T_w) \quad \text{[eqn 42]}$$

Where; P is rate of heat production, L is rate of heat loss, $\left(h_F - h_p\right)$ is the enthalpy change of reaction, A is the pre-exponential factor, T is the

124

temperature of the system, T_w is the wall temperature, γ is the heat transfer coefficient and S is the system surface area.

- Frank-Kamenetskii's analysis of explosions[32]
  - o The Semenov model assumes a uniform temperature throughout the thermodynamic system, whereas in reality there will be a temperature profile between the centre of the system and the system wall
  - o Kamentskii accounted for this by replacing Newtonian heat transfer with Fourier heat transfer, thus accounting for thermal diffusion
  - o The energy balance equation is as follows:

$$-k\frac{d^2 x\,T}{dx^2} = \left(h_F - h_p\right)\rho\,A\,e^{\frac{-E}{RT}} \quad \text{[eqn 43]}$$

  - o A convective heat flux term can also be added to the function at the system wall boundary
  - o The equation can be solved as a quasi-steady solution

4.5. Species modelling

Details of the SAGE chemical kinetics solver that is used within a CFD environment are described in the next section, but a brief overview of reduced models used to predict emissions is provided here.

- NO$_X$ prediction is commonly conducted using the Zeldovich (Y.B. Zeldovich, 1946) model. This consists of a series of Arrhenius equations representing NO/NO$_2$ reactions competing for reactive species. Conservation of species is maintained.

125

- Various soot models exist that provide empirical relationships for the inception, growth and oxidation of soot particles. Hiroyuki et al [36] suggests Soot formation can be modelled assuming the first order reaction of vaporised fuel. The reaction of soot is modelled assuming second order oxidation.

- Most models assume the HC composition comes from the fuel that is present in the piston crevice volume, and the width of the volume is narrow enough to quench the flame and prevent it from burning the Hydrocarbons inside it. Lavoie [37] describes an approach involving modelled using a two plate flame quenching model to establish if the approximated HC volume will be burned by the flame or if the flame will be quenched, based on the Peclet number (ratio between heat loss and heat production)

- The CO2 and CO reactions are also characterised using established Arrhenius equations and dominate the competition for oxygen. One of the relationships for CO reaction rate constant was proposed by Heywood [27]

4.5.1. **SAGE chemical kinetics solver**

For chemical reactions in the fluid domain which have known reaction pathways and the rate functions are established, a chemical kinetics solver such as SAGE [39] can be used to calculate the rate of reaction and the resulting thermodynamics within each finite volume of a 3D CGD domain. The reactions that will be active will be subject to the species available, concentration and temperature. The SAGE chemical kinetics solver described by Senecal et al [39].

A multistep chemical reaction can be represented in the following format:

$$\sum_{j=1}^{J} V'_{ji} \delta_j \iff \sum_{j=1}^{J} V''_{ji} \quad \text{[eqn 44]}$$

Where; V'_{ji} and V''_{ji} are the stoichiometric coefficients of the reactants and products, j is the specie being conserved, J is the total number of species, I is the reaction being assessed and δ_j is the chemical name of species j. This equation is a representation of the need for species to be conserved for each one of the system of reactions.

The production rate of j is given by:

$$\dot{\omega}_j = \sum_{i=1}^{I} V_{ji} q_i \quad \text{[eqn 45]}$$

For a given species j the production rate will be the sum of that produced by all reactions from i to I.

$$V_{ji} = V''_{ji} - V'_{ji} \quad \text{[eqn 46]}$$

The rate progress variable q_i is calculated as a product difference function:

$$q_i = k_{fi} \prod_{j=1}^{J} [X_j]^{V'_{ji}} - k_{ri} \prod_{j=1}^{J} [X_j]^{V''_{ji}} \quad \text{[eqn 47]}$$

Where; $[X_j]$ is the molar concentration of species j, k_{fi} and k_{ri} are the forward and reverse rate coefficients for reaction i.

Both forward and reverse rate coefficients can be calculated from Arrhenius functions.

The equations above can then be coupled to the mass and energy conservation equations for each cell in the fluid continuum, by the equations:

$$\frac{d[X_j]}{dt} = \dot{\omega}_J \quad \text{[eqn 48]}$$

$$\frac{dT}{dt} = \frac{V\frac{dP}{dt} - \sum_j(\overline{h_J}\,\dot{\omega}_J)}{\sum_j([X_j]\,\overline{c_{p,J}})} \quad \text{[eqn 49]}$$

Where; $\overline{h_J}$ and $\overline{c_{p,J}}$ are molar enthalpy and specific heat capacity of species j.

4.6. 3D CFD Diffusion combustion and Autoignition prediction

A model that is commonly used within the 3D CFD domain, when the computational expense of a SAGE solver is not justified is the Shell autoignition model. It was originally developed for predicting Knock in Gasoline engines but has proven to be useful in predicting ignition delay in CI combustion. The model was originally validated against Iso-Octane, n-Heptane and Toluene using results from a rapid compression machine (compression ratio of 9.6:1) [38].

A reduced reaction pathway is suggested [38]:

128

k_q: RH + O_2 =>2R* (Initiation)

k_p: R* =>R* + products + heat (propagation cycle)

f_1,k_p: R* =>R* + B

f_2,k_p: R*+Q =>R* +B

f_3,kp: R*=> linear termination

f_4,k_p: R* => R*+ Q (propagation forming Q)

k_t: 2R* => quadratic termination

k_b: B => 2R* (degenerate branching) [eqn 50 – 57]
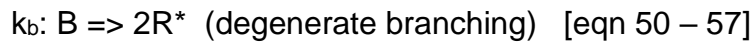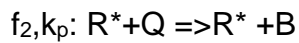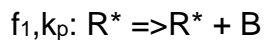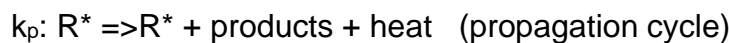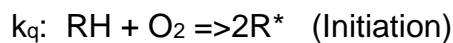
The rate constant (k_q, k_p, k_t, k_b) are characterised using Arhenius fucntions and the constants (f_1, f_2, f_3 and f_4) are used to calculate the rate of reaction.

If the chemical structure is C_nH_{2m}, it is assumed 2 H atoms are abstracted during a single propagation cycle. The enthalpy change can then be calculated assuming a constant CO/CO_2 ratio for the complete combustion process (to termination).

The chemical heat release if given by:

$$Q_k = k_p\, q\, V[R^*] \text{ [eqn 58]}$$

Where; Q_k is the chemical heat release rate, V is volume and q is the change in enthalpy per cycle

129

This can then be used as part of an energy balance equation comprising of; heat from combustion, heat transfer to walls and work done on the gas during compression to calculate the temperature derivative.

One the initial autoignition has been predicted by the Shell model, the calculation transitions to a scheme such as CTC (characteristic time combustion model) [63] for the main heat release and diffusion flame phase.

The CTC model uses the initial species and calculated the change in density of those species. The density temporal derivative is calculated using the difference between the current density and the equilibrium density, divided by a characteristic time. The characteristic time will be specific to the reaction being computed and will be a decomposition of a chemical and turbulent component. Equilibrium constant will be calculated for water and CO reversible reactions depending upon the environmental conditions.

4.7. Molecular diffusion and Reactive molecular dynamics

A common constraint of simulating reactions in the CFD space is that the modeler is completely dependant upon reaction pathways and rates obtained from literature or specific testing. This often poses challenges as; reactions for novel or uncommon molecules are not available, the reaction mechanism available may only be for a specific temperature range, although reaction pathways for specific components may be available but it may not contain the cross reactions between components. For this reason, a reaction prediction technique is often employed.

The most accurate way of predicting reactions is by using Quantum modelling, which will account for the density and exchange of electrons. However,

hydrocarbons consist of several reactions and the simulation would need to be repeated at a few temperatures in order to generate an Arrhenius plot. This make the timescales associated with Quantum modelling unfeasible.

A more practical approach may be to use ReaxFF [64], a reactive molecular dynamics technique. This technique uses forcefield characterisation to predict the intermolecular interactions in s system. To predict reactions it assess the energy state between two atoms, each interaction is assumed to be in simple harmonic motion as energy interchanges between kinetic and potential energy. The mean energy state will be determined by the frequency and amplitude of the oscillations. The models are characterised to assume a bond is formed or broken between two atoms based on the energy state. The distance between the assumed valence orbitals will determine the bond order.

4.8.   0-Dimensional Reactor simulations

Reactor models such as those offered by Aspen plus are very useful in understanding specific reactions for specific species at controlled boundary conditions. The models normally involve defining the input species, flow rate, temperature, pressure and for some model's humidity. Depending on the type of model used the reactor will predict the rate of reaction or the equilibrium state. The heat release and final species will then be provided.

Depending on the information that is available for the reactions and the method of their mathematical representation the reaction output may be calculated as a conversion factor, reaction extent or yield.

Depending on what is known about the boundary conditions different reactors can be used within Aspen plus [73]:

131

RStoic – When the reaction stoichiometry is known but the information on kinetics is not important or known.

RYield – For complex reactions the kinetics or stoichiometry is not known so the outputs based on yield; the yield is a ratio between the mass produced and mass feed.

REquil – The reaction stoichiometry is known and one or more of the reactions are equilibrium reactions, it predicts chemical and phase equilibrium calculations.

RCSTR & RPlug – Used for rigorous simulation of reactions under very specific conditions. Commonly used for catalyst reactions

RGibbs – Does not require stoichiometry and finds equilibrium condition at which the minimum Gibbs energy is achieved.

The RGibbs model will be used later in the study and thus a more detailed explanation of its function will be provided.

The equilibrium constant is defined as:

$$K = \frac{\prod_r^R p_r^{v_r}}{\prod_s^S p_s^{v_s}} \quad \text{[eqn 59]}$$

Where; r is the reactant specie being assessed, R is the total number of reactants, s is the product being assessed and S is the total number of products, v is the stoichiometric constant of the species, p is the partial pressure of the species.

The equilibrium constant can also be expressed as:

$$k = e^{-\frac{\Delta G^0}{RT}} \quad \text{[eqn 60]}$$

Where; ΔG^0 is the change in Gibbs energy and R is the universal gas constant

The change in Gibbs free energy can be calculated from the difference in standard free energy between the products and reactants.

In cases where the stoichiometry is not known, such as in reversible reactions, and if phase change is unknown the Gibbs energy change derivative can be used to calculate the minimum total Gibbs energy (when derivative equals zero).

Assuming an ideal mixture and a two component reaction:

$$\frac{dG_m}{dx_I} = G_I - G_{II} + \left(\frac{x_I}{1-x_I}\right) \quad \text{[eqn 61]}$$

Where; where subscript I is for the product in the forward direction and II is for the reverse direction, x is the mass fraction, G is the Gibbs energy and G_m is the total Gibbs energy of the mixture.

5. Simulation methodology and development

In this chapter a Multiphysics approach will be developed to simulate the key steps involved in LSPI, arrived at as a result of the literature survey. These steps are illustrated in Figure 6. The section will proceed in approximately the same order as the flow in Figure 6, the roman numerals at each step will be referenced throughout the section so that the reader has a clear understanding or what is being achieved and how it fits into the overall process.

The methodology used to simulate each aspect of the LSPI process will be clarified and justified, as will the inputs, setup and assumptions.

A sensitivity study will be carried out for each step that leads to an LSPI event to understand the significance of that step on the overall process. The hope is that by the end of the study we will have attained an understanding of the nature of the LSPI ignition and the most likely series of events that lead to it, with numerical substantiation.

5.1. Proposed key stages leading to LSPI based on literature research

Figure 6 shows the suggested sequence of events that lead to LSPI based on the finding of the literature survey so far. The flow diagram begins right at the beginning of the LSPI initiation process when the oil film form on the liner, initially due to the piston cooling jet, then the thickness is maintained by hydrodynamic action with piston rings. What follows is the eventual transport of fluid from the crevice volume to combustion chamber. There are then three steps which could take place sequentially, in parallel or in interchangeable order; the reactions of hydrocarbons, detergent reaction and interaction with

135

fuels, that create the ignition and heat release. The process ends with investigation of the impact of water injection on LSPI and to establish if a LSPI is a local detonation or deflagration.
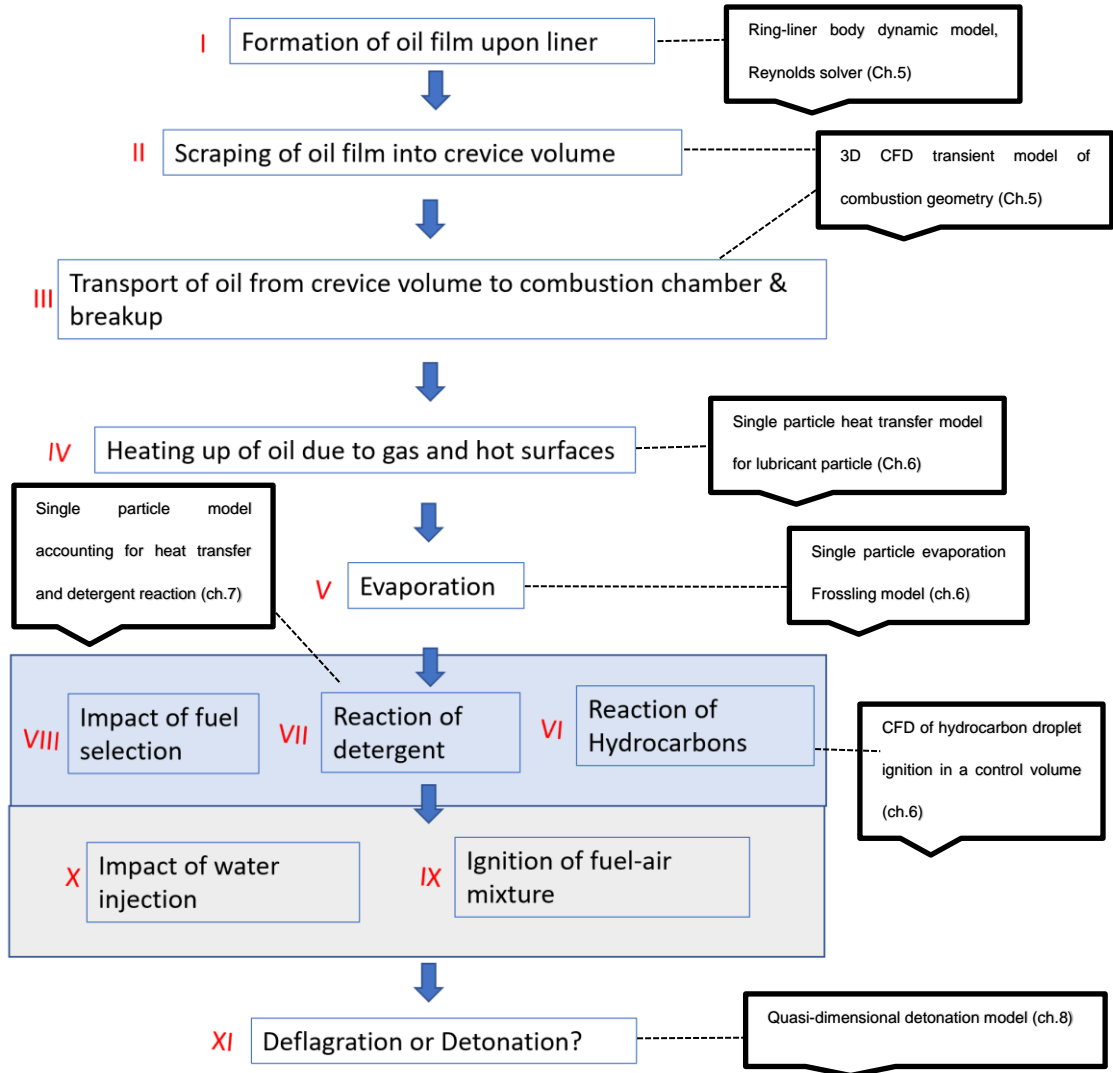
Figure 6 - Proposed sequence that leads to LSPI and modelling step for each stage

5.2. Validated 1D CFD gas exchange and combustion model

To establish boundary conditions for subsequent modelling of detergent particles, a 1D gas exchange and 0D combustion engine model was

developed using GT Suite (Gamma Technologies software). The benefit of such an approach is that an entire engine system can be simulated in a computationally inexpensive way. Most of the intake and exhaust comprise of pipes and ducts, in which case the most dominant fluid behaviour is in the primary direction of travel. This makes the 1D Navier-Stokes's solver ideal for such as case, especially as it has the ability to account for the pressure loss due to any bends. The cell plenum, intake manifold and exhaust manifold are 0D, charge and discharge volumes that assume a homogeneous fluid. For a conventional engine it could be argued some of the accuracy is compromised when using a 0D volume, as there is a significant 3-dimensional flow aspect in the manifold. However, in the case of a single cylinder engine the impact is significantly reduced, as there are no adjacent cylinders creating pulsating pressure waves. The larger compromise comes with predicting combustion, in cylinder turbulence and in cylinder fuel breakup and vaporisation, as these are all 3-dimensional aspects.

Evaporation can be accounted for in terms of its impact on the enthalpy of mixture components or even the flame itself, but for SI engines it is often assumed the fuel is fully vaporised soon after entering the cylinder. We will be using the SI turb model for combustion, which is a predictive flame speed model. For this reason, it was important that accurate tumble and flow coefficient values are specified because of their impact on the turbulence model. However, if a reasonable agreement with test data can be achieved,

this provides confidence that the model will provide directionally plausible results even when deviating away from validated operation.

At the beginning of each section the inputs and outputs of the modelling process carried out will be specified, in order to provide the reader with a summary and context to carry forward into the section.

A 1D gas dynamics and predictive 0D combustion model was developed to the specifications of a single cylinder engine (SC1). The model layout is shown in figure 7, model setup in table 3 and engine specification in table 2.
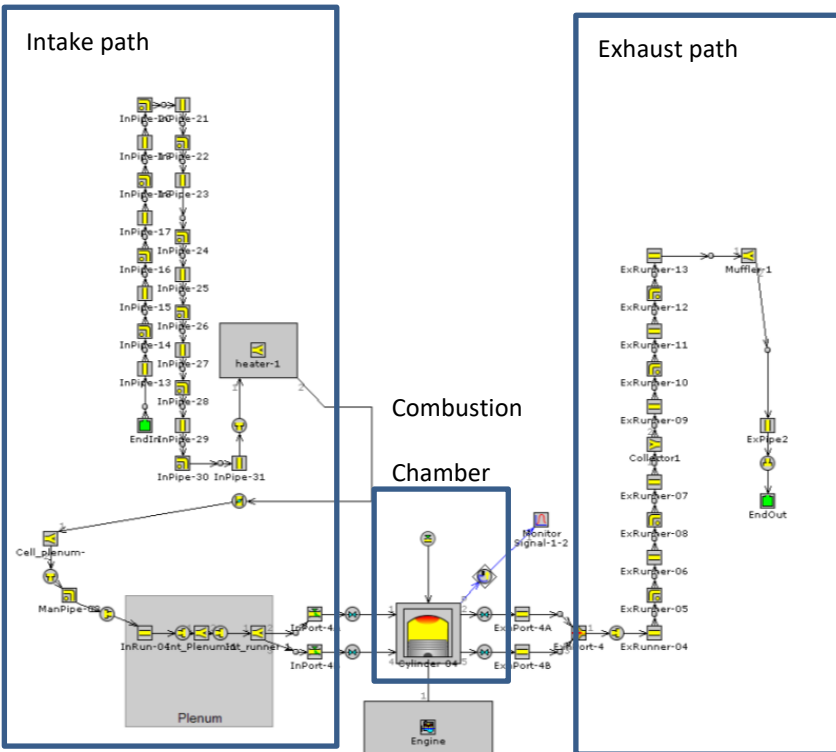
Figure 7 - Schematic of the SC1 single cylinder GT 1D gas dynamics/combustion model

	1
Number of cylinders	
Cycle stroke number	4 stroke
Valves per cylinder	4
Compression ratio	10:1
Bore	79mm
Stroke	81.4mm
Injection	Direct injection

Table 2 – SC1 Single cylinder engine hardware specification

Combustion model	Comb SI Turb
Knock model	GT Kinetics fit (multi-zone)
Cylinder Heat transfer model	WoschniGT
Injector	Sequential Injector with Imposed A/F Ratio
Navier-Stokes solution method	Explicit Runge-Kutta
Fuel	Iso-Octane

Table 3 - Selection of sub-models for GT SC1 single cylinder model

A WOT curve was simulated using the GT SC1 single cylinder model and calibration inputs such as spark timing, injection pressure, injection timing, injection duration, Intake & exhaust pressure, intake temperature, valve timings and FMEP were taken from test data (courtesy of BP UK)..

It can be seen in Figures 8 a and b, that there is excellent agreement between test data and simulation. Given that 0D predictive flame model is a simple

approach for a very complex combustion process, comprising of influential turbulence motion, mixing of various phases, evaporation, heat transfer and reactions. The excellent agreement between test data and simulation provides confidence it can be used to simulate conditions not presented in the test data

As explained earlier in this thesis the model uses an empirical flame speed model for laminar and turbulent flames speed, the turbulence model is empirical, and the heat transfer model is simplistic. The gas dynamics used to calculate residual levels are 1 dimensional in terms of the pressure differential between intake, cylinder and exhaust that causes residual gases. Any residuals that are a result of turbulent motion will not be accounted for. Given the simple approach the level of agreement between test and simulation makes this a suitable technique to quickly acquire in cylinder conditions for a variety conditions that are accurate enough to attain a directional understanding.
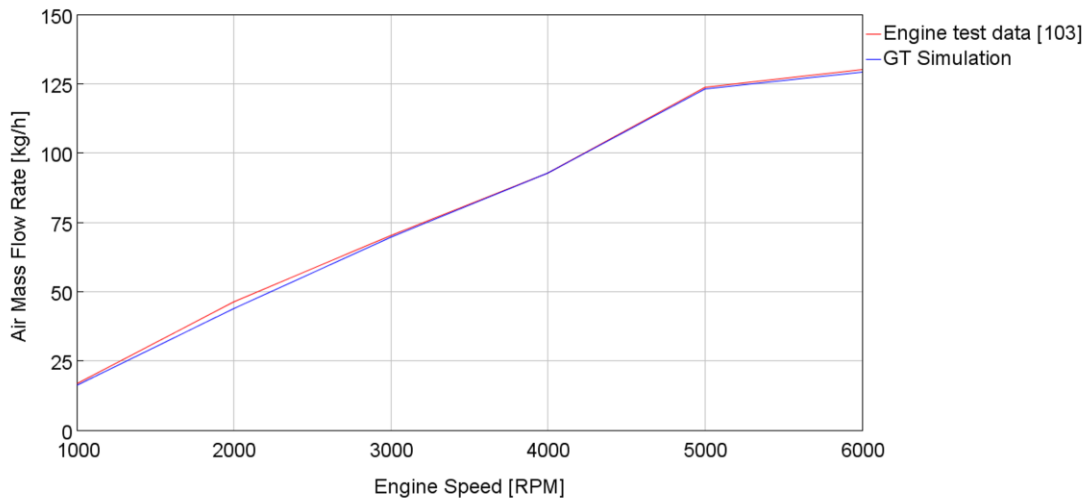
(a)
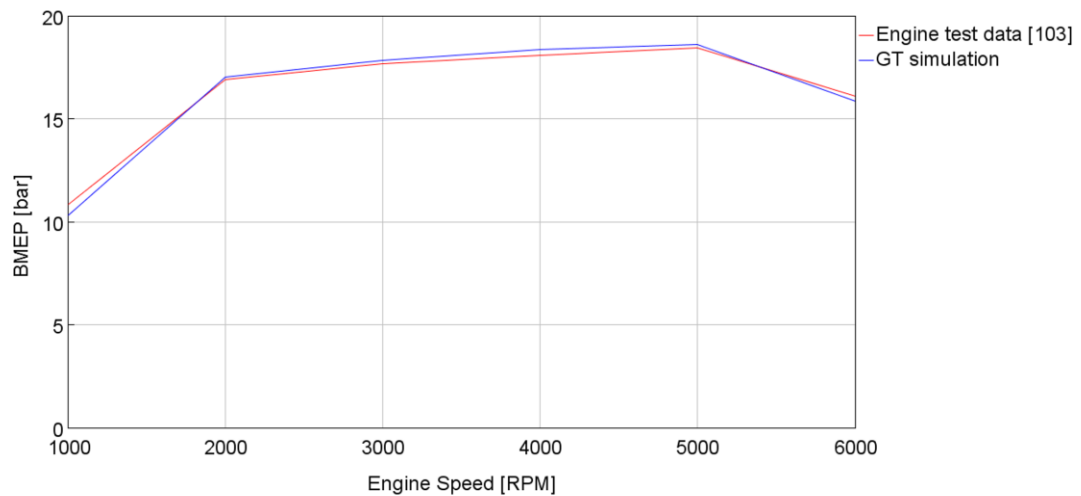
(b)

Figure 8 – (a) Comparison between predicted and actual Air mass flow for the SC1 engine (b) Comparison between predicted and actual brake mean effective pressure (BMEP) for the SC1 single cylinder engine

6. Establishing cylinder liner oil film thickness and transport for different oils

This section will focus on developing a simulation process and capability to model steps I-V illustrated in Figure 6. This includes the formation of the film, deformation and stress of the film, transport, and evaporation. The journey of the oil film inside the combustion chamber is illustrated in Figure 6 but a detailed explanation is provided below.

1. The piston cooling jets spray oil on the back of the piston throughout the engine cycle to avoid plastic deformation of the piston and oil coking. Oil is also splash fed to the liner to lubricate the contact between ring-liner and skirt-liner.

2. As the piston travels upwards the oil will also be scraped upwards by the piston rings. Similarly, when the piston moves downwards the oil is scraped downwards. In both cases the oil trailing behind the motion of the piston rings will just be the hydrodynamic film of the contact between ring and liner.

3. Once oil has been scraped off the liner it will collate in the crevice volume. The crevice volume is relatively cool as the liner wall and piston ring are cooled by the water-jacket. As the piston moves the oil volume in the crevice volume will be exposed to shear due to Couette flow as a result of one static wall and one dynamic wall.

4. Piston velocity is sinusoidal, with TDC and BDC having a velocity of zero and mid stroke having the maximum velocity. As the piston accelerates from BDC the crevice volume of oil will accelerate at the same rate. As the piston decelerates beyond mid-stroke, the oil will retain its momentum and not decelerate at the same rate, making it possible for the oil to escape the crevice volume.

5. The inertia of the fluid will be driving it to escape from the crevice volume, the adhesion at the fluid-surface boundary and the resulting shear stress through the fluid will be working to retain the fluid in the crevice volume. The balance between these two forces will determine the extent to which the fluid escapes to the combustion chamber.

6. The gas temperature during the expansion stroke will be very high, so the oil on the wall will have evaporated by the time the piston reaches BDC. The only oil remaining is likely to be that contained in the crevice volume. Chowdhury et al [60] completed a multi-dimensional simulation to understand gas flow past the piston rings during an engine cycle. The study shows there is significant circumferential flow between the rings, this gas is pressurised and forced towards the combustion chamber during the expansion stroke. So, there could be some blowby. It is possible some of the oil be released onto the liner above the maximum ring position during the exhaust stroke. Due to the pressure differential and piston bowl shape the oil could avoid interaction with the hot exhaust gas and remain on the liner. In addition, the fresh air supply during the overlap period could supply cooling.

7. Again, a hydrodynamic oil film will be formed during the intake stroke. Because the intake stroke is a relatively cool stroke the oil will remain in its liquid state. The oil will be scraped upwards during the compression stroke and sheared due to Couette flow. The oil film inertia will act for the fluid to escape as the piston decelerates. Viscous forces within the fluid and cylinder pressure are all that oppose fluid motion. The gas temperature will increase as the piston progresses, this may increase the amount heating to the oil, but the increasing pressure will also raise the boiling temperature.

8. Once the oil is released into the combustion chamber, it will be heated, will evaporate, diffuse and possibly react.

143

6.1. Aims of Lubricant transport simulation

Model	Purpose	Inputs
Rescaled 1D/0D combustion model	Gas pressure, gas temperature, heat transfer coefficient, percentage burned gas residuals and mean surface temperatures to be used as boundary conditions for future simulations.	SC1 engine GT combustion model scaled to simulate the geometry provided by Convergent Science
Body dynamics model	Predict Hertzian contact area for contact, contact entrainment velocity and contact pressure. So that boundary conditions can be provided to Reynolds solver	SC1 engine GT body dynamics model upscaled to represent geometry provided by Convergent Science, Cylinder pressure profile from GT into body dynamics model
Reynolds FDM model	Film thickness at each ring position	Contact Hertzian area, contact entrainment velocity, contact pressure (all from body dynamics model) and fluid properties
CFD oil film mode	Transport and position of oil parcels, breakup of oil film, interaction with boundary surfaces	Film thickness along liner from Reynolds solution, nominal intake and exhaust conditions from GT combustion model.

Table 4 - Summary of models, their purpose, and inputs for oil film transport prediction

The aim of this chapter is to understand the mechanism of transport and trajectory of lubricant as it travels from the crevice volume to the combustion chamber, as well as the distribution in location at a point in time when LSPI is typically observed. The impact of fluid transport properties will be investigated, the change in fluid properties due to heat transfer will be captured but at this stage the oil will remain in liquid state.

To assist the reader in navigating through this section table 4 has been provided to summarise the inputs and purpose of each model that will be discussed in this chapter. It is hoped this table will provide an overview of why each model is required and its dependencies. In summary, a 1D combustion model will be used to provide boundary conditions to a body dynamics model. Ring-liner contact boundary conditions are then taken from the body dynamics model and provided to the Reynolds solver to predict film thickness for each point in time. A transient 3D CFD model of the engine combustion geometry is developed, the 1D combustion model is used to inform the 3D model of the state of the gaseous domain. The prediction of the Reynolds solver is used to

impose the oil film thickness on the liner at the beginning of the compression stroke.

6.2.   Rescaled 1D/0D predictive combustion model for boundary condition data

To protect intellectual property, it was important a production engine geometry was not used as part of this study. Instead, Convergent Science (supplier of Converge CFD software) kindly provided a DI combustion model geometry from their library for a non-production engine. The dimensions in the SC1 models were replaced with that of the Convergent Science supplied geometry, this includes dimensions such as port length and diameters, bore, stroke, combustion chamber dimensions, connecting rod length, piston height, piston top deck thickness, cylinder length, water jacket height, valve face diameters, valve positions, valve reference diameter for flow coefficients. The compression ratio remained the same as SC1, as this could be varied for the Convergent Science 3D geometry too, by adjusting the Bdc and Tdc position of the piston. The valve lift maximum heights were scaled to the ratio of the stroke lengths between the two engines, but the valve timing remained the same as SC1.

The 1D engine model was used to provide boundary conditions to the 3D engine simulations for aspects where the long run times associated with the more sophisticated sub-models would not be justified by the accuracy benefit or the boundary condition that is being predicted has a smaller influence on the result. In addition, it will be used to provide boundary conditions for the piston ring-cylinder liner body dynamics model and for the specialist LSPI codes that will be developed.

Now that sufficient confidence had been attained with the 1D engine model it was felt one could upscale the same model as appropriate for the 3D engine

geometry available. The very purpose a predictive flame speed model, is that once calibrated to a known data set, the model inputs can then be varied and the model will provide a prediction of corresponding performance, of sufficient accuracy for a directional understanding. The 3D geometry provided by Convergent Science can be found in Figure 9. The combustion geometry consists of a side mounted injector and has a bore stroke ratio approximately equal to 1 (bore = 101.6mm, stroke = 100mm). The piston geometry has been modified to be flat as initially we will just be investigating oil droplet behaviour without combustion, so a piston bowl will not be required as there is no spray event (Fig 9). The simpler geometry will be more conducive for an orthogonal mesh, thus reducing error and runtime. A typical crevice volume was also created between the side of the piston and cylinder liner, having a flat piston made this modification far easier. The dimensions of the crevice volume are 0.39mm (width) x 1.71mm (height). The impact of the bowl shape on the tumble motion is generally small, tumble is mainly influenced by port design, so a flat piston should not compromise the result, especially as fuel injection is not included.

(a)   (b)
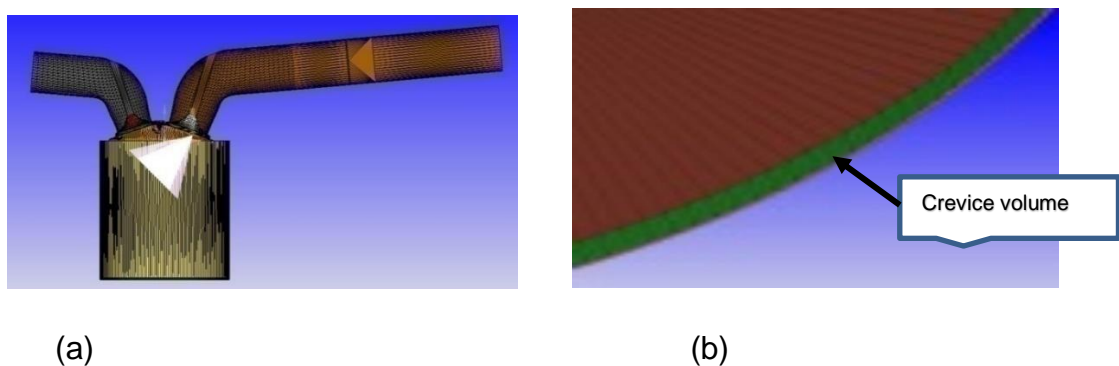
Figure 9 - (a) Cross-section of 3D cylinder, piston, ports and head geometry used for CFD study (b) Crevice volume created to simulate oil droplet motion (green region). The head, valve and port geometry are generic geometries (not representative of any production engine) courtesy of Convergent Science

A full wide-open throttle (WOT) curve was simulated using the resulting model; some cycle averaged outputs from the simulation can be found in Figures 10 (a) – (g). To account for Knock the spark timing was varied to achieve the maximum BMEP whilst not exceeding the maximum end gas temperature reached by the original combustion model for each condition (autoignition temperature). The results were deemed plausible based on internal engine data from BP.

(a)

(b)

Air Flow Rate

(c)

Maximum Pressure

(d)

Combustion Delay (0-2%)
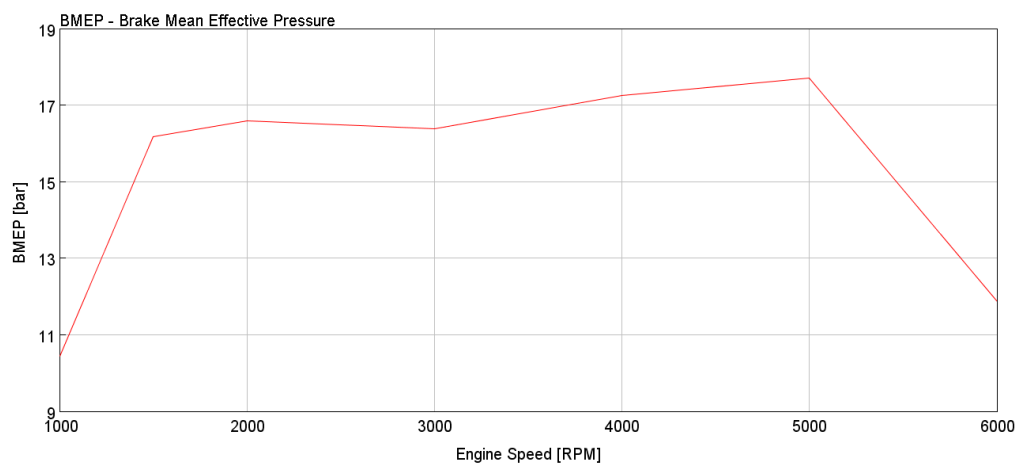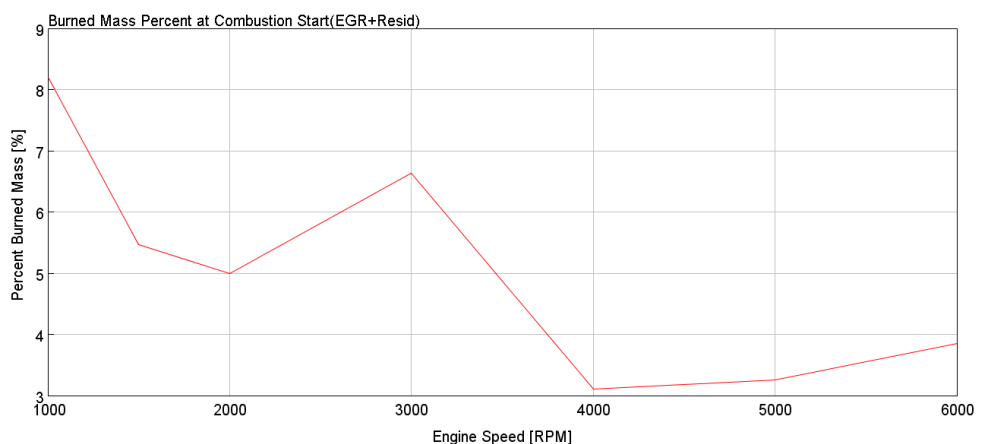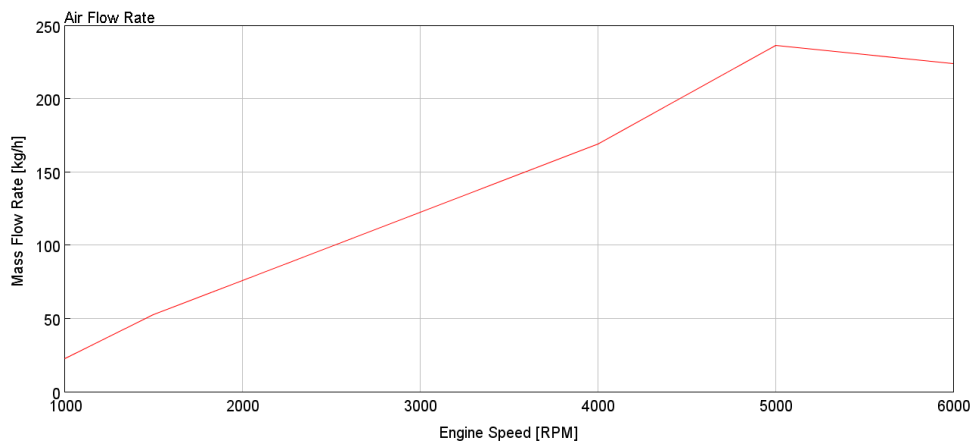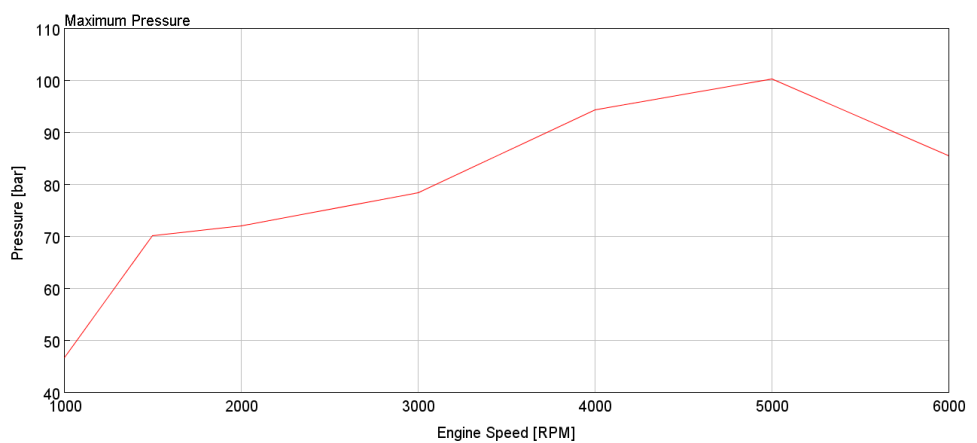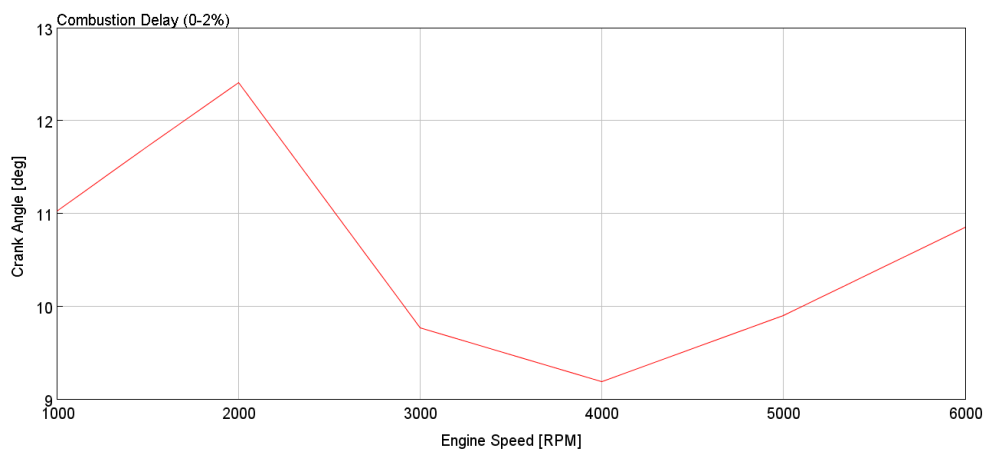
(e)
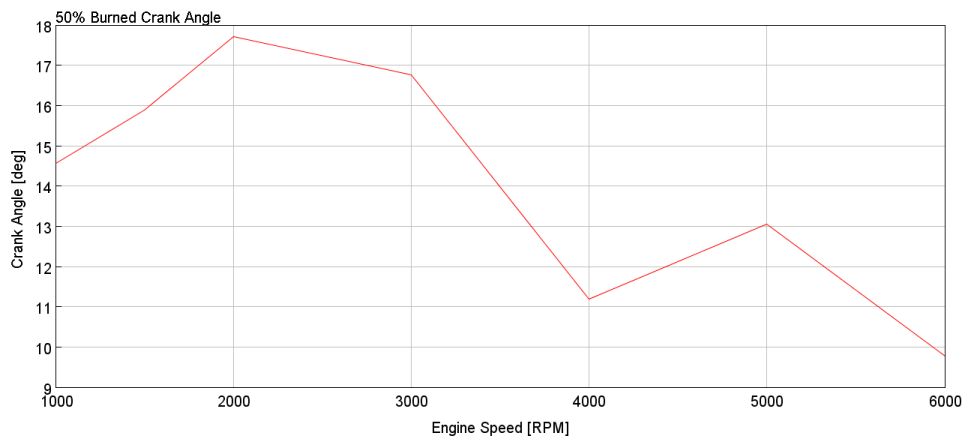
(f)
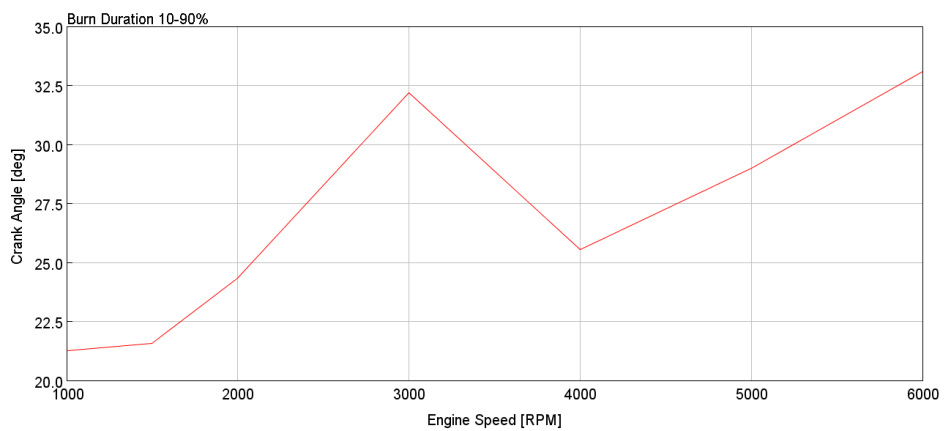
(g)

Figure 10 - Results from WOT curve simulation of the new scaled version of SC1 single cylinder engine using a 1D engine model

149

6.3. Piston Ring-Cylinder liner dynamics, leakage and Elasto-Hydrodynamic contact model

As will be discussed later in the thesis, the compression stroke is of primary importance, being the stroke during which the LSPI event takes place. To complete an accurate 3D CFD simulation of droplet motion from the crevice volume as the piston moves towards TDC it is important the thickness distribution of the oil film on the liner is represented accurately for each of the oils of interest. It is reasonable to assume the oil film remaining on the liner at the end of the intake stroke, is the hydrodynamic film thickness remaining as the piston rings passes over each axial location, as the charge gas will be cool, and evaporation will be minimal.

It is possible to calculate the film thickness profile along the length of the cylinder, for the whole engine cycle using an Elasto-Hydrodynamic lubrication model. The model will require boundary condition inputs for the lubricated conjunction between a piston ring and liner; namely the entrainment velocity, radial load and Hertzian area. The boundary conditions and fluid properties specific to the lubricant of interest can be used in conjunction with an EHL model to calculate the quasi-steady film thickness for each time step. The process employed is like that of Mahmood et al [42].

The crank train and piston ring-cylinder liner body dynamics model of a single cylinder of a production engine was developed and upscaled so that the dimensions were appropriate for the geometry being investigated. In certain cases, dimensions were corrected as a factor of the bore ratio (between production and the geometry being investigated) for radial dimensions and similarly the stroke ratio for axial dimensions. The body dynamics model can be seen in Figure 11. The ring-liner body dynamics model itself will require cylinder pressure boundary conditions in order to solve the system of forces exerted on the ring. The 1D predicted combustion model discussed earlier was used for this purpose.

150

A brief description of the methodology employed by the ring liner model is provided below. It must be noted, although the GT model does possess a Reynolds solver for film thickness, it was decided the GT model will only be used to provide instantaneous boundary conditions to a self-developed Reynolds solver, to assure the rheology and density change is computed in the same way as Mahmood et al [42].

The GT model is based on the following literature: Keribar, et al [157]. The GT model offers a full body dynamics and EHD solution, but for this study the model will be only used for body dynamics boundary conditions and the film solution will come from a developed Reynolds solver. A summary of its functionality is found below:

- The model is based on a body force diagram for the piston ring being solved for each time-step. The predicted acceleration is solved using moments and translational forces.
- Axial and rotational (toroidal twist) motions of the ring are calculated
- Deformation of the ring (bending and twisting), and thus the resistance to deformation is accounted for.
- A simple cylinder model is included and provides a spatial and time-based deformation output. It accounts for deformation due to pressure and temperature.
- A FDM EHD (Secant method) lubrication model is used for the contact between increments of the ring and liner. The deformation is Hertzian and dose not account for local deformation within the contact or subsurface stresses.
- The FDM model will only be used for the portion of the ring that is within a defined boundary threshold.
- When outside the threshold, the ring will be assumed to be detached from the surface. A compressible orifice flow equation is used to model

151

blowby from the liner side of the ring. The state of the gas is represented by the ideal gas equation.

- Pressure in the ring groove is calculated using a compressible orifice flow equation into and out of the groove. The pressure will also contribute to the radial force of the ring.

- Greenwood Williamson model is used for asperity contact [158]

- Loads imposed by the ring will consist of inertial forces, tang loads, load change due to gas pressure and thermal expansion.

- A similar model exists for the piston skirt. However, piston secondary and primary motions are used for contact force and area. Thermal deformation of the piston is also accounted for.

- Heat transfer is via gas convection and conduction from surfaces.

- A flash heating formula can also be added. Currently the only form of heat transfer to the lubricant is via conduction from the adjacent surfaces.

Piston

Piston ring and liner

contact

Connecting rod

Crankshaft
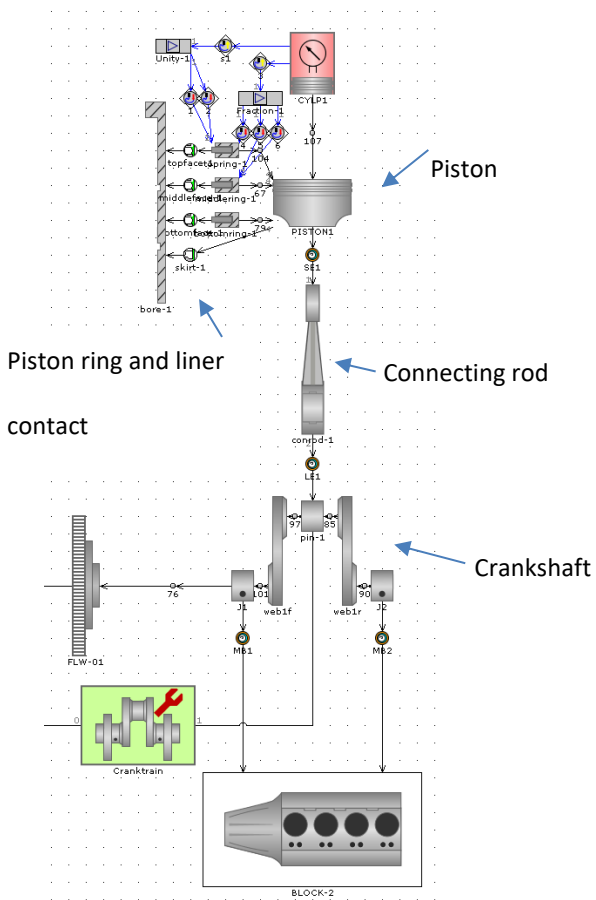
(a)
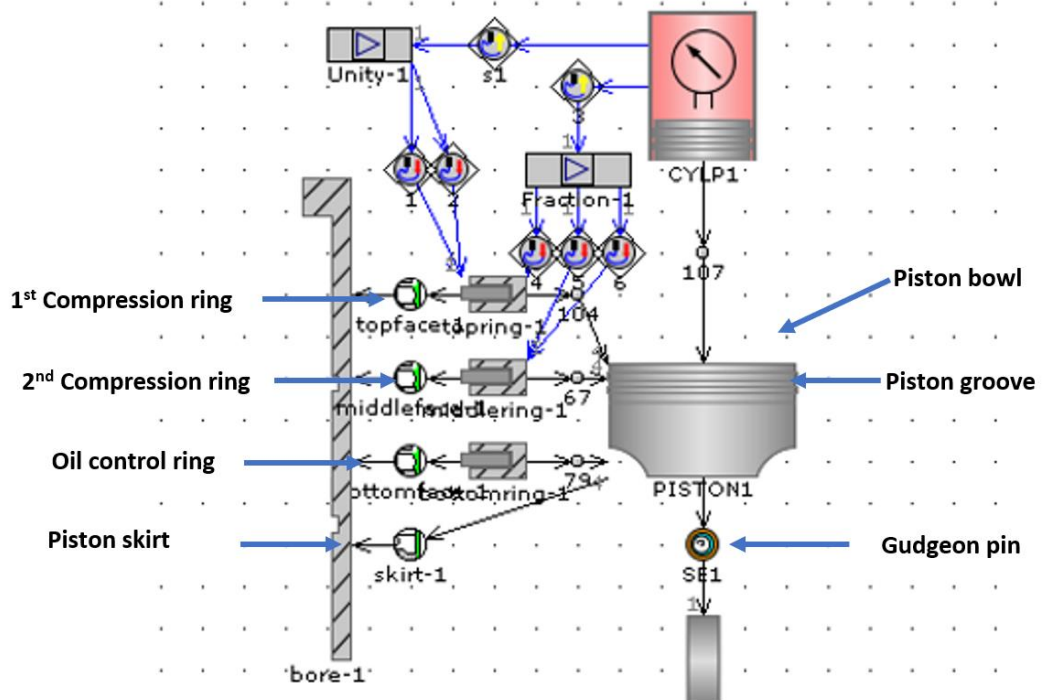
(b)

Figure 11 (a) - Piston ring-cylinder liner GT body dynamics model (b) detailed schematic of piston assembly

Figure 12 shows the process and sub-models used to define fluid properties used by the Reynolds solver for each time step. Although the Barus equation, which modifies viscosity as function of pressure was not included [66], the EHD rig validation (discussed later) confirmed it was not required for a good correlation. Mahmood et al [42] also mentions the Barus correction only has a small impact on the solution.

The Walther equation [42] provides Kinematic viscosity as function of temperature, it is then converted to a dynamic viscosity (using density) and provided to the Cross equation which corrects the dynamic viscosity as a function of shear rate. Finally, a density is calculated using an equation of state, for the film pressure solution at each node. The calculated density is

then fed back to the Walther equation for conversion from kinematic viscosity to dynamic.
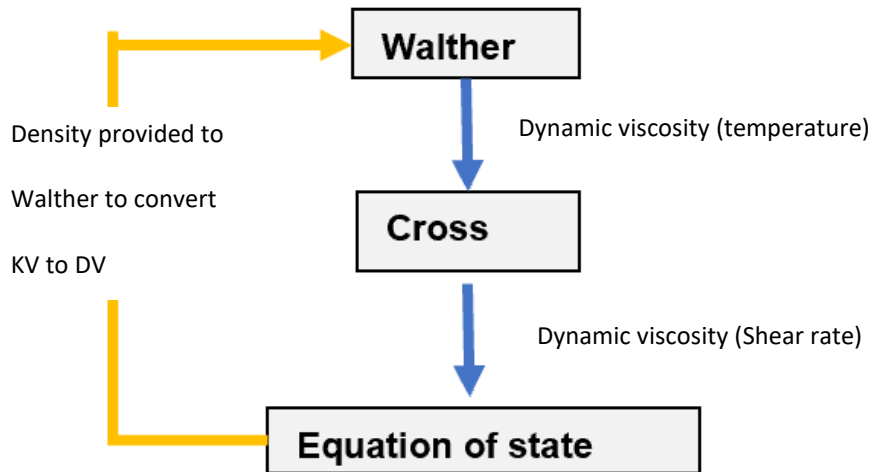
Figure 12 - Diagram adapted from Mahmood et al, showing the sub-models that define the fluid properties used by the Reynolds solver

The Walther equation shown below, relates temperature to the Kinematic viscosity. The kinematic viscosity term can be replaced by the KV40 and KV100, providing a simultaneous equation that can be solved to derive constants A and B [42].

$$\log \log \; (v + 0.7) = A + B \log T \qquad \text{[eqn 62]}$$

T is absolute temperature, A and B are fitting constants and v is Kinematic viscosity.

155

As the world moves towards low viscosity oils to improve fuel economy [146], it was decided that 0W oils of varying viscosity should be the starting point. Figure 13 shows the Walther curves for the 6 oils that were selected. All viscometric data was provided by BP.
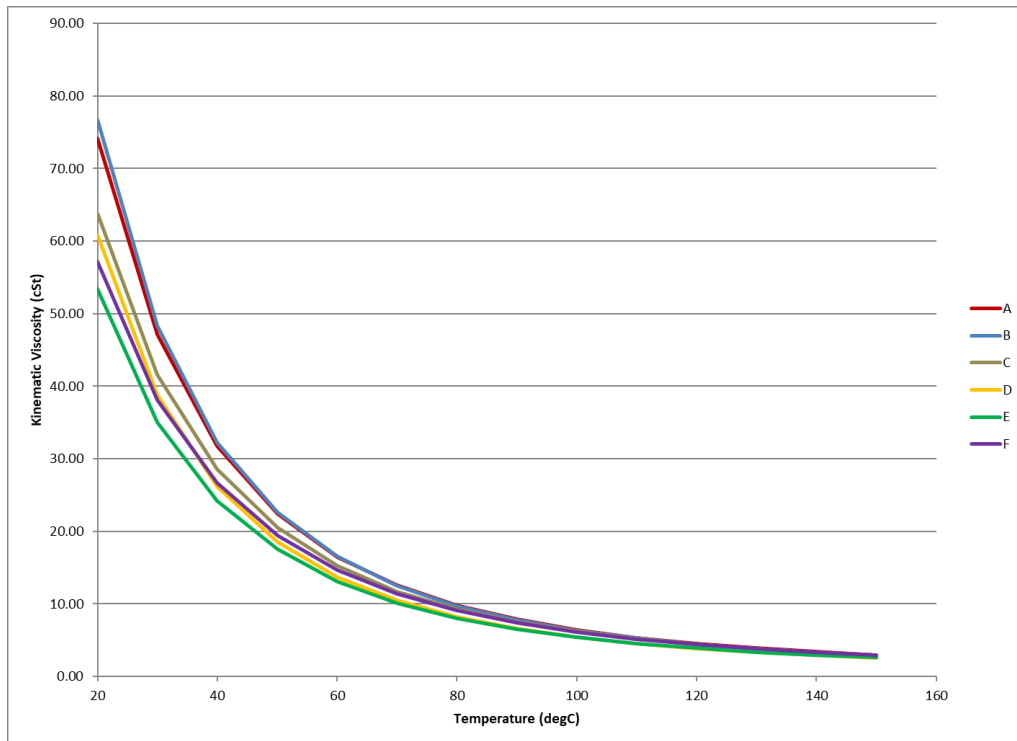
Figure 13 - Walther model results for the six oils that were simulated, Kinematic Viscosity vs Temperature

The Cross equation found below, corrects the Walther viscosity as a function of strain rate.

$$\mu_c = \mu_\infty \frac{\mu_0 - \mu_\infty}{1 + (\mu_0 \, \lambda/G)^n} \qquad [\text{eqn 63}]$$

μ_c is the shear corrected viscosity, μ_0 is the low shear viscosity, μ_∞ is the high shear viscosity, λ and G are fitting coefficients and n is a fitting exponent.

The low strain viscosity is provided by the Walther equation, using the appropriate density. The high strain viscosity is obtained from an Ultra High Shear viscometer [42]. It can be seen the function provides low shear and high shear asymptotes.

The resulting Cross equation curves can be found in Figure 14.
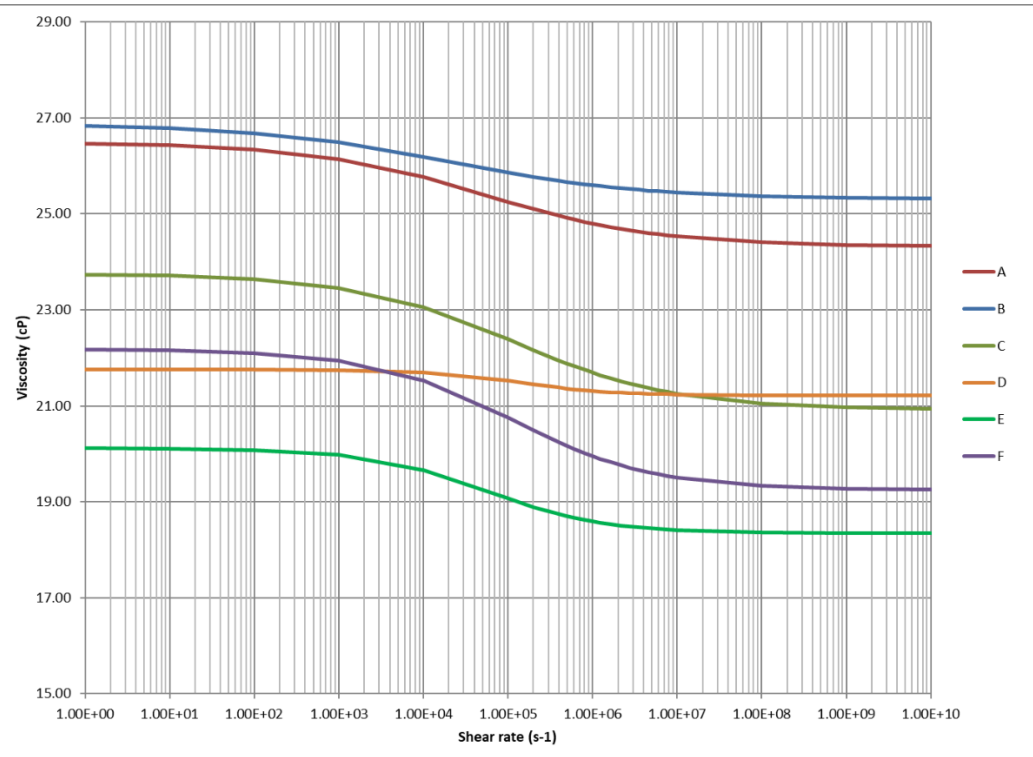
Figure 14 - Cross function results for the six oils that were simulated, the low shear viscosity is the output by the Walther model. The data is obtained from a high shear viscometer

For the Equation of State (EOS) – Mahmood et al [42] uses a modified version of the Pascal Vinett equation of state. This equation that relates pressure to the dimensionless 'characteristic linear compression', from which a volume ratio changes due to pressure and thus density can be calculated (as mass will be constant).

157

$$P = \frac{3B_0}{x^2} (A - x)e^{\eta(A-x)}$$

$$x = \left(\frac{V}{V(p=0)}\right)^{1/3} \qquad \text{[eqn 64]}$$

B_0 is the Bulk Modulus at standard atmospheric conditions, x is linear compression (cube root of the ratio between current volume and initial volume), η is a fitting coefficient, P is pressure and A is a fitting constant that has been introduced (not in original Vinett equation).

Because EOS data was not available specifically for the six oils of interest, a nominal oil EOS was of an oil of similar viscosity grade. A multiplier was then applied to the function to provide a best fit between the film thickness predicted by the model for a circular contact and that measured on the EHD ball on disk rig (discussed later). This iteration is acceptable as the equation of state is the only remaining unknown that is in input to the Reynolds solver, as the viscosity characteristics are derived from test data. Any remaining error between simulation in test must be due to the EOS. Figure 15 shows the EOS data range of interest and the multiplier that was placed to the reference curve to achieve good correlation with the EHD rig results. It can be seen for three of the oils the EOS was unchanged, and only a maximum change of 5% for the remaining ones. The comparison between simulated results and predicted for two of the oils can be found in Figures 17(a) and 17(b).
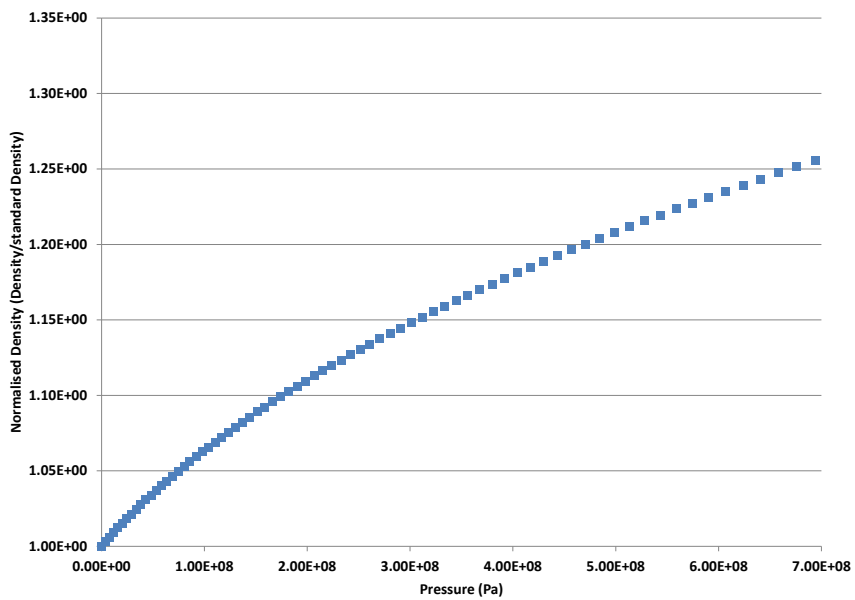
(a)

Oil	Density curve multiplier
A	1
B	1
C	1
D	1.02
E	1.05
F	1.05

(b)

Figure 15 - (a) Pressure vs normalized density with multiplier of 1 (b) mulripliers applied to reference curve for candidate oils
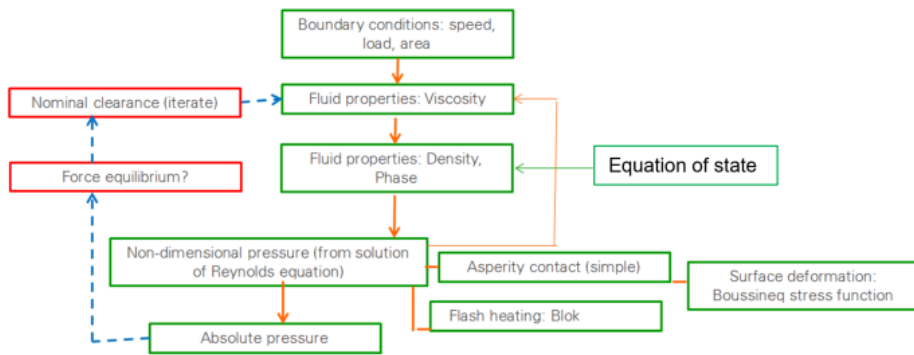
Figure 16 - Schematic showing a simplified explanation of the EHD model calculation process

Figure 16 provides a modelling process diagram for the EHL simulation model. A brief explanation of the process follows:

- GT suite provides boundary conditions for each time step; normal load, entrainment velocity, Hertzian contact area

- Film pressure, temperature and shear rate for the given iteration are used to calculate fluid properties

- The Reynolds solver coupled with flash heating (created from asperity contact and fluid shear) and asperity contact model.

- The nominal film thickness will iterate until the sum of the film pressure integral, and the total load supported by asperities equals the total normal load

The calculated densities for each node will be provided as an input to the to the Walther viscosity model, in the conversion from Kinematic to Dynamic viscosity.

A simplified asperity contact model such as that used in Mahmood et al [42] was used. A mean asperity height was assumed. The contact model uses a mean asperity height and asperity density, the asperity compression is calculated for each film thickness iteration, the asperity load is subtracted from the total load and then the film solution reiterates for the new hydrostatic load. The Boussinesq fuction [42] was also used for 2D surface deformation.

The Reynolds equation is the traditional equation used to model lubricated contacts. It is derived from mass and momentum conservation equations. The inertia terms from the momentum equation are dismissed on the basis that they are negligible in comparison to the viscous forces, due to the contact being thin and long. The equation can be found below. It conveniently separates Couette terms and Poiseuille terms on separate sides of the equation [42].

.

$$\frac{\partial}{\partial x}\left(\frac{\rho h^3}{12\mu}\frac{\partial p}{\partial x}\right) + \frac{\partial}{\partial z}\left(\frac{\rho h^3}{12\mu}\frac{\partial p}{\partial z}\right) = \frac{1}{2}\frac{\partial (U)\rho h}{\partial x} + \frac{\partial \rho h}{\partial t} + \frac{1}{2}\frac{\partial (W)\rho h}{\partial z} \qquad \text{[eqn 65]}$$

h is film thickness, U and W are velocities in x and z directions, p is pressure, t is time μ is dynamic viscosity and ρ is density.

For a quasi-steady solution, the temporal term will not be included.

For convenience, the non-dimensional version of the Reynolds equation is used [42] [65], shown in eqn 66.

$$\frac{\partial}{\partial \bar{x}}\left(\bar{h}^3\frac{\partial \bar{p}}{\partial \bar{x}}\right) + \frac{X^2}{Z^2}\frac{\partial}{\partial \bar{z}}\left(\bar{h}^3\frac{\partial \bar{p}}{\partial \bar{z}}\right) = \left(\frac{C}{X}\frac{\partial \bar{h}}{\partial \bar{x}} + 2\frac{\partial \bar{h}}{\partial \bar{t}}\right) \qquad \text{[eqn 66]}$$

161

$\bar{x}$ is non-dimensional distance in direction of entrainment, $\bar{h}$ non-dimensional height, $\bar{z}$ is non-dimensional distance in direction normal to direction of entrainment, $\bar{p}$ non-dimensional pressure, C is nominal film height, X and Z are maximum domain dimensions.

The non-dimensional Reynolds equation can be discretised in the spacial domain by converting it into a Taylor series expansion. H.Hirani offers a discretized version of equation 63 [1], using a Taylor Series formation. Mahmmood [42] modifies the formula provided by Hirani [65] and includes nodal density (density value at solution node). The resulting equation can be found in eqn 67, as mentioned the temporal term has not been included.

$$\overline{P_{i,j}} = \left(\frac{\overline{h_{i+0.5,j}^3}}{\left(\overline{h_{i+0.5,j}^3} + \overline{h_{i-0.5,j}^3} + \frac{2X^2}{Z^2}\right)\left[\frac{\Delta\bar{x}}{\Delta\bar{z}}\right]^2 \overline{h_{i,j}^3}\left(\overline{\rho_{i+0.5,j}} + \overline{\rho_{i-0.5,j}}\right)} * \overline{P_{i+1,j}} + \right.$$

$$\left. \frac{\overline{h_{i-0.5,j}^3}}{\left(\overline{h_{i+0.5,j}^3} + \overline{h_{i-0.5,j}^3} + \frac{2X^2}{Z^2}\right)\left[\frac{\Delta\bar{x}}{\Delta\bar{z}}\right]^2 \overline{h_{i,j}^3}\left(\overline{\rho_{i+0.5,j}} + \overline{\rho_{i-0.5,j}}\right)} * \overline{P_{i-1,j}} \right) +$$

$$\frac{\frac{X^2}{Z^2}\left[\frac{\Delta\bar{x}}{\Delta\bar{z}}\right]^2 \overline{h_{i,j}^3}}{\left(\overline{h_{i+0.5,j}^3} + \overline{h_{i-0.5,j}^3} + \frac{2X^2}{Z^2}\right)\left[\frac{\Delta\bar{x}}{\Delta\bar{z}}\right]^2 \overline{h_{i,j}^3}\left(\overline{\rho_{i+0.5,j}} + \overline{\rho_{i-0.5,j}}\right)} * \left(\overline{P_{i,j+1}} + \overline{P_{i,j-1}}\right) -$$

$$\frac{\Delta\bar{x}}{2}\frac{C}{\bar{\bar{X}}} \frac{\left(\overline{h_{i+1,j}} - \overline{h_{i-1,j}}\right)}{\left(\overline{h_{i+0.5,j}^3} + \overline{h_{i-0.5,j}^3} + \frac{2X^2}{Z^2}\right)\left[\frac{\Delta\bar{x}}{\Delta\bar{z}}\right]^2 \overline{h_{i,j}^3}\left(\overline{\rho_{i+0.5,j}} + \overline{\rho_{i-0.5,j}}\right)}$$

[eqn 67]

$\bar{\rho}$ is the non-dimensional density, i and j are node numbers in the x and y axis. This arrangement is ideal for an iterative solution using the Secant method.

Figures 17(a) and (b) show the film thickness predicted by the finite difference model with the measurements obtained from the EHD rig (measured at Catrol BP UK). The EHD rig is a rig that can accurately measure the fluid film thickness for a rotating ball and rotating disc contact, the normal load and entrainment velocity can be varied. It can be seen the methodology can be used with confidence as the simulation are in good agreement with test results.
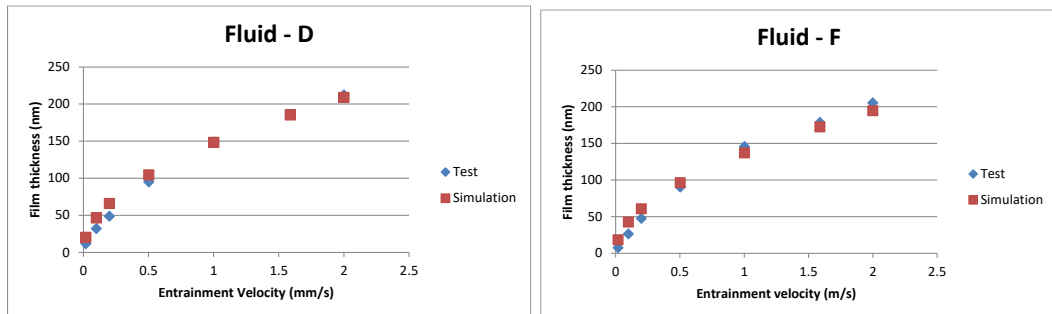
Figure 17 - (a) & (b) Comparison of EHD rig test results gains FDM simulation results for 30N normal load, with varying entrainment velocity, film thickness is measured using ultrasonics

The Reynolds solution for a piston ring- cylinder liner contact solution is simpler as it only needs to be solved in the direction of entrainment. Upon the assumption that the forces on the ring are radially uniform, the lateral component of the fluid film will have the same pressure at all locations around the ring, meaning there is not fluid transport in the lateral direction.

Under normal operation the oil temperature is typically at a nominal temperature of 95deg°C-100deg°C. We can see from the Walther function curves in Figure 13 that the viscosities of all the oils are virtually identical at this high temperature. For this reason, the simulation will be completed assuming an instant during a warm-up condition when the oil temperature is 50C, from literature we know that cooler water jacket temperatures promote LSPI.

163

It is known from published engine testing that LSPI takes place at the 'knee point' of a GTDI (minimum speed at which the engine can achieve maximum torque), which is nominally 1500RPM [136], for this reason this was the simulation condition of interest. A piston ring-cylinder liner body dynamics and friction model was developed using the geometry details available for the 3D geometry and the cylinder pressure profile predicted by the 1D engine model was used as a boundary condition. As discussed in the earlier section, the model accounts for ring dynamics and deformation due to gas and inertial loads but does not account for thermal expansion. The entrainment velocity, radial load and Hertzian area predicted by the body dynamics model can be used as boundary conditions for the FDM model and allow us to obtain film thickness throughout the strokes. From early testing of the 3D CFD engine model it was found the droplet behaviour was highly dependent upon the initial film thickness assumed on the cylinder liner. For this reason, the predicted film thickness will be mapped onto the 3D liner geometry when the piston is in its BDC position. The results from the piston ring-cylinder liner FDM simulation for the five selected oils are shown in Figure 18 (a) & (b).

 It should also be noted that at this stage the Reynolds simulation assumes the oil is always in its liquid phase and calculates a film thickness for all stages of the engine cycle. In reality, the oil will mostly have evaporated for the exhaust and expansion strokes. However, the intake stroke film thickness profile is of interest for this study, for which the oil will be in its liquid phase. The film thickness profile for a given oil is predominantly influenced by the entrainment velocity (mean velocity between the two surfaces). At the TdC and BdC positions the entrainment velocity is zero and thus a minimal film thickness is observed. The maximum film thickness will be achieved close to mid-stroke when the entrainment velocity is at its highest. The higher the viscosity of the oil the thicker the film because of the increased shear pressure. The same simulation has been conducted by other researchers modelling the ring-liner contact [152][153][154], showing very similar film thickness profiles to those achieved in this study.

164
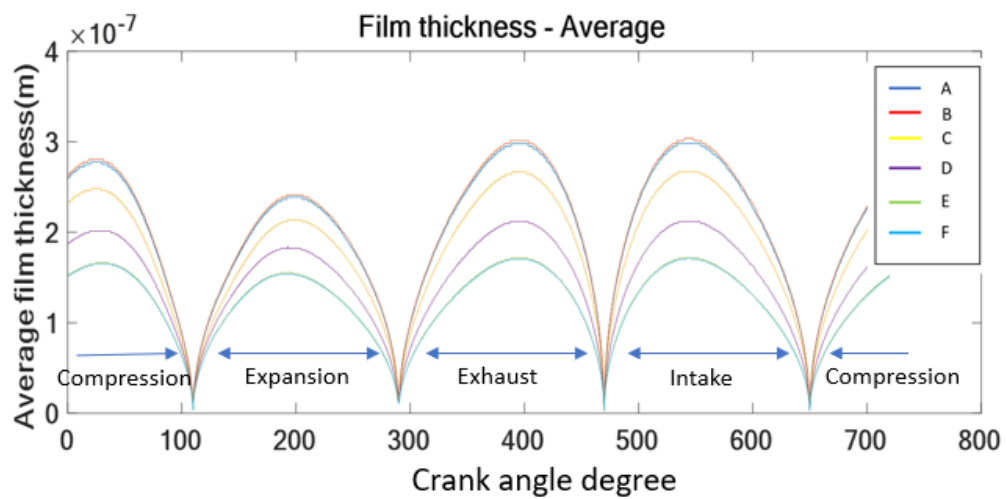
(a)

0W grade engine oils					
High viscosity		Mid viscosity		Low viscosity	
A	B	C	D	E	F
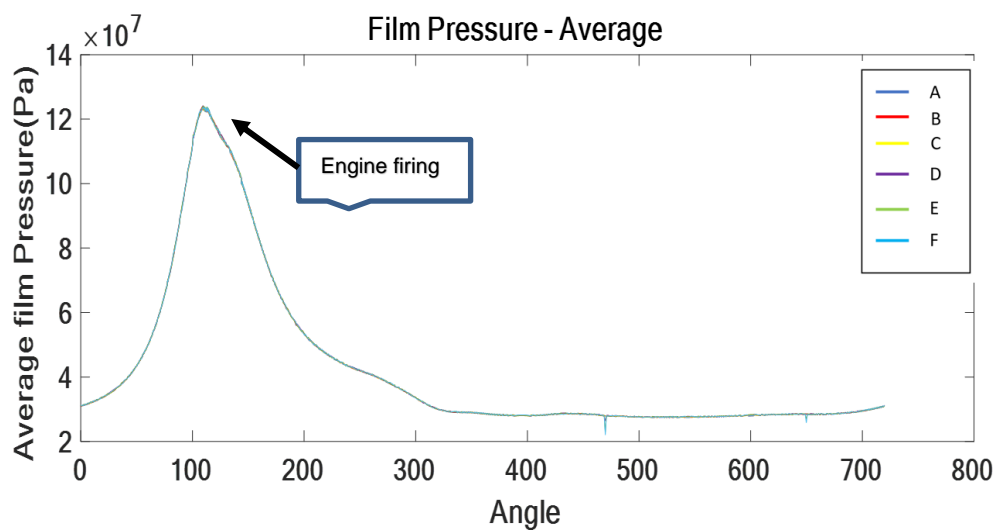
(b)

Figure 18 - FDM results of the Piston ring-cylinder liner contact at 1500RPM, WOT operation. The geometry defined is that of the 3D CFD model

165

6.4. Lubricant transport, breakup & Impact of lubricant fluid properties

In this section a 3D CFD model will be developed to simulate the scraping of the oil film from the liner, during the compression stroke in particular. Both the Reynolds model and GT combustion models developed earlier in this section will be used for boundary conditions. The location and size of fluid parcels close to the point when LSPI is observed will begin to provide some insight as to the origin of this behaviour. In addition, the impact of fluid properties will be investigated.

Following some initial testing it was decided using the VOF scheme (described in chapter 4.2.2) would be impractical for the number of cases that needed to be run, due to it being very computationally expensive, resulting in extended run times. It was decided a Lagrangian approach would be the optimal solution due to its inexpensive run time, but also because the model could be set up such that the inter-droplet interactions are insignificant, making it similar to the continuous domain solution of Eulerian approaches (such as VOF).

A script was developed to initialise an oil film along the cylinder liner. It works by assuming an initial droplet radius. The film thickness along the length of the liner can be characterised using a polynomial function, the script will allocate the correct number of droplets along the liner to achieve the thickness specified by the polynomial. It will be assumed the oil below the maximum ring position will be scraped off from the cylinder liner such that only the elasto-hydrodynamic film remains. For this reason, the oil film will be re-initialised using the code each time the piston is in its Bdc position for all of the experiments.

Although the film thickness is established from the ring-liner simulation described above the initial droplet size and thus the number of coalescent

166

droplets making up this thickness as well as the droplet density in the axial direction of the cylinder has to be pre-defined. This is difficult to measure on a real engine and so a sensible value has to be approximated.

The model setup is summarised in table 5, the theory associated with the main functionality and sub-models has been covered in earlier sections and some will be covered in this section.

Mesh type	Orthogonal, structured, Adaptive mesh refinement (AMR)
Gas Equation of state	Redlich-kwong
Global Prandtl number	0.9
Global Schmidt number	0.78
Gas flow solver	Compressible
Liquid flow solver	Incompressible
Gas domain	Eulerian (RANS)
Oil film domain	Lagrangian
Lagrangian – collision model	NTC collision
Lagrangian- Breakup model	Rayleigh-Taylor
Oil film splash model	O'Rourke
Turbulence model	K- ω (RANS)

Table 5 - Summary of CFD model setup and sub-model selection

- A detailed explanation of the Rayleigh-Taylor breakup model, Eulerian and Langrangian solutions and the K-ω turbulence model is provided in chapter 4. For the additional models used in the setup, a brief explanation of each can be founds below [71]:

- Adaptive mesh refinement (AMR) – This is a scheme that refines the mesh within the continuum depending on the gradient of the predicted property. These properties can be density, velocity, or temperature of the droplet.

- O'Rourke splash model – This model dictates if a fluid parcel travelling towards a dry surface or film thickness will splash (breaking into discrete particles and a velocity component in the opposite direction to the original parcel), or if it will simply attach itself to the film. In this model a E^2 value is calculated as a function of; the Weber number (=drag force/cohesive forces = density * velocity^2 *characteristic length/surface tension), local film thickness, impinging drop diameter and boundary layer thickness. The E^2 is a parameter that determines if a particle has splashed and thus broken into smaller particle or rebounded and not broken up. When the calculated E^2 value is greater than the critical E^2 value then the splash criteria has been fulfilled.

- No time counter (NTC) collision model – The NTC model predicts the likelihood of fluid parcels colliding within a cell. A subsample of particles from within a cell are randomly selected for each time step, a stochastic collision model is used to calculate the probability of a collision occurring. The probabilities are multiplied by the reciprocal of the sample fraction. The process will be repeated several times over a

timestep, the probabilities will be summed to calculate the total probability of a collision occurring.

The initial cell base size was optimised to 4mm,4mm,3mm (dx, dy, dz). The mesh size was optimised by beginning with a small size and increasing it to the maximum size that did not compromise the TKE (turbulent kinetic energy) and droplet location prediction.

6.4.1. Investigating fluid properties influence on droplet transport

For the 4-stroke engine cycle it is the upstrokes, from BdC to TdC, that are of most importance, as these are the strokes that potentially scrape oil from the liner and transport it towards the combustion chamber. Although it is possible for a mixed phase oil-crank case gas mixture to leak past the rings on the down stroke, most of the oil will be scraped downwards towards the crankcase. However, only a small amount of oil from the crevice volume will on the surface during the exhaust stroke, as most of it will evaporate. The compression stroke is crucial, firstly because it is the stroke in which LSPI occurs, but also because the oil is most likely to stay in liquid phase prior to combustion due to the higher pressure (increased boiling point) and cooler gas temperature.

For this reason, a small amount of oil is initialised in the crevice volume at Bdc of the exhaust stroke. The exhaust stroke is then simulated, resulting in a small number of parcels being placed above the maximum position of the top ring, several parcels also escape into the exhaust path. A small number of parcels do rebound off the head and attach to the liner and piston as the intake stroke progresses. Again, this is plausible, as the cooler intake air enters, the parcels that remain in the cylinder are likely to maintain a liquid state. The difference in film thickness between the intake stroke and compression stroke predicted by the Reynolds solver was calculated for each axial position along the liner. At the Bdc position of the compression stroke this calculated film thickness profile predicted by the Reynolds solver is

169

imposed upon the liner. As there is no gap between the ring and liner, all the oil film at each location will be removed as the piston proceeds. The assumption is that the only oil removed is the difference in hydrodynamic film between the intake and compression strokes, at each piston position i.e., once the piston cooling jets spray oil onto the liner, the film thickness remaining at each location during the intake stroke will be the hydrodynamic film thickness between piston ring and liner for that location. The difference in hydrodynamic film thickness at each location between the intake and compression stroke will be the mass removed and contained in the crevice. This is the mass that will be removed by the ring flush against the liner in this case. The mass of oil transported by blowby gases was very small in comparison to that transported by the motion according to the testing carried out by Yilmaz [145], so will be assumed to be negligible in this case.

To create the film thickness profile along the liner, a script was provided by Convergent Science. A film thickness profile is provided for each location along the cylinder liner. The script then creates a map file that places droplets adjacent to one another for the full stroke length and stacks the required number of droplets in the radial direction to achieve the film thickness at each location. An initial fluid parcel size is assumed.

The initial droplet size assumed does have a small impact on the results. Following some preliminary testing it was found the best way to reduce the impact of the size of discrete particles was to set the droplet surface tension to a very low value. This reduces the boundary effects between droplets making the interaction viscous dominant, makes it easier for droplets to coalesce and thus allows the film to behave like a continuous parcel. Also, in most hydrodynamic calculations the surface tension aspect of film deformation is ignored, as it is deemed insignificant in comparison to the viscous resistance to deformation.

170

The inlet and exhaust port pressure and temperature boundary conditions in the 3D CFD model were set to that predicted by the rescaled 1D combustion model for WOT, 1500RPM. At this stage evaporation is not being accounted for or heat transfer to the droplets as the purpose of this study is to investigate the impact of viscosity on oil transport behaviour in its liquid phase. For this reason, the simulation was independent of phase change. Similarly, only the exhaust, intake and compression were simulated as the initial pressure and temperature of the in cylinder gas was re-initialised to that predicted by the GT model at Bdc of the compression and exhaust strokes.

For this part of the study only fluid parcel breakup due to boundary shear, turbulent deformation, surface impingement and parcel collision will be accounted for.

The film thickness predictions shown in figure 18(a) were used as initial conditions for the simulations conducted, although A was not simulated as the film thickness is very similar to that of B. Similarly, E was not simulated due to its similarity to F. The viscosity changes as a function of temperature, as well as density change as a function of temperature in the CFD model was defined to be the same as that assumed in the FDM model.

The specific heat capacity and thermal conductivity characteristics were taken from Wrenick et al [3] and were assumed to be similar for all oils. When looking at oil specification data this seems to be a reasonable assumption, as thermodynamic properties do not vary much for oils of the same viscosity grade [3].

Figure 19 provides images of the CFD engine simulation at the beginning and towards the end of the compression stroke. The images show the droplet size and motion as well as the origin of momentum indicated by the droplet flag,

171

where; 1 = parcel in wall film, 2 = rebounded parcel, 3 = splashed parcel, 4 = separated parcel and 5 = stripped parcel.

Droplets do not escape from the crevice volume whilst the piston is acceleration because it is the piston that determines the velocity of the droplets. The droplets become detached when the piston decelerates past the mid-point, the droplets maintain most of their momentum as there is really only air pressure and some shear retention trying to decelerate them. As the piston decelerates further the relative velocity difference between the droplets and piston surface increases, more and more droplets are released. As mentioned, the extent to which the droplets will decelerate will be impacted by viscous forces, and the number of droplets that escape into the gaseous domain by a specific time (20deg BTdc) will be determined by their velocity out of the crevice volume. Therefore, viscous forces impact the number of droplets that can escape the crevice volume and reach the combustion chamber (refer to figure 19 for an illustration of the described behaviour).

This simulation assumes no gap between the ring and liner, all the droplets are scraped off by the ring. As can be seen from the Reynolds solver a thinner film remains during the compression stroke. The number of droplets removed should be the amount that corresponds to the difference in film thickness between the intake and compression stroke for a given ring position. Accounting for the ring-liner gap would be very complicated and time consuming. As you would need to modify the geometry to allow for a certain amount of leakage past the rings at each time step. This would require a specialist script, and the solution to continuum equations would need to be modified to conserve mass and momentum as some particles would effectively disappear from the analysis, this would make the simulation very unstable. The latter would require dynamic morphing of the geometry which has long run times but simulating flow through a very small gap such as the

172

ring-liner interface will almost certainly cause the model to diverge. The assumption of all of the droplets being removed is acceptable if the film thickness at each ring position is of a thickness that is the difference between that predicted for the intake and compression strokes. The difference in film thickness between the two strokes will be the mass of oil that is contained in the crevice volume, the oil that will eventually be transported to the combustion chamber.

The stress between the fluid and crevice wall is define by the contact angle. Keller et al [142] investigated the impact of viscosity on contact angle for various hydrocarbons. Contact angle usually increases with oil viscosity and advancing velocity. An approximate polynomial was fit to the viscosity vs contact angle data presented in this literature; The data point used was at the highest advancing velocity at an oil temperature of 25degC. We can then lookup the contact angle for any dynamic viscosity at an oil temperature of 25degC. With this being the best data available, it is possible to make a temperature extrapolation to find viscosity and contact angle values that are representative of the 50degC being simulated. However, with the data set only offering two temperatures for each oil, the extrapolation would be linear and thus problematic. For this reason, it was decided the contact angle corresponding to the viscosity of the oil at 25degC will be used, as a trend relating to the viscosity will be accounted for. Also, the impact on contact angle over small temperature changes for the same oil is very small compared to viscosity grade and advancing velocity. The data used for the lookup can be seen in Table 6.

	Pt M Crude	HydroCal 300	IFO-120
Dynamic viscosity @15C (mPaS)	24	342	1540
Dynamic viscosity @25C (mPaS)	14	162	487
Contact Angle (deg)@15C	23	52	67
Contact Angle (deg)@25C	22	36	54

Table 6 - Contact angle for oils of differing viscosities [142]

173
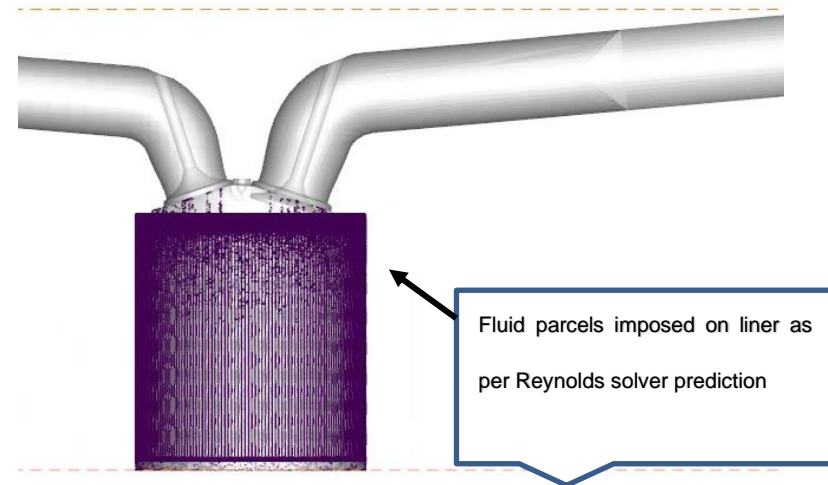
(a)
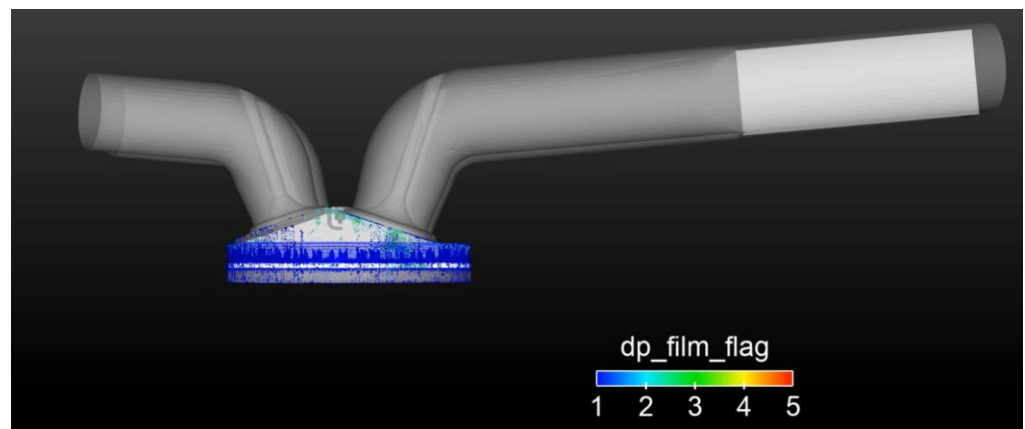
(b)

Figure 19 - (a) initialised parcel positions at the beginning of the compression stroke (b) Droplet motion and momentum origin results from CFD analysis of compression stroke. Note, for ease of visibility the spheres shown identify the position of the parcel and do not reflect the actual size of the parcel

6.4.2. **Oil Transport CFD model Results, validation and Discussion**

0W grade engine oils					
High viscosity		**Mid viscosity**		**Low viscosity**	
A	B	C	D	E	F
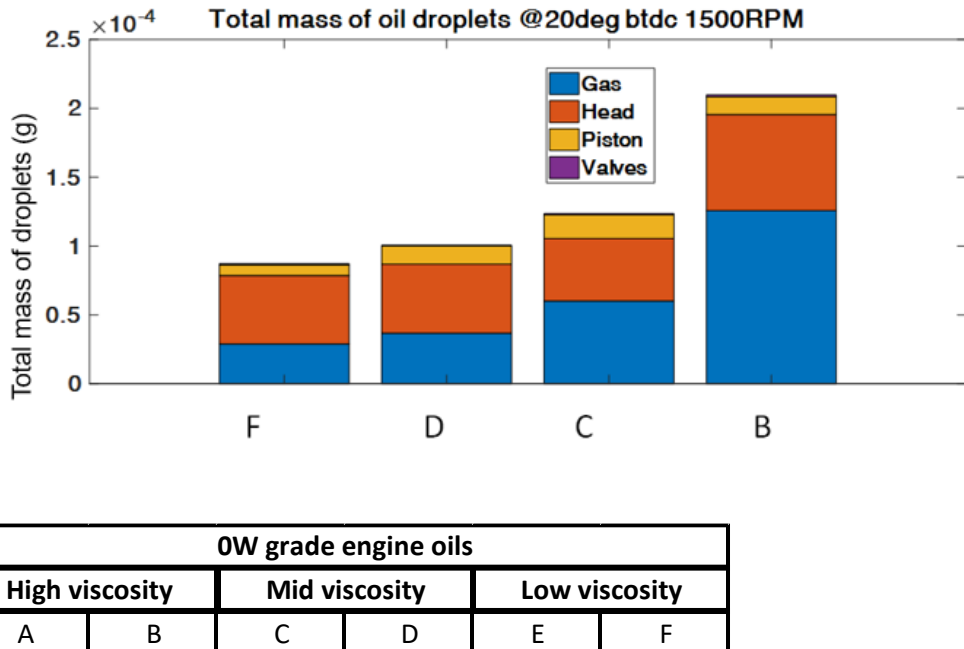
Figure 20 – Stacked bar plot of oil droplet location with varying oil viscosity along liner

Figure 20 shows a summary of the total mass of oil droplets on the various surfaces 20deg bTDC of the compression stroke for each of the oils, a reference point often used as the nominal point at which LSPI mechanisms initiate. The oil viscosities of the oils are in the order of (starting with the highest); F>D>C>B. Most of the oil droplets remain in the gas domain or on the head which makes sense, as the gas is the major transport domain, and the momentum of the droplets will be in the direction of the head. The amount of oil mass transported from the crevice volume reduces with increasing oil viscosity even though the initial hydrodynamic film is thicker (film thickness shown in Figure 18). This is because the sub-surface droplet viscous forces are higher as well as the shear force between the fluid and dynamic boundaries. These act as retention forces countering the inertia of the droplet as the piston decelerates towards TDC. It is important to remember that

175

viscosity is only accounted for within each droplet itself, as the interaction between fluid parcels is modelled as a series of collisions, so the viscosity and surface tension will determine the droplet's ability to deform as parcels attempt to move relative to one another, which ultimately determines the retention force on the droplets attempting to escape. In this case the surface tension is very low, making viscosity the dominant contributor. We know from the O'Rourke scheme described in chapter 4.2 that often, when the collision takes place with sufficient momentum, or if parcels are forced together with reasonable force the parcels will coalesce into one.

Although the overall trend on surface suggests a lower viscosity leads to a larger mass of ejected oil, there is more variation in the fractional distribution of the oil. This is because surface droplets can be in various phases e.g. splashed, attached, rebound etc, impacted by factors such as droplet size, velocity and angle of impingement. Certain boundaries such as the head, has a large number of droplets impacting with it. The head area available in line with the trajectory leading from the crevice volume is very limited, some droplets will attach to the area available, any in excess will rebound. This limitation in area available for attachment is why the mass of oil on the head is largely constant. The increase in mass with the lowest viscosity oil is most likely because the droplets have a higher velocity (due to lower viscous forces decelerating them),there are also a larger number of droplets impinging, meaning some of the excess droplets that cannot attach to a surface because of insufficient available area, will coalesce with those attached.

As a sanity check, we can compare the oil transport with the oil consumption predicted by the direct cylinder measurements in Yilmaz [145], although the bore and stroke are slightly bigger in this study. The paper confirms most of the oil is transported or evaporated from the walls, and very little is lost to blowby. At this stage of the study evaporation is not being accounted for, so all the oil from the walls will be transported by the piston rings. The publication

records oil consumption of approximately 0.1mg/engine cycle at an engine condition of 2500 rev/min and 100% load. This oil consumption is very similar to the oil transport recorded for a single cycle in Figure 20. This does not provide direct validation as the engine geometry, engine running condition and oil are different to that assumed in this study but does confirm the oil transport values being predicted are plausible.

It was interesting that Konigsson [51] found increasing the viscosity of lubricant oil to a maximum rating of 15W actually increased the LSPI occurrence. Hence, the next stage will involve assessing if further increasing the viscosity of the oil droplets continues to increase their resistance to inertia and thus reduces the total mass of oil transported from the crevice volume to the combustion chamber.
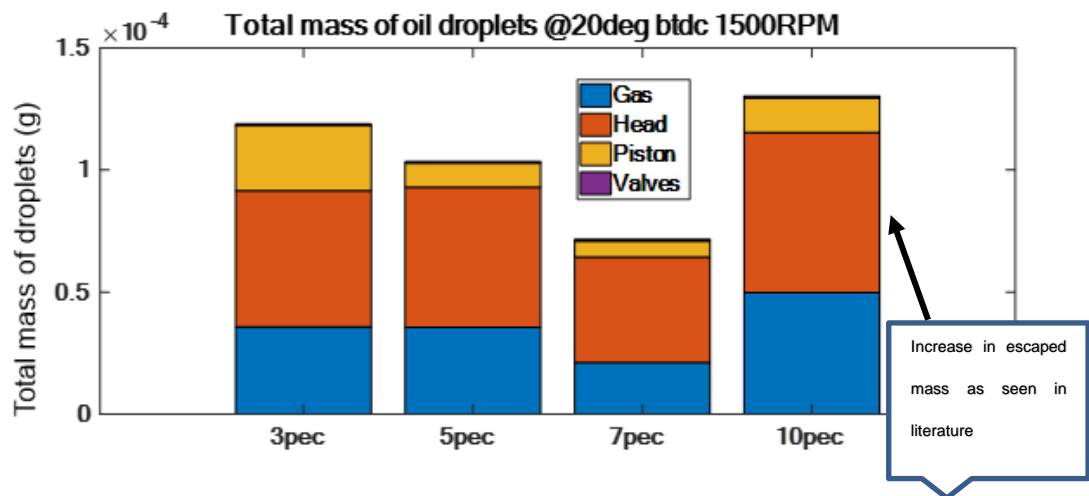
Figure 21– Stacked bar plot of oil droplet attachment with varying droplet viscosity by applying a multiplier to the viscosity characteristic of fluid B (pec indicates percentage increase)

As fluid B was the oil of highest viscosity it was decided it will be the reference oil that will characterise the baseline viscosity change as a function of temperature. A viscosity multiplier of 3%, 5%, 7% and 10% was applied to the

fluid B viscosity-temperature characteristics (Walther curve). Figure 21 shows the results from the CFD droplet simulation for the four viscosity multipliers.

Interestingly a sudden increase in oil mass releases is observed when the viscosity is increased by 10%. Deformation and the eventual breakup of droplets is dominated by the tangential force acting on the surface of the droplet, the surface tension and viscosity. The summation of the outer droplet surface tension force and internal viscous forces determine the resistance to deformation. In this case the surface tension of the droplets is set to a very low value, making it easier for droplets to coalesce, and reduce the interfacial surface tension component of force, thus allowing the film to behave more like a single body fluid volume. For low viscosity, the droplets break up into much smaller sub-droplets which generally have low inertia. Motion of discrete particles is opposed by aerodynamic forces from adjacent particles. The loss in kinetic energy will depend on the surface tension, viscosity of the particle providing the opposing force as well as the angle of collision. As the surface tension is low the viscosity will be the dominant contributor to the opposition of droplet motion. For this reason, increasing the viscosity generally means the mass of oil escaping the crevice volume is reduced, as the viscous retention forces resisting particle motion increase.
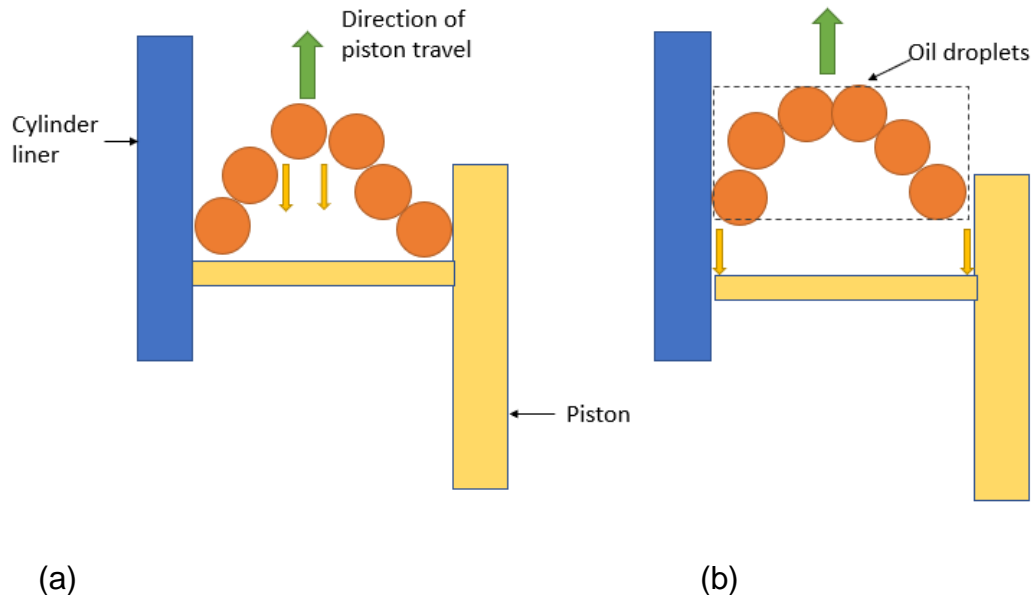
Figure 22– Simple illustration showing the weakest shear force being within the fluid film for low viscosity oils and at the fluid-wall interface for high viscosity oils (a) Low/mid viscosity film behaviour (b) Very high viscosity film behaviour

It is evident from the results that there is a change in inertia-viscous regime between low-mid viscosity oils and high viscosity oils, as there is a point at which increased viscous forced no longer assist in retaining th oil in the crevice volume. Figure 22 describes the two scenarios. When the piston decelerates, the fluid will continue to travel at the higher velocity until acted on by a fluid shear force. This leads to an almost parabolic velocity profile across the crevice volume. The parabola will be biased towards the piston as the relative motion of the liner creates a Couette shear force that acts to decelerate the fluid. The droplet at the highest velocity will detach from the body of the fluid if the shear force between droplets (shown in yellow) is not able to decelerate the droplet to the wall velocity quickly enough. The higher the viscosity the greater the deceleration of droplets. The greater the deceleration the less droplets that are able to escape the crevice volume 20deg BTdc.

179

In the case of scenario (b) in Figure 22 the viscous force between droplets is very strong. When the piston slows down the shear force is transmitted between droplets but also between the droplet and surface interface. In this case the shear force is greater than the surface contact force, meaning the surface-fluid interface becomes the weakest link. Large boulders of fluid with high inertia, detach from the surface boundary.

To gain an appreciation of the extent to which the fluid parcels coalesce and shear into sub-parcels we can look at the average droplet size at each point of` the simulation. Figure 23 shows the change in mean droplet radius for each crank angle interval in the gas domain, during the compression stroke, again evaporation effects have been neglected at this stage. The reduction in droplet radius is due to surface stress and deformation of the droplet as well as break up due to turbulence. The droplets are quite large in this case as it is simulated using the thickest oil.
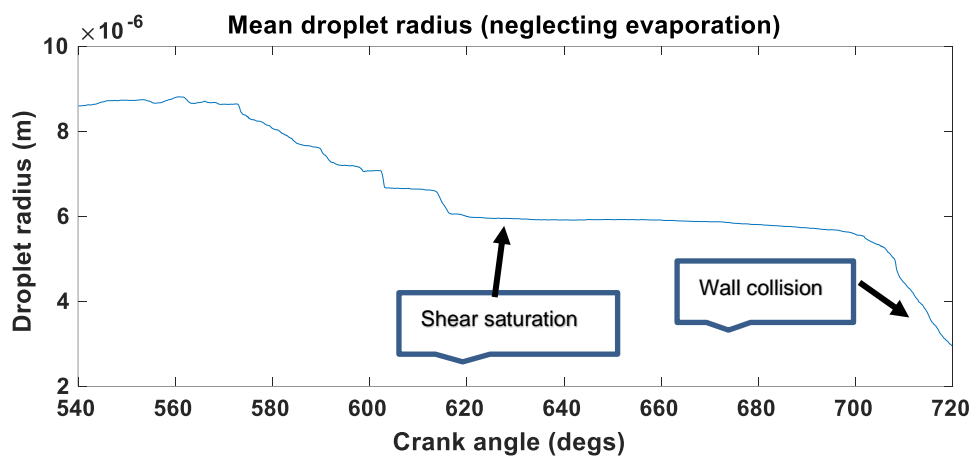
Figure 23 - Change in mean droplet radius in the gas domain for each crank angle during the compression stroke

Droplet breakup is minimal at the beginning of the compression stroke as the fluid volume in the crevice volume is low and velocity is still increasing in an approximately simple harmonic manner. As the volume inside the crevice volume increases the shear stress between the droplets increases due to the relative motion of the walls, this causes the droplets to break up, especially as

180

the piston velocity approaches its maximum speed. The high piston velocity also creates more turbulence, causing further break up of those droplets already in the gas domain. The piston then decelerates from mid-stroke and the droplet break up remains constant until 10deg bTDC when the droplets splash as they impinge on the head, and droplets are also deformed by the increased flow due to 'squish' flow created at high pressure (although the squish flow is minimal in this case as there is no bowl) [148].

It is also very interesting that 700deg CA is the timing normally used as a reference timing for LSPI [43], and according to Figure 23, it is about 700deg CA when the bulk of the oil is released from the crevice volume and eventually splashes onto boundary surfaces.

6.5. Oil Transport closure and summary

Droplet transport from the crevice volume was modelled for oils of varying viscosity using a 3D CFD model. The mass of oil that escapes from the crevice volume to the combustion chamber generally reduces with increasing viscosity, despite a thicker hydrodynamic film being predicted by the Reynolds solver. Most of the oil finds its way to the head or remains in the gaseous domain. The higher viscous forces counteract the inertia of the oil in the crevice volume and thus resisting escape. However, if the viscosity is increased significantly the inter-film shear force becomes much higher than the contact angle stress at the fluid-surface boundary, and the film behaves like a single body with high inertia, resulting in a large mass of oil escaping the crevice volume. Viscosity can impact the level of LSPI observed but most likely only during warm up (prior to opening of thermostat), as for most oils the viscometrical characteristics become very similar towards 100°C. This will be driven by the coolant temperature because the wall temperature will be governed by the water-jacket cooling. Moriyoshi [19] also reported an increase in LSPI events with a reduced coolant temperature. Because the results obtained are aligned with what is found in literature and also make

181

scientific sense, it is concluded a Lagrangian approach is an appropriate methodology for modelling oil droplet motion, and the effect of boundaries between discrete parcels is negligible when assuming a very low surface tension.

7. Thermodynamic behaviour of transported droplets

The impact of heat transfer and phase change of oil parcels was largely ignored in chapter 6. In this chapter the process will be developed to include thermodynamic aspects. The approach taken in this chapter develops a single particle model. A nominal Sauter mean droplets (representative of the entire population of droplets) will be used to complete this part of the investigation. The single particle approach has several benefits; run times are very short and serval iterations can be completed in a short space of time, there is no need to investigate several particles in stochastic phases and positions as would be required in a 3D CFD model just a single particle and for sensitivity studies, the boundary conditions and assumptions about the droplet can be closely controlled. Unlike a 3D CFD analysis where the particle can have different properties depending on its history and the particle boundary conditions will vary spatially. Because boundary conditions for a single particle model will be extracted from a validated combustion model it is a credible approach. Although the thermal and pressure boundary conditions will be average values for the cylinder mixture at that point of time, the unsteady change in conditions as a result of piston motion (which is provided by the combustion model) will be far greater than special variation within the combustion volume.

7.1. Aims of Oil droplet thermodynamic simulation

The aim of this study is to firstly understand at which point an oil droplet suspended in the combustion gas will vapourise during the compression stroke. This is key as a liquid droplet will need to vaporise and diffuse into air to eventually ignite. The study will then proceed to investigate the factors that determine whether or not a droplet will ignite, hopefully providing closure on why lubricant hydrocarbon ignition is observed in an RCM and not in actual engines. A cursory though will also be given to the impact of hydrocarbon chain length (within range found for engine lubricants).

The first part of this chapter will focus on developing a heat transfer model for the single particle approach, and the latter part will investigate evaporation. As

evaporation is a behaviour that will occur once the particle has exceeded its saturation temperature, it is important a robust heat transfer model is developed to predict the unsteady temperature distribution across the particle.

The heat transfer model will be developed to predict evaporation of the droplet for each time step of the compression stroke, using a combination of Clausius-Clapeyron and Frossling model.

Finally, a constant volume CFD simulation of an oil droplet inside gas conditions representative of those during an LSPI event will be carried out.

7.2. Single particle heat transfer model

This chapter addresses stage IV referred to in Figure 6. It is important to predict the temperature of the droplet at different points through its cross section accurately for each time-step of the engine cycle, as this will impact reaction rates, diffusion rates and fluid properties. For this reason, an unsteady heat transfer formulation and associated code was developed. Initially, a conceptual model will be described using fundamental heat transfer theory.
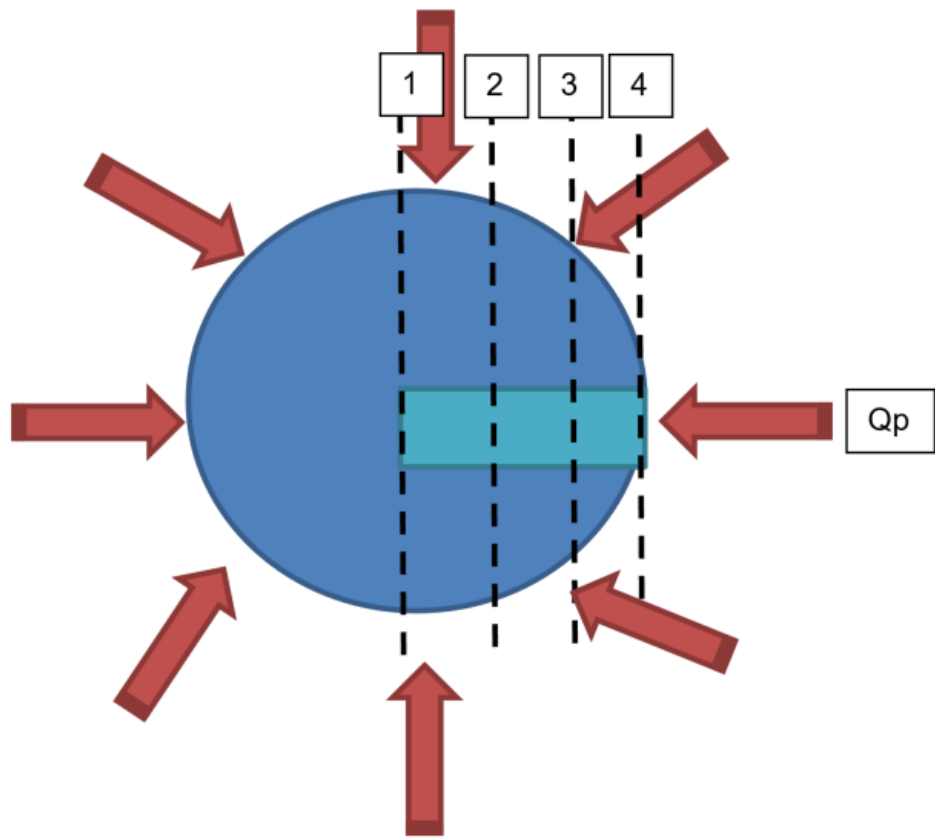
Figure 24 - A schematic showing the radial nodes for each cross-sectional plane of the droplet used in the unsteady heat transfer calculation. Convective heat is transferred (Qp) all over the particle (red arrows). The four calculation nodes are shown on a plane (light blue)

Figure 24 illustrates the problem being solved. Heat transfer will occur from the external gaseous environment to the outer surface of the particle. Heat will then conduct towards the centre of the particle. The rate of heat transfer will be determined by the varying temperature derivative along the radius of the particle. To monitor the spatial temperature distribution and allow for a finite difference approach, 4 radial nodes will be assumed for the particle. This number of nodes should be sufficient for such a small particle.

Using the classic Fourier derivation for unsteady heat transfer, we can initially formulate the standard equations for our four nodes.

185

$$Qp = htc\, A\, (T_{gas} - T_{4,p}) \qquad\qquad\qquad\text{[eqn 68]}$$

$$Qp = -K\, A\, \left(\frac{\partial T}{\partial x}\right)_4 \Delta t \qquad\qquad\qquad\text{[eqn 69]}$$

Equation 5.1.1 can be integrated and rearranged to give:

$$T_{4,p} = \frac{Qp}{K\, A\, \Delta t}\, (x/2) + T_{3,p} \qquad\qquad\qquad\text{[eqn 70]}$$

The constant terms can be grouped together for each nodal solution:

$$F_0 = 1/4 = \frac{k\, \Delta t}{\Delta x^2} \qquad\qquad\qquad\text{[eqn 71]}$$

F_0 can then be used as a coefficient for the calculation of each node as shown in eqn 72 – 74 (value of ¼).

The temperature at each node for each time-step can be calculated iteratively using the finite difference method:

$$T_{3,p+1} = \frac{1}{4}\left(T_{4,p} + T_{2,p} + 2T_{3,p}\right) \qquad\qquad\qquad\text{[eqn 72]}$$

$$T_{2,p+1} = \frac{1}{4}\left(T_{3,p} + T_{1,p} + 2T_{2,p}\right) \qquad\qquad\qquad\text{[eqn 73]}$$

$$T_{1,p+1} = \frac{1}{4}\left(T_{2,p} + T_{end,p} + 2T_{1,p}\right) \qquad\qquad\qquad\text{[eqn 74]}$$

$T_{end,p}$ = End temperature of previous time step

K = thermal diffusivity = thermal conductivity/(density * specific heat capacity)

A = surface area of droplet

htc = heat transfer coefficient

The system of equations above are solved using a finite difference method. Despite the simplicity of the methodology described above it is inappropriate in its classical form for a spherical body, as it assumes the droplet surface area is the equivalent of a flat surface and heat travels through a constant surface area and the cross section-volume ratio is linear.

Instead, we can use the approximate solution of a Fused-Quartz sphere. This is an acceptable approach as evaporation is not being explored at this atge and thermal expansion is negligible in the liquid phase, internal motion within the droplet is beyond the scope of this study.The temperature at a point at the centre of the sphere can be approximated using the formulation below at any time when immersed in a convective field [72].

$$\emptyset_{n,r=0}^{*} = \frac{T_{n,r=0} - T_\infty}{T_{n-1,r=0} - T_\infty}$$ [eqn 75]

$$= C_1 \exp(-\varphi_1^2 F_0)$$ [eqn 76]

$$F_0 = \frac{\propto t}{R^2}$$ [eqn 77]

187

$$B_i = \frac{hR}{k}$$ [eqn 78]

We can gain the values for φ_1 and C_1 using the linear approximations below:

$$\varphi_1 = 0.664\, B_i + 0.9068$$ [eqn 79]

$$C_1 = 0.244\, B_i + 1.0292$$ [eqn 80]

Where; n is the current time step, t is the absolute time, F_0 is the Fourier number, T is temperature, r is the radial distance of the point of interest, R is the radius of the sphere, B_i is the Bile number, h is the heat transfer coefficient, k is the thermal conductivity and T_∞ is the temperature of the convective environment.

For each time step the gaseous environment and heat transfer coefficient can be updated, $T_{n,r=0}$ can be made the subject of the equation and be calculated for each timestep.

We can now calculate the temperature for any time step, at any radial distance of the sphere, using the following subsequent formulation.

$$\emptyset^{*}_{n,r} = \frac{T_{n,r} - T_\infty}{T_{n-1,r} - T_\infty}$$ [eqn 81]

188

$$= \emptyset^*_{n,r=0} \frac{1}{\varphi_1 r^*} \sin(\varphi_1 r^*) \qquad\qquad \text{[eqn 82]}$$

$$r^* = \frac{r}{R} \qquad\qquad \text{[eqn 83]}$$

The temperature at several radial distances can now be calculated for each timestep.

Because the droplet is heated over its whole surface area and heat proceeds in the radial direction, there is nowhere for the heat to escape once reaching the centre of the droplet. Because of this, the droplet capacitates the heat until it reaches a thermal equilibrium with the surrounding gas, at which point there is no convective heat transfer. The simulation code works by dividing the droplet into four radial nodes. The htc, gas temperature, droplet surface area and temperature of the outer droplet node can be used to calculate the heat flux from the gaseous domain due to convection. The temperature of each node can be calculated using the scheme above. The end temperatures of the current time step will form the initial condition of the following time step. Evaporation will not be accounted for in this chapter but will be in the next, at this stage the temperature of the droplet will be allowed to exceed its boiling point for the given pressure and there will be no oil mass diffusion due to phase change.

Because it is anticipated inputs from the 3D CFD droplet model discussed in chapter 6.4.2 will be required for the evaporation model discussed later, for consistency the rescaled 1D predictive combustion model was used to provide heat transfer coefficient and gas temperature for each time step of the engine cycle. Again, the reader is reminded using a rescaled predictive model that originated as a validated engine model is completely acceptable as extrapolating from a known reference is its ultimate purpose. A similar approach was taken by Pandey et al [147] for a parametric study. Tempelhagen [151] also used the same model to assess the impact of using electric machines to modify the piston motion profile. Initially the model was

parameterised on a given piston profile, then used to simulate other profiles. A very good agreement between test and simulation was achieved.
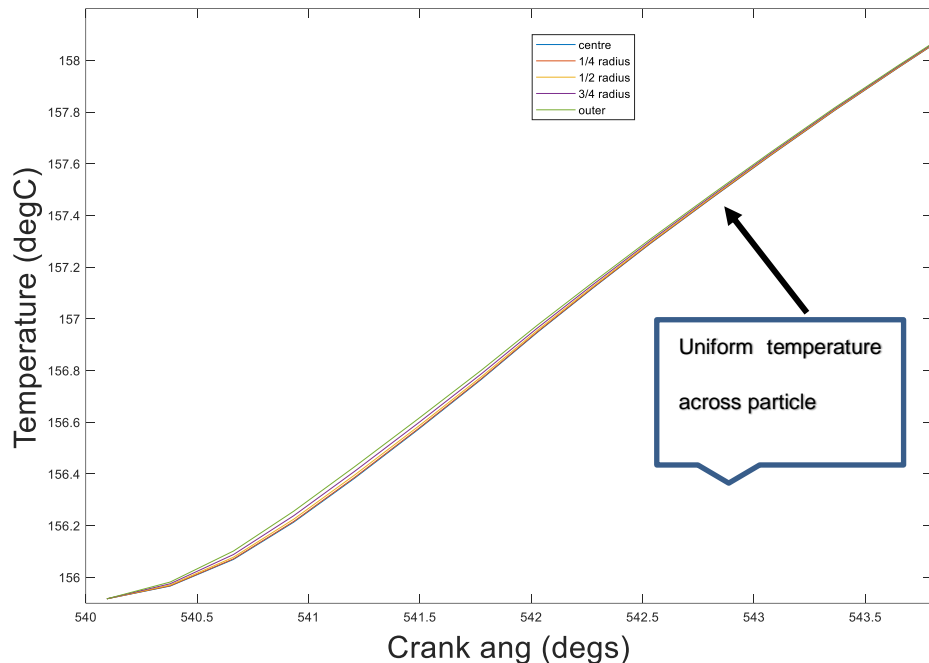
Figure 25 - unsteady radial temperature prediction of droplet during the beginning phase of the compression stroke

It can be seen from Figure 25, the sphere heats up very quickly as there is little difference in temperature between the nodes, and the nodal temperatures converge as the compression stroke progresses. A Fused Quartz sphere is one that neglects thermal expansion, this is acceptable as the change in diameter associated with expansion will be negligible in the liquid phase, in comparison with the dimensional change due to phase change.

7.3.   Single particle Evaporation model

 In this chapter the single particle heat transfer model discussed in the previous section will be progressed to account for evaporation and diffusion due to phase change. The process is complicated due to droplets splashing

190

onto various surfaces once they escape from the crevice volume close to TdC (>700degs CA in Figure 23).

The scheme must represent the reduction in diameter due to splashing, in addition to the reduction due to evaporation and diffusion, A reduction in radius due to stress is ignored for most of the stroke as the average radius does not change much. It can be seen from Figure 23, there is reduction in radius for the first 80degs of the compression stroke, but initial Clausius-Clapeyron calculations confirmed there is unlikely to be any evaporation occurring during this phase (the particle is not warm enough). Thus, it is acceptable to use the nominal SMD up to 700deg CA and not account for the impact of stress breakup, prior to this, because evaporation will not have played a role in the droplet size reduction prior to this point and so stress breakup was the only breakup mechanism. The ratio of droplet diameter change due to stress breakup between the current time step and previous time step will be calculated beyond 700deg CA. The ratio will be applied as a correction to the evaporated droplet size for each time step, only once the crank angle is greater than 700deg CA. The ratio due to stress break up, would most likely be different as the droplet size now includes evaporation, but the splashed droplet size is a stochastic phenomenon which will change from one engine design to another. So, the ratio correction allows for a consistent and fair way to account for splash break up within a single particle model.

The Frossling [4] evaporation model was used to simulate the rate of phase change diffusion from a Sauter mean diameter droplet that is representative of the total population of droplets in the gas domain at each time step.

The formulation used by Frossling to calculate change in droplet size on a convective environment can be found in chapter 4.3 but is also repeated below:

191

$$R = \frac{\rho_{air} D_{air}(\widetilde{T})}{2\rho_d\, r} \frac{Y_1^* - Y_1}{1 - Y_1^*}\, Sh_d \qquad\qquad \text{[eqn 84]}$$

$$Sh_d = \left(2 + 0.6 Re_d^{\frac{1}{2}} Sc_d^{\frac{1}{3}}\right) \frac{\ln(1 + B_d)}{B_d} \qquad\qquad \text{[eqn 85]}$$

$$Re_d = 2\rho\, \frac{|u + u' - v|\, r\,(\widetilde{T})}{\mu_{air}} \qquad\qquad \text{[eqn 86]}$$

$$Sc_d = \frac{\mu_{air}\,(\widetilde{T})}{\rho_{air} D_{air}(\widetilde{T})} \qquad\qquad \text{[eqn 87]}$$

$$B_d = \frac{Y_1^* - Y_1}{1 - Y_1^*} \qquad\qquad \text{[eqn 88]}$$

$$(\widetilde{T}) = \frac{T_{gas} - T_{drop}}{3} \qquad\qquad \text{[eqn 89]}$$

Where;

R = rate of change of droplet radius

$\rho_{air} D_{air}(\widetilde{T})$ = mass diffusivity of vapour in air

ρ = density of gas

r = initial droplet radius

u = local mean gas velocity

u' = turbulent gas velocity

v = droplet velocity

μ = viscosity

Y_1 = vapour fraction within droplet

Y_1^* = Vapour fraction at droplet surface

T = temperature

For each crank angle timestep the average droplet radius is extracted as well as the average droplet velocity vector and average turbulent gas velocity vector. The resultant relative velocity between droplet and gas can be calculated.

$$VR_{CA} = \sqrt{(\overline{ug}_{CA} - \overline{ud}_{CA})^2 + (\overline{vg}_{CA} - \overline{vd}_{CA})^2 + (\overline{wg}_{CA} - \overline{wd}_{CA})^2} \quad \text{[eqn 90]}$$

Where, VR_{CA} is the resultant relative velocity for a given crank angle time step.

Where; u v and w are the velocity components in directions x, y and z. The letter g indicates gas and d indicates droplet.

During the compression stroke the main droplet transport phase occurs when the piston approaches tdc, as the piston decelerates and eventually reverses in direction. The droplets transported will be those with sufficient kinetic energy from the crevice volume as well as those remaining on the piston and gas domain, from the previous exhaust and intake stokes. During the expansion and exhaust strokes the majority of the oil will have evaporated due to the elevated gas temperatures the droplet is exposed to during combustion and exhaust. So, what is observed as a droplet remnant of the previous cycle is more likely a particle from the oil.

Although, the droplets do not escape the crevice volume for the majority of the compression stroke they are constantly in a state of oscillation, as they gain kinetic energy and then it is consumed in overcoming resistance due to gas and viscous forces due to wall losses and adjacent droplets. For this reason it will be assumed the crevice volume droplets are constantly suspended. Hence, they are also hotter than those attached to the wall, as those on the
193

wall are cooled by the water-jacket. The droplets that will promote autoignition are ones that are in their liquid phase for the majority of the stroke and fully vapourise close to the spark ignition timing. This allows for concentration gradient to be formed between the liquid but evaporating droplet and the gaseous domain, within this gradient will be a thick stoichiometric layer to be maintained around the droplet, with a high rate of reaction which could lead to autoignition. The fact that the droplet is in its liquid phase allows for a high local concentration and thus a high energy intensity once it vapourises and auto-ignites close to the spark timing. Our assumption of the suspended droplets in the crevice volume is conservative as the significantly cooled droplets that enter the combustion chamber later in the stroke and at a lower initial temperature are potentially of greater concern.

We will only consider the droplets being scraped from the liner and collating in the crevice volume during the compression stroke. For most of the compression stroke the droplets of interest will remain within the crevice volume, they will circulate within the volume under shear and be heated when exposed to the gas domain at the top of the crevice volume.

Vapour pressure for the oil droplet can be calculated for varying temperature using the Clausius-Clapeyron equation. The vapour pressure for each time step will be used to calculate the Y* value used for the Frossling model (ratio between droplet vapour pressure and surrounding gas pressure). Whilst the Y* ratio is below 1 the droplet will be in a slow evaporation regime and fully vapourised when greater than 1. Droplet evaporation inside the cylinder will be simulated assuming the droplet is made up of $C_{20}H_{42}$, $C_{30}H_{62}$ (as most of the hydrocarbons present within a lubricant are C20-C30) and Hexadecane. All to be assessed individually. The droplet radius used for each time step will be the Sauter radius, as it accounts for the surface area-volume ratio that is representative of the total population of droplets. For unsteady heat transfer calculations, it is important to use a proportionate and representative surface

194

area to volume ratio. The surface area controls the area available for convective heat transfer, the volume will determine the thermal capacitance and resistance of the body, which in-turn determines the heat transfer rate and external temperature.

Sauter mean diameter (SMD):

$$SMD = \frac{\sum_{i=1}^{n} n_i d_i^3}{\sum_{i=1}^{n} n_i d_i^2}$$

[eqn 91]

$n = population\ number$

$d = diameter$

$$P_{vap} = P_{ref}\ e^{\left(\frac{-Hvap}{R}\left(\frac{1}{T_{vap}} - \frac{1}{T_{ref}}\right)\right)}$$

[eqn 92]

$$Y^* = P_{vap}/P_{cylinder}$$

[eqn 93]

Where P_{vap} is the calculated vapour pressure at temperature T_{vap}, Tref is the boiling temperature at pressure P_{ref}, H_{vap} is the enthalpy of vapourisation and R is the universal gas constant, $P_{cylinder}$ is the cylinder pressure.

Single particle evaporation model Results and discussion
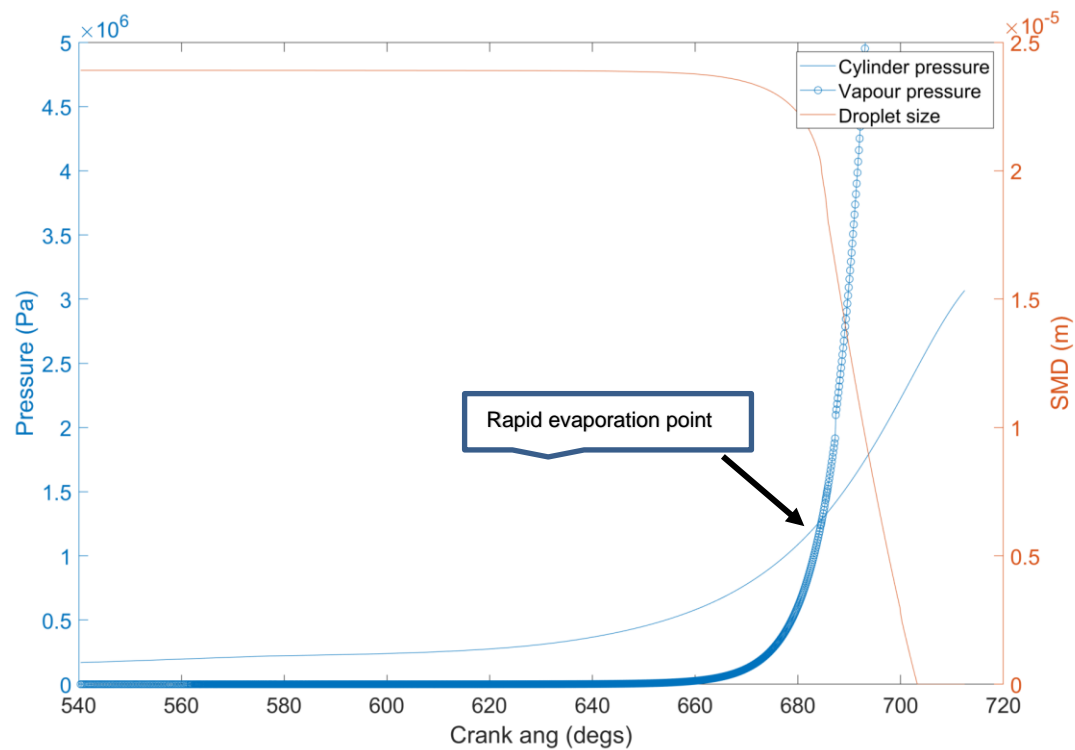
Figure 26 - Conventional Frossling evaporation model results for C20H42 for a simulated engine cycle (a) SMD over engine cycle (b) pressure over engine cycle
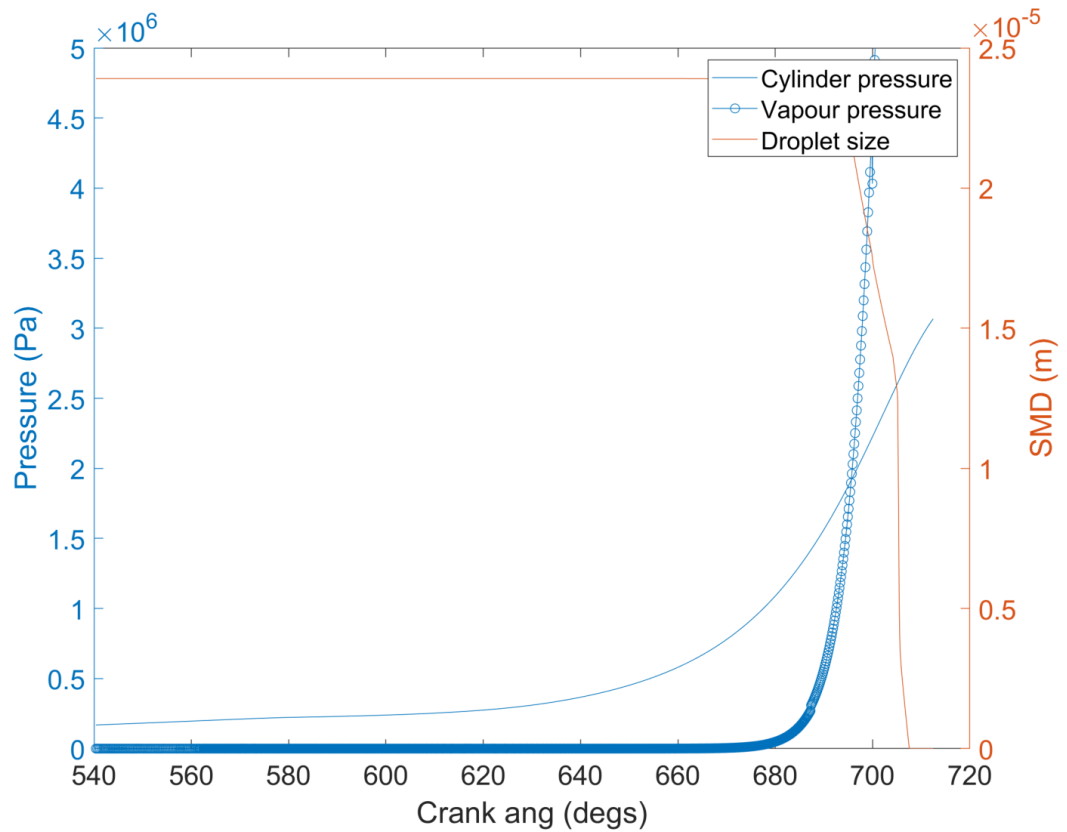
Figure 27– Conventional Frossling evaporation model results for C30H62 for a simulated engine cycle (a) SMD over engine cycle (b) pressure over engine cycle
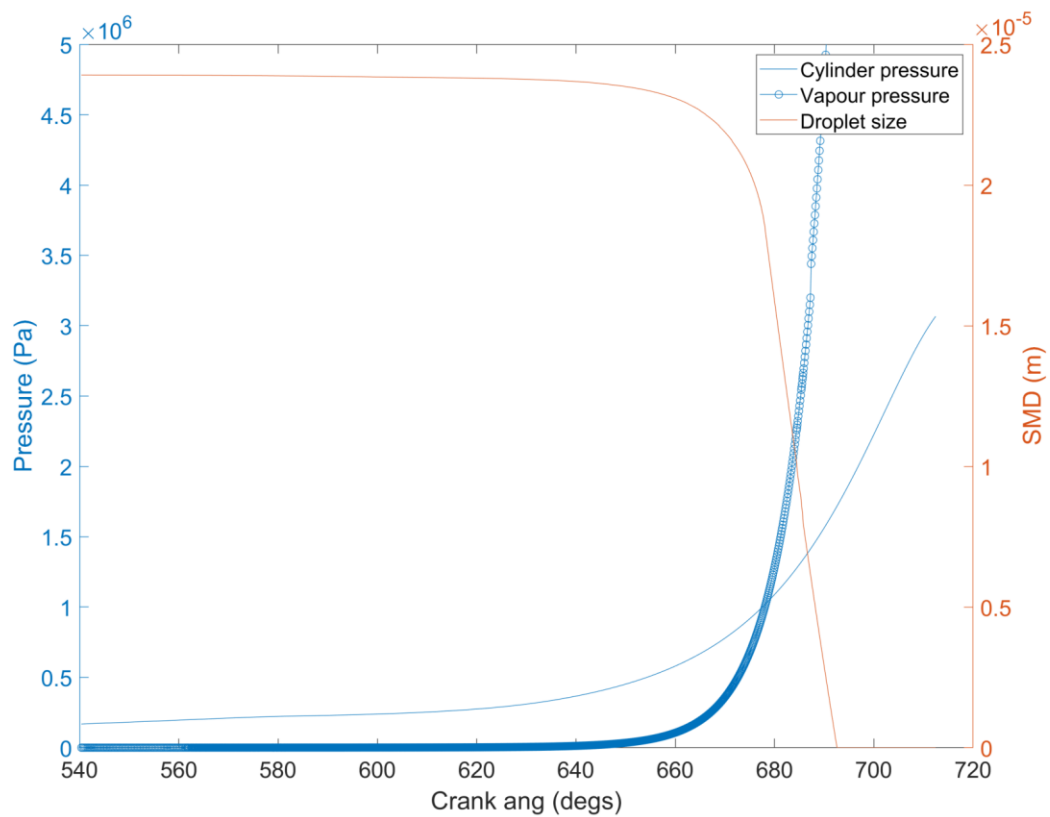
Figure 28– Conventional Frossling evaporation model results for Hexadecane for a simulated engine cycle (a) SMD over engine cycle (b) pressure over engine cycle
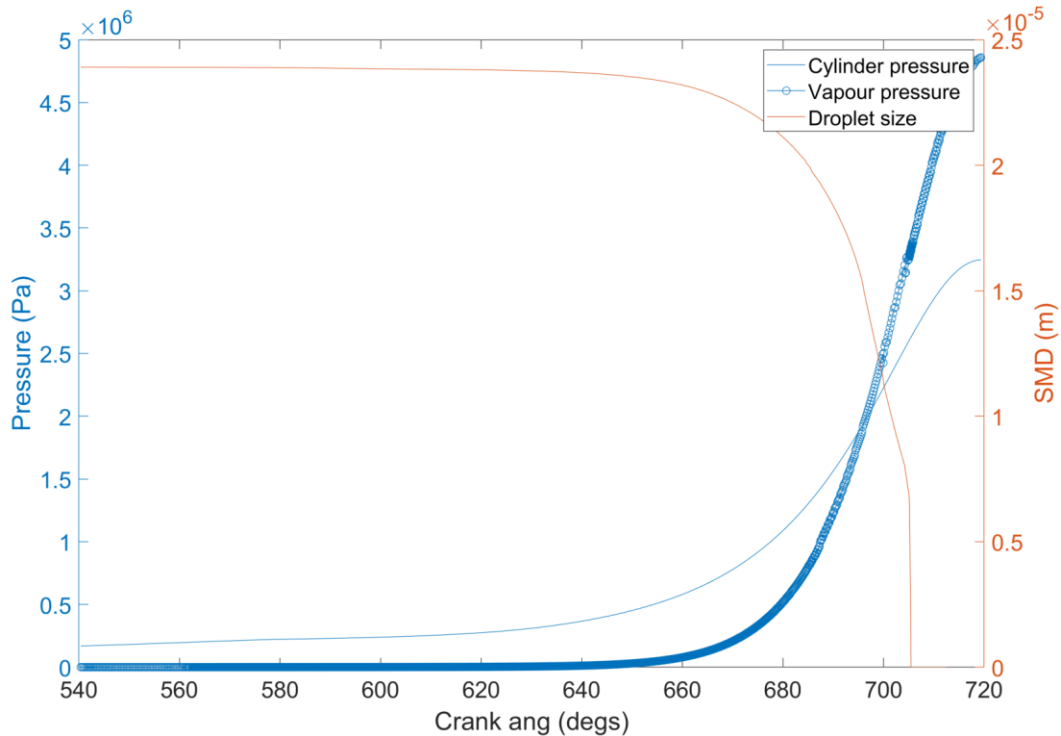
Figure 29 - Conventional Frossling model results for Hexadecane, using 'wet bulb' boundary condition at the surface interface of the droplet

The original Frossling model maintains the same initial radius for a whole engine timestep. The initial radius for the next engine timestep is then reset to the final calculated radius of the timestep before.

Figure 26 shows the results from the Frossling evaporation model for $C_{20}H_{42}$. No evaporation or very slow evaporation is observed from most of the compression stroke, and there is a dramatic reduction in the SMD at around 680deg CA when rapid evaporation takes place. Figure 26(b) demonstrated the point at which the $C_{20}H_{42}$ vapour pressure exceeds the environmental gas pressure, is also when a rapid reduction in droplet diameter is observed. The part of the codes that reduces the droplet diameter due to splashing beyond 700deg CA hardly plays any role, as the droplet has already experienced rapid evaporation before that point.

199

The Frossling calculation was repeated assuming the droplet is made up of C30H62 (heat of vapourisation, standard boiling temperature, thermal conductivity and specific heat capacity changed accordingly).

As can be seen from Figure 27, C30H62 is fully vapourised later in the compression stroke (by 8CAD), suggesting longer chain hydrocarbons are more likely to cause LSPI as the phase change occurs closer to the spark ignition timing, assuming the aforementioned oil ignition hypothesis.

Because in a later part of the study the autoignition propensity of an oil droplet as Hexadecane will be assessed, the Frossling model was repeated for Hexadecane (Figure 28).

There is currently no maximum distillation mass for each temperature (only the available mass of the relevant fraction evaporating at that temperature will diffuse at which point diffusion will seize), as initially we only single hydrocarbon component fluids will be assessed.

The evaporation modelling methodology adopted above assumes the vapourised fluid is transported by the turbulent cylinder charge gas and thus the oil vapour spends little time at the droplet surface interface. For this reason, boundary conditions for evaporation at the droplet boundary were that of the in cylinder gas state. However, it is possible that the speed of vapour advection by cylinder gas is slower than the rate of diffusion due to phase change. This means the boundary condition at the droplet surface needs to be that of an oil vapour state. When the liquid oil evaporates it will initially be at a temperature and enthalpy equal to that required for vapourisation. Once it has diffused to the periphery of the droplet volume there will be a temperature and phase gradient across the vapour zone thickness. When fluid parcels evaporate from the surface of the droplet, the vapour will initially be at a

200

temperature lower than the gas, meaning it will cool the gas in the vicinity of the droplet surface. Because of latent heat transfer during phase change the fluid parcels will initially maintain a constant temperature. The 'wet bulb' is the lowest temperature the air will reach during adiabatic evaporation (without adding or taking away heat via other means from the vapour-gas mixture)[149]. As the vapor continues to diffuse into the gas phase it will become more and more superheated until it eventually is of a temperature equal to the gas phase, obviously the amount of cooling the vapour offers will also reduce at it increases in temperature.

The wet bulb temperature can be found by using the Clausius-Clapeyron equation:

$$Ceq = \frac{P_0}{R\,T_{wd}}\,e^{\left(\frac{-Hvap}{R}\left(\frac{1}{T_{wb}} - \frac{1}{T_0}\right)\right)}$$

[eqn 94]

Where $Ceq(= P_{vap}/R\,T)$, is the vapour concentration in equilibrium, P_0 is the vapour pressure at temperature T_0 and T_{wd} is the wet bulb temperature.

The Clausius-Clapeyron equation will need to be coupled with an energy equation for an extensive fluid dynamics solution. The heat transferred from the cylinder gas to the wet bulb volume by conduction should be equal to the energy consumed in latent phase change.

$$Hvap\,D\,\frac{C_{eq}}{L_{st}} - k\,\frac{T_{cyl} - T_{wb}}{L_{st}} = 0$$

[eqn 95]

201

T_{cyl} is the cylinder gas temperature, T_{wb} is the wet bulb temperature, L_{st} is the stagnation length (term cancels out), k is the gas-vapour thermal conductivity and D is the diffusion coefficient of the droplet volume into the gas.

A simplified version of the Chapman-Enskog equation [10] can be used to estimate the diffusion coefficient.

$$D_{ij} = \frac{0.00186\,T^{\frac{3}{2}}}{P\,\sigma_{ij}^2 \Omega}\left[\frac{1}{M_i} + \frac{1}{M_j}\right]^{\frac{1}{2}}$$ [eqn 96]

Where σ_{ij} is average collision diameter of the two species, p is pressure, T is temperature, Ω is the molecular characteristic coefficient (generally equal to 1), M_i and M_j are the molecular masses of the two species Oil and gas composition in this case).

Because the T_{wb} term appears as an exponent and first order denominator in the Clausius-Clapeyron equation, the solution will need to be established iteratively. A mathematical scheme was set up to solve the system of equations for Twb until the energy equation equalled zero. The Frossling model results for Hexadecane can be found in Figure 29.

The fully vapourised point is retarded to later in the stroke then the earlier model, because the liquid vapour interface is cooler, the phase and the concentration gradient is also smaller due to the presence of oil vapour at the boundary. The inclusion of wet bulb temperature makes the prospect of oil droplet hydrocarbon causing LSPI a lot more plausible as much of the oil droplet is still in its liquid phase close to TdC, allowing for a high intensity heat release in the event of autoignition. For most of the compression stroke the only form of evaporation present is slow evaporation, which is a stochastic

202

phenomenon of a certain number of molecules at a sufficient energy level to escape the surface of the droplet, this is captured by the Frossling model.

The fully vapourised point although retarded is still significantly earlier than the main spark event, meaning it is possibly too early for the ignition to be relevant to LSPI. The vapourisation must occur very quickly and late, followed by a fast reaction that occurs before the fluid diffuses across the volume significantly (in turn reducing local concentration), to assure significant energy intensity to cause autoignition. The difference between the wet bulb solution and that of cylinder gas at the droplet boundary, suggests the evaporation of the droplet will be impacted by the level of turbulent kinetic energy in the cylinder as the rate of convective transport of the vapour will determine if you have a wet bulb boundary condition or in cylinder gas. This is particularly applicable to LSPI as it occurs at low engine speeds when the charge turbulence is low. The rate of reaction will generally be highest towards tdc due to temperature and higher gas density resulting from the reduced volume. The scenario above is exploring a droplet that is present in the chamber and completely exposed to the in-cylinder gas from the beginning of the compression stroke, as explained earlier much of the oil from the crevice volume is transported into the gas phase very close to tdc and these droplets will be cooled by the crevice walls. This means that it is entirely possible many droplets will be retained in the crevice volume for much of the compression stroke, and maintained at a temperature that assures liquid phase, and the droplet may only escape from the crevice volume very close to TDC, as the piston decelerates significantly. Such a scenario will substantially retard the fully vapourisation point such that it is closer to the spark timing, this is also in agreement with the oil film transport CFD modelling in section 6.4, the images show oil being released late in the compression stroke.

7.4. Heat release and reaction kinetics of lubricant Hydrocarbons

With the lubricant oil being an amalgamation of predominantly Hydrocarbons of various lengths and forms, it is an obvious starting point for assessing ignition sources, especially as the combustion characteristics of common hydrocarbons are so well established. Although distillation data can provide us with the relative population of Hydrocarbons with regards to number of Carbon atoms in the chain, it is difficult to deduce their isomeric structure or any additional functional groups.

As an initial step the characteristics of such long chain hydrocarbons will conducted assuming they are all alkanes, as alkanes are representative of the nature of hydrocarbons present within engine oils [150].

The distillation curve shown in Figure 30 suggests most of the hydrocarbons are between C21 and C32 for a typical lubricant. Thus, these are the chain lengths that will be analysed for combustion.
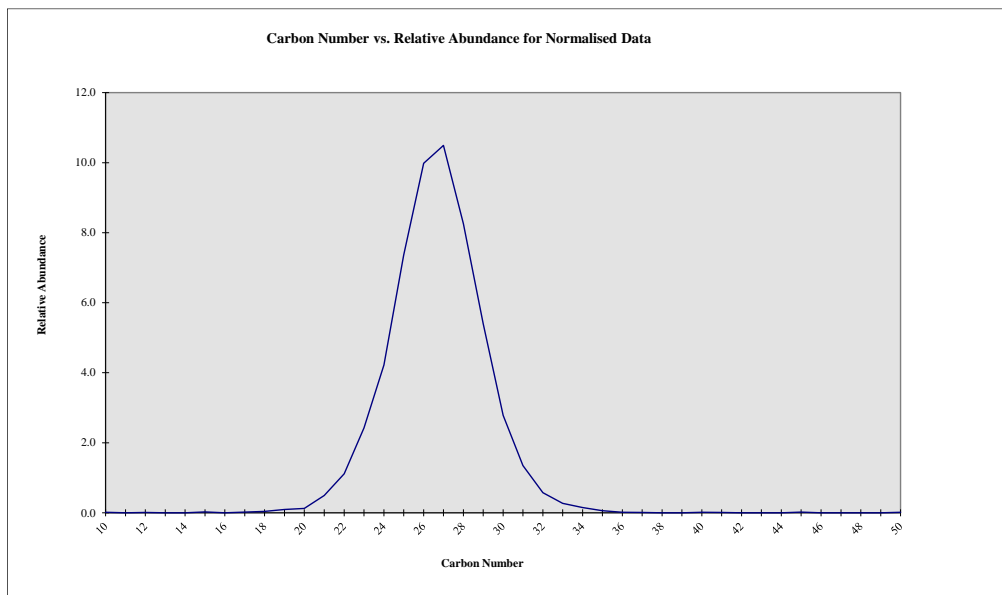
Figure 30 - Distillation curve for base oil, showing Carbon chain length and relative abundance

7.4.1. Investigating the impact of chain length on Combustion

Assuming ideal and complete combustion i.e. with CO2 and H2O as products, the activation energy of reaction and the corresponding increase in temperature required will be calculated for each alkane length. The reaction can be defined by the following equation:

$$C_nH_{2n+2} + AO_2 => BCO_2 + EH_2O \qquad \text{[eqn 97]}$$

$$B = n$$

$$E = n+1$$

$$A = (2B+E)/2 = (2n+n+1)/2 = (3n+1)/2 \qquad \text{[eqn 98]}$$

Basevich [4] et al suggests the following compact equation for the approximation of activation energy associated with oxidation reactions of 'n' length hydrocarbons.

$$Ei(n) = Ei(n = 3) - 0.25[\Delta Hi(n) - \Delta Hi(n = 3)] \qquad \text{[eqn 99]}$$

for exothermic reactions,

$$Ei(n) = Ei(n = 3) + 0.75[\Delta Hi(n) - \Delta Hi(n = 3)]$$

for endothermic reactions,

Where $E_{i(n)}$ is the activation energy of an alkane of length n, and $\Delta Hi(n)$ is the enthalpy change of reaction.

These equations are derived from the following, well established phenomenology.

205

$Ei = 11.5 - 0.25\Delta Hi$ *for exothermic reactions*   [eqn 100]

and

$Ei = 11.5 + 0.75\Delta Hi$ *for endothermic reactions*   [eqn 101]

The enthalpy of formation for each one of the alkanes were taken from Abu-Awwad [5]. These were calculated using a DFT (density functional theory) program, and then validated against experimental data. Enthalpy of reaction can be calculated by subtracting the total enthalpy of formation of the reactants from the products.

Table 7 below shows the number of moles of reactants and products for each alkane and the standard enthalpy of formation of each alkane, assuming ideal combustion described in eqn 97.

	Hf(HC)	Hf(HC)	Moles of O2	Moles of CO2	Moles of H2O
	Kcal/mol	kJ/mol	moles	moles	moles
C21H44	-113.98	-476.892	32	21	22
C22H46	-118.92	-497.561	33.5	22	23
C23H48	-123.86	-518.23	35	23	24
C24H50	-128.79	-538.857	36.5	24	25
C25H52	-133.73	-559.526	38	25	26
C26H54	-138.67	-580.195	39.5	26	27
C27H56	-143.6	-600.822	41	27	28
C28H58	-148.54	-621.491	42.5	28	29
C29H60	-153.48	-642.16	44	29	30
C30H62	-158.41	-662.787	45.5	30	31
C31H64	-163.35	-683.456	47	31	32
C32H66	-168.29	-704.125	48.5	32	33

Table 7 - Showing the enthalpy of formation of the alkanes investigated and the number of moles for each product and reactant

Although the fundamental combustion reaction shown above is simplistic and does not account for the numerous intermediate reactions or the rate of reaction, we can assume the empirical activation energy calculated assuming the reaction enthalpy change for the universal reaction is an approximate integral of the intermediate activation energies. This assumption is solely to allow us to understand how the energy invested in activation compares to the energy gained from the enthalpy change of reaction, for each chain length, the reaction rate constant and enthalpy of reaction will be calculated.

The effect of temperature on reaction rate coefficient is corrected using the Arrhenius function:

$$K = A \, e^{\frac{-Ea}{RT}}$$ [eqn 102]

Where; k is the reaction rate coefficient, A is the pre-exponential factor, Ea is the activation energy, T is the temperature and k is the universal gas constant.

The pre-exponential factor can be estimated by the empirical equation suggested by Abu -Awwad et al [5]:

$$A_{in} = A_{in3} * e^{\left(\frac{(\Delta Sin - \Delta Si3)}{R\,T}\right)}$$ [eqn 103]

Where; A_{in} is the pre-exponential factor of an alkane of n chain length, A_{in3} is the pre-exponential factor of propane, Δsin is the change in entropy of the reaction for an alkane of length n and Δsin is the change in entropy of the reaction with propane. However, it is felt this empirical approach is not comprehensive enough to provide meaningful absolute results for the rate of reaction of hydrocarbons but is useful for a directional understanding of the impact of chain length. A more extensive methodology will be employed later in the study.

	Total Hf (O2)	Total Hf (CO2)	Total Hf (H2O (g))	Total Hf (HC)	reac H	Ea	Molar mass (HC)
	kJ	kJ	kJ	kJ	kJ	(kJ/mol)	kg/mol
C21H44	0	-8263.71	-4131.16	-12394.9	-11918	2990.994	0.296
C22H46	0	-8657.22	-4318.94	-12976.2	-12478.6	3131.15	0.31
C23H48	0	-9050.73	-4506.72	-13557.5	-13039.2	3271.305	0.324
C24H50	0	-9444.24	-4694.5	-14138.7	-13599.9	3411.471	0.338
C25H52	0	-9837.75	-4882.28	-14720	-14160.5	3551.626	0.352
C26H54	0	-10231.3	-5070.06	-15301.3	-14721.1	3691.781	0.366
C27H56	0	-10624.8	-5257.84	-15882.6	-15281.8	3831.947	0.38
C28H58	0	-11018.3	-5445.62	-16463.9	-15842.4	3972.102	0.394
C29H60	0	-11411.8	-5633.4	-17045.2	-16403	4112.257	0.408
C30H72	0	-11805.3	-5821.18	-17626.5	-16963.7	4252.423	0.422
C31H64	0	-12198.8	-6008.96	-18207.8	-17524.3	4392.578	0.436
C32H66	0	-12592.3	-6196.74	-18789.1	-18084.9	4532.734	0.45

Table 8 - Showing the calculated total enthalpy of formation of the products, the estimated activation energy and molar mass

Table 8 shows the total enthalpy of formation for all the moles of products and reactants, for the generic combustion equation of each alkane. Once the enthalpy of reaction is calculated, eqn 100 can be used to calculate the activation energy associated with the reaction.

The problem with using an all-encompassing Arrhenius function is that it only accounts for enthalpy change assuming CO2 and H2O are the only combustion products, it also neglects the intermediate steps described in section 2.7. The propagation and Degenerative chain branching phases play a dominant role in combustion rate. Also, this method would provide a trend of the ignition delay increasing with carbon chain length, this is the opposite trend to what was reported by Hellier et al [144]. Hellier et al tested fuels of varying straight chain moiety length on a compression ignition engine and recorded the ignition delay. The ignition delay reduces exponentially with increasing chain length, the difference in ignition delay due to an increase in carbon length is only approximately 1CAD between a carbon length of 16 and 20. Beyond a carbon length of 20 the ignition seems to be trending towards an asymptote.

Based on this small difference in ignition timing and the very small difference full evaporation timing between Hexadecane and C20-C30 alkanes, it is reasonable to assume Hexadecane to be the hydrocarbon that represents the lubricant.

7.4.2. **CFD modelling of droplet reaction in control volume**

For an oil droplet to offer energy of sufficient intensity to propagate into a mega knock event it will need to be predominantly in its liquid state with a cloud of vapour at its surface boundary (the vapour will ignite first). The higher density would mean the energy created from the reaction following latent heat transfer will initially diffuse to a relative low mass of gas adjacent to the reaction zone, resulting in high gas temperatures. If the reaction rate is much slower than mass diffusion of the oil vapour, due to a more dispersed oil volume, even if the reaction was to occur it is unlikely to propagate as the lower energy intensity is diffusing into a larger gas medium resulting in lower temperatures. In addition, it is important the droplet is in its liquid state close to the ignition timing, as an overlap is required between the two propagating fronts to induce mega knock.

As mentioned earlier, it is important to remember the mass and state of enthalpy of droplets inside cylinder are stochastic and thus it is possible a droplet could be attached to a wall within the crevice volume, maintaining a temperature close to the water jacket temperature and be released into the combustion zone as the piston decelerates towards tdc. A similar observation was made by Ohtmo et al [16], where it was found most of the hydrocarbon autoignition occurs close to the exit of the crevice volume. For our assessment we will assume the oil hydrocarbon is n-Hexadecane. As discussed in the previous section, Hexadecane provides a good representation of lubricant hydrocarbons, both in terms of phase change and reactions. Hexadecane is prone to autoignition and is used as a benchmark to

210

measure the 'cetane' number of a fuel. Some thermodynamic quantities under standard conditions can be found below.

Hcomb (n-Hexadecane) = 2557.15kcal/mol   (Heat of combustion)

Taa (Hexadecane) = 205degC   (Autoignition temperature)

Tboil = 281C (@ 1atm)

There are two possibilities with regards to reaction mechanism; the ignition could take place before full evaporation takes place (with the thin cloud of vapour present during slow evaporation) or due to the reduced likelihood of collision with oxygen of the lower concentration of vapour around the droplet, ignition may take place instantaneously upon complete phase change. Another possibility is mechanism that is a combination of the two; a micro autoignition take place in the stoichiometric cloud of vapour and air causing a fast reaction at the droplet surface, and the resulting heat propagates into the liquid phase resulting in rapid evaporation followed by combustion. This conjecture will be scrutinised later in the study.

Figure 29 shows the droplet evaporation calculation for Hexadecane, this helps establish the rate of evaporation during the compression stroke. As this is most likely a diffusion limited combustion process, the rate of phase change will give us a good indication of the rate of reaction. We can now run a CFD constant volume simulation whilst specifying the appropriate boundary conditions, in a micro pilot fuel-air mixture to gain insight into the likelihood of autoignition.

The droplet size simulations for Hexadecane during the compression stroke can be seen in Figure 29. It can be observed that the fully vapourised point is a little later in the stoke than the C20 and C30 alkanes simulated earlier.

211

Although this provides a relative assessment, it is important to remember we are now looking at the case when a droplet remains in the much cooler crevice volume wall until close to tdc, this means the fast evaporation could take place much closer to the spark ignition event.

The droplets that exist inside the crevice volume are generally only introduced into the combustion volume very close to tdc because of the high upstream pressure resisting them, and because the droplet is most likely to precede the piston as the piston decelerates. The droplet enters the combustion chamber at a temperature slightly higher than the water jacket temperature and in its liquid phase.

For this reason, it was deemed appropriate to analyse the behaviour of droplets introduced late in the compression stroke by using the 'bomb simulation' as this will allow us to control charge gas pressure, temperature, turbulence and gas composition as well as droplet composition, evaporation characteristics, droplet size and velocity. Whereas, the phase change, droplet breakup and reaction rate during an engine cycle will be the result of an unsteady accumulation of transient boundary conditions, making it difficult to establish the most dominant factors.

The droplet was assumed to be made up of Hexadecane for the bomb simulation, and the following reactions were included in the mechanism file for the Sage chemical kinetic solver. A reduced reaction pathway suggested by Shuojin, Ren et al [11] was used and all associated coefficients were taken from Chang et al [12] (reaction mechanism file provided by Convergent Science). Hexadecane was chosen because it is the longest chain hydrocarbon for which an established reaction mechanism is available, and a lubricant comprises mainly of long chain hydrocarbons. Also, from the previous chapter it has been established that the difference in behaviour in terms of point of through evaporation and ignition delay between Hexadecane

212

and C20-C30 alkane is very small. It is a very large reaction mechanism comprising of several subsequent reactions after the free radical phase. For a cursory understanding the early reactions associated with Hexadecane are shown in table 9. The initial decomposition reactions and corresponding Arrhenius reaction parameters can be seen in table 9. The mechanism proceeds to include other small chain, radical branching and termination reactions A temperature exponent term has been added to the Arrhenius equation (eqn 102). Moriyoshi et al [43] also conducted a similar static volume simulation.

	A	B	Ea
	cm^3/(mol s)		cal/mol
c16h34+o2<=>c16h33+ho2	4.20E+13	0	27800
rev	6.00E+12	0	0
c16h34+oh<=>c16h33+h2o	2.00E+08	1.85	58.5
rev	2.46E+09	1.95	21910
c16h34+h=>c16h33+h2	1.00E+08	2	2500
c16h33+o2<=>c16h33oo	3.00E+12	0	0
rev	2.51E+13	0	27400
c16h33oo<=>c16h32ooh	1.51E+11	0	19000
rev	1.00E+11	0	11000
c16h32ooh+o2<=>ooc16h32ooh	5.56E+10	0	0
rev	2.51E+13	0	27400
ooc16h32ooh<=>c16ket+oh	8.91E+10	0	17000
c16ket=>ch2o+3c2h4+c5h11co+oh+c3h6	1.20E+16	0	43000
c16h33+o2=c16h32+ho2	3.16E+11	0	6000
rev	3.16E+11	0	19500
c16h32+o2=>2c3h6+3c2h4+c2h5+ch2o+hco	3.16E+13	0	10000
c16h33=>2c3h6+c2h5+4c2h4	7.00E+12	0	28810

Table 9 - Reactions and associated Arrhenius values for Hexadecane

It was decided to track the production of C16H32 as its formation takes place during the early free radical formation process (can be seen as a reaction close to the bottom in Table 9), which is the rate determining step, and initial testing suggested it was present for much of the reaction process until the

rapid heat release at the end (metastable species). Charge gas was a mixture of N2 and O2 of atmospheric composition.

Once again, the base size of the mesh was optimised to find the largest size that will not compromise the results. Comparison was based on local concentration and TKE.

7.4.2.1.   Droplet ignition control volume Results, Validation and discussion
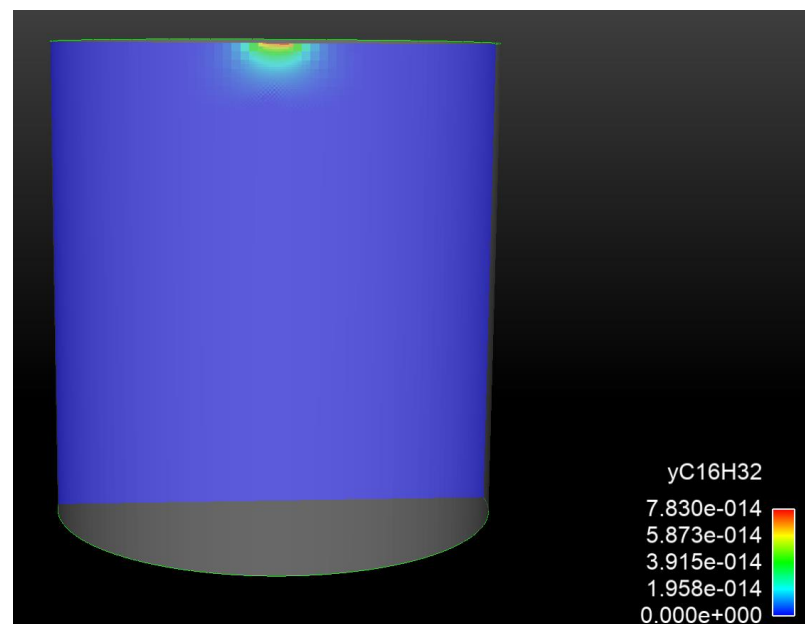
Figure 31– Case 1, initial travel of Hexadecane droplet upon entering O2-N2 mixture, showing cell mass fraction of C16H32
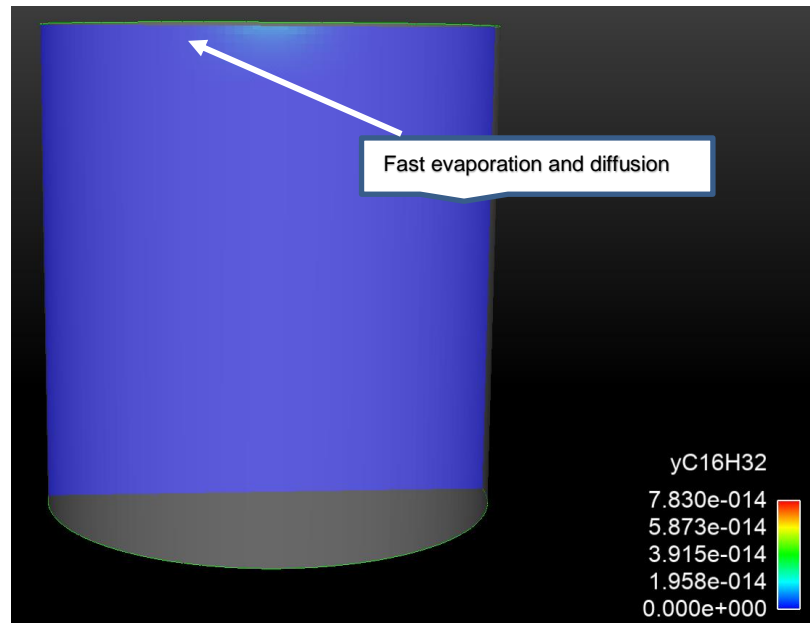
Figure 32 – Case 1, Showing cell mass fraction of C16H32 5e-03s after entering mixture

In the first instance we will analyse a droplet that is representative of a parcel being introduced into the combustion chamber from the crevice volume around 20 deg BtdC. The instantaneous pressure and temperature boundary conditions can be taken from the GT combustion model. A small droplet size of 1e-06m was assumed as it is likely a smaller droplet will change phase, diffuse and react faster, providing a high local heat release. Pressure of the N2 + O2 charge gas was 25 bar and temperature to 700K, composition was that of ambient air, and the initial TKE of the gas was set to $45m^2s^2$ a typical level or turbulence for an engine at the given engine cycle stage [135].

Figures 31 and 32 show the small droplet representative to that present in an engine, heat up and vaporise almost instantaneously upon entering the chamber gas because of the lower gas pressure allowing for a lower boiling point, and lower droplet thermal capacitance. Owing to the much lower gas pressure and the turbulent environment, the vapour is able to diffuse through the vessel volume very quickly. The local concentration is very low because the initial mass is small and diffusion rate through gaseous medium is very

high. The colour contour has been rescaled in Figure 33 from a typical scale (that will be used for subsequent cases) to show the extent of oil vapour diffusion 1e-02s after droplet entering the vessel. Although this equates to several crank angles, the species diffuse across the volume so that they are more visible for demonstration purposes. It can also be seen there are pockets of poor mixing which lead to no/partial reactions, due to the slightly lower turbulence and lower mass of available oil vapour. Because C16H32 is observed upon entry, it suggests the early initiation reactions take place very quickly, but the oil has diffused across the volume very quickly prior to the highly exothermic reactions occurring.
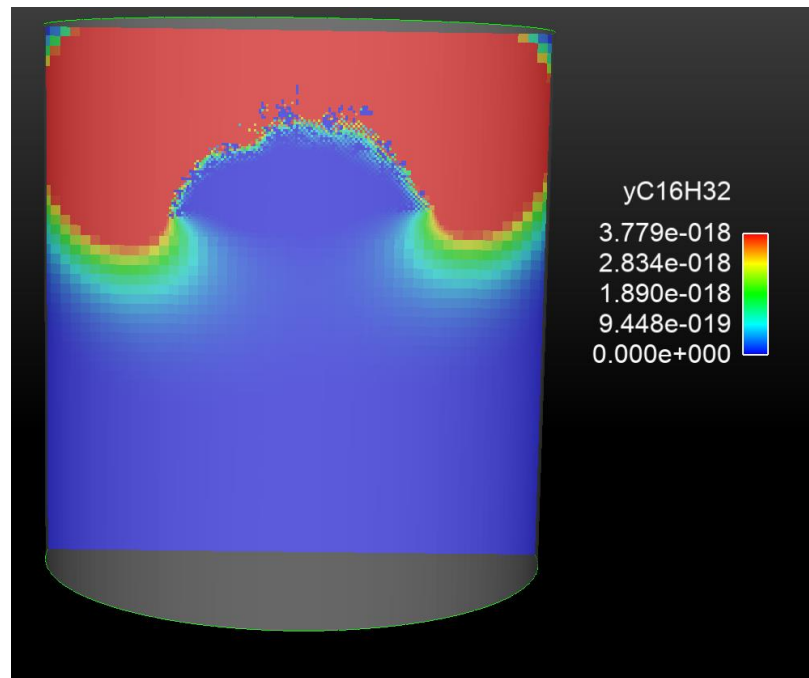
Figure 33 – Case 1, a rescaled contour plot of C16H32 cell mass fraction showing the extent of vapour diffusion 1e-02 s after the droplet entering the vessel(NOTE: change in colour contour scale)
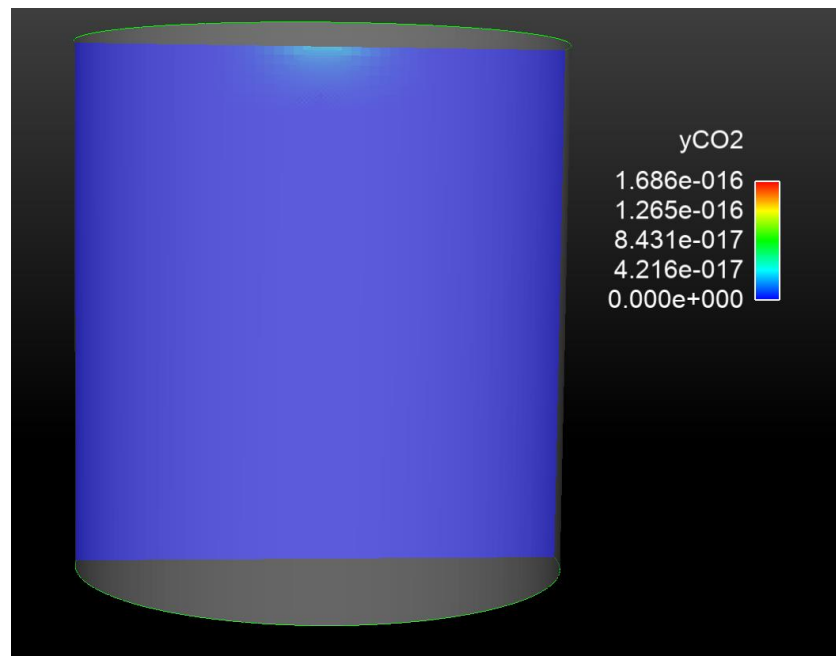
Figure 34 – Case 1, Showing cell mass fraction of CO2 1e-02s after entering mixture
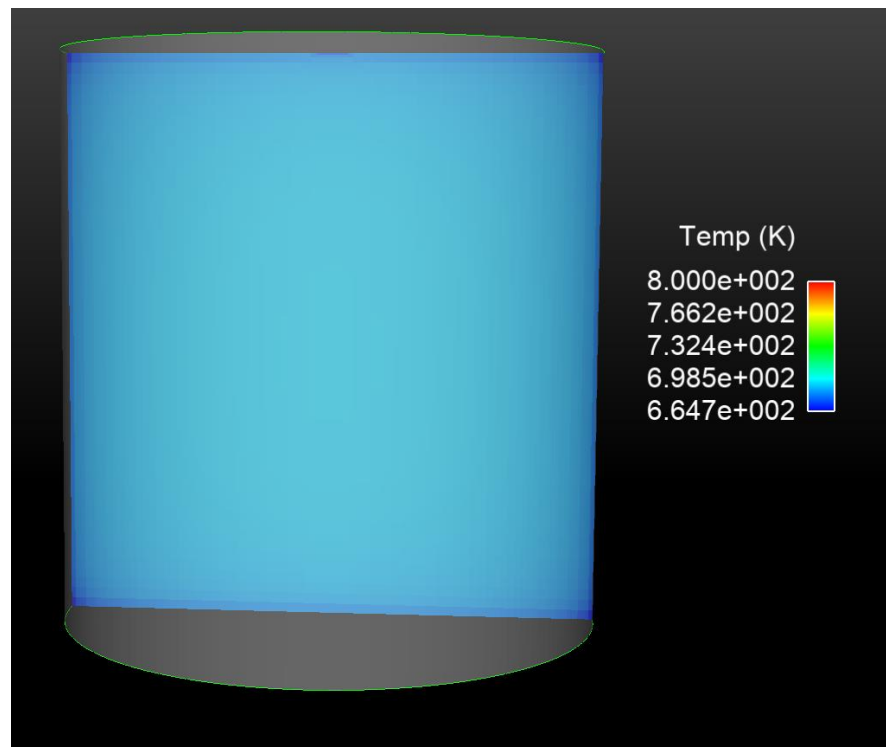
Figure 35 – Case 1, showing cell temperature
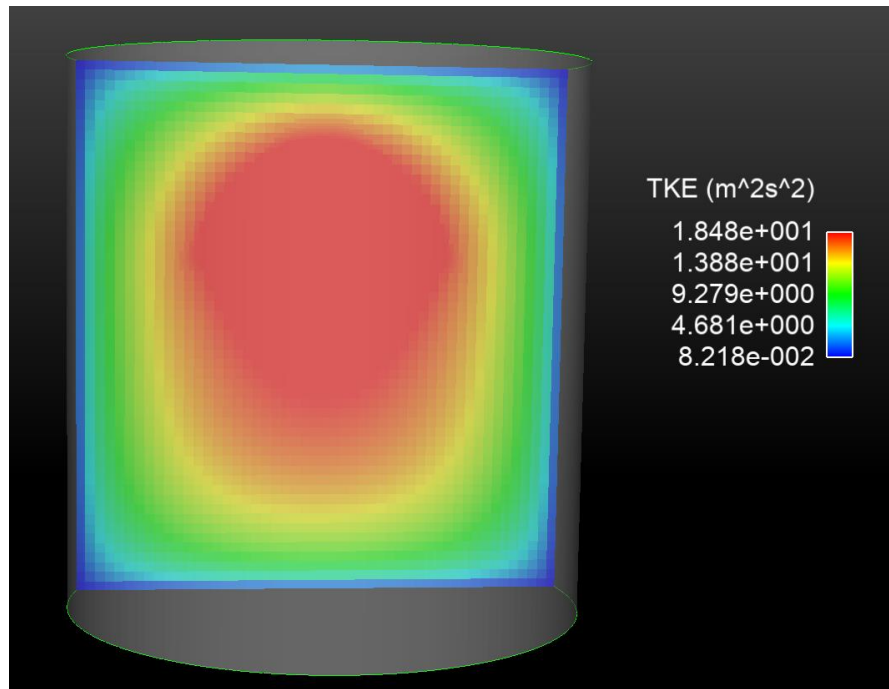
Figure 36 – Case 1, showing cell TKE

Figures 34 and 35 show the rate of reaction is very slow as the CO_2 concentration is negligible, and the gas temperature is undisturbed. This is because the droplet is small and thus it heats up and vapourises quickly (also requires a lower vapour pressure because of the low gas pressure). The slow evaporation period is non-existent at this condition, the diffusion rate is substantially faster than the rate of reaction because of the lower gas pressure, the low total mass of the droplet also results in low concentration and the relatively low gas temperature will contribute to reducing the rate of reaction.

Because the diffusion is so fast, the droplet is small and thus the concentration drops very quickly, so does the rate of reaction, and thus the low increase in temperature due to reaction. Local thermal diffusivity will be high in the highly convective environment; the volume occupied by the small mass of oil is large, meaning the small amount of energy released from a local reaction zone will be spread over a relatively large interfacial area of gas in

the local non-reactive zone (in addition to that gas consumed by the reactions).

The cyclone shape of the reaction zone shown in Figure 33 is very interesting. It appears the rate of reaction is faster towards the outside of the vessel than the centre. This is because the turbulence originates in the middle and forms a cyclone about the centre (as shown in the TKE plot in Figure 36). The centrifugal acceleration forces the denser oil vapour towards the outside of the vessel, increasing the concentration in that region.

Based on the learning from the previous case, it is important to slow down the rate of diffusion to maintain a high local concentration. From an academic point of view, the simulation investigated if an ignition would take place in the end gas if a lubricant droplet did manage to remain in its liquid state after ignition. The gas representing the end gas zone will not contain fuel to assure the ignition due to the lubricant is more apparent and not merged with ignition of the fuel-air mixture. Pressure was held at 70bar, temperature was 850K, the droplet size is 1mm in diameter (high thermal capacitance required to assure the droplet survives post spark ignition) and the turbulence (initial TKE) is high. The learning from such an extreme case will also help in understanding why droplet ignition takes place in RCM cases because of the much larger droplet, be it to a much lesser extent. It was presumed; the high pressure will result in slow evaporation of the droplet, and slow diffusion as there will be a larger force opposing the kinetic energy of the oil vapour. The slow diffusion after full evaporation of the droplet will mean a higher concentration at the original position of the droplet, the high level of turbulence will encourage improved local mixing, the larger volume droplet will have a higher reaction rate and the higher temperature will also increase the rate of reaction. The initial temperature of the droplet as it enters the chamber is 62degC.
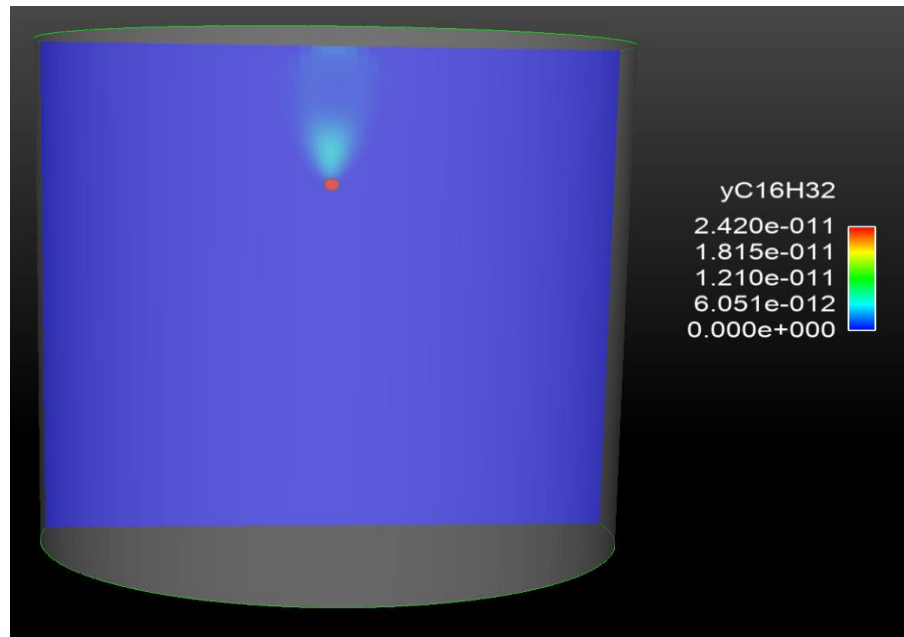
Figure 37– Case 2, initial travel of Hexadecane droplet travelling through O2-N2 mixture, showing cell mass fraction of C16H32
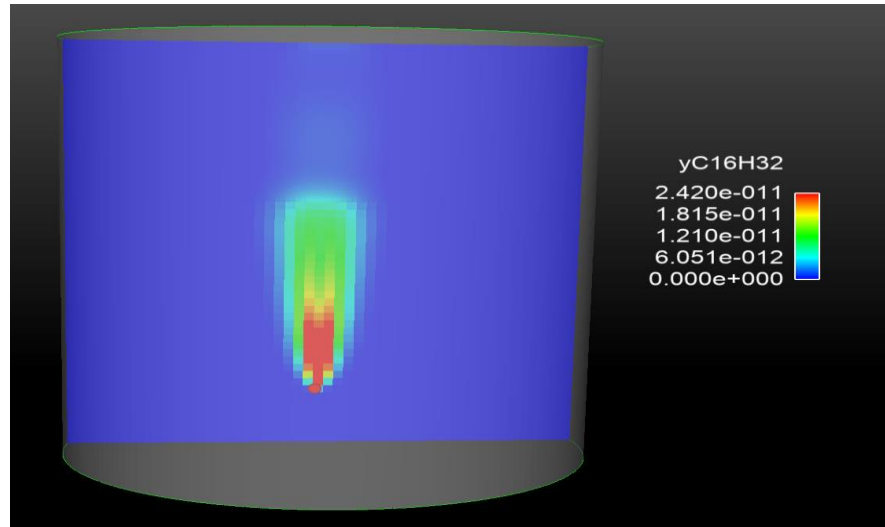
Figure 38– Case 2, Travel of Hexadecane droplet travelling through O2-N2 mixture as it approaches the bottom of the vessel, showing cell mass fraction of C16H32, 0.015s

In can be seen in Figure 37-38, the rate of evaporation of the droplet increases as it pursues its travel and heat is transferred from the surrounding gas. However, the local vapour concentration is still very low as the droplet is large and thus has a high thermal capacitance resulting in slow

221

heating/evaporation. Whilst the droplet is travelling it will also have a low residence time in each location again resulting in a small local concentration. During its travel, the droplet is also becoming deformed due to viscous stresses exerted by the turbulent gas.
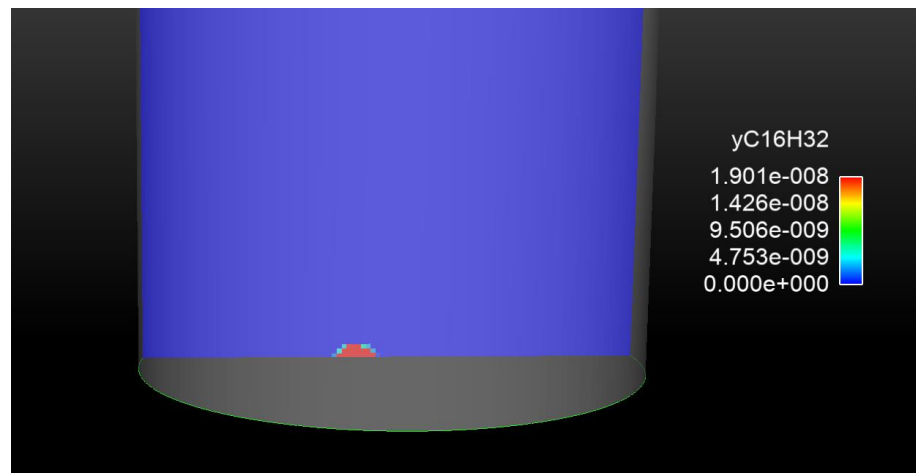
Figure 39 – Case 2, Travel of Hexadecane droplet travelling through O2-N2 mixture as it sits at the bottom of the vessel, showing cell mass fraction of C16H32 (NOTE: change in colour contour scale) , 0.05s
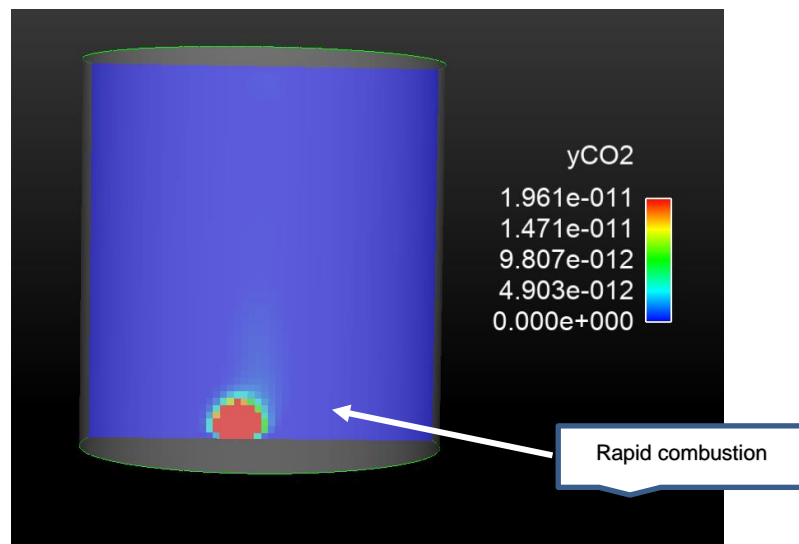
Figure 40 – Case 2, Travel of Hexadecane droplet travelling through O2-N2 mixture as it sits at the bottom of the vessel, showing cell mass fraction of CO2, 0.07s
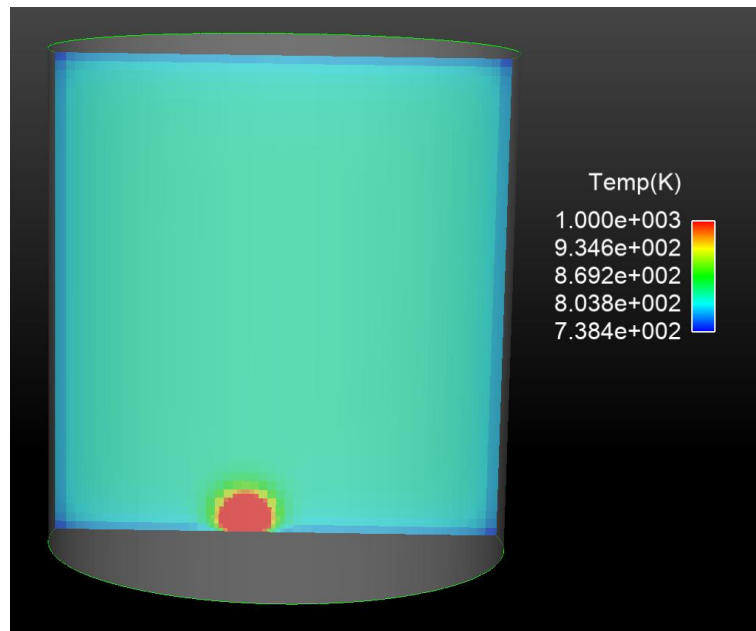
Figure 41 – Case 2, Travel of Hexadecane droplet travelling through O2-N2 mixture as it sits at the bottom of the vessel, showing cell temperature, 0,07s

Once the droplet reaches the bottom of the vessel, the static droplet takes a long time to heat up due to its higher thermal capacitance and lower resultant htc (low velocity relative to gas), thus spending more time in the slow evaporation regime. The droplet will have a concentration gradient from its surface to a distance within the gaseous domain that comprises of only ambient gas for that moment in time. Within the gradient will exist a stoichiometric layer with the highest rate of reaction and thus highest propensity to autoignition, this can be observed in Figures 39-41. The slow evaporation allows for more time for mixing and a high concentration gradient for a prolonged period, thus a larger stoichiometric zone is present.

The droplet is static so will be releasing vapour into the same volume in space, the gaseous diffusion from the droplet vapour cloud to the surrounding gas will be slower than the rate of evaporation (high gas pressure) resulting in

223

high concentration at the droplet boundary, this layer will be well mixed due to the high level of local turbulent kinetic energy, again increasing the rate of reaction. The heat transferred from the reaction in the stoichiometric layer and the rest of the vapour cloud helps vapourise the liquid droplet and increase its subsequent rate of reaction. The relatively high concentration of CO_2 shown in Figure 40 and the high temperature from autoignition in Figure 41 show that mixing occurs very quickly following total vapourisation of the droplet, as the high-pressure gas in the chamber is able to penetrate the oil vapour volume rapidly. The highest energy intensity being at the droplet origin suggests the rate of reaction is substantially faster than the rate of vapour diffusion for these boundary conditions as a high enough concentration was maintained at the origin with sufficient mixing for a high heat release; it is evident the liquid phase vapourises, mixes and reacts faster than it can be transported within the vessel.

There are various findings that lend hydrocarbon ignition in an RCM scenario and not in an engine. Firstly, the micro pilot injection introduced in an RCM are relatively large. Packets of fluid released in an engine are much smaller. Secondly, it was observed that most of the reactions for Hexadecane are too slow to be influential for the time window allowed in an engine cycle, for the boundary conditions observed in a SI engine. However, an RCM will hold the piston at the maximum position for a prolonged period.

In order to validate this bomb simulation approach, it was decided 2 points of test data from Ohtomo et al [16] rapid compression machine data will be simulated. The bomb simulation will assume the boundary conditions when the plunger is at its maximum position. Obviously, the pressure and temperature increase in a RCM is progressive, but the plunger velocity is very high. The relatively large ignition delay from the point the plunger reaches its maximum position suggests the rate of any reactions and phase change taking place are negligible during the gas compression velocity required to achieve the desired pressure and temperature. The simulated conditions will be 1.9MPa and 530degC. In the thesis the droplets are suspended using a

tungsten wire if there was a risk of them reaching a wall or injected sufficiently slow enough. To emulate the same scenario, the droplets were injected with a very low velocity, with the hope that ignition will take place before the droplet reaches the bottom wall of the volume. Figure 42 and 43 show ignition taking place well before the droplet reaching the cylinder wall for both cases. Table 10 shows the comparison between tested and simulated ignition delay for both validation cases. Ignition delay is defined as the time between the plunger reaching its maximum position and an ignition taking place, as this is the point when a steady temperature and pressure is maintained. It can be seen very good agreement was achieved between simulation and test results.
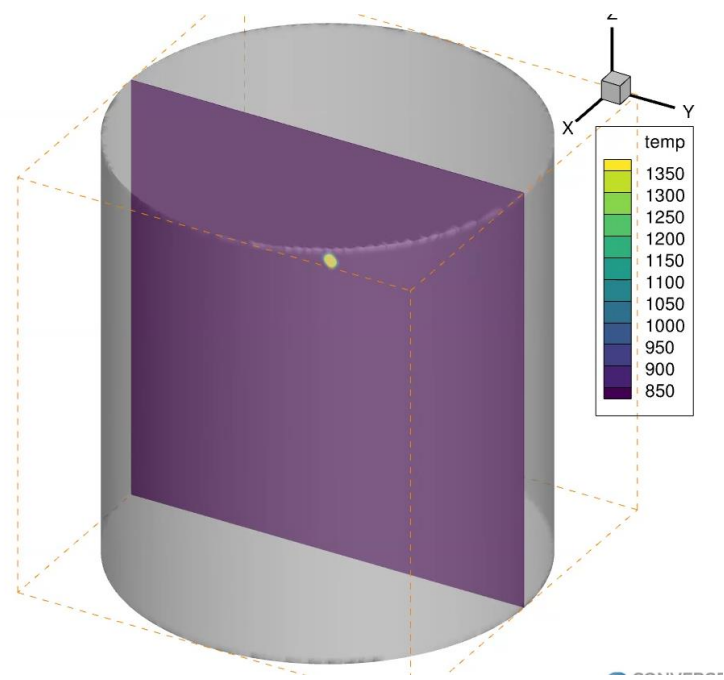
Figure 42 – Validation case 1, Ignition of a 200e-03 mm droplet in an O2-N2 gas mixture
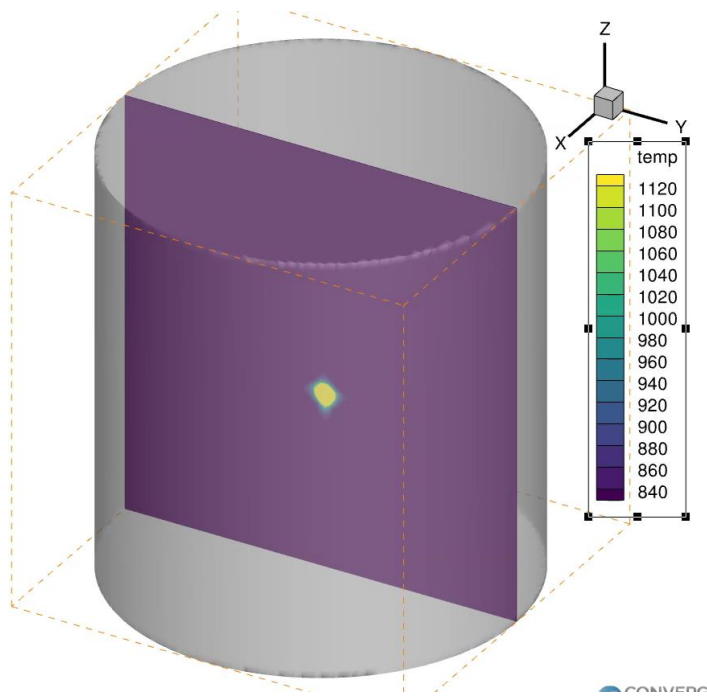
Figure 43 – Validation case 1, Ignition of a 430e-03 mm droplet in an O2-N2 gas mixture

Droplet size, m	Pluger Tdc time, s	Ignition time, s	RCM Ignition delay, s	Simulated ignition delay, s
2.00E-04	4.00E-02	8.50E-02	4.50E-02	4.50E-02
4.00E-04	4.00E-02	2.35E-01	1.95E-01	1.85E-01

Table 10 - Comparison of ignition delay measured on RCM against that from bomb simulation

7.5. Closure & Summary - Droplet transport, Hydrocarbon evaporation and Hydrocarbon reactions

Multi-node heat transfer model was developed for the single particle heat transfer. The multiple nodes add little value, as the particle has very low thermal capacitance and resistance, meaning the temperature gradient between the nodes is small. A lump mass thermal model could provide similar value. The heat transfer model was coupled with a Clausius Clapeyron evaporation model. The evaporated mean particle size was calculated using the Frossling model. It was found the full evaporation point became more retarded with longer alkane chain length. The full evaporation point was also very close to a typical LSPI timing. The timing could be even more retarded and thus closer to the spark timing as the model assumes the droplet is always exposed to gas phase, whereas in an engine the oil could reside on the cool crevice volume for much of the compression stroke. It is important to complete the Clausius Clapeyron equation by calculating the wet bulb temperature as it will also retard the ignition timing to some extent.

The reaction of hydrocarbons in the lubricant was investigated in two stages; an initial exercise that estimates the rate of reaction and change in enthalpy for appropriate alkanes using empirical equations, and a more detailed 3D CFD reactor simulation. The empirical exercise confirmed that it will be the shortest chain alkanes that will have the highest rates of reaction and highest rate of heat release. Although this approach is not suitable for exact predictions it is very useful for quickly understanding relative trends. The 3D CFD reactor simulation of a lubricant droplet confirmed the amount of heat release from hydrocarbon reactions is heavily dependent upon the size of the droplet. When a large droplet is introduced, the higher thermal capacitance and thus slower phase change results in a concentration gradient between the liquid and gas phases. Within the gradient is a thick stoichiometric layer with a high rate of reaction, a high local heat release ensues. When a small droplet is introduced, it rapidly evaporates and diffuses across the mixture, the rate of diffusion is faster than the rate of reaction, the local concentration is low resulting in a very slow rate of reaction. This explains why ignition due to

227

lubricant hydrocarbons is observed on an RCM but not on engines, because the pilot injection in an RCM is normally a relatively large droplet and suspended it on a tungsten wire if it impinges on a wall, the velocity of the particle is also slower making it less susceptible to break up, whereas an engine shears and releases very small parcels of fluid into the combustion zone at high velocity causing further beak up as a result of drag and wall impingement.

7.5.1. Hydrocarbon ignition modelling process validation summary

Once again, LSPI is a stochastic phenomenon, very unrepeatable and variable in frequency. Validation in absolute terms is a fallacious concept for this problem. Nevertheless, every effort has been made to validate sub-models where possible, in certain cases the formulation used is implicitly validated as the parameters have been derived from test data. Where, direct validation is not possible, the findings are compared with experimentation from literature to assure the two are directionally aligned. A summary of the validation relating to LSPI due to hydrocarbon ignition is provided below:

• Initial 1D predictive combustion model was validated to test data

• The Reynolds solver used to predict the film thickness between ring and liner was applied to a 2D ball on disc scenario, very good agreement was achieved between the film thickness measured on the EHD rig and simulation.

• Predicted film thickness were also compared with similar predictions to assure values and profiles were plausible

• The evaporation model used boundary conditions from a validated 1D engine model. The Clausius-Clapeyron approach is an established method of predicting vapour pressure, both the heat of vapourisation and standard boiling temperature are obtained from testing. This approach is implicitly validated.

• The boundary conditions for the oil transport CFD models were obtained from a rescaled 1D engine model. To support the validity of the

228

rescaled combustion model, literature was referenced, where researchers had made modifications to a validated model and achieved good agreement between test and simulation. The film thickness the simulation is initialized with is also obtained from a validated approach.

•   The mass of oil transported was compared to experimental oil consumption results from literature to assure they were plausible.

•   The trend of oil viscosity against mass of oil transported was directionally aligned with what is found in literature

•   The boundary conditions for the engine related bomb simulation were taken from a validated 1D engine model. A reference was also made to a paper where a researcher had taken a similar approach.

•   The bomb simulation approach was used to simulate the maximum compression conditions for two points from RCM testing in literature. The case was also using a micro-pilot injection of Hexadecane. A very good agreement was achieved between simulation and test.

8.   Influence of MgCO3 and CaCO3 Detergents on Pre-ignition

This chapter presents an investigation into the likelihood of a detergent particle present in the engine oil causing a pre-ignition event, considering both Mg based and Ca based detergents. This chapter therefore addresses stage VII of the ignition process hypothesised in Figure 6.

From the literature survey it was found Ca based detergents (present in the engine oil) dramatically increased the number of LSPI events, whereas the presence of a Mg based detergent has no impact on LSPI. Moriyoshi et al [43] suggests this is because the $CaCO_3$ thermally degrades to CaO, the Cao subsequently reacts with CO_2 during the compression stroke, this reaction is exothermic and therefore acts as a source of ignition.

8.1.   Aims of Detergent ignition simulation

The following research questions will be addressed in this chapter:

- Why does Ca cause ignition and not Mg
- The plausibility of thermal degradation of $CaCO_3$ causing ignition
- Impact of particle size and CO_2 concentration
- Why an increase in burned gas residuals increases LSPI
- What causes the LSPI event to occur so close to the spark event
- Is heat release the only ignition source or can it also be caused by a hot particle.

Obviously, the in-cylinder pressure and thus gas concentration will gradually increase as the piston proceeds towards TdC, but the first part of the chapter analyses the 1D combustion model outputs to establish if there are any sudden changes in boundary conditions close to the spark ignition point. A steady state Gibbs reactor simulation will be carried out for a preliminary comparison of the carbonaceous reaction of Mg and Ca detergents. Finally, a transient, single particle reaction model for a detergent

will be developed using instantaneous boundary conditions of the intake and compression strokes. This model will be used to predict particle temperature, reaction timing and the sensitivity to boundary conditions that impact both detergents. As explained in chapter 7, a single particle approach is credible on the basis that the average temporal boundary conditions predicted by the combustion model provide a much greater change for each time step than the special variation.

8.2.   Thermal considerations from 1D model prediction

In this chapter the heat transfer related boundary conditions predicted by the 1D combustion model will be analysed. It is important to understand this because the thermal predictions will be used as boundary conditions for models later in this chapter, but also because it will provide an early-stage insight as to whether any abrupt changes take place close to the ignition angle that allows the pre-ignition to take place at the observed timing. Obviously, pressure and thus gas concentration will increase as the piston proceeds through the compression stroke, as the mixture volume reduces. Figures 44-45 obtained from the validated 1D predictive combustion mode discussed in chapter 5, show there are no sudden change in mean HTC or gas temperature close to spark ignition (spark timing is 3.5deg ATdc), and therefore the initiation of LSPI at the observed timing (20 deg BTdc) cannot be caused by an abrupt change in boundary conditions.
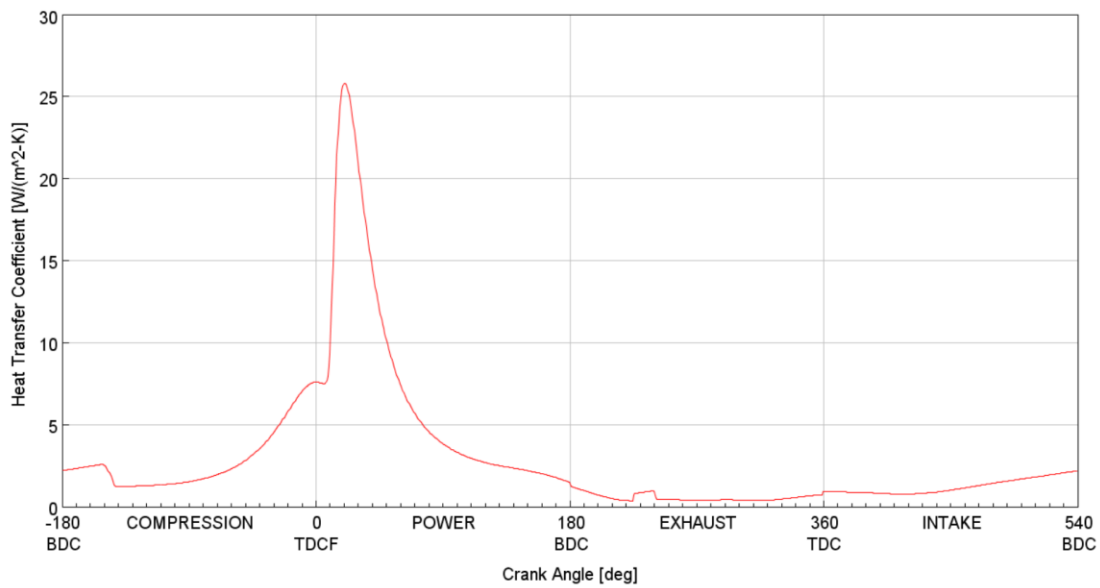
Figure 44 – Mean in cylinder heat transfer coefficients (Woschni) predicted by the validated GT engine combustion model for 1500 rpm, WOT
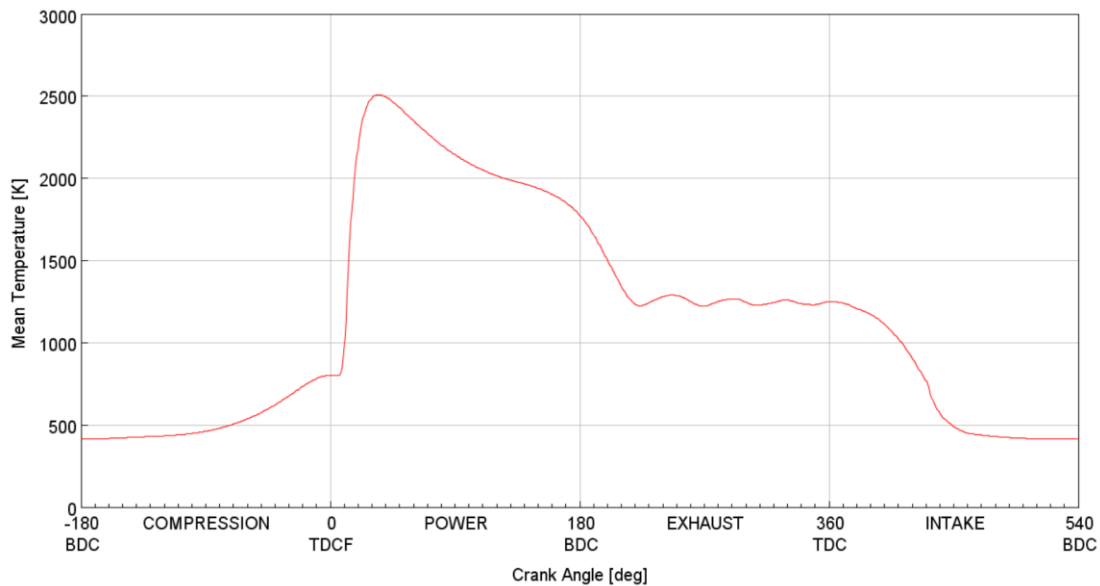
Figure 45 - Mean in cylinder gas temperature predicted by the validated GT engine combustion model for 1500 rpm, WOT

232

Another possibility is that a calcium particle sticks to the face of the exhaust valve, the valve retains a hot temperature until undergoing intense cooling as the piston approaches TDC of the compression stroke. If the wall was to rapidly cool, the equilibrium will shift such that a CaO particle will react with CO_2.
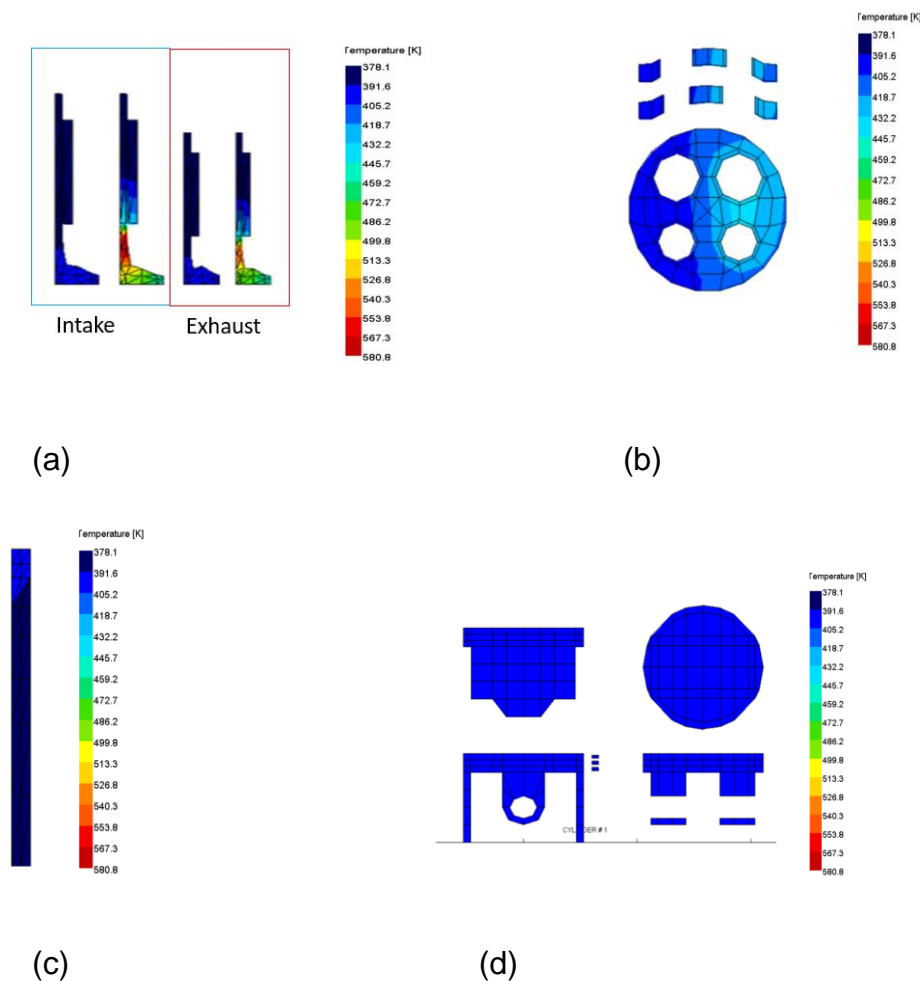
Figure 46 - FEA heat transfer simulation using GT, showing cycle average temperature for (a) Valves (b) combustion dome (c) liner (d) piston

233

The finite element analysis (FEA) solution in Figure 46 demonstrates the maximum cycle averaged valve temperature is 580K. With the compression stroke being one of the cooler strokes (although the valve will have a high thermal capacitance so the temperature will not fluctuate much throughout the cycle), once again it is unlikely the exhaust valve will remain hot enough for the Calcium particle to retain a temperature above 1000K for much of the compression stroke and then suddenly cool just before spark timing.

A major assumption made in the analysis that will follow in this section is that the particle is smooth; this assumption is inaccurate and possibly critical. While the very rough topography of the particle the surface area is larger, the air does not necessarily have access to this area during most of the compression stroke, because of the turbulent length scale being larger than the crevice/orifice size [156]; turbulent separation at the surface will stop the high velocity air interfacing with the inner crevice area. This means the effective surface area gas can interface with is most likely less than that of a perfect sphere. The length scales will reduce as the piston proceeds due to viscous stress but this is a gradual process rather than a rapid change.

It should be remembered compressible flow is generally non-linear in its behaviour. A possible explanation is that due to the highly porous medium, at high pressure, jets of air travelling into the particle may be present, and

234

momentum diffusion transports the air into the internal crevices. Due to the nature of compressible flow this will only occur above a certain gas pressure. The micro-jets will increase the rate of cooling and the surface area available for reaction.

It is very difficult to simulate fluid behaviour at length scales small enough to observe the impact of porosity without encountering numerical instability. For this reason, this aspect will just be noted for consideration.

8.3. Aspen plus Reactor simulation to compare reaction equilibrium of Ca and Mg detergents

Once again, the reader is reminded, it has been widely recognised that the addition of Calcium, an efficient detergent to engine lubricant increases combustion propensity to LSPI, whereas the addition of Magnesium which like Calcium is an alkaline metal does not show this effect.

A lubricant oil containing calcium will store it in the form of clusters of $CaCO_3$-CaO mixture which have $CaR-SO_4$ formed by ionic bonds around the surface of the clusters. The purpose of this study is to assess the behaviour of Ca and Mg based additives using the mechanism suggested by Mayer et al [13] and Moriyoshi et al [19], the relevant reactions can be seen below (eqn 104 & eqn 105). The mechanism ignores the impact of the Sulfonate molecules and focuses solely on the Oxide and Carbonate cluster at the core. This is a sensible assumption as the total mass of Sulfonate molecules around the surface area of the cluster will be substantially less than the mass in the cluster core itself. It is unlikely the small Sulfonate mass can create sufficient
235

energy intensity to initiate an autoignition event. In addition, we have already discussed how the controlled addition of CaO into the mixture of an RCEM was found to cause an autoignition by Moriyoshi et al.

$$CaO + CO_2 <=> CaCO_3 \qquad \text{[eqn 104]}$$

$$MgO + CO_2 <=> MgCO_3 \qquad \text{[eqn 105]}$$

A second potential reaction described in Rudnick et al [80] also takes place at the surface of the detergent particle and forms an outer layer of species ionically bonded to the surface. The reaction is as follows:

$$Ca(OH)_2 <=> CaO + H_2O \qquad \text{[eqn 106]}$$

$$Mg(OH)_2 <=> MgO + H_2O \qquad \text{[eqn 107]}$$
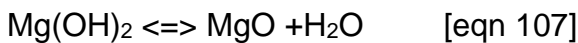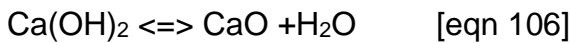
This reaction could be a useful contributor to an exothermic event even if the particle itself is CaCO3, as at appropriate conditions, CaO could form once a H2O molecule detaches itself.

8.3.1. Aspen model setup

A Gibbs reactor simulation was set up using Aspen (discussed in chapter 4.8) as shown below (Figure 47) for both Ca and Mg. Both CO2 (gas) and CaO/MgO (solid) are inserted into the Gibbs reactor at a rate of 1kmol/hour

and temperatures will be incremented from 300ºC to 800 ºC. The gas composition was 1 part CO_2 and 4 parts N_2, if we assume the total gas pressure is 1 bar this means the maximum partial pressure for CO_2 is 1/5 * 1bar = 0.2bar.

In addition 0.2kmol/hour of $Ca(OH)_2$/ $Mg(OH)_2$ are inserted into the reactor at the same time to investigate the Hydroxyl reaction.

A steady state simulation was conducted so the results obtained are those at which the reaction is in equilibrium. Table 11 and 12 show the equilibrium results for Ca and Mg results respectively, it can be seen the mass fraction, partial pressure, mass flow can be calculated for each species as well as the heat released for each equilibrium condition. The maximum partial pressure for CO2 is 0.2bar but reduces under equilibrium conditions as it is consumed with the formation of $CaCO_3$/$MgCO_3$. Just from an initial assessment it is evident the two reactions exhibit very different response to temperature; the Ca comprises of complete CaO (and CO2 is 0.2bar) at 800degC, whereas the Mg mixture is 100% MgO at only 400degC.

We know from literature, a cooler water jacket temperature helps push the reaction towards the formation of $CaCO_3$, as does the increase in humidity. However, both will suppress the severity of an LSPI event as the charge will be cooler, although the frequency may be increased.
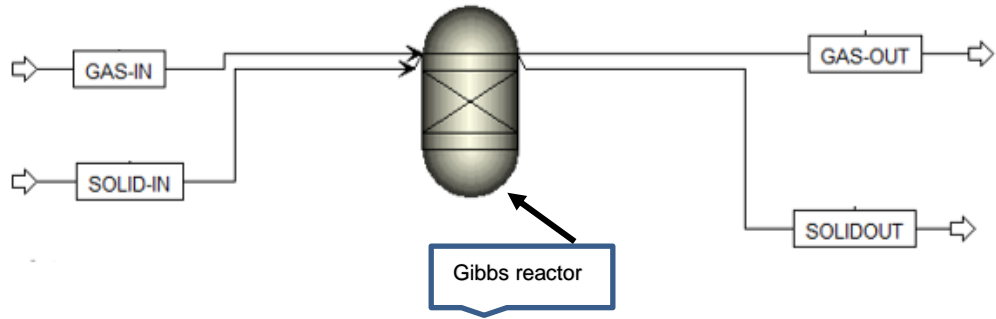
Figure 47– Aspen, Gibbs reactor model of CaO and and MgO reactions with CO2

8.3.2. Aspen model results and discussion

Equilibrium Temp	Molar fraction CaO	P(CO2), 1/5 bar total	Heat release	Molar flow, CaO	Molar fraction, CaOH2	Molar flow, H2O	Molar flow, CaCO3
deg C	*Fraction*	*bar*	*GJ/hr*	*kMol/hr*	*Fraction*	*kMol/hr*	*kMol/hr*
300	0.009	0.000	-0.177	0.011	0.158	0.011	1.000
350	0.054	0.000	-0.171	0.065	0.113	0.065	1.000
400	0.167	0.000	-0.156	0.200	0.000	0.200	1.000
450	0.167	0.000	-0.156	0.200	0.000	0.200	1.000
500	0.167	0.000	-0.156	0.201	0.000	0.200	0.999
550	0.170	0.001	-0.155	0.204	0.000	0.200	0.996
600	0.181	0.005	-0.153	0.217	0.000	0.200	0.983
650	0.218	0.018	-0.144	0.262	0.000	0.200	0.938
700	0.338	0.058	-0.119	0.405	0.000	0.200	0.795
750	0.704	0.165	-0.043	0.845	0.000	0.200	0.355
800	1.000	0.238	0.018	1.200	0.000	0.200	0.000

Table 11 - Gibbs Reactor simulation results for CaO

Equilibrium Temp	Molar fraction MgO	P(CO2), 1/5 bar total	Heat release	Molar flow, MgO	Molar fraction, MgOH2	Molar flow, H2O	Molar flow, MgCO3
deg C	Fraction	bar	GJ/hr	kMol/hr	Fraction	kMol/hr	kMol/hr
300	0.248	0.028	-0.090	0.298	0.000	0.200	0.902
350	0.835	0.199	-0.008	1.002	0.000	0.200	0.198
400	1.000	0.238	0.015	1.200	0.000	0.200	0.000
450	1.000	0.238	0.015	1.200	0.000	0.200	0.000
500	1.000	0.238	0.015	1.200	0.000	0.200	0.000
550	1.000	0.238	0.014	1.200	0.000	0.200	0.000
600	1.000	0.238	0.014	1.200	0.000	0.200	0.000
650	1.000	0.238	0.014	1.200	0.000	0.200	0.000
700	1.000	0.238	0.014	1.200	0.000	0.200	0.000
750	1.000	0.238	0.014	1.200	0.000	0.200	0.000
800	1.000	0.238	0.013	1.200	0.000	0.200	0.000

Table 12 - Gibbs Reactor simulation results for MgO
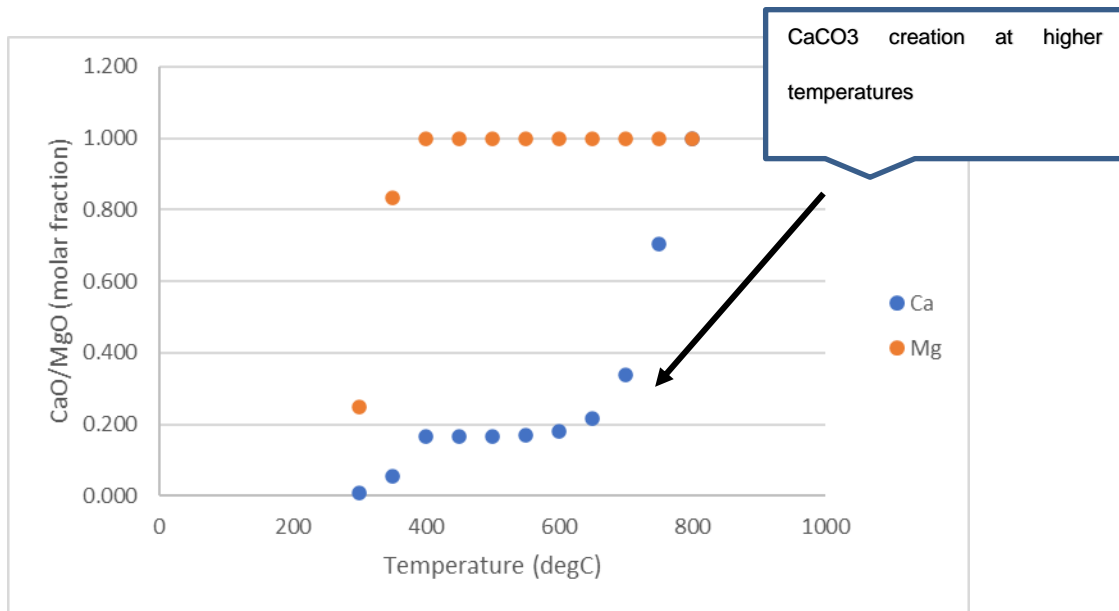
Figure 48 - Plot comparing molar fraction of detergent oxide at equilibrium for constant temperature

From Figure 48, we can see the large difference in thermodynamic behaviour between a Ca based detergent and an Mg based detergent under similar boundary conditions; temperatures that are typical of an engine cycle. The Ca particle will require much higher temperatures to be in its CaO state, similarly

239

it will begin to react with CO_2 at higher temperature compared to that of the Mg particle. In order for the Moriyoshi theory of Calcium detergent reaction to hold weight the CaO particle would need to be heated to a temperature above 1000K during the expansion and exhaust stroke, it is only cooled slightly during the intake stroke because of the lower charge density and finally it is cooled rapidly close to spark timing of the compression stroke (when the charge density and TKE is high).

The challenge with the proposition of this study is accepting the cooling of the particle takes place fast enough completely from convection, and as a step change at the correct timing, for the reaction to be spontaneous in an actual engine. As the change in volume (and the resulting pressure, temperature and density) of charge gas in an engine are driven by the sinusoidal motion of the piston, and thus gradual in change rather than the step change simulated above. This is also demonstrated in Figure 44 (chapter 8.2), which shows the Woschni heat transfer coefficient (htc) increases gradually during the compression stroke after the intake valve closing (IVC).

8.4.   Development of a transient single particle Detergent reaction model

Up until now the XCO_3-XO particle has been assumed to be a unified chemical system, a cluster that changes in its composition depending on the equilibrium balance. Whilst this approach is physically valid it is incorrect from a chemical equilibrium perspective; the XCO_3 and XO proportions are separate chemical systems that coexist together. This is of particular interest

in the event of a CaO particle being introduced as part of an oil droplet during the intake stroke, as oppose to being a remnant from the previous combustion cycle. It should also be remembered the particle will initially have access to the CO_2 of the residual gas during both the intake and compression strokes, as the piston moves down during the intake stroke only then will the fluid above the ring position have access to CO_2. In the first part of this section a scheme will be developed to track the chemical state of the particle throughout the intake and compression stroke; we can assess the state of conversion of the particle based on its chemical stability as a function of the surrounding boundary conditions.

8.4.1. Detergent reaction onset prediction model development and setup

The equilibrium equation now quite simply becomes [104][105]:

$$K(T) = 1/P(CO_2) \quad \text{[eqn 108]}$$

In the event the initial condition for a given time step is; $1/P(CO_2) < K(T)$, the XCO particle is unstable as the concentration of CO2 locally is higher than it should be in equilibrium, and will react with CO_2 until the concentration of CaO, CaCO2 and local concentration of CO2 satisfies the above equilibrium condition for the local temperature. As this condition is a global boundary condition; meaning it will apply to each part of the XCO particle until the reaction starts, at which point the reaction with CO_2 will continue until the local

241

equilibrium concentration/partial pressure of CO2 has been reached for the whole particle. As before the reaction of CaO is exothermic and the equilibrium temperature will change the equilibrium constant.

The following equation can be used to calculate the initial equilibrium constant from the change in Gibbs free energy of the reaction:

$$\Delta G_{reaction} = -R\, T \ln{(K_{eq})} \qquad \text{[eqn 109]}$$

$$\Delta G_{reaction} = Gf_{XCO3} - Gf_{XO} - Gf_{CO2} \qquad \text{[eqn 110]}$$

Where; $\Delta G_{reaction}$ = Gibb free energy of reaction, -R = Universal gas constant, T = temperature, K_{eq} = equilibrium constant, Gf_{XCO3} = Gibbs free energy of detergent carbonate, Gf_{XO} = Gibbs free energy of detergent oxide, Gf_{CO2} = Gibbs free energy of CO2

The reasonable assumption of 5% (from 1D analysis) of the total intake charge gas being burned gas residuals can be maintained, and so the partial pressure can be calculated from the total cylinder pressure for each time step. The concentration of burned gas during the beginning of the intake stroke will be high, and the concentration will reduce as the volume increases on the down stroke. The concentration will also reduce as the burned gas is scavenged during the valve overlap period, due to the intake pressure being higher than the cylinder and exhaust pressures. However, due to the high

mass flow of intake charge and the increasing volume the burned gas will not be homogeneously mixed until the end of the intake stroke or even during the compression stroke. This means the concentration of burned gas during the intake stroke becomes position dependant; and may be less than 5% in some positions (for a given crank angle) and greater than 5% for others. In order to establish this a full combustion simulation will be required and may not add much value for the objective of this study as it is the compression stroke that is of utmost interest. It will also vary from one engine design to another and possibly even between cylinders. For this reason, simulations will be completed with a 5% concentration of burned gas being maintained throughout the intake stroke. As a sensitivity study a10% burned gas fraction will also be simulated to understand impact.

As the heat transfer coefficient and gas temperature is known the temperature change of a particle can be calculated for the intake and compression strokes by using the specific heat capacity of the particle and assuming an initial temperature. Thus, a stability assessment can be made by assuming a particle size and calculating the energy extracted from its surface due to convection over each time step, the specific heat capacity can be used to calculate the change in temperature of the particle associated with the thermal energy extracted. The change in Gf_{XO} as a function of temperature can be characterised by fitting polynomial functions to data offered by NIST, due to lack of robust data Gf_{XCO3} and Gf_{CO2} will just be calculated using the change in enthalpy and entropy as a function of temperature. A script was developed to

243

compare the initial Keq calculated at each time step of an engine cycle with the partial pressure of CO_2. The results for both CaO and MgO can be found in figures 49 and 50.

Gibbs free energy for CaO as a function temperature is characterised as polynomial fitted to data from NIST;

$$Gf_{CaO}(T) = 3.96794E\text{-}09T^3 - 3.91162E\text{-}05T^2 - 2.90918E\text{-}02T - 6.33534E\text{+}02$$

[eqn 111]

$$Gf_{MgO}(T) = 3.74802E\text{-}09T^3 - 3.70698E\text{-}05T^2 - 1.72911E\text{-}02T - 6.00561E\text{+}02$$

[eqn 112]

The change in Gibbs free energy for CaCO3 can be calculated from the change in entropy and enthalpy for a given temperature change;

$Gf_{caco3, 298K}= -1128.8 \text{ kJ/mol}$

$\Delta Gf_{caco3}(T) = \Delta hf_{caco3}(T) - T^* \Delta S_{caco3}(T)$ [eqn 113]

$\Delta hf =$ change in enthalpy,
$\Delta S =$ change in entropy

244

Change in enthalpy can be calculated by integrating the specific heat capacity between the standard temperature and the temperature of the thermodynamic system;

$$\Delta hf_{caco3}\ (T) = \int_{To}^{T} C_p\ dT \qquad \text{[eqn 114]}$$

If C_p is assumed to be constant for all temperatures (as the difference is small for the expected temperature range, and consistent between the two detergents);

$$\Delta hf_{caco3}\ (T) = C_p\ (T - T0) \qquad \text{[eqn 115]}$$

The change in entropy between the standard temperature and that of the thermodynamic system can be calculated by rearranging the equation below and integrating with respect to dT between the two temperatures;

$$C_p = T\ \frac{\partial s}{\partial T} \qquad \text{[eqn 116]}$$

$$\Delta S = \int_{T0}^{T} \frac{C_p}{T}\ dT \qquad \text{[eqn 117]}$$

$\Delta S = C_p\ \ln(T) - C_p\ \ln(T0)$

$\qquad = C_p\ \ln(T/T0) \qquad \text{[eqn 118]}$

Now that the change in enthalpy and entropy has been calculated for the thermodynamic system at a constant temperature the change in Gibbs free energy relative to the Gibbs free energy at the standard temperature can be calculated and added to the standard value;

$$Gf_{CaCO3}(T) = \Delta Gf_{caco3}\ (T) + Gf_{caco3,\ 298K} \qquad \text{[eqn 119]}$$

A similar calculation can be used to calculate the Gibbs free energy associated with $MgCO_3$;

$Gf_{MgCO_3, 298K}$ = -1012.1 kJ/mol

$C_p(MgCO_3)$ = 75.52 $Jmol^{-1}K^{-1}$

$C_p(CaCO_3)$ = 83.5 $Jmol^{-1}K^{-1}$

The Gibbs free energy for CO2 as a function of temperature can be calculated using the polynomial below. The equation is derived from a curve fit for data obtained from J.L. Silveira [24].

$Gf_{CO2}(T) = (-1.11957E-06*T^2 + 3.57779E-03*T + 3.93407E+02)*-1;$
[eqn 120]

At this stage the assessment was purely a stability assessment to understand during which phases the exothermic reaction is likely to occur. For this reason, only convective heat transfer was considered at this stage, heat transfer due to the reaction was ignored.

The initial temperature of the particle was the final gas temperature of the exhaust stroke, this is reasonable assumption as the elevated temperatures of the expansion and exhaust stroke as well as the high residence time should

assure the particle is at a high temperature. The calculation for the particle temperature due to convection can be found in Appendix I.

8.4.2.   **Detergent reaction onset Results and discussion**

(a)

(b)

247
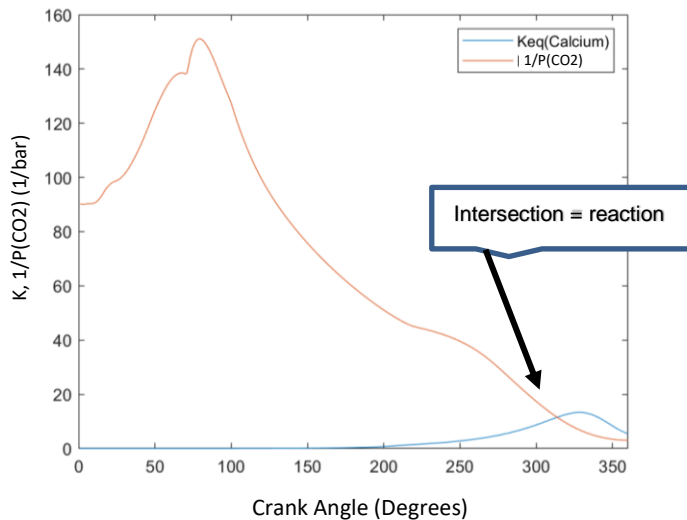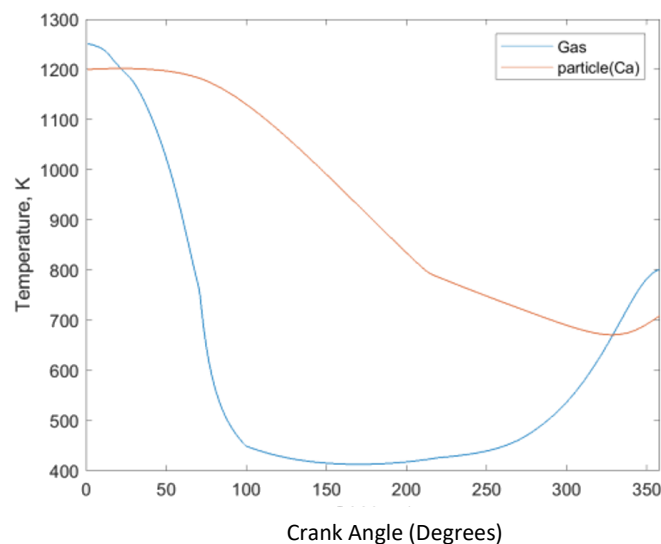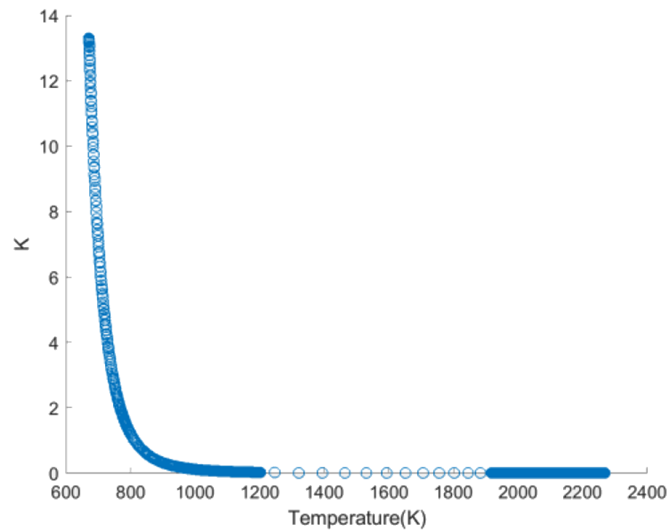
(c)

Figure 49– Assuming a particle size of 5e-08m, burned gas residuals = 10% (a) Comparison of Calcium initial equilibrium constant and reciprocal partial pressure of CO2 during the intake and compression strokes of an engine cycle (b) Particle and gas temperature during the intake and compression strokes, neglecting heat released due to reaction (c) change in equilibrium constant with change in temperature for the CaO/CaCO3 reaction
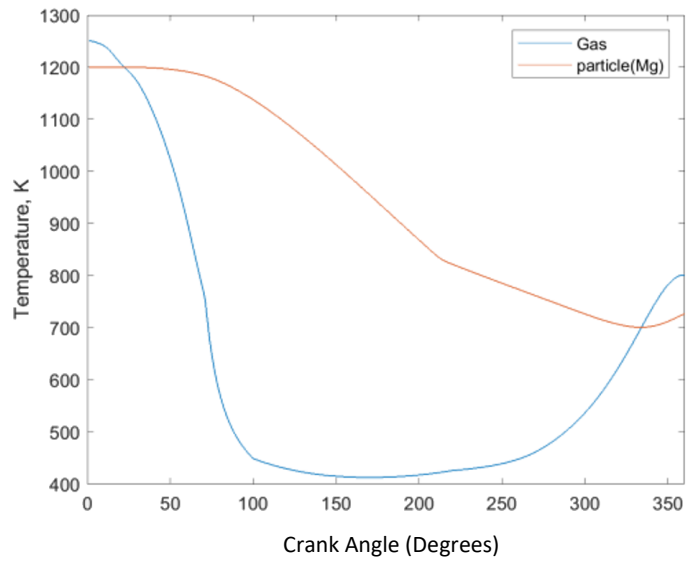
(a)
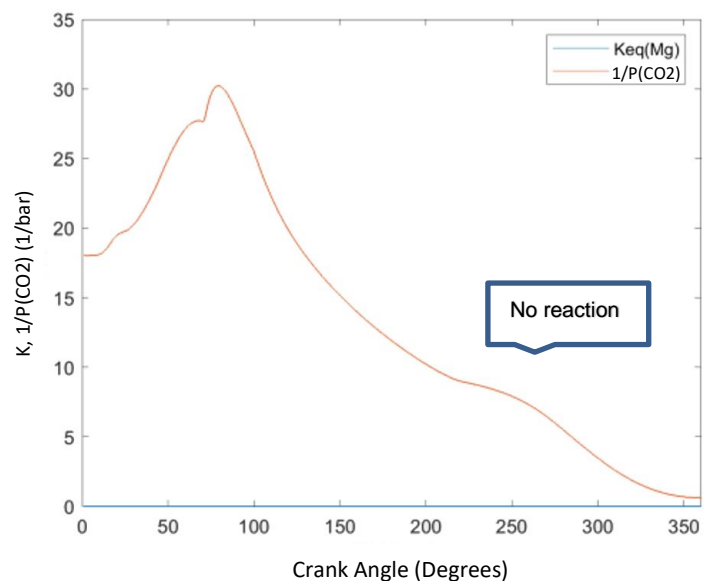
(b)
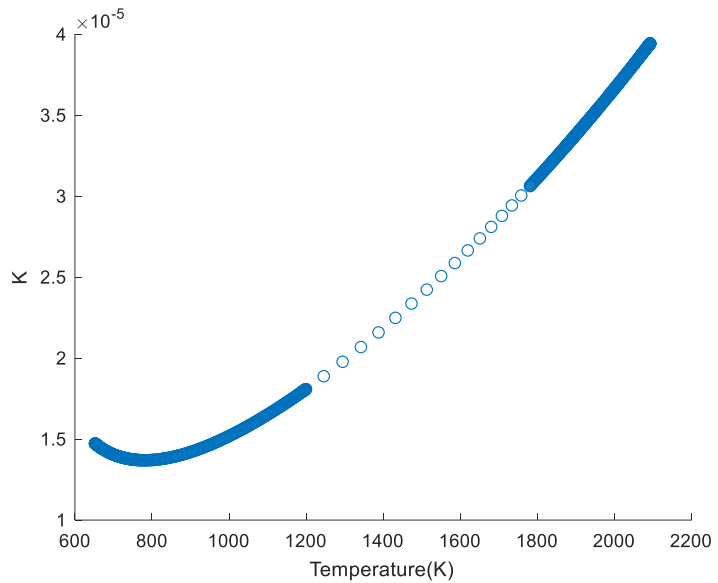
(c)

Figure 50– Assuming a particle size of 5e-08m, burned gas residuals = 10% (a) Particle and gas temperature during the intake and compression strokes, neglecting heat released due to reaction (b) Comparison of Magnesium initial equilibrium constant and reciprocal partial pressure of CO2 during the intake and compression strokes of an engine cycle (c) change in equilibrium constant with change in temperature for the MgO/MgCO3 reaction

(a)

(b)

251
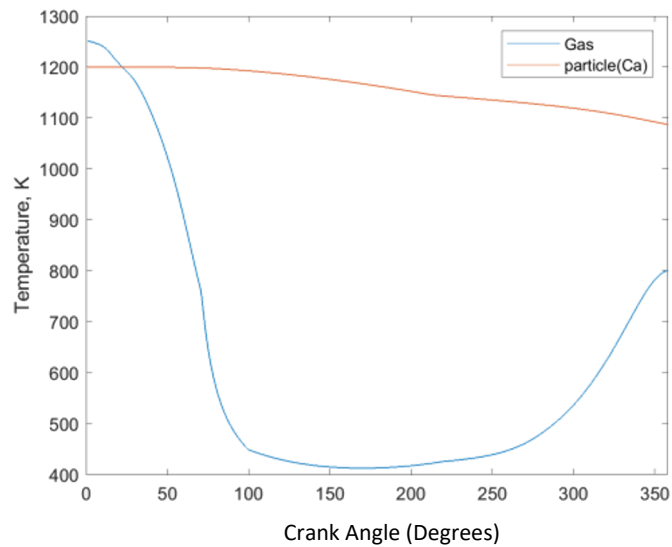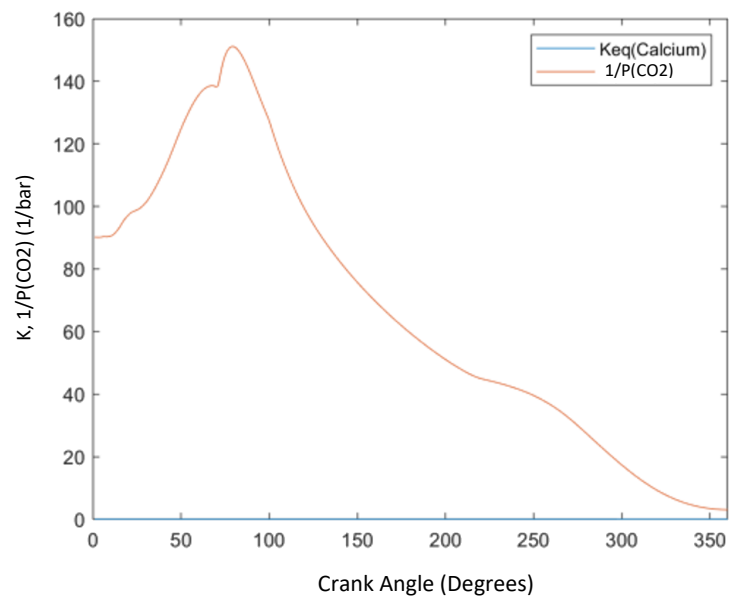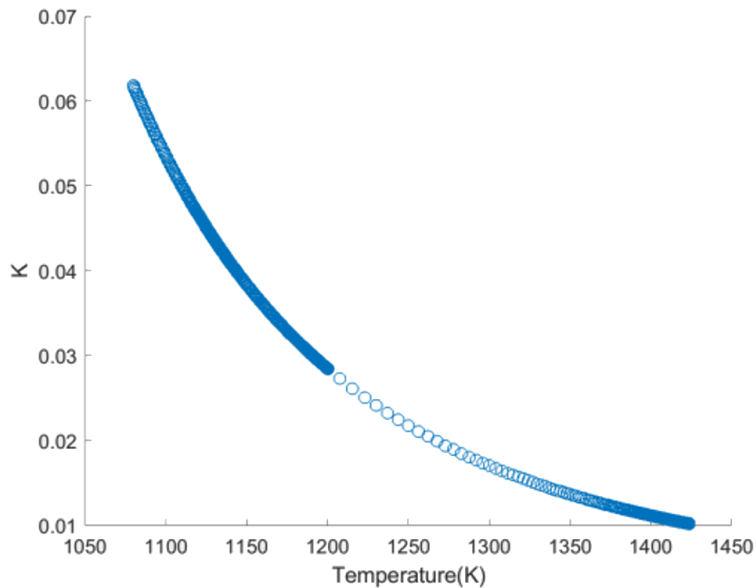
(c)

Figure 51– Assuming a particle size of 5e-07m, burned gas residuals = 10% (a) Particle and gas temperature during the intake and compression strokes, neglecting heat released due to reaction (b) Comparison of Calcium initial equilibrium constant and reciprocal partial pressure of CO2 during the intake and compression strokes of an engine cycle (c) change in equilibrium constant with change in temperature for the CaO/CaCO3 reaction

In the first instance a 10% burned gas fraction was assumed. This represents the maximum local concentration that may be observed locally before the charge is uniformly mixed [138]. Later resulting in a nominal 5% concentration when the mixture is homogeneous. The results of the simulation can be found in Figures 49-51.

From the $1/P(CO_2)$ plot we can see the partial pressure reduces during the early part of the intake stroke, as a depression in created in the cylinder. The boost then pressurises the charge and causes the pressure to increase. A

252

small step reduction in $P(CO_2)$ is observed at around 100CAdeg due to the late closing of the exhaust valve. Obviously, the pressure will continue to increase during the compression stroke.

The response of the two detergents is very different. The Mg based detergent (Figure 50) demonstrates very low equilibrium constant values from the beginning of the intake stroke, much lower than the inverse partial pressure of CO_2. The MgO particle will not react with the CO_2 present in the gas domain to form MgCO3 throughout the intake and compression strokes.

The CaO particle initially has very high equilibrium constant values at low temperatures which reduce dramatically as the temperature approaches 800K. The particle starts at a high temperature and then becomes cooler during the intake stroke, followed by a slight increase in temperature again during the compression stroke. For this reason, the equilibrium constant starts low, increases and then reduces again. Very interestingly Figure 49 suggests the reaction with CO_2 will begin around 40deg BTdC of the compression stroke (when; $Keq > 1/P(CO)$), which is a plausible point for the onset of LSPI. Figure 51 shows the simulation of a CaO particle of a larger size (5e-07m), because of the higher thermal capacitance the particle retains an elevated temperature. The higher temperature means the equilibrium constant value is always lower than the 1/P(CO2) and thus a reaction never takes place. Obviously, at this point the onset of reaction is being predicted, the reaction duration and heat release has not been included at this stage but will be

253

included later in the chapter. Already, one can begin to gain an understanding for why research papers observed LSPI with Ca based detergents but not Mg based detergents.

The theory explored in the study above is believed to be the strongest explanation for autoignition due to the presence of a Ca based detergent. Similar to the study that was based on Aspen predicted equilibrium constants this study demonstrates a difference in chemical behaviour between the Ca based detergent and Mg based. The study conducted above that assesses the CaO as an individual system suggests the propensity of autoignition increases with increasing gas temperature. Most importantly, the study is showing a difference in reaction behaviour between Mg and Ca based detergents, with regards to the reaction with CO_2, close to the spark ignition event. Proximity to the spark ignition point is what will determine the propensity to mega-knock.

For completeness calculation assuming a particle size of 5e-07m was completed for the Mg particle. It is known a reaction will not take place because of an even higher particle temperature; the purpose was to compare the thermal capacitance response to that of a Ca particle. Figure 52 shows the heat transfer characteristic of a non-reacting Mg particle is similar to Ca.
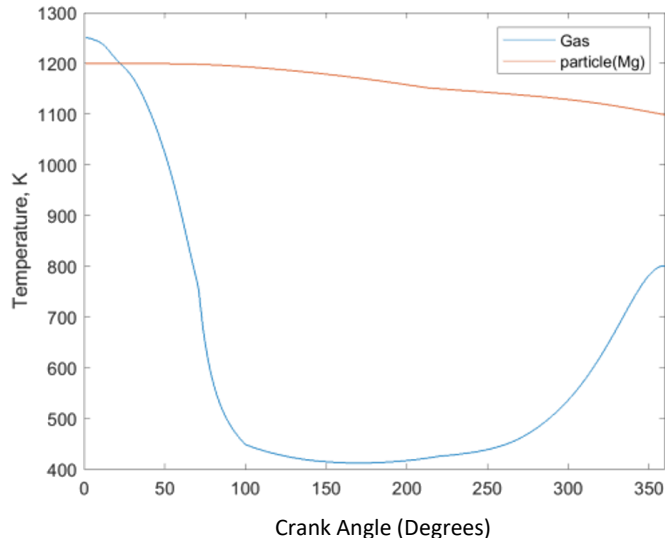
Figure 52– Temperature of Magnesium based particle during intake and compression strokes, accounting for reaction heat and convective heat transfer, particle radius = 5e-07m, burned gas residuals = 10%

The impact of reducing the burned gas residual concentration to 5%, as would be found for a homogeneous mixture, can be observed in Figure 53. The reaction timing has become significantly more retarded in the case of a particle size of 1e-08m, in comparison to the 10% burned gas residual case.
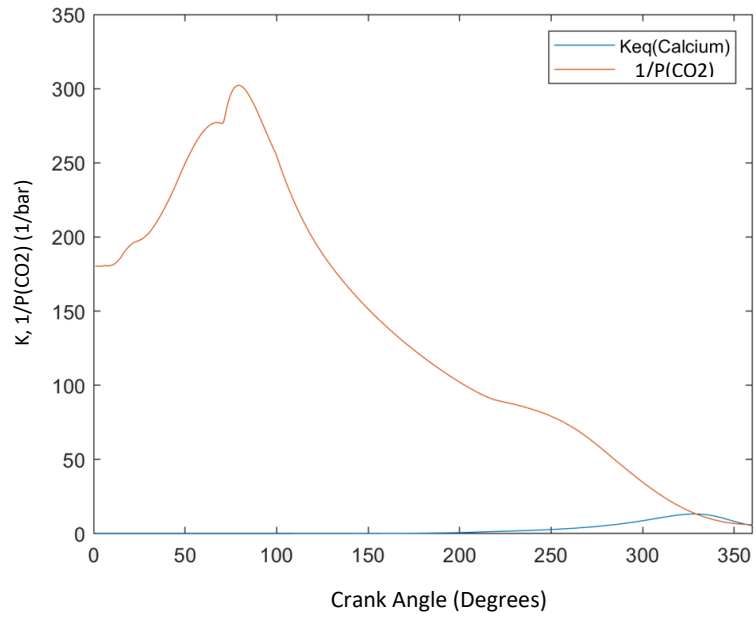
Figure 53 - Assuming a particle size of 5e-08m, burned gas residuals = 5%. Comparison of Calcium initial equilibrium constant and reciprocal partial pressure of CO2 during the intake and compression strokes of an engine cycle
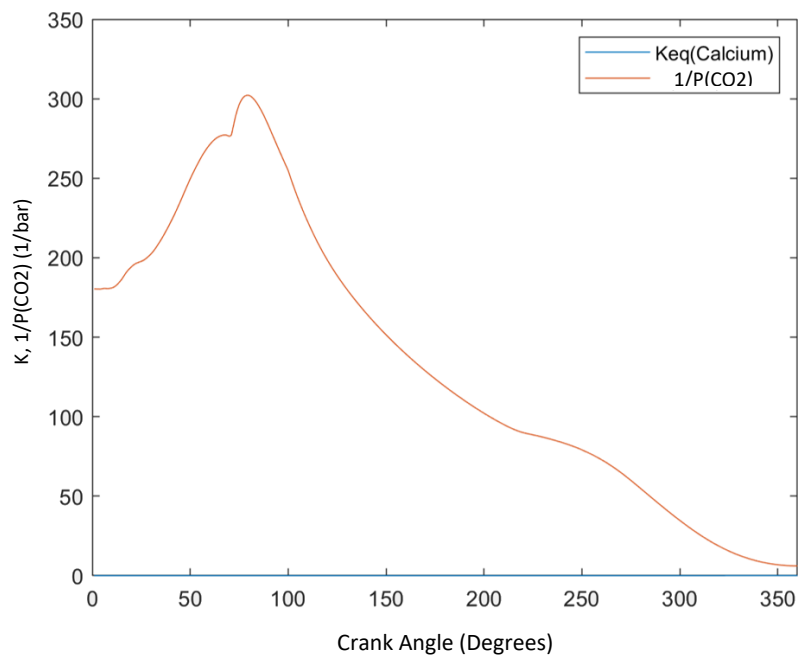
Figure 54– Assuming a particle size of 5e-07m, burned gas residuals = 5%. Comparison of Calcium initial equilibrium constant and reciprocal partial pressure of CO2 during the intake and compression strokes of an engine cycle

256

To summarise, the response of differently sized CaO particles during the intake and compression strokes of an engine was investigated and will be explored further. It was found very small particles had low thermal capacitance and thus responded to changes in gas temperature rapidly, the resulting particle temperature was generally closer to the gas temperature. However, the much quicker cooling meant the equilibrium constant increased early in the intake stroke and exceeded the reciprocal of CO2 partial pressure, meaning the reaction had been initiated. Because the mass of the particle is so low, it is consumed, and the reaction terminates quickly. The intake stroke is also a period when the reaction is very unlikely to cause an autoignition as the local air-fuel concentrations are low because of lower pressure and also because the mixture is not yet uniform. In addition to this the enthalpy of the air fuel mixture will be lower; again, making it less likely an autoignition reaction will be propagated.

The study was extended to investigate a particle size of 5e-07m, it can be seen in Figure 51 that the thermal capacitance is so high the particle temperature changes very little and remains high throughout the intake and compression strokes. Although the reaction is not activated throughout the engine cycle the temperature of the particle is very high during the compression stroke, making an autoignition highly likely.

As has already been established the reaction of MgO with CO_2 is not triggered at any stage throughout the intake or compression strokes. For the case with a particle size of 5e-08m the particle temperature is actually lower than the gas temperature towards tdc; because of the higher thermal capacitance and because the gas temperature is increasing. When the MgO particle was increased to a radius of 1e-07m, the thermal capacitance was high enough to demonstrate behaviour similar to a CaO particle of similar size (no reaction, just heat due to thermal capacitance). This scenario is unlikely as the radius of the particle is of a similar order of size as an EHL film thickness, and also it has been found from engine testing that Mg based detergents do not promote LSPI. The reaction timing for the Ca particle is significantly influenced by the CO2 concentration, whereas the Mg particle seems to be indifferent.

Figure 55 provides a summary of the findings of this section. The particle size range was estimated as being sensible given the oil film thickness. Once again; a reaction was only observed with the Ca detergent but only if the particle is not too large and a higher CO2 concentration advances LSPI ignition timing.
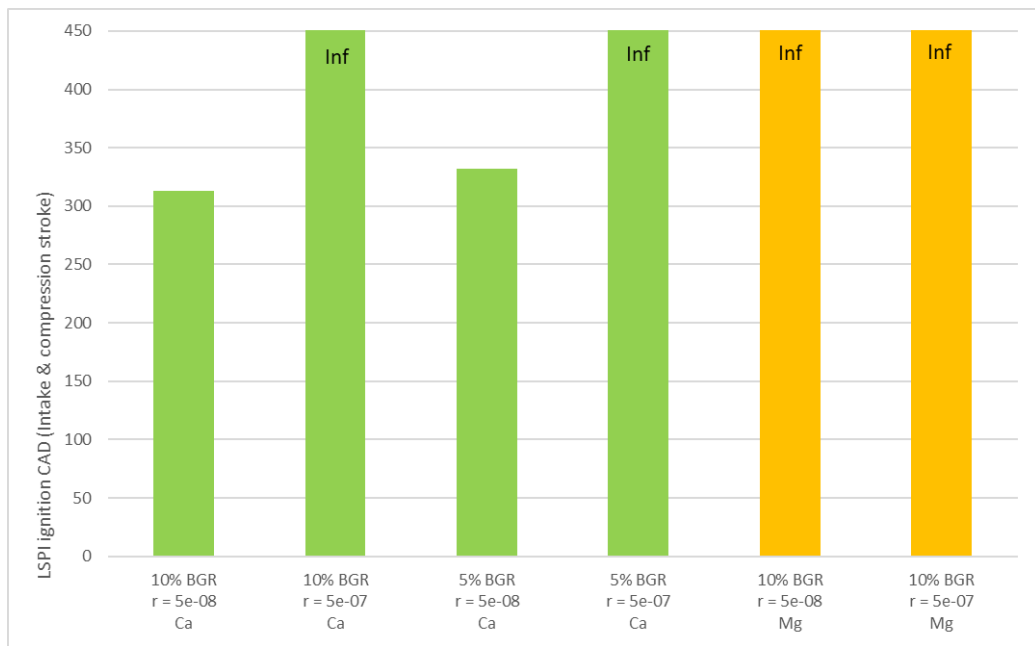
Figure 55– A summary bar chart of all the cases simulated for onset of LSPI, each case states the percentage burned gas residuals (BGR), the particle diameter, and the type of detergent. Cases that state 'inf' represent an infinite ignition angle i.e., a LSPI event did not occur

259

8.4.3. Arrhenius Analysis of detergent reaction

It could be argued that the particle behaviour in the previous section makes two underlying assumptions; 1) The reaction begins immediately as the concentration of CO_2 surrounding the particle deviates from its equilibrium concentration 2) the reaction with the particle takes place instantaneously when a CO_2 molecule approaches it, with the diffusion of the molecule being the only rate determining step. Modelling reaction kinetics is very difficult in this scenario as it will be impacted by porosity, surface action and catalytic behaviour of the particle. Most of the reaction rate characterisation for the carbonation and calcination reactions of Calcium are based on Limestone at very different pressures and concentrations of CO_2 compared to an engine. For this reason, we need to exercise an extreme level of caution when applying such reaction rate functions to an LSPI scenario. Ramezani et al [58] lists various Arrhenius parameters that can be used to calculate the rate function for these reactions, the values vary substantially. We will use the Grasa et al parameters as it was developed for natural Limestone, for higher levels of reactivity (better for higher concentrations, as the rate of reaction will increase with CO_2 concentration). The equation assumes the reaction is first order with respect to CO_2 concentration. The reaction rate for the Carbonation reaction will be tested, as this is the exothermic event, we are interested in, and because we know the equilibrium shifts towards the Carbonation reaction under the chosen conditions. It was decided we would initially test the formula at the low temperature and concentration it was characterised for.

260

$$K = A \, e^{\frac{-Ea}{RT}} \quad \text{[eqn 121]}$$

A = 10.5e03 $m^4 kmol^{-1} s^{-1}$, Ea = 230 kJ/mol

Because the particle will be present during the intake stroke, and it is possible given the correct conditions and ignition could take place early, it was decided a system pressure and temperature representative of the intake stroke will be used, with the mind that if the reaction is fast during induction conditions it will be even faster during compression, when concentration and temperature are higher.

The constant temperature and pressure conditions representative of the intake stroke are:

T (System temperature) = 400K, P (System pressure) = 5bar

Assuming 5% CO2 due to the presence of burned gas residuals, the partial pressure of CO_2 can be calculated:

P(CO2) = 0.025bar

Therefore, the concentration can also be calculated:

[CO2] = 0.7517 mol/m^3

Now the rate constant can be calculated using eqn 121:

K = 9.33e07 m3 kmol-1 s-1

The rate constant and concentration can be used to calculate the reaction rate (RR):

$RR = [CO2] * K = 7.02e10 \text{ mol s}^{-1} \text{ m}^{-3}$

A plausible size of the particle will be assumed:

Particle radius (part_rad) = 5e-09m

Assuming the particle is spherical the volume, mass and number of moles can be calculated:

Particle volume (part_vol) = 5.24e-25m

Particle mass (part_mass) = 1.42e-21kg

Moles of CaO (MCaO) = 2.53e-20 moles

Assuming the particle volume represents the CO2 reaction volume the overall reaction rate (ORR) is as follows:

ORR = RR * part_vol = 3.67e-14 mol/s

Finally, the time take for the particle to react can be calculated:

MCaO/ORR = 6.89e-07 s

For an engine speed of 1500rev/min, the reaction time equates to 6.2e-03 deg CA. Which is extremely fast, almost instantaneous, therefore the equilibrium calculation approach is valid.

When the calculation was repeated for a more applicable 800K, 30bar pressure, with 5% burned gas fraction the particle will react to completion in 2e-03 deg CA.

8.4.4. Single particle detergent reaction model with heat release

Having now arrived at a theory which possibly explains the timing of the CaO/MgO exothermic reaction, the next stage must be to understand if the heat release and reaction duration, are sufficient to cause the fuel-air mixture at the particle surface boundary to ignite.

Although the reaction has been assumed to be spontaneous in equilibrium calculations, the local CO_2 concentration will be based on the rate of diffusion of CO_2 from gaseous environment to the vicinity of the particle as the CO2 at the boundary of the particle is consumed. Similarly, the local particle temperature will be subject to the thermal diffusivity of the gaseous domain and the rate at which heat diffuses from the particle to the surrounding environment. In essence it will be the physical behavioural aspects of the system that will determine the rate of reaction, rather than kinetics.

263

The enthalpy of reaction can be calculated using Hess's law by using polynomial equations from NIST for hf_{CaO} and using standard values for h_{CaCO3} and h_{CO2}.

Enthalpy change of formation as a function of temperature can be calculated for CO_2 by integrating specific heat capacity as a function of temperature:

$$\Delta hf_{CO2}\,(T) = \int_{T_o}^{T} C_p\, dT \qquad \text{[eqn 122]}$$

An extract of the Matlab code that demonstrates the calculation of heat release can be found below.

```
Hf_CaO_stnd = -635.09; %kj/mol

Aj = 49.95403;

Bj = 4.887916;

Cj = -0.352056;

Dj = 0.046187;

Ej = -0.825097;

Fj = -652.9718;

Gj = 92.56096;

Hj = -635.0894;




Temp = 700;

tj = Temp_loc/1000;


Hf_cao_t    =Aj*tj+Bj*tj^2/2+Cj*tj^3/3+Dj*tj^4/4-Ej/tj+Fj-
Hj+Hf_CaO_stnd;%kj/mol



Hf_caco3_stand = -1206.9;%kj/mol



cp_co2 = 37.11; %j/mol/K

Hf_CO2_stand = -393.51;%kj/mol

Hf_CO2  = cp_co2*(Temp-298)/1000+Hf_CO2_stand;


cp_caco3 = 83.5;

Hf_caco3    =   cp_caco3*(Temp-298)/1000+Hf_caco3_stand;
%kj/mol

H_react = Hf_caco3-Hf_CO2-Hf_cao_t;%kj/mol
```

It is important to remember than all the heat from the reaction will not be transferred to the gaseous environment, some of the thermal energy will be

265

retained within the particle itself. The resulting temperature of the particle will determine if it will be a source of autoignition for the air-fuel mixture.

Energy balance equation between energy retained in the particle and that transferred to the thermal diffusion layer over the reaction time:

$$Q_{react} = \left(m_{part}\, Cp_{part}\Delta T\right) + \frac{K_{gas}\left(\Delta T + T_0 - T_{gas\_loc}\right)}{L_t} * time_{react}\, SA_{part}$$

[eqn 123]

$$T_{part} = \Delta T + T_0$$

Where; Q_{react} is the energy released by reaction,

m_{part}, Cp_{part}, SA_{part} are the mass of the particle mass, particle specific heat capacity and particle surface area

K_{gas}, T_{gas_loc} are the temperature and thermal conductivity of gas in the region adjacent to the particle surface

$time_{react}$ is the reaction time, L_t is the thermal diffusion length

ΔT, T_0 are the increase in particle temperature and the initial particle temperature

For CO_2 diffusion to the detergent particle we will use the Chilton-Colburn J factor analogy.

266

Mass transport equation (Fick's law of diffusion):

$$j_d = \frac{D\left(\frac{P(CO2)}{R\,T_{gas}} - \frac{K_{equil}}{R\,T_{part}}\right)}{L_{st}}$$
[eqn 124]

Where; L_{st} is the effective thickness of the Peclet layer (characteristic length over which advection and diffusion occur); j_d is the mass diffusion flux (mol/m^2/s), $C_{CO2} = p(CO_2)/RT$; $C_{eq} = p_{eq}/RT_{loc}$ (equilibrium concentration of CO2 close to particle surface boundary) ; D is the mass diffusivity in the gas domain and T_{part} is the temperature at the boundary of the particle surface.

$$Q_{react} = j_d \; SA_{part} \; time_{react} \; h_{react}$$
[eqn 125]

$$time_{react} = mols_{init}/(j_d \, SA_{part})$$
[eqn 126]

As suggested by the formulation, each timestep will have an initial temperature. Residual internal energy remaining from the previous time-steps is transferred to the convective environment before and after the reaction. For this reason, the scheme will switch between the equilibrium temperature calculation and a purely convective heat transfer scheme. The equilibrium temperature calculation assumes an instantaneous reaction that creates heat, because the time step is so small during this event we can assume the surrounding gaseous environment is static and infinite in size, and so the

initial heat transfer is just that permitted by the gaseous diffusivity. However, over the whole engine cycle, convective heat transfer will play a role, and thus the instantaneous heat transfer coefficients for the gas domain calculated by the GT combustion model will be used during the non-reacting phases. The convective calculation will be activated until the reaction initiates and from the point the reaction terminates. The temperature change due to convection is calculated for the time step by using the particle equilibrium temperature, instantaneous htc and gas temperature to calculate the total heat extracted from the particle. The resulting particle temperature will be calculated using the specific heat capacity and will form the initial particle temperature for the following time-step.

It should also be noted the reaction will terminate once all the available CaO mass has reacted with CO_2. We can use the calculated mass diffusion flux value to calculate the mass of CaO consumed for each time-step. Because the mass diffusion flux of CO2 is known (j_D), based on the size of the Ca particle it is possible to calculate the time required for the whole particle to react with the CO_2. As the whole reaction consists of single mole species, the reaction duration can be directly based on the number of CO_2 moles that diffuse. The duration of the reaction is important because it determines the time steps during which the particle will maintain an elevated temperature due to reaction heat. Because the size of Ca based particles in engine oil are most likely variable and cannot be established with a reasonable level of confidence, the sensitivity to particle size will be investigated in this study.

268

L_{st} can be estimated by dividing the particle volume by the surface area (assuming it is spherical), and the diffusivity is approximated by dividing the thermal conductivity of gas by the specific heat capacity (volumetric).

From initial testing and calculations, the time required for most particles to react is about 3 orders of magnitude less than the time for 1deg CA, this is also substantiated by the Arrhenius calculation performed in the previous chapter. It was deemed sensible to assume the heat from reaction is available instantaneously within a single time step, rather than solving` for smaller time scales which capture the flux rate, but the higher accuracy of such a small portion of the overall simulation adds virtually no value to the overall result.

Because heat released by a reaction is transferred by electromagnetic radiation it is difficult to establish how much of the energy is reflected from the particle and how much is absorbed/transmitted from the point of reaction being the particle surface. It is a reasonable approximation to assume 50% of the heat enters the particle and the remainder is gaseous domain, as the reaction heat will most likely emit in a spherical manner from the reaction point. We will be assessing two scenarios; the first case is one that assumed 50% of the reaction heat is transferred to the particle and the remainder to the gaseous environment, the second case will assess a particle that must first evaporate all the hydrocarbons surrounding it before it can be exposed to the

269

gaseous environment. The 50% heat being transferred directly to the gas is important too and this will be assessed in the next chapter. This chapter is looking at a heated particle, that may not ignite in the location where the reaction takes place, as it could be surrounded by CO2. The hot particle may need to move to another location by turbulence before it causes an ignition.

As the temperature of the particle increases the equilibrium constant reduces, and the reaction will be deactivated once the equilibrium constant is less than $1/P(CO_2)$. For this reason the temperature at which the equilibrium constant is equal to $1/P(CO_2)$ will be the maximum temperature that can be achieved due to reaction heat, for a given time step. For this reason the equilibrium constant was calculated for a range of temperatures, for each time step the temperature associated with an equilibrium constant equal to $1/P(CO_2)$ will be obtained using an interpolated look-up table, the particle temperature will then be truncated at this temperature.

The first calculation initiates a particle temperature of 1200K from the beginning of the intake stroke, the particle cools due to convective heat transfer. Once the reaction occurs, 50% of the reaction heat will be instantaneously transferred to the particle and the heated particle will transfer heat to the gaseous thermal diffusion layer throughout the time-step, the thermal energy remaining in the particle at the end of the time-step will be used to calculate the particle temperature. Once the particle heats up to the equilibrium temperature threshold and the reaction is deactivated, the particle
270

will only need to cool a marginal amount (and increase the equilibrium constant) to activate the reaction again. This mild fluctuation will continue until all the CaO mass has been consumed. The mean temperature will be the equilibrium temperature. The equilibrium temperature is the temperature corresponding the $Keq(T)$, when $1/P(CO2) = Keq$ for $P(CO2)$ at that given instant in time. The calculation assumes the heat is distributed uniformly in the particle, which is acceptable given that the particles are very small in size (low thermal capacitance). When calculating the heat transferred to the thermal diffusion layer during the reaction, it was assumed the particle was constantly at its upper heated temperature throughout the reaction phase, although in reality it will cool as it loses heat. This assumption was deemed acceptable because of the very short duration required for the entire particle to react, meaning the timesteps would need to be extremely small in order to capture the temperature decay during the reaction itself and would impact the thermodynamic calculation very little.

As we are assuming 50% of the heat is transferred to the particle, the remaining must be transferred to the gaseous domain. The temperature differential between the gas region adjacent to the particle and the gas domain far away can be calculated from the heat transfer rate over the reaction time. This means that we can use the following equation to calculate T_{gas_loc} for the formulation above. So, the calculation now accounts for the local gas heating due to the reaction heat being directed to the gas domain and the heat transfer from the particle to the gas domain local to its surface.

In this calculation we are assuming the heat released directly into the gas from reaction and the heat transferred from the particle to the immediate gas is within the same diffusion length. Only difference being that the temperature local to the particle is the maximum temperature created by the temperature differential required to transport the heat of reaction directly into the gas.

So, the reaction energy is provided instantaneously. The particle stores 50% of it in the particle and 50% is transferred across the diffusion layer. Simultaneously (as the reaction to consume all the mass proceeds) the particle is trying to transfer heat to the gas adjacent to it. The temperature difference between the particle and the gas will be the temperature of the particle at that instant and the maximum of the temperature difference between the adjacent gas and the gas far away that was previously required to transfer the 50% of energy that went to the diffusion layer. Depending on whether the particle is hotter or local gas is hotter this could heat or cool the particle. Both the heat transfer to diffusive layer due to reaction (EM waves - photons) and that transferred from the particle to the surrounding from its heat capacity takes place over the same peclet thickness. Only difference is that reaction temp gradient assumes the temp of the gas far away to be the local temp, and the heat transfer from particle assumes the higher temp required of the gradient for EM heat transfer to be the local temp. Once the reaction occurs the calculated particle temperature will be limited to a maximum of the equilibrium temperature at that instant. The impact of the reaction energy will

272

depend on the difference between the particle temperature and the equilibrium temperature. Because the reaction will be initiated when the particle is at the equilibrium temperature, this difference in temperature between the equilibrium temperature and particle temperature will only be large if the mass diffusivity is much lower than the thermal diffusivity i.e. if the particle cools much faster than CO2 molecules can reach it, and once they do reach the particle a large heat is released instantaneously allowing the particle to reach the equilibrium temperature. However, it does need to be included for completeness and will play a larger role in the latter part of this study.

$$T_{gas\_loc} = \frac{Q_{react}\, L_t}{K_{gas}\, time_{react}\, SA_{part}} + T_{gas} \quad \text{[eqn 127]}$$

T_{gas} is the global average gas temperature

The script that was used for the simulation can be found in Appendix II.

8.4.5. Detergent reaction with Heat release Results and Discussion
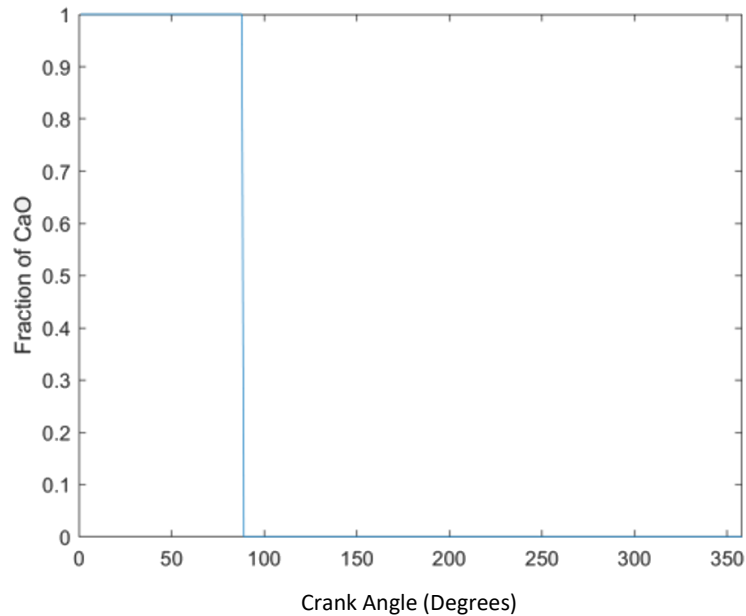
(a)
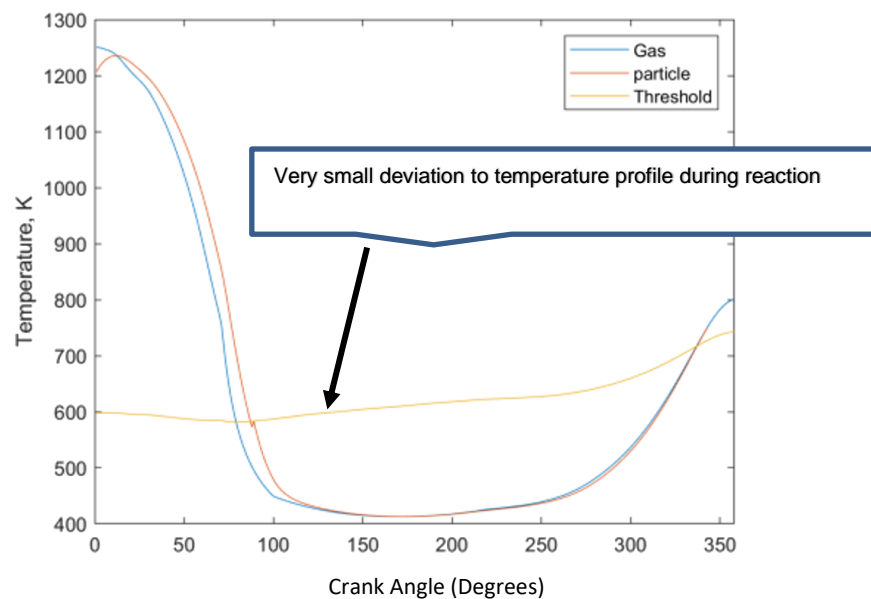
(b)

Figure 56 – Temperature of Calcium based particle during intake and compression strokes, accounting for reaction heat and convective heat transfer, particle radius = 1e-09m, 10% burned residuals (a) CaO mass fraction (b) Particle, gas and threshold temperature
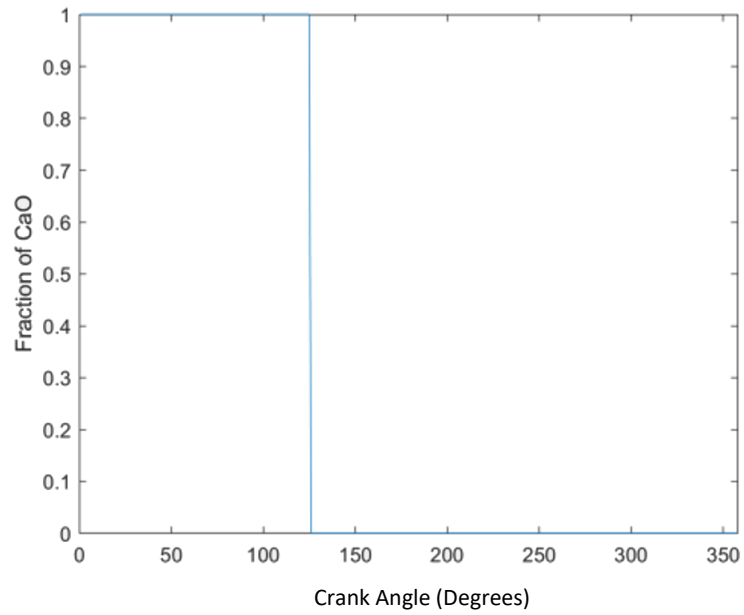
(a)
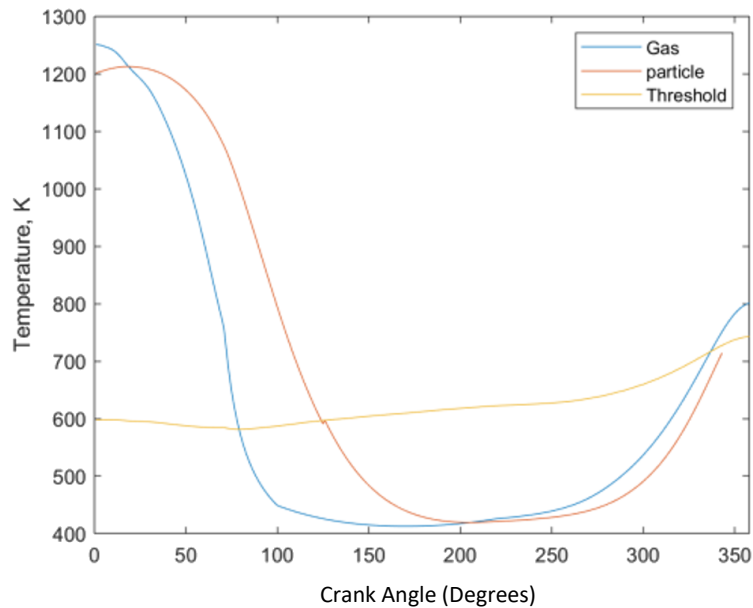
(b)

Figure 57– Temperature of Calcium based particle during intake and compression strokes, accounting for reaction heat and convective heat transfer, particle radius = 6e-09m, 10% burned residuals (a) CaO mass fraction (b) Particle, gas and threshold temperature
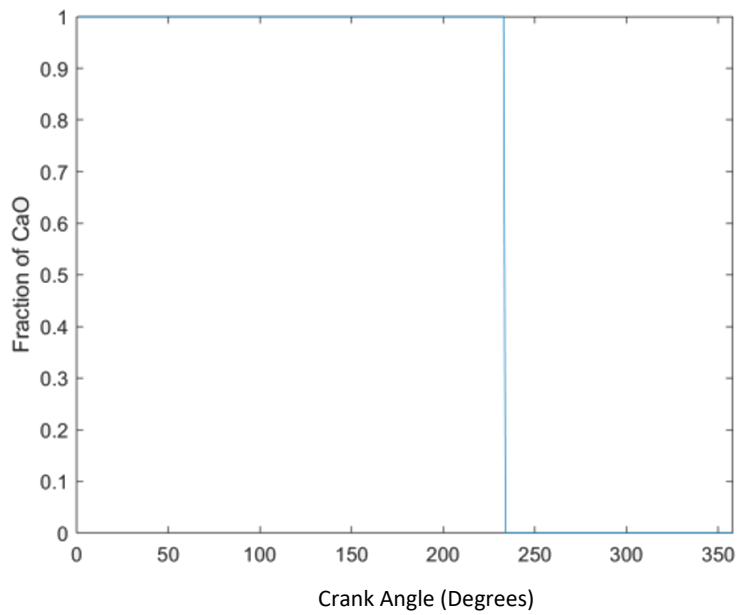
(a)
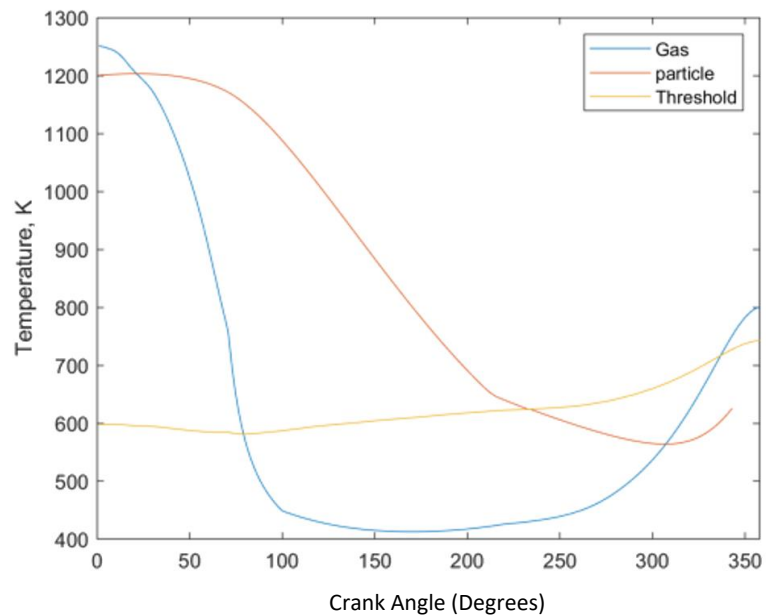
(b)

Figure 58– Temperature of Calcium based particle during intake and compression strokes, accounting for reaction heat and convective heat transfer, particle radius = 3e-08m, 10% burned residuals (a) CaO mass fraction (b) Particle, gas and threshold temperature
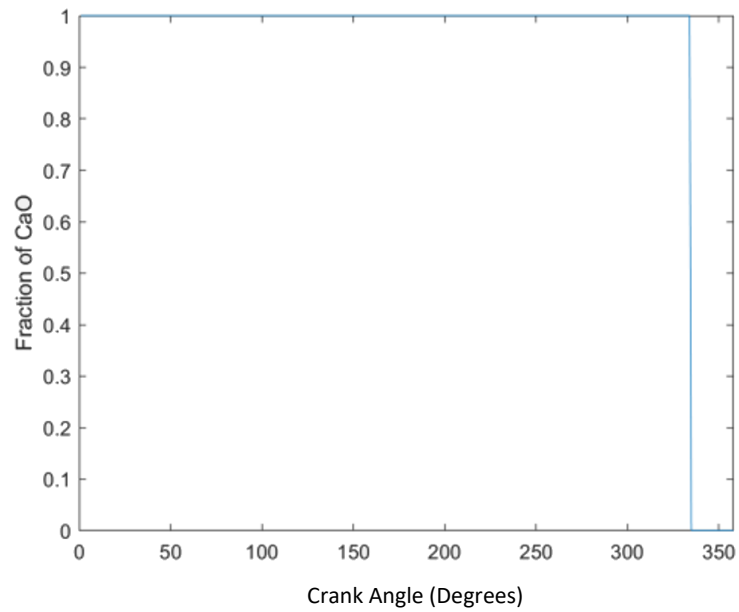
(a)
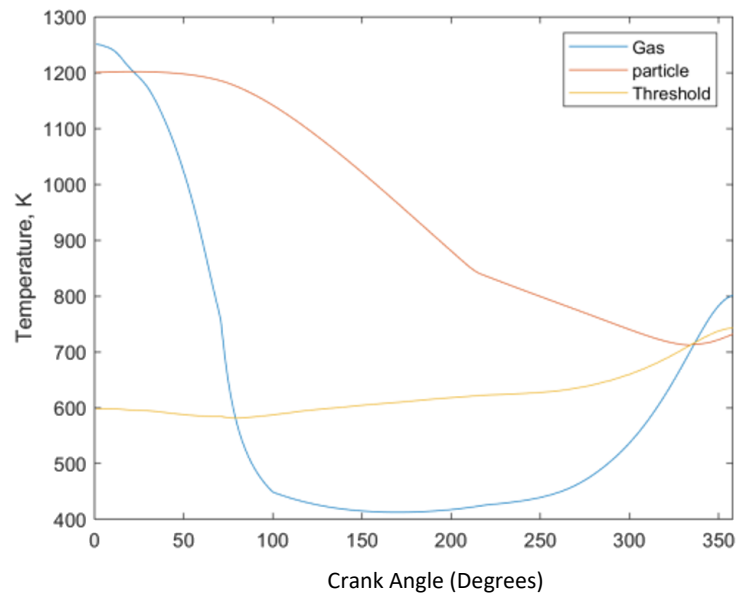
(b)

Figure 59– Temperature of Calcium based particle during intake and compression strokes, accounting for reaction heat and convective heat transfer, particle radius = 6e-08m, 10% burned residuals (a) CaO mass fraction (b) Particle, gas and threshold temperature
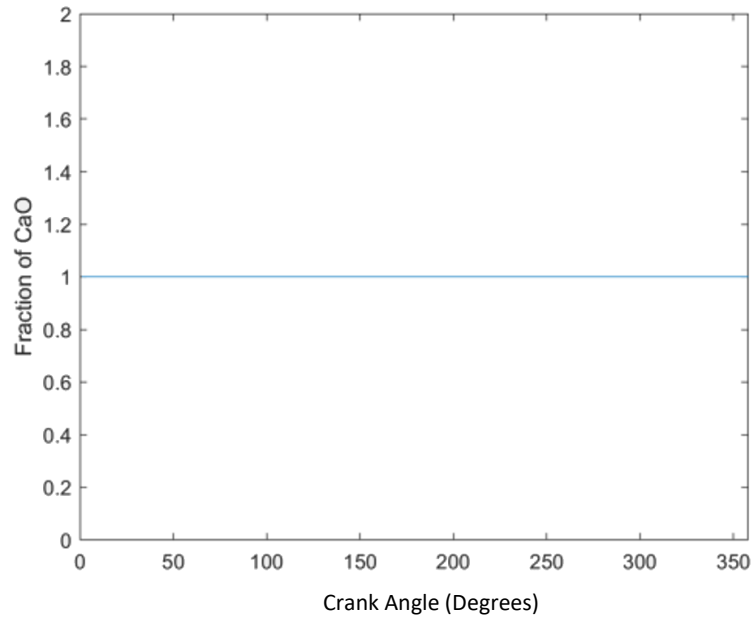
(a)
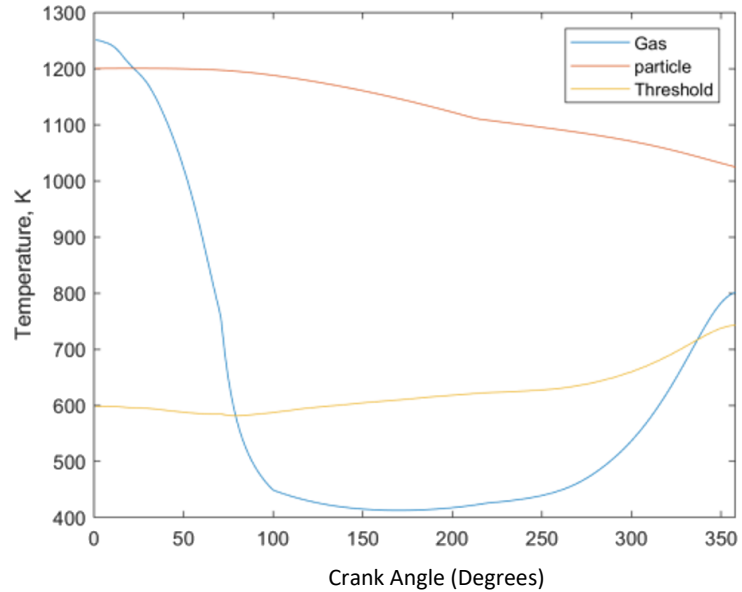
(b)

Figure 60– Temperature of Calcium based particle during intake and compression strokes, accounting for reaction heat and convective heat transfer, particle radius = 3e-07m, 10% burned residuals (a) CaO mass fraction (b) Particle, gas and threshold temperature
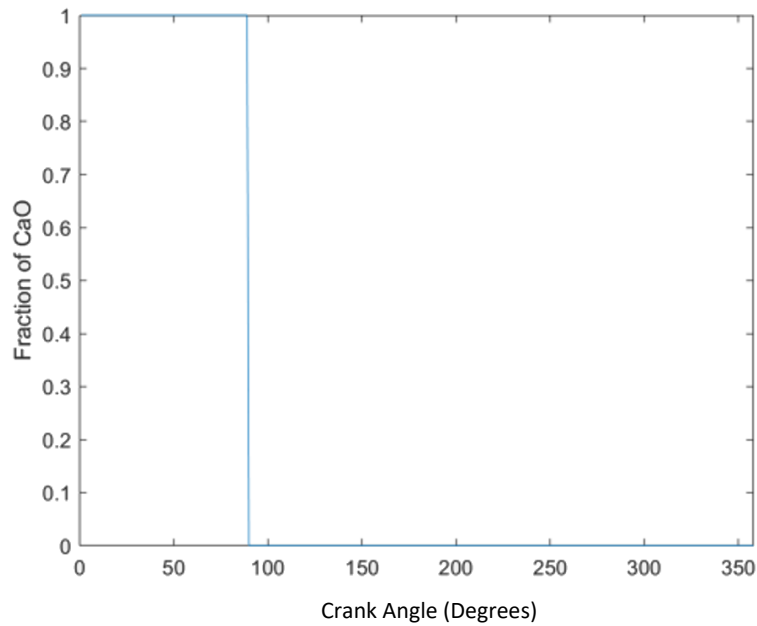
(a)
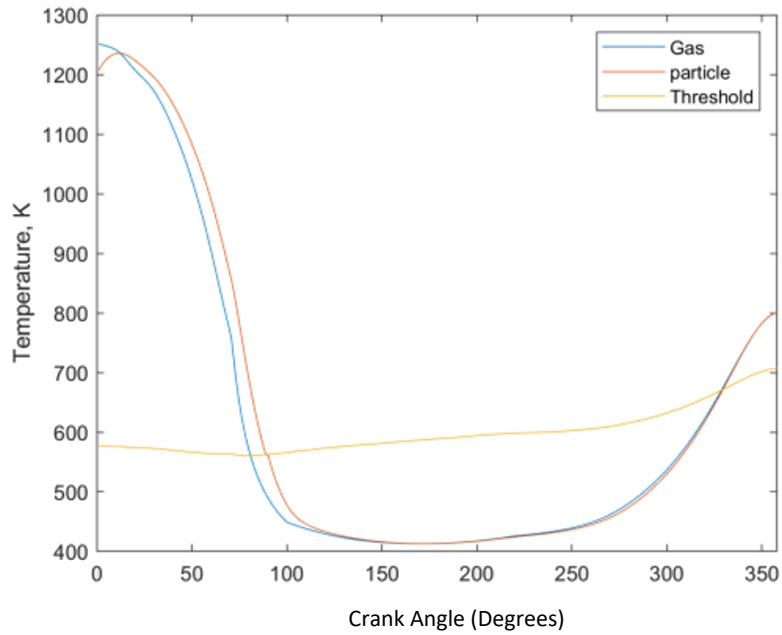
(b)

Figure 61– Temperature of Calcium based particle during intake and compression strokes, accounting for reaction heat and convective heat transfer, particle radius = 1e-09m, 5% burned residuals (a) CaO mass fraction (b) Particle, gas and threshold temperature

279
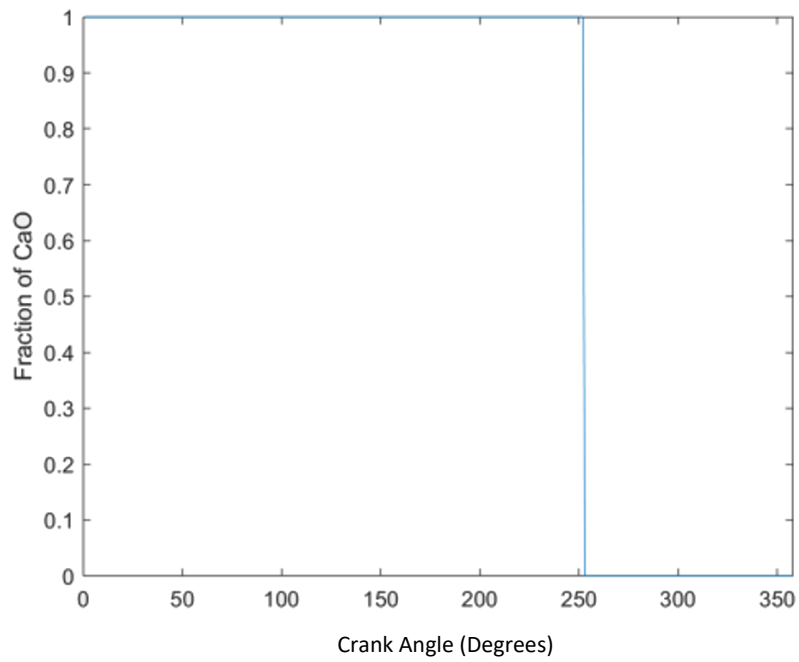
(a)
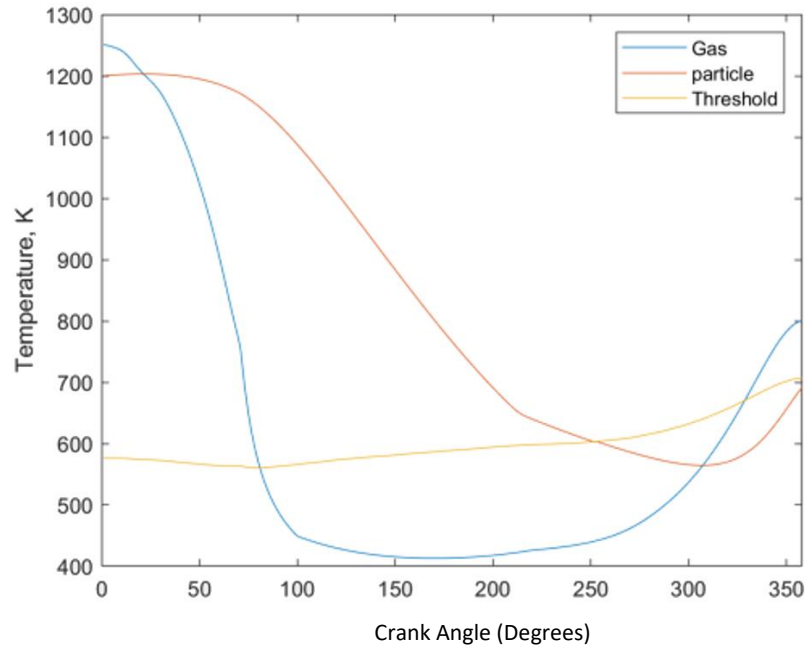
(b)

Figure 62 – Temperature of Calcium based particle during intake and compression strokes, accounting for reaction heat and convective heat transfer, particle radius = 3e-08m, 5% burned residuals (a) CaO mass fraction (b) Particle, gas and threshold temperature
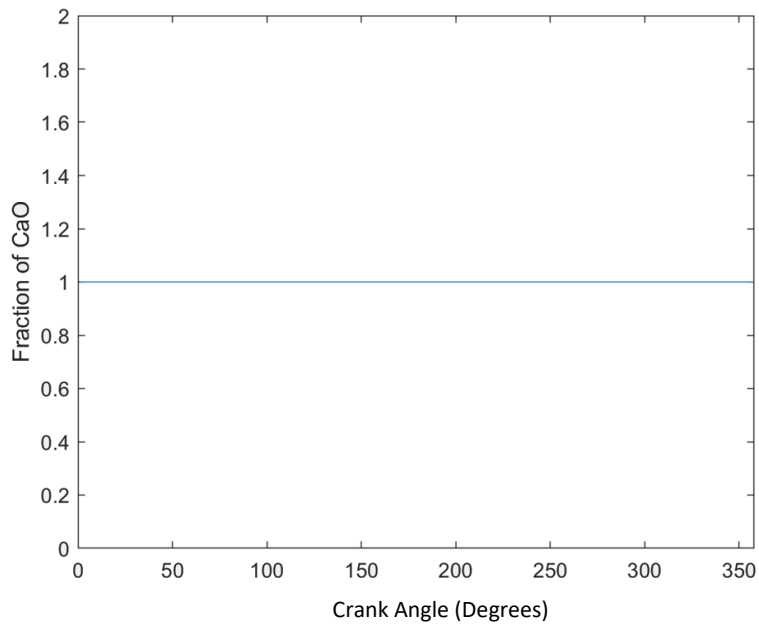
(a)
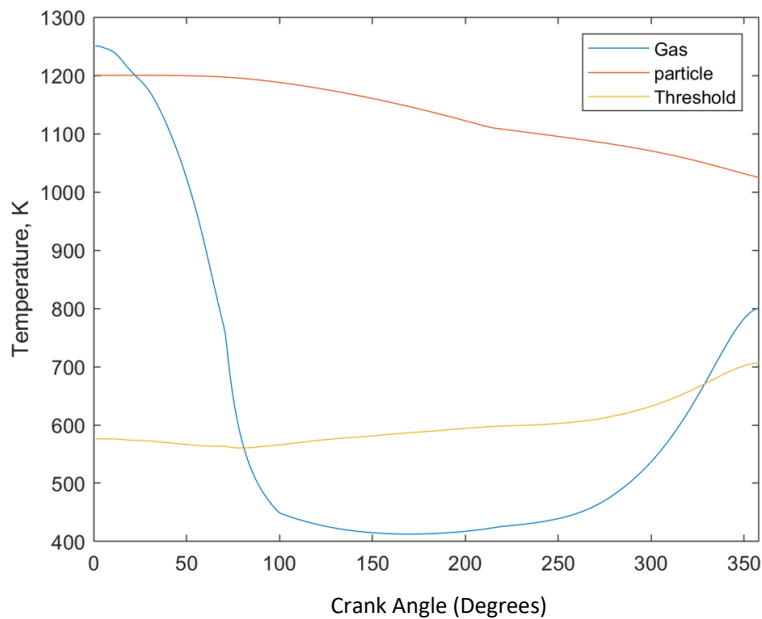
(b)

*Figure 63 – Temperature of Calcium based particle during intake and compression strokes, accounting for reaction heat and convective heat transfer, particle radius = 3e-07m, 5% burned residuals (a) CaO mass fraction (b) Particle, gas and threshold temperature*
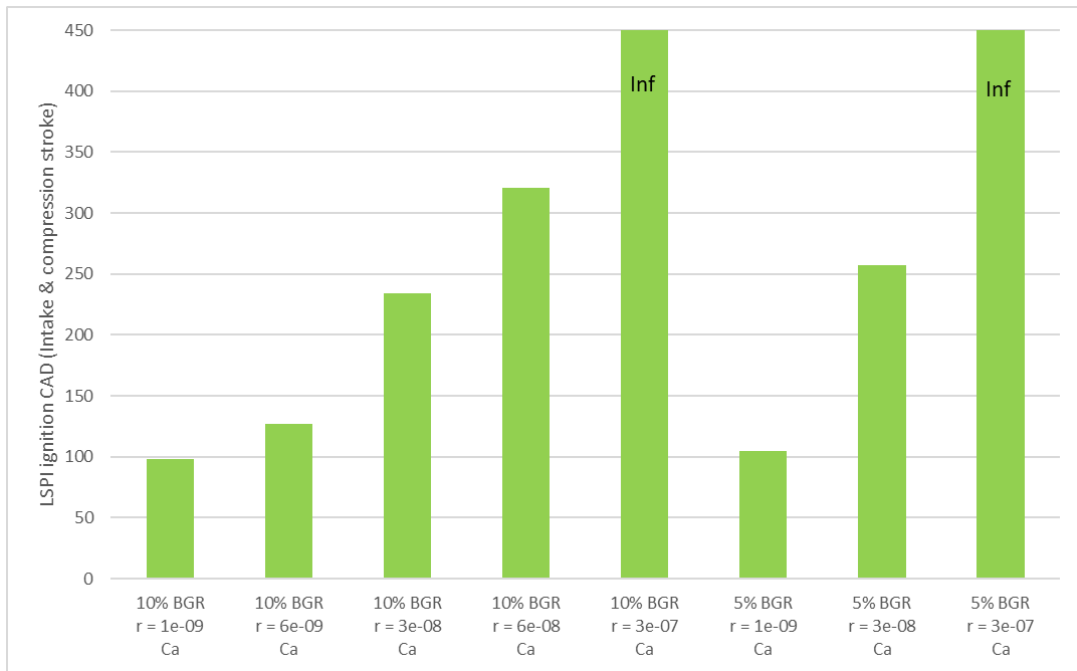
Figure 64– A summary bar chart of all the cases simulated for onset of LSPI including reaction heat release, each case states the percentage burned gas residuals (BGR), the particle diameter, and the type of detergent. Cases that state 'inf' represent an infinite ignition angle i.e., a LSPI event did not occur

The results from the simulation that accounts for heat release due to the reaction of CaO with CO_2 are shown in Figures 56-63, with a summary of all the results of this section demonstrated in Figure 64. Because there will be a range of sizes the detergent particle can exist as, the simulation was repeated for a larger range of different particle sizes that are plausible given the film thickness predicted in section 6.3. Depending on the level of turbulent kinetic energy, the structure of turbulence, the amount of egr/burned gas residuals and combustion chamber geometry there will be a period of time required for the burned residuals to become homogeneously mixed with the rest of charge. For this reason, the local partial pressure assumed during the simulation was varied.

282

The timesteps during which CaO mass fraction is reducing, provide an indication of when the reaction is taking place. Because the temperature always increases to the maximum of equilibrium temperature during reaction, a complementary indication is when the particle temperature is equal to the equilibrium temperature.

In each case it was assumed the initial temperature of the particle after the exhaust stroke was 1200K, and the Woschni heat transfer coefficient and gas temperature during the intake and compression strokes was that predicted by the GT combustion model.

It can be seen that irrespective of particle size the reaction is complete for the whole particle within 1 timestep, as the molar fraction of CaO reduced from 1 to zero in a single timestep. Because it is assumed the particle is always in chemical equilibrium, the reaction is assumed to be instantaneous. This is a reasonable assumption as it is evident from testing this is a very fast reaction that results in a deflagration. The rate limitation is that of mass diffusion and thermal diffusion. The simulation suggests the mass diffusion of CO_2 towards the particle is very fast. Similarly, the thermal diffusion of heat from the particle is also fast, as slower thermal diffusion would mean the reaction would be deactivated for longer periods of time as the particle would generally be hotter and take longer to cool to a temperature that allows for the reaction

to be activated again, in turn prolonging the period required for the whole particle to react.

When analysing the cases for 10% burned gas fraction, it was found that a small particle (1e-09m) cools very quickly and the reaction is complete during the early stage of the intake stroke, achieving a maximum reaction temperature of 590K. As the size of the particle is increased, the higher thermal capacitance means the reaction temperature is reached later in the engine cycle. A particle size of 6e-08m allows for the reaction point to take place late in the compression stroke, the point at which one would expect for an ignition event to take place in the case of LSPI, achieving a maximum reaction temperature of 700K. When the particle size was increased to 3e-07m it was found the thermal capacitance was so high that that the particle did not cool down to the reaction temperature throughout the intake and compression strokes but did maintain a high temperature throughout because of the residual energy retained in particle. The reaction is so fast that the impact of the reaction temperature has very little impact on the temperature profile; the achieved temperature trajectory is very similar to that which would have been achieved purely from convection. Because of this, although there is a difference in the chemical behaviour, the temperature trend between Ca and Mg based detergents is very similar, because the thermodynamics are dominated by convection and both particles have similar specific heat capacities. There is reason to believe that some particles will be large and thus have sufficient thermal capacitance to cause an autoignition, because of

284

the large amount of thermal energy stored in the particle. However, this is a mechanism that has a very low probability as it has been established from literature that when only a Mg based detergent is used the number of LSPI events reduce dramatically. Also, because the size of the particle is large and unrealistic when compared to the hydrodynamic film expected on the liner.

As the percentage burned gas residuals are increased the concentration within the vicinity of the particle increases at a greater rate through the cycle. This means the local CO_2 concentration exceeds the equilibrium condition earlier in the cycle. The higher partial pressure of CO_2 also allows for higher equilibrium temperatures. Despite the higher equilibrium temperature, it appears at this stage the inhomogeneity of the charge mixture resulting in higher local CO2 concentration is not always assisting in explaining LSPI, as it seems to advance the pre-ignition point because the concentration builds up faster and reaches a level that causes chemical instability earlier in the cycle. In order to get LSPI at the correct timing, an optimal particle size and concentration of burned gas residuals must be achieved. However, what has been neglected is that the local gas temperature will also be hotter with an increased concentration of the hot burned residual gas. The nominal intake manifold temperature is known as well as the exhaust temperature before the intake valve opening. The following equation can be used to calculate a correction factor (CorT) than can be multiplied to the gas temperature predicted by the GT combustion model.

285

$$T_{gas,comp,5\%} = T_{ef}(0.05) + T_{in}(0.95) \quad \text{[eqn 128]}$$

$$T_{gas,corr} = T_{ef}(mfegr) + T_{in}(1 - mfegr) \quad \text{[eqn 129]}$$

$$CorT = \frac{T_{gas,corr}}{T_{gas,comp,5\%}} \quad \text{[eqn 130]}$$

Where; $T_{gas,comp,5\%}$ is the baseline temperature of the gas during the beginning of the compression stroke with 5% burned gas residuals, T_{ef} is the temperature of the exhaust gas before the IVO event, T_{in} is the nominal intake manifold temperature, ΔT is the temperature offset relative to the 5% residuals case, and $mfCO2$ is the mass fraction of egr.
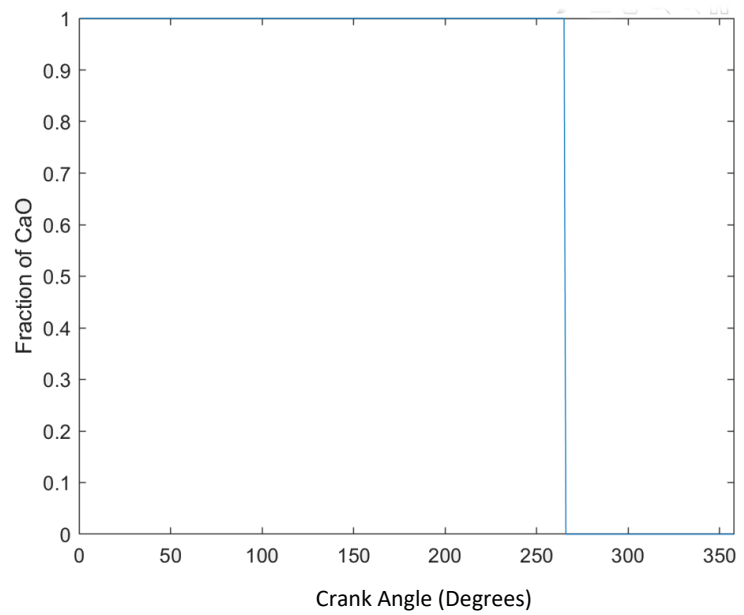
(a)
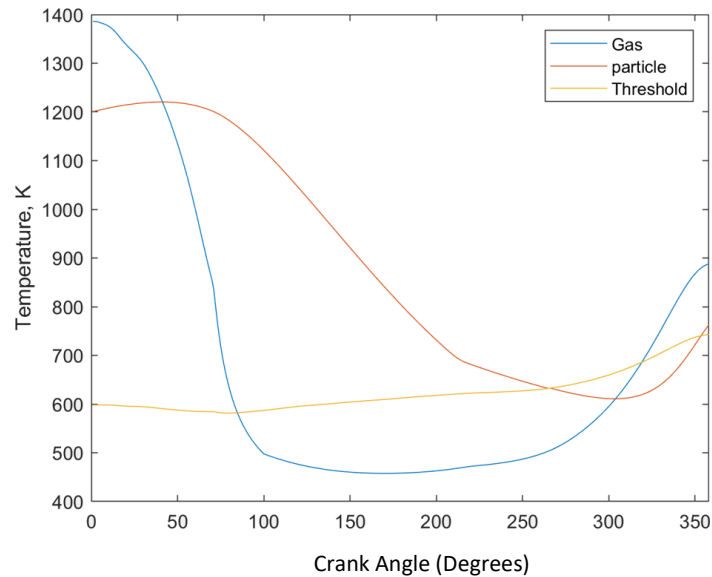
(b)

Figure 65 – Temperature of Calcium based particle corrected for burned residual gas fraction, during intake and compression strokes, accounting for reaction heat and convective heat transfer, particle radius = 3e-08m, 10% burned residuals (a) CaO mass fraction (b) Particle, gas and threshold temperature
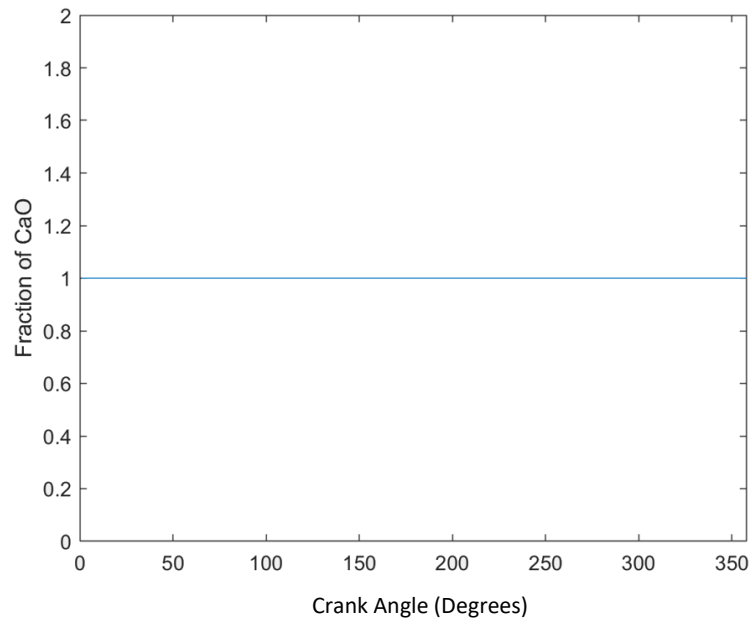
(a)
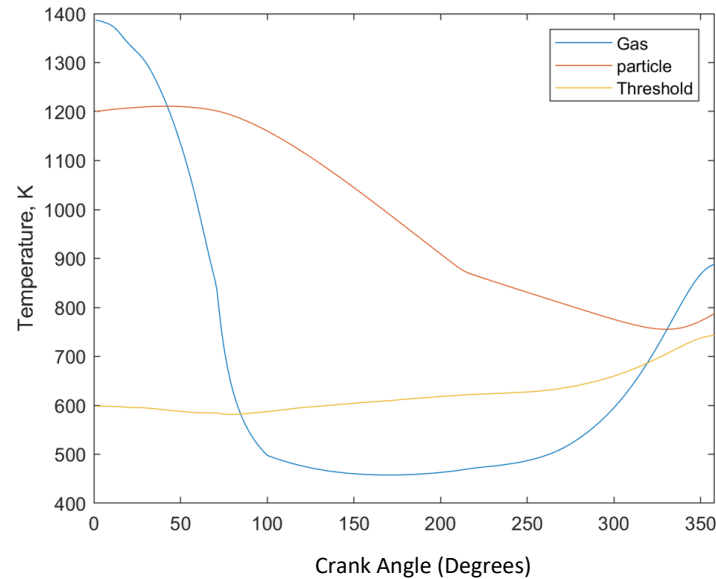
(b)

Figure 66– Temperature of Calcium based particle corrected for burned residual gas fraction, during intake and compression strokes, accounting for reaction heat and convective heat transfer, particle radius = 6e-08m, 10% burned residuals (a) CaO mass fraction (b) Particle, gas and threshold temperature

288

Figure 65 shows the case with 10% burned gas residuals, a particle size of 3e-08m, with the corrected gas temperature, it shows the temperature correction does retard the pre-ignition point closet to the spark ignition timing but because the particle is already hot and the reaction time is short the impact on the temperature profile relative to the trajectory just due to convection is minimal, achieving a maximum temperature of 657K during the reaction. In the case of 10% burned gas residuals and a particle size of 6e-08m the reaction no longer takes place, as the particle retains a higher temperature due to the corrected gas temperature.

As suggested, the difficulty in explaining the mechanisms leading up to LSPI seem to be that the reaction is so fast that it does not impact the temperature profile significantly, this is compounded by the limitation of equilibrium temperature. Although it is plausible the local temperature of gas will be a mass averaged temperature of the burned gas residuals and fresh charge air, it could also be argued that the relatively large mass of fresh air will be able to cool the burned residual gas at a rate faster than the mass diffusion rate. This means that there could be moments and regions where the local concentration of CO_2 is high, yet the temperature is close to the mean gas temperature. The increased difference between the gas temperature and equilibrium temperature that this proposition allows will be important in the following suggested mechanism.

289

For the particle to experience a rapid change in temperature at a time that is close to the spark timing, the particle would need to be in its CaO state and protected from CO2 for the majority of the compression stroke and suddenly be exposed to the gaseous environment close to the spark ignition point. In the earlier study, when the evaporation of a Hexadecane droplet was predicted using the Clausius-Clapeyron equation it was noticed the droplet spends most of its time in a slow-evaporation regime and suddenly fully vaporises late in the compression stroke. This assumes the droplet is suspended in the combustion volume throughout the stroke, in reality many droplets will be contained in the cooler crevice volume or attached to the liner and then introduced to the main volume as the piston decelerates towards tdc, this will shift the point of full vaporisation to even closer to the spark timing. Because most of the oil film remaining on the liner wall following the intake stroke will be fresh and 'unburned', the Ca based particles will be in their original state. The state of the detergent in its additive form will consist of $CaCO_3$, $Ca(OH)_2$ and crucially CaO. So, it is plausible that the CaO is protected by the hydrocarbons in the oil for most of the compression stroke until exposing it to CO_2 in the gas domain when the hydrocarbons evaporate. Another possible path involves the thermal decomposition of Calcium hydroxide; $Ca(OH)_2 => CaO + H_2O$, the CaO can then react with the CO_2. However, this reaction path is more of a possibility in engines with high compression ratios as the decomposition temperature range begins at 793K (according to Aspen analysis).

The simulation was modified to expose the Ca detergent to the gas domain late in the compression stroke, with an initial temperature equal to the gas temperature assuming it is in the CaO form. This is sensible because it will be surrounded with hydrocarbon molecules up until the point of vapourisation, and the hydrocarbons will be at a temperature close to the gas temperature. The particle will cool slightly as the liquid phase fully vapourises but this is likely to be a very small effect.

The plots below show the same point of full vapourisation but the equilibrium temperature line is different for different levels of residuals.
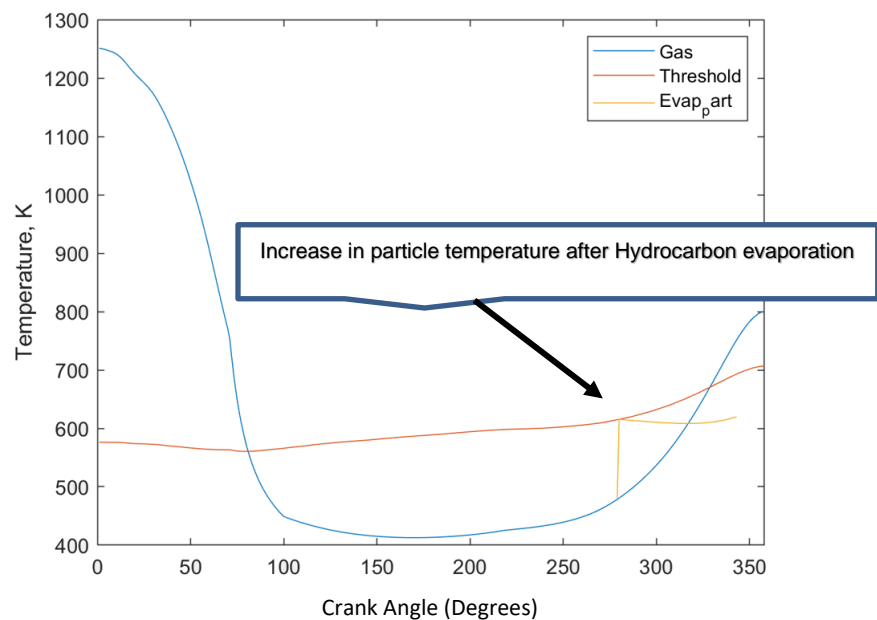
Figure 67– Temperature of Calcium based particle (Evap part) during intake and compression strokes, accounting for reaction heat and convective heat transfer, particle radius = 6e-08m, 5% burned residuals. Plot shows a particle that is only exposed to the cylinder gas once all HC's have evaporated
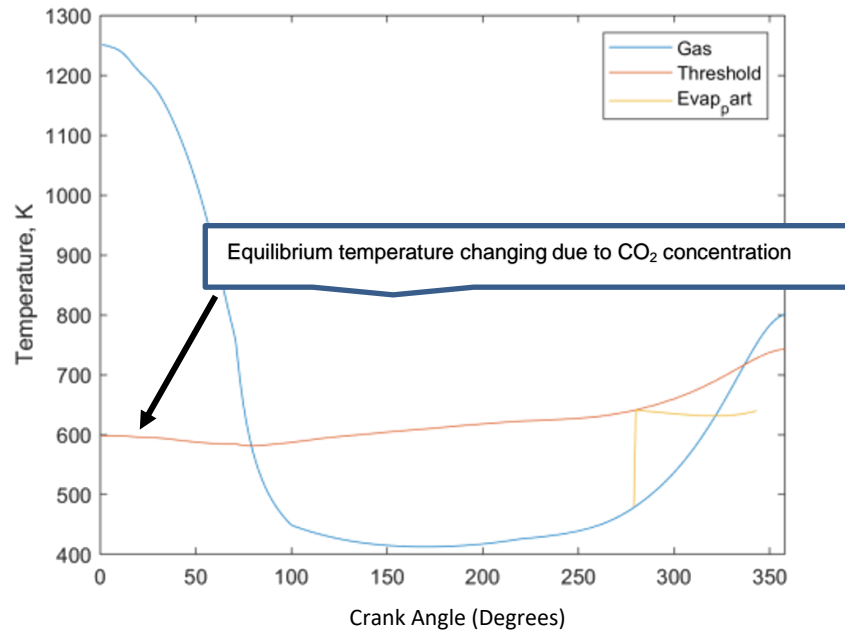
Figure 68– Temperature of Calcium based particle (Evap part) during intake and compression strokes, accounting for reaction heat and convective heat transfer, particle radius = 6e-08m, 10% burned residuals. Plot shows a particle that is only exposed to the cylinder gas once all HC's have evaporated
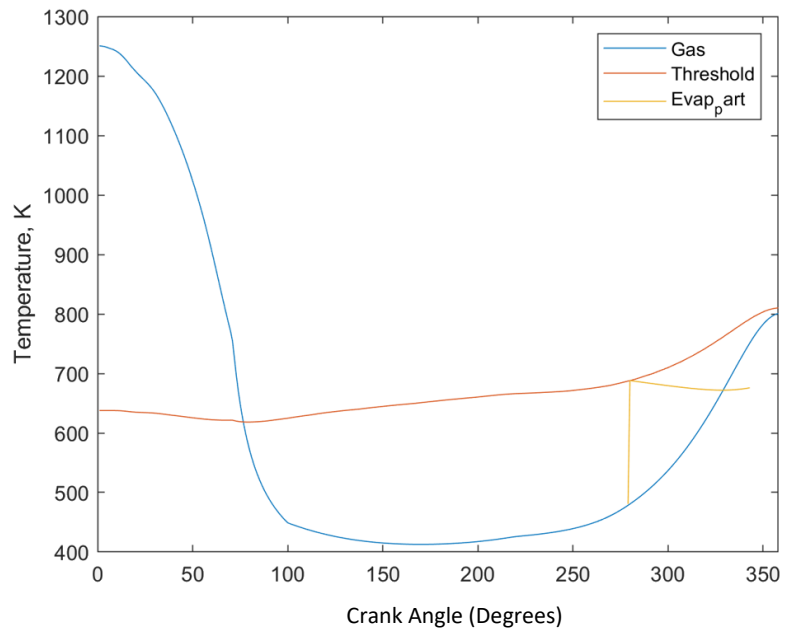
Figure 69– Temperature of Calcium based particle (Evap part) during intake and compression strokes, accounting for reaction heat and convective heat transfer, particle radius = 6e-08m, 30% burned residuals. Plot shows a particle that is only exposed to the cylinder gas once all HC's have evaporated

292

Figures 67-69 show the previously mentioned scenario with varying levels of CO_2 concentration. The difference in burned residuals is reflected in the threshold temperature curves, the higher the CO_2 concentration the higher the permitted temperature. It can now be observed that there is a sudden increase in the temperature of the particle once all the hydrocarbon-based components vapourise close to TDC. The concentration in the vicinity of the particle has a large impact on the maximum temperature reached during reaction.

This is a far more plausible explanation for LSPI, as the reaction occurs suddenly, and close to the spark timing, it also explains how LSPI could occur with particles of all sizes as the dependence of convective heat transfer on the particle size becomes redundant. The proposed mechanism for LSPI is illustrated in Figure 70.

Lubricant sprayed on to cylinder liner during exhaust stroke

↓

Oil scraped downwards during intake stroke

↓

Oil remaining on cylinder is hydrodynamic film of ring-liner contact

↓

Oil is scraped from liner into crevice volume during compression stroke

↓

Oil parcels escape from the crevice volume into the combustion chamber as piston decelerates towards TdC

↓

Hydrocarbon component of lubricant evaporates

↓

Exposed Ca detergent reacts with residual CO2

↓

Heat release

Figure 70- Schematic showing proposed mechanism for LSPI due to detergent reaction

8.4.6. CFD model of a pre-heated particle inside a fuel-air mixture

A Converge model (Convergent Science CFD) of a reaction chamber was developed consisting of a stoichiometric mixture of IsoOctane and air, the temperature of the gas domain was 600K and pressure was 25bar. The temperature of the gas domain is slightly lower than the usual 700K because the previous study confirmed the reaction would need to take place earlier (when the gas temperature is lower) in order to significantly impact the gas temperature. Although, the gas temperature and concentration will be lower

294

earlier in the compression stroke, the local CO2 concentration will be lower and less uniform (allowing for high levels of O2 in local spaces). Although the previous simulation confirms once the particle has been heated at the latter stage of the compression stroke, it tends to retain a high temperature as the gas temperature is rising, in this CFD simulation we allow the particle to retain the specified temperature for an extended time, just so a fully developed deflagration can be illustrated. The investigation is still valid, as the time window corresponding to the approximately 50deg CA period approaching TdC of the compression stroke for which the particle temperature is elevated based on the previous simulation is visible and ultimately what conclusions will be based on.

A low temperature combustion reaction mechanism file for Iso-Octane was provided by Convergent Science, a file that was developed by Dalian University. The initial decomposition reactions and corresponding Arrhenius reaction parameters can be seen in Table 13 [21] (reaction mechanism file provided by Convergent Science). The mechanism proceeds to include other small chain, radical branching and termination reactions.

Reactions											A cm^3/(mol s)	B	C cal/mol
IC8H18	+	O2	=	C8H17	+	HO2					6.00E+15	0	46000
		REV									1.00E+12	0	0
C8H17	+	O2	=	C8H17O2							1.00E+12	0	0
		REV									2.51E+13	0	27400
		C8H17O2	=	C8H16OOH							1.51E+11	0	21800
		REV									1.00E+11	0	11000
C8H16OOH	+	O2	=	O2C8H16OOH							1.16E+11	0	0
		REV									2.51E+13	0	27400
		O2C8H16OOH	=>	C8KET	+	OH					8.91E+10	0	17000
		C8KET	=>	C6H13CO	+		CH2O	+	OH		3.98E+15	0	43000
C6H13CO	+	O2	=>	C3H7	+	C3H5	+	CO	+	HO2	3.16E+13	0	10000
IC8H18	+	OH	=>	C8H17	+	H2O					2.00E+13	0	3000
C8H17	+	O2	=	C8H16	+	HO2					3.16E+11	0	6000
		REV									3.16E+11	0	19500
C8H16	+	O2	=>	C3H7	+	C3H6	+	CH2O	+	HCO	3.16E+13	0	10000
IC8H18	+	HO2	=>	C8H17	+	H2O2					1.00E+13	0	16950
		C8H17	=>	C3H7	+	C3H6	+	C2H4			1.12E+17	-1.27	29700

Table 13– Reactions for IsoOctane and corresponding Arrhenius parameters [21]

Figures 71 and 72-73 show the results of the Converge simulation assuming a particle temperature of 700K and 800K respectively. It is evident that an autoignition event does take place with an 800K particle temperature and not with 700K, providing further support for the chemical equilibrium theory arrived at previously. A very small heat release was observed after 0.001s (9CA degs) in the case of a 800K particle temperature. The reaction front is a very slow deflagration, but it should be remembered this is only simulating a single particle, in an engine several of these occurrences may take place within a small timeframe. It should be noted at this stage, the assumption is that of a $CaCO_3$ particle, post reaction.
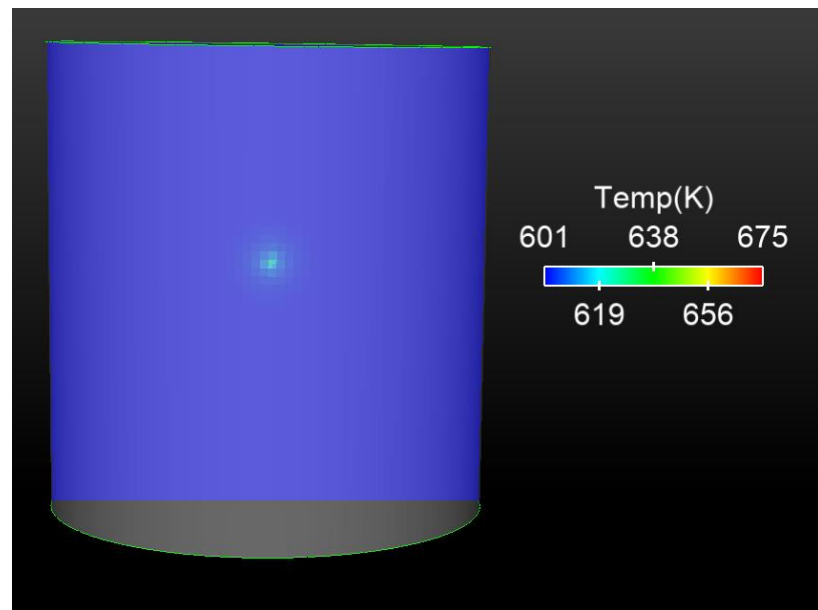
Figure 71 - Reactor simulation showing temperature contour after 0.1s: particle temperature is 700K, diameter of particle is 1e-07m, air is of standard composition, stoichiometric mix of Iso-Octane and air, gas temperature is 600K, gas pressure is 25bar
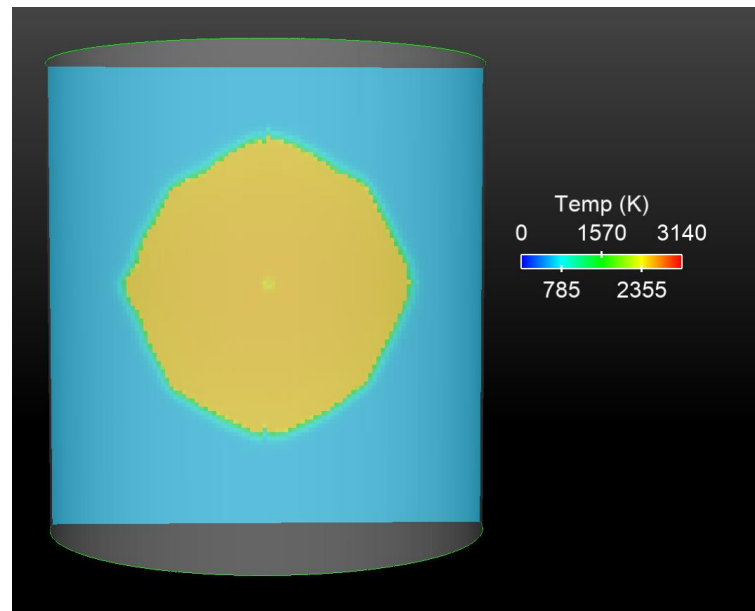
Figure 72- Reactor simulation showing temperature contour after 0.085s: particle temperature is 800K, diameter of particle is 1e-07m, air is of standard composition, stoichiometric mix of Iso-Octane and air, gas temperature is 600K, gas pressure is 25bar

297
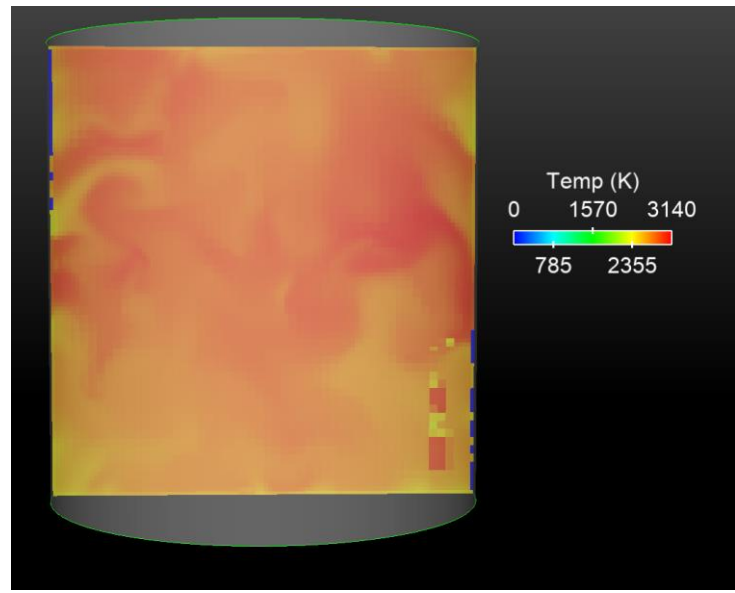
Figure 73- Reactor simulation showing temperature contour after 0.1s: particle temperature is 800K, diameter of particle is 1e-07m, air is of standard composition, stoichiometric mix of Iso-Octane and air, gas temperature is 600K, gas pressure is 25bar

For the sake of understanding of variable sensitivity, the simulation was repeated at a higher pressure, the results can be seen in Figure 74.
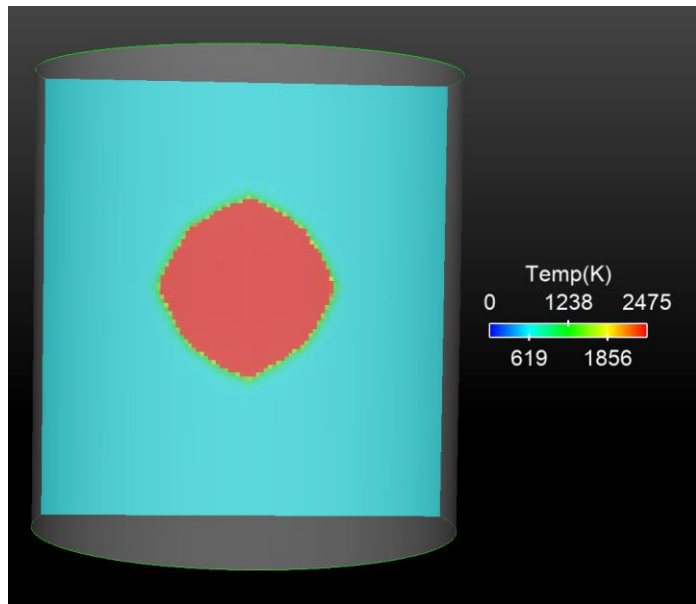
Figure 74- Reactor simulation showing temperature contour after 0.1s: particle temperature is 800K, diameter of particle is 1e-07m, air is of standard composition, stoichiometric mix of Iso-Octane and air, gas temperature is 600K, gas pressure is 100bar

At high pressure, the density/mass of fuel-air mixture is higher meaning higher thermal capacitance, more mass to heat suggests lower gas temperatures and thus slower flame propagation. Obviously, this is the time taken for it to propagate through this large volume, in reality the volume will be smaller as the piston moves and our interest will only be with regards to a very local heat transfer. There is also a lot more total mass as normally the engine will be at the simulated pressure and temperature, but the volume will be much lower, so the time taken for all the fuel to be consumed will be a lot lower. The environment is convective so residence time of the fluid at the particle boundary will need to be sufficient in order to reach ignition temperature otherwise the particle will need to heat the majority of the fluid considerably before it will ignite. The gas temperature will impact the propagation speed as

299

for a cooler gas it will take longer for the gas to get up to ignition temperature (this could be another cause for the late ignition), but it will not impact the maximum local temperature, at its maximum temperature can only be at thermal equilibrium with the particle (time permitting). From this investigation we find that in some cases the LSPI event will just result in local convective heating of the unburned gas mixture. Certain cases with high local concentration of CO_2, could cause a high heat release meaning the particle will be at a much higher temperature. Given that it is a very turbulent environment, the hot particle may later move to a location with a higher concentration of Air-fuel, causing an ignition, or if all the CO_2 has been consumed by the reaction, then it may cause an ignition in situ.

8.4.7. **CFD simulation of ignition due to Ca particle reaction heat release**

A similar bomb simulation setup as the previous section was used to predict the effect of the portion of reaction heat energy transferred to the air-fuel mixture directly. In this instance the 1e-07m particle is just used as a body to emit energy. The total energy emitted from the body can be calculated from the change in enthalpy for the number of moles. The duration over which the energy is released will be calculated using the Arrhenius function demonstrated in chapter 8.4.3 to establish the rate of reaction. An assumed concentration of CO_2 was used for the Arrhenius calculation, but the bomb simulation just consisted of fuel-air, as the objective was to investigate the ignitability of fuel-air once the CO_2 surrounding the particle has been consumed in the reaction.

Because the rate of reaction was significantly faster than the thermal diffusion through the gaseous domain, the temperature surrounding the emitting particle was high enough to cause an ignition.

Figure 75 shows the mean temperature of the bomb domain during the simulation, the first 0.01s of the simulation are a stabilisation period with no energy release, the energy release starts at 0.01s. Once all the fuel has been burned at around 0.021s, the gas domain begins to cool gradually because the wall temperature is held at the initial gas temperature. The wall boundaries were held at a constant temperature to allow for a temperature gradient from the ignition point, similar to an engine scenario, although because our interest in ignition is at the early stage when the kernel is very small, the wall boundary condition has very little impact.
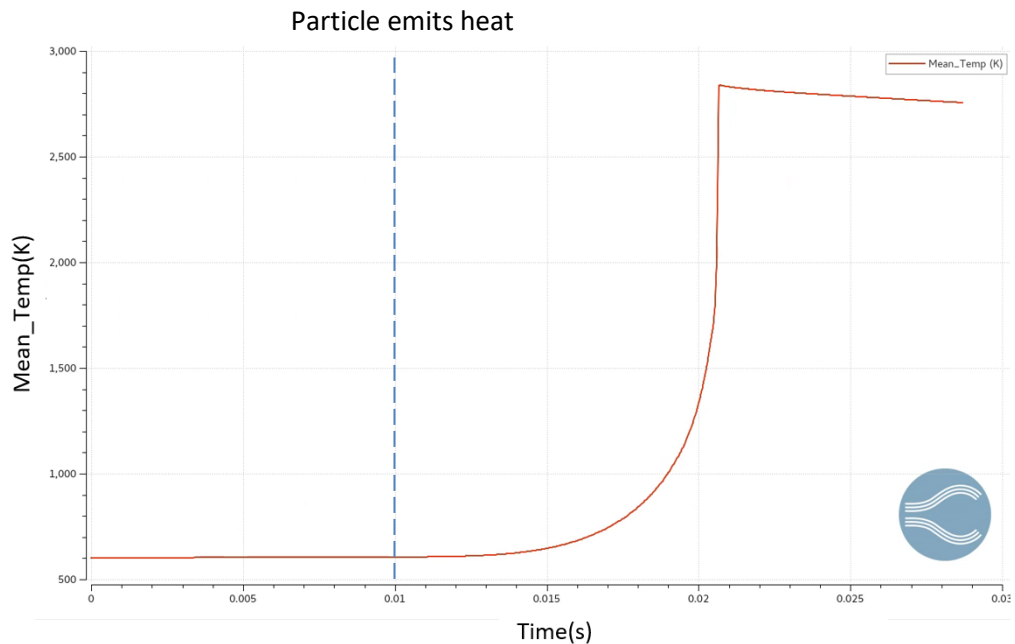
Figure 75- Reactor simulation showing mean temperature of gas domain throughout simulation, particle emits heat energy after 0.01s, diameter of particle is 1e-07m, air is of standard composition, stoichiometric mix of Iso-Octane and air, gas temperature is 600K, gas pressure is 25bar
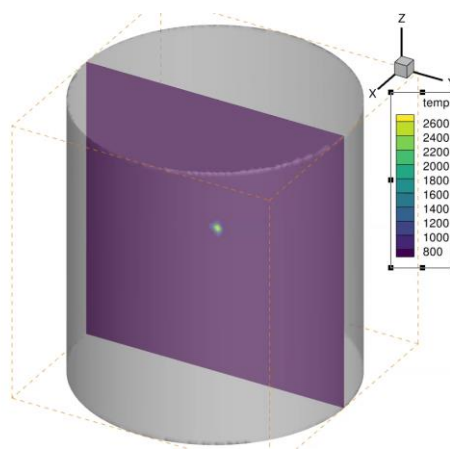

Figure 76- Reactor simulation showing temperature contour of ignition propagation, 4.92e-05s (0.442 degs CA) after start of heat release, diameter of particle is 1e-07m, air is of standard composition, stoichiometric mix of Iso-Octane and air, gas temperature is 600K, gas pressure is 25bar
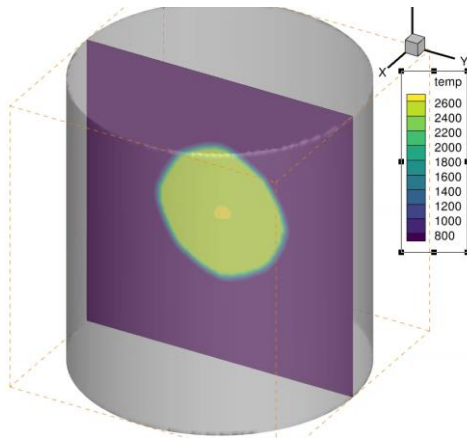
Figure 77- Reactor simulation showing temperature contour of ignition propagation, 5e-03s (45 degs CA) after start of heat release, diameter of particle is 1e-07m, air is of standard composition, stoichiometric mix of Iso-Octane and air, gas temperature is 600K, gas pressure is 25bar

The SAGE solver used in this study, does not have turbulent closure, and therefore neglects the sub-grid strain of the reaction front. However, this is not a concern as the reaction is very slow and for much of the time the turbulent length scale is much larger than the reaction front [156], meaning there is very little wrinkling of the reaction front.

303

8.5. Closure & Summary - Detergent heat transfer, reactions and ignition

Initial objectives of the study also mention the impact of detergent selection on LSPI. The notion that Calcium based detergents dramatically increase the number of LSPI cases, and in most cases will be the cause is the most salient in literature. In several experiments described in literature, it was found removing the Calcium from a lubricant the LSPI events dramatically reduce, whereas the presence of Magnesium has no impact on LSPI.

Initially, the in-cylinder conditions predicted by the GT combustion model were examined to see if a sudden change in heat transfer characteristics or concentration close to spark ignition timing. No abrupt changes were observed close to a typical LSPI timing. The next stage was to understand if there was a difference in chemical reaction behaviour of the two detergents. A steady state Aspen simulation confirmed the temperature at which the equilibrium shifts such that carbonate reaction takes place is very different between Mg and Ca. Following this, a script was used to simulate both chemical equilibrium for both detergents throughout the intake and compression strokes, using in cylinder boundary conditions from the GT model. The rate of reaction was CO_2 diffusion limited and heat release was predicted. An Arrhenius calculation was completed to substantiate the assumption that the reaction is instantaneous once the CO_3 molecule reaches the detergent particle. The single particle simulation was completed assuming particles of various size and different levels of burned gas residuals. The main findings from the study are found below:

- Magnesium does not react with CO_2 throughout the intake and compression stroke simulation, irrespective of burned has residual concentration or particle size.

- The Ca particle does react with CO_2 but generally reacts during the intake stroke or early part of the compression stroke

- Reducing particle size or increasing the burned mass fraction advances the point of ignition.

- The conduction and heat capacitance characteristics of a Mg and Ca particle are very similar. For the same size particle the temperature change due to convection is very similar until a reaction occurs with the Ca particle.

- An energy equation was used to calculate the particle temperature increase during reaction, but temperature rise is almost instantaneous to the equilibrium temperature.

- The maximum temperature a particle can reach during reaction phase is the equilibrium temperature for that condition, as the reaction will intermittently activate and deactivate about that point. The equilibrium temperature will change with local CO_2 concentration.

- If a Ca particle is particularly large it will have sufficient thermal capacitance to retain a temperature high enough to avoid a reaction taking place. However, the temperature of the particle may still be as hot as one that has reacted. It is unlikely a particle is large enough for this to occur, based on the typical hydrodynamic oil film thickness.

- The equilibrium temperature is often only slightly higher than the pre-reaction temperature of the particle, meaning the temperature rise during reaction is very small. This thesis postulates that the most likely sequence of events; fresh oil sprayed onto the liner during the intake stroke. Some CaO and $Ca(OH)_2$ molecule exists in the oil but is protected from the gaseous domain by the hydrocarbons. As predicted by the Clausius-Clapeyron calculation the hydrocarbons will vapourise

close to the LSPI timing, exposing the Ca(OH)2 and CaO particles to gas. The Ca(OH)2 will relinquish H2O, resulting in more CaO. The CaO then reacts with CO2 to release heat at the correct timing. When assuming a small particle, an abrupt temperature change will also be observed.

As the heat release is rapid, thermal energy is released into the particle body and directly to the air-fuel mixture. Meaning an ignition could be caused from the direct heat release or from a hot particle. From the CFD reactor simulation it was concluded that it was unlikely a hot particle could cause an ignition event with a nominal concentration of CO2 but given the inhomogeneity inside a combustion chamber it is possible a particle could be temporarily surrounded by a higher concentration. Far more likely is the effect of direct heat release into the gaseous domain causing an ignition, as was found from the CFD analysis.

8.5.1. Detergent ignition modelling process validation

An extensive literature survey was carried out to attempt to find validation data for the diffusion, reaction and heat release predicted by the simulation process in this section Most of the literature found was reporting the carbonation reaction of CaO for limestone for energy storage purpose [138][139][140][141][143]. However the pressure and thus the P(CO2) tested for in the literature is much lower than the in cylinder conditions relevant to this thesis. Simulating at such low pressures add little rigidity to the approach in this section. However, there is much described in literature that is aligned with our findings:

- CaO carbonation is dependent on temperature
- CaO carbonation is dependent upon P(CO2)
- Likelihood of ignition depends upon equilibrium concentration
- Temperature of particle increases to an equilibrium maximum

306

- Diffusion and the reaction itself take place very quickly. According to [140] at high temperatures the diffusion and reaction take place within nanoseconds, time scales much shorter than the solution time in this section.

In addition to the above, the boundary conditions assumed for the simulation come from a GT combustion model that has been validated to test data. The thermodynamic and transport equation used to calculate the ignition point, diffusion rate, heat release and heat absorption have been established from test data. The chemical calculations assumed are all established practices.

9. Investigating fuel composition, detonation propagation and impact of water injection

There are several supplementary questions that should be answered to complement the understanding achieved thus far in modelling the initiation of LSPI. What are deemed to be the most important three will be investigated in this section; Exhaustive and highly detailed calculations will not be required for this section, as it should be possible to obtain an understanding of their respective contributions from a simplistic approach.

9.1. Aims of supplementary investigations

Fuel composition is optimised to reduce conventional Knock and emissions. However, it is known from literature that fuel properties and composition can increase the likelihood of LSPI although the initiation is thought to be mainly attributed to the lubricant (section 2.9.3), and so its impact on LSPI will be investigated in this chapter. The literature survey suggests physical properties of the fuel and the extent to which it wets the wall the determines its impact on LSPI, rather than chemical characteristics.

Little information is found in literature with regards to the nature of reaction propagation of an LSPI event. The CFD simulation in previous sections has predicted it to be a micro-deflagration event which could possibly transition to a detonation in the case of mega-knock. The remaining question is that in a hypothetical scenario that an extremely fast heat release ensues due to a very high local concentration of CO_2, is it plausible that a detonation occurs from the onset and increases in speed with increasing temperature (speed of sound increases with temperature). A simple calculation will be carried out to investigate the possibility of such an event.

Finally, the impact of water injection will be discussed in detail. From the literature it was found water injection can significantly reduce LSPI, especially when injected late in the compression stroke and in the latter phase of

compression (section 2.9.2). This is possibly a very good solution for mitigating LSPI, if the engine designer is prepared to make compromises on performance, as it will displace air volume and slow down primary combustion. However, it does not provide much insight into the mechanism causing LSPI, and for this reason an exhaustive investigation is outside the scope of this thesis.

9.2. Impact of fuel composition on LSPI
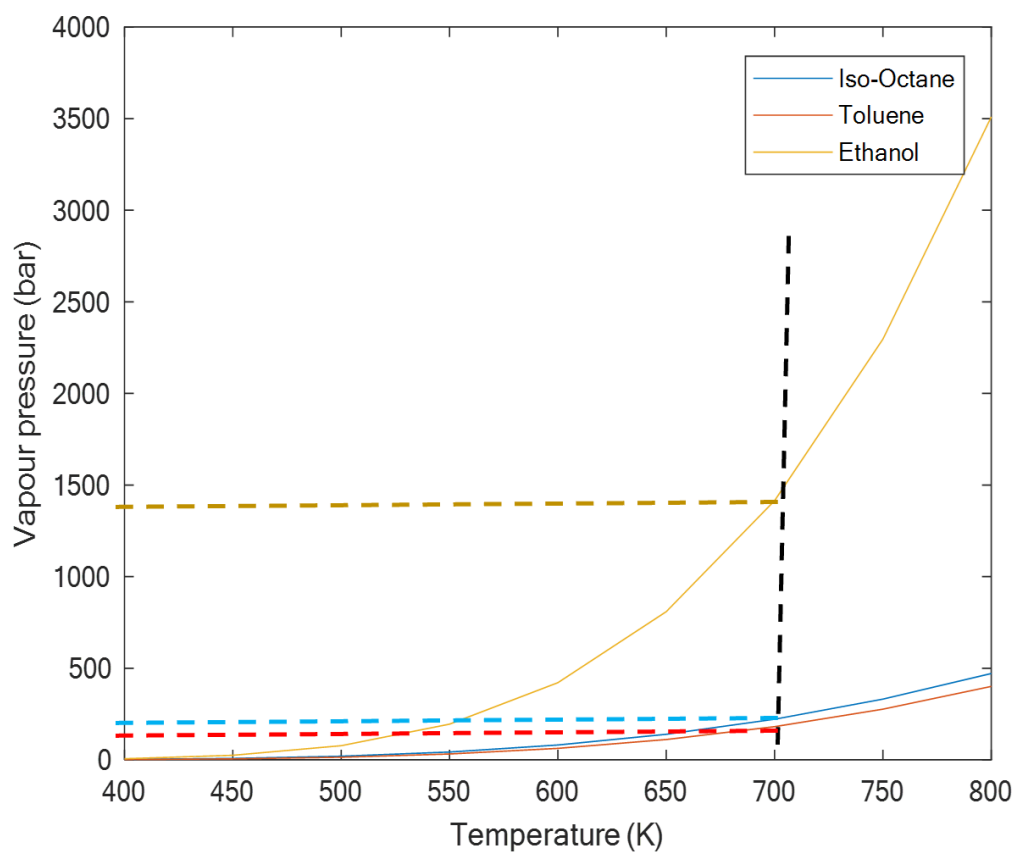
Figure 78– Vapour pressure against temperature of some Gasoline fuel components that have historically exacerbated LSPI

	Isooctane	Toluene	Ethanol
Boiling point (degC)	99.2	110.6	78.2
Latent heat of vaporisation (kJ/mol)	39.4	38	42.32
MON	100	107	89.7
RON	100	121	108.6

Table 14 – Autoignition and evaporation related properties of the three fuel components being investigated

The impact of fuel composition on LSPI has been reported by several pieces of literature such as Mattias et al[29], Morgan et al[28] and Haenel et al [30]. Some consideration of the impact of fuels will be given in this chapter, with a limited investigation of evaporation characteristics.

From the papers mentioned above and the survey in section 2.9.3 we deduce that the main three fuel components that increase propensity to LSPI were Toluene, Ethanol and Iso-Octane. Autoignition and evaporation related data for the three fuel components can be found in table 14. It is a point of discussion as to whether it is the RON value that provides indicative direction for LSPI or the MON. Most likely it is the MON value, being a more arduous test that will be more representative of the gas state close the spark ignition point, for a GTDI engine that generally has a high compression ratio, volumetric efficiency and thus power density.

If a typical LSPI initiation gas condition if 700K and 30 bar, a Clausius-Clapeyron calculation was carried out on the three components mentioned above for the range of temperatures that would be observed in an engine during thr compression stroke. it can be seen from Figure 78 that all three components will be in their vapour phase as their vapour pressure is greater than 30bar. So, in the case of the three hydrocarbons considered, the fuel composition and its impact due to latent heat of phase change is unlikely to impact the propensity of LSPI close to the spark timing. We also know LSPI mainly occurs on DI engines so it unlikely to be due to composition reactions

with the lubricant, as Abhishek et al [53] found from testing the amount if LSPI reduced with reducing fuel volatility. Splitter et al [47] also found the amount of LSPI increased with increased wall wetting from DI injection. This leads to the suggestion that the impact of fuel is most likely in its liquid state.

In a GTDI engine the fuel is injected during the intake stroke. It is possible the components plotted in Figure 78 remain in their liquid state for the majority of the compression stroke as fuel droplets impinge on the much cooler liner and mix with the oil droplets. The cooler water jacket will assure the mixture does not evaporate throughout the intake stroke and most of the compression stroke, until ejected into the combustion chamber. The fuel components will reduce the effective viscosity of the oil-fuel mixture and will remain as a liquid mixture for a prolonged period of time due to a slightly higher boiling point relative to lighter components. The combined result of a thicker film due the two mediums mixing, and a lower effective viscosity is that more droplets are transported from the liner and crevice volume to the combustion zone. This will increase the probability of a LSPI event occurring. This is known from the oil transport CFD model discussed in chapter 6.

Of the three components, it is obvious Ethanol is the most volatile, both [29] and [30] suggest to an extent an increase in Ethanol blended in gasoline will reduce the LSPI events latent heat transfer due to phase change of Ethanol, it also helps cool end gas, but in excess the presence of Ethanol will drastically increase the number of LSPI events, the impact of volatility making ignition more likely begins to dominate, with combustion being a phase change limited process. The most prominent explanation for the decrease in LSPI events for a reduced amount of Ethanol is that the Ethanol quenches the charge mixture throughout the compression stroke; due to latent hear transfer during evaporation. The more the charge gas is quenched the lower the subsequent rate of evaporation of the remaining fractions, which is why an increased level of Ethanol increases LSPI events because more time is spent in the liquid

phase for the remaining components. More time in liquid phase allows more opportunity for fuel to impact the viscosity of the fuel-oil mixture along the liner later in the compression stroke, as the piston decelerates. Allowing for more oi-fuel to escape to the combustion volume. Also, a higher composition Ethanol means it will proportionately dominate the combustion process, because it evaporates so easily its oxidation is less phase change limited and therefore more ignitable.

Although some insight can be gained from reasons why Ethanol may increase or decrease the level of LSPI, it is difficult to establish why Toluene and Iso-Octane provide such a response as their heat of vapourisation and boiling points are similar to that of N-Heptane, a common fuel component that does not seem to exacerbate LSPI. There are several other properties that could be investigated in further work such as surface tension, viscosity, contact angle and chemical action.

9.3. Analysis to investigate if LSPI can be a Detonation Propagation

As was discussed in section 2.2, a deflagration is a slow reaction wave that propagates due to direct heat transfer from the reaction front to the adjacent unburned zone. The ignition process investigated in the previous section is predicting a deflagration, as the thermal diffusion is the only mode of reaction activation, as is also evident from its subsonic propagation. Small deflagrations on their own, are generally less of a concern as depending on the initial heat flux and total heat energy released, the reaction front velocity is much slower relative to detonation. Because the propagation of the reaction front is subsonic (relative to the unburned gas), no shock wave is created in the previously simulated cases.

It is quite possible that there are some combustion events such as that of carbonaceous particles that will release heat, until the whole particle has been oxidised, but the rate of reaction/surface temperature will not be sufficient to

ignite the fuel-air mixture. In this event the cylinder pressure may increase by a small amount temporarily only whilst the particle is reacting.

A detonation event is far more detrimental, as the much higher rate of reaction means the reaction front propagates at supersonic velocities relative to the unburned gas, resulting in a shock wave being created in front of the reaction front. The shock wave compresses the downstream fluid, increasing its enthalpy, the increased heat transfer from the reaction front and the localised work by the shock wave assure the supersonic detonation wave is sustained.

In the case of the Calcium reaction discussed in chapter 8, it should be remembered that the mixture in the cylinder is not homogeneous until late in the compression stroke [138], for this reason it is entirely possible that the CaO is present in a location of high CO_2 concentration (burned gas residuals) and thus a rapid exothermic event takes place, and thus making detonation a possibility.

This chapter will investigate if it is plausible for a LSPI event to be a detonation, by predicting the detonation speed at a range of timings that are typical of LSPI, then assessing the burn length at the point of spark ignition.

Now that shock waves are being accounted for, as the reaction front propagates into the unburned zone at supersonic speeds, the gas phase beyond the reaction front experiences abrupt compression and expansion meaning the gas cannot be assumed to be isentropic (some of the losses will not be recoverable). For this reason, the reaction front is represented as a discontinuous surface of zero thickness. The conservation of mass, momentum and energy must still be satisfied at the boundaries of each element along the discontinuous surface.

313

In order to manage the complexity of the mathematical problem and be able to understand the impact of a detonation event relative to the spark timing, a few simplifying assumptions must be made.

A detonation will propagate radially and axially from its point of initiation; in fact, the reaction front will be a spherical surface propagating from the autoignition point. For the purpose of this study the calculation will be conducted in 2 dimensions along the radial plane of the detonation and the axial propagation will be ignored.

If the pressure ratio between the burned zone and the unburned zone is high, and $Q >> C_{v1}T_1$, then the following approximation can be made for the velocity of the detonation front [31] [32].

$$U_1 = \sqrt{2(\gamma^2 - 1)Q} \qquad \text{[eqn 131]}$$

A more complete solution for single point, 1 dimensional detonation front is as follows [31]:

$$U_1 = \left\{ \frac{\gamma_2 - 1}{2} \left[(\gamma_2 + 1)Q + (\gamma_1 + \gamma_2)C_{v1}T_1 \right] \right\}^{\frac{1}{2}} + \left\{ \frac{\gamma_2 + 1}{2} \left[(\gamma_2 - 1)Q + (\gamma_2 - \gamma_1)C_{v1}T_1 \right] \right\}^{\frac{1}{2}} \qquad \text{[eqn 132]}$$

$$U_2 = \left\{ \frac{\gamma_2 - 1}{2} \left[(\gamma_2 + 1)Q + (\gamma_1 + \gamma_2)C_{v1}T_1 \right] \right\}^{\frac{1}{2}} + \frac{\gamma_2 - 1}{\gamma_2 + 1} \left\{ \frac{\gamma_2 + 1}{2} \left[(\gamma_2 - 1)Q + (\gamma_2 - \gamma_1)C_{v1}T_1 \right] \right\}^{\frac{1}{2}} \qquad \text{[eqn 133]}$$

Where; suffix 1 is for the unburned zone and suffix 2 is for the burned zone, γ is the ratio of specific heats, Q is the enthalpy of reaction reduced to the absolute zero of temperature, U_1 is the velocity of the detonation front relative to the motion of the unburned gas, U_2 is the velocity of the detonation front relative to the motion of the burned gas, T is temperature and C_v is the specific heat capacity at constant volume.

The enthalpy of reaction at absolute zero is difficult to obtain, especially as the reactions of Isooctane can take several paths. We know the unburned gas temperature is nominally around 800K (from combustion model in chapter 5), and because it is a detonation front it will be supersonic relative to the unburned gas. The detonation front relative to the burned gas zone is likely to be closer to sonic, as the speed of sound increases with gas temperature. We can approximate Q by knowing the lowest temperature in the unburned zone is 800K, At this temperature we can assume the Chapman-Jouguet (CJ) point i.e. $U_2 = a_{s2}$ (speed of sound in burned zone), so the equation for U_2 can be used to reverse calculate Q to satisfy the CJ criteria. In this case Q was calculated to be 500kJ/mol. We can now simulate the 2-dimensional detonation propagation for an LSPI condition, by using the burned and unburned gas temperatures as well as the primary flame speed/size predicted by the GT model at 1500rev/min WOT (any time the primary combustion event or associated gases are mentioned, the combustion event from the spark event is being referred to).

Figure 79 shows the predicted detonation speed assuming the temperature of the burned and unburned is the nominal temperature predicted by the GT engine model. The detonation has a velocity much higher than the primary flame front (Turbulent flames speeds are only 20-40m/s according to the predictive flames speed model), and all the fuel-air mixture has reacted by 21 degATdc.

The assumption of using nominal gas temperatures is not realistic, as there is heat transfer between the two zones and unburned gas temperature will increase as the detonation propagates due to unburned gas volume reducing and burned gas volume increasing. For a given instant the temperature of the burned gas left immediately behind the flame front will be at the combustion temperature, but the unburned temperature close to the flame front is more likely to be a mass averaged temperature between the isolated burned and unburned temperatures. Because this is a 2-dimensional solution, the unburned temperature will be an area averaged temperature of the primary burn area, detonation burn area and unburned area. Although the temperature of the burned products can be calculated using eqn 134, it was found the temperature predicted was too high for the conditions being simulated, for this reason it was assumed the temperature of the burned gas from the detonation was the same temperature as the burned gas from the primary flame [31].

$$T_2 = \frac{U_2^2}{\gamma_2(\gamma_2-1)C_{v2}} \qquad \text{[eqn 134]}$$

The spark timing for the case shown in Figures 78 and 79 below is 3deg ATdc .

(a)

(b)

317
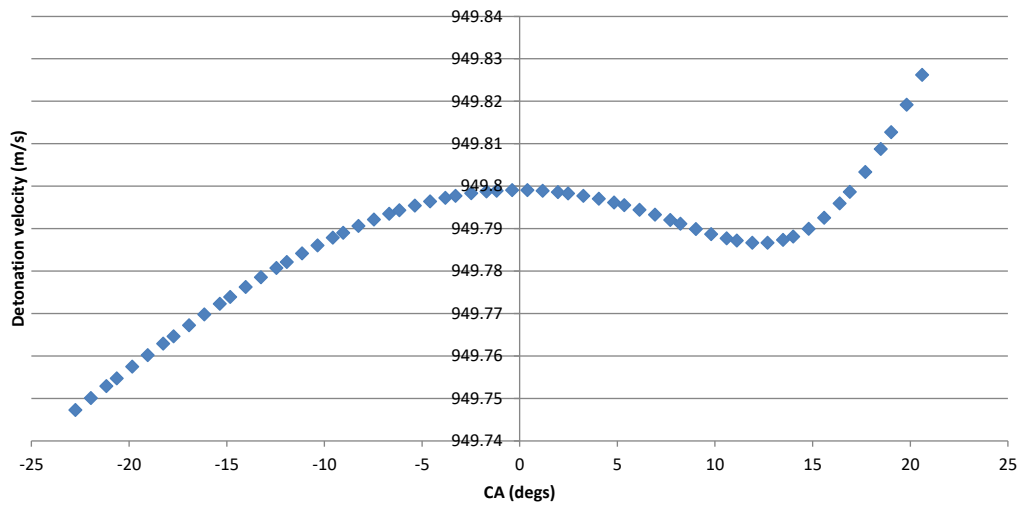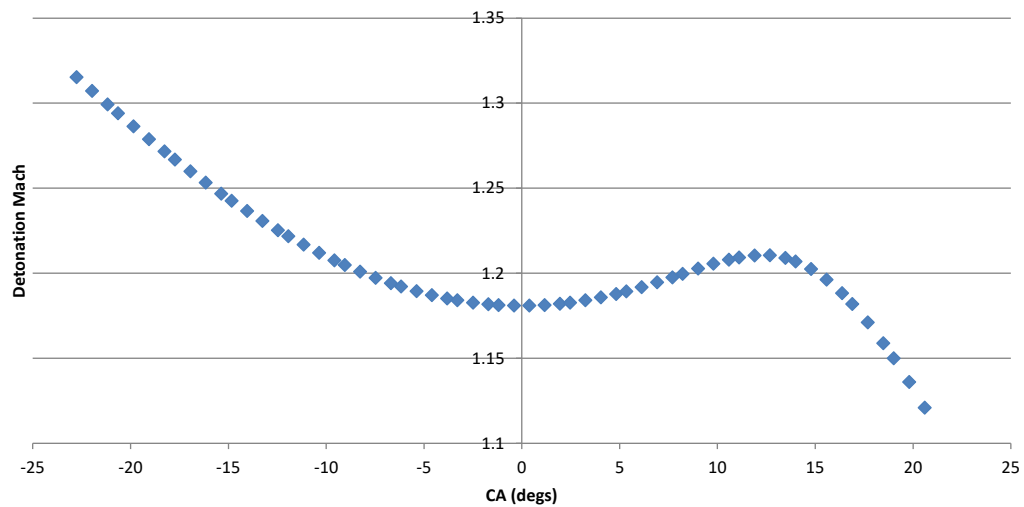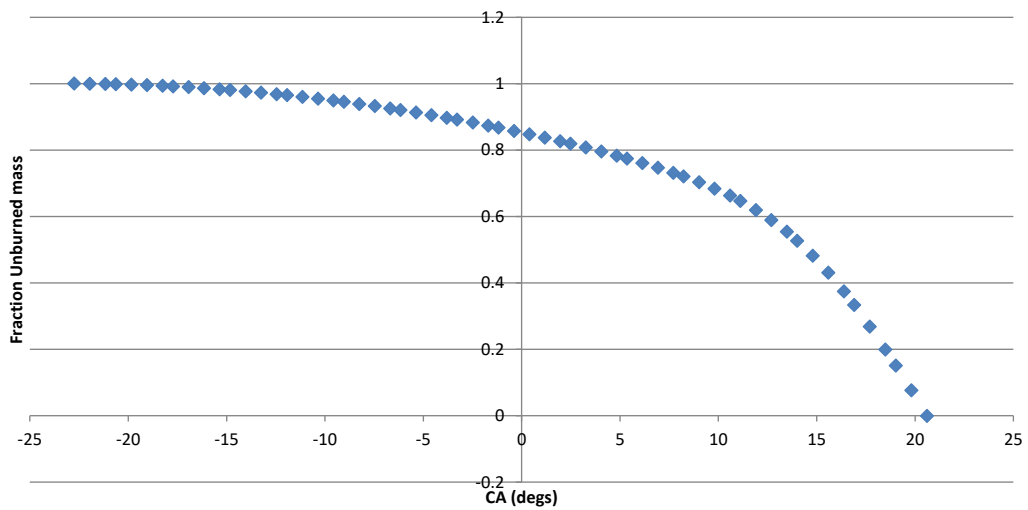
(c)

Figure 79– Simulation of a detonation event occurring 23deg BTdc, using nominal gas temperatures from the GT predictive combustion mode @ 1500rev/min WOT (a) Detonation velocity (b) Mach number (c) Unburned gas fraction

(a)

(b)

319
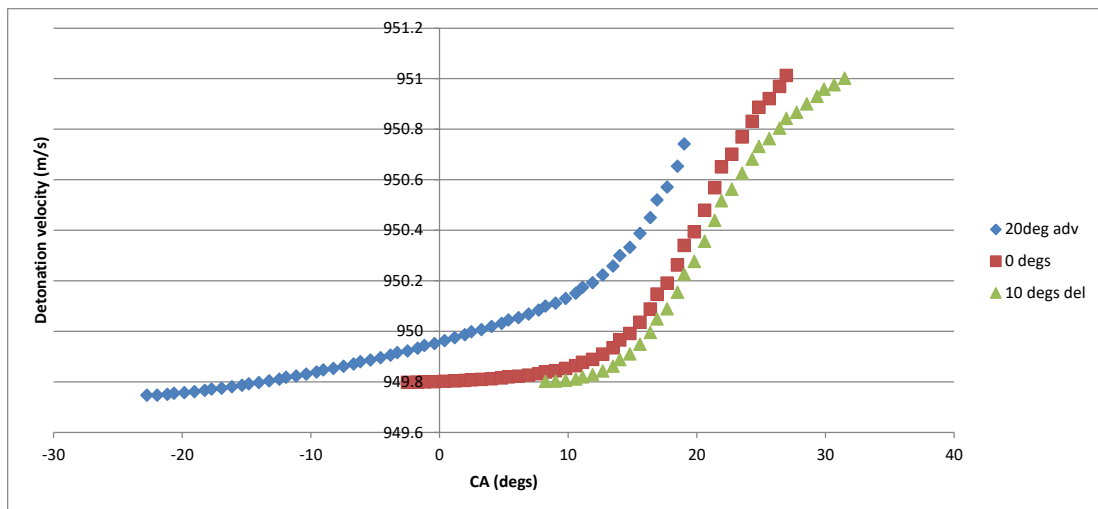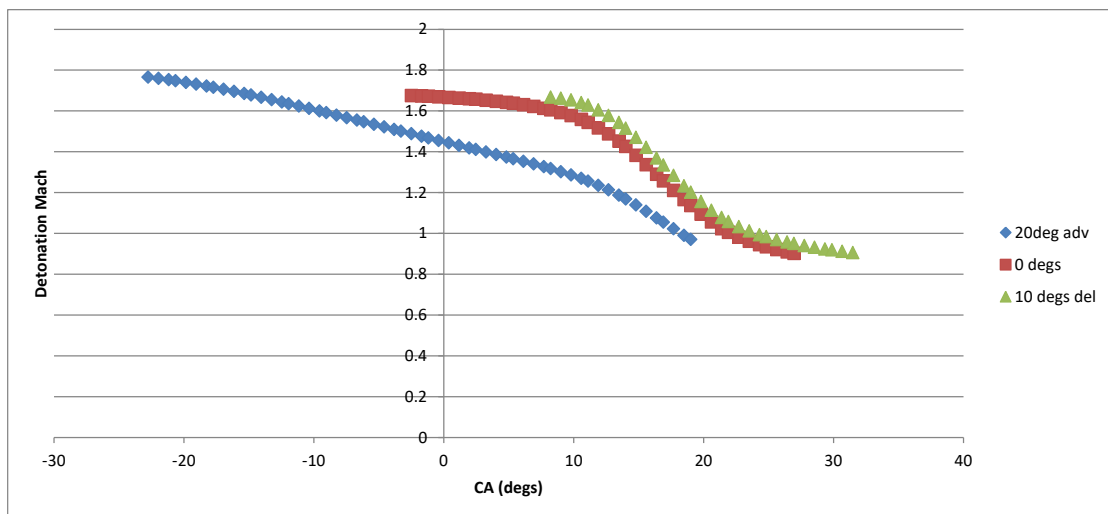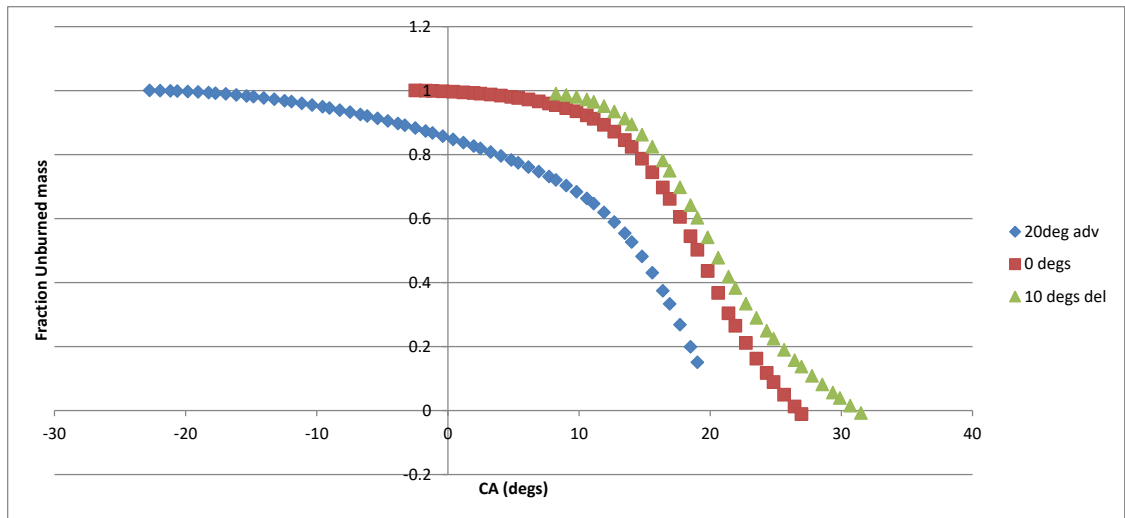
(c)
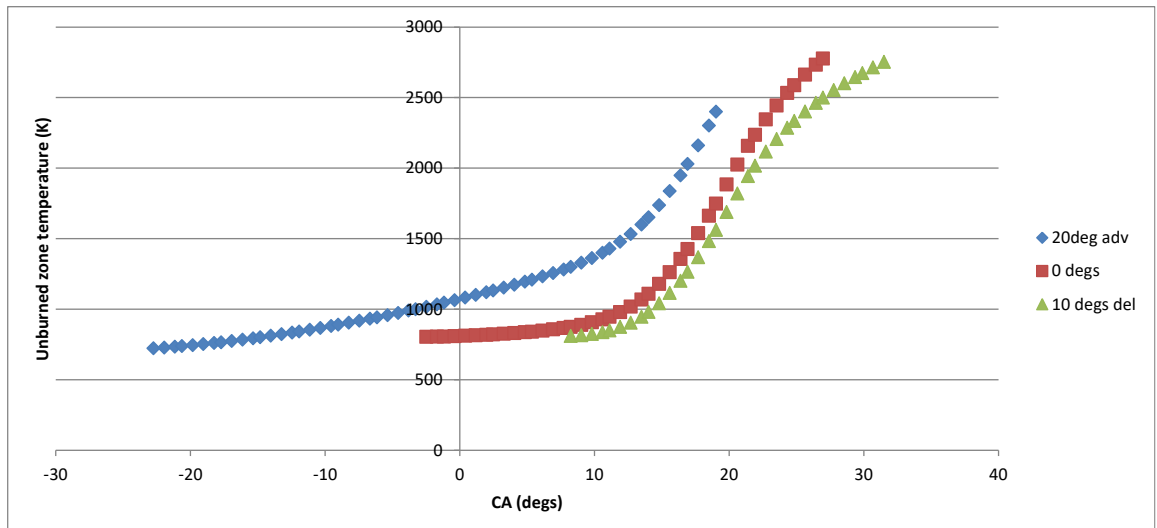
(d)

Figure 80– Simulation of a detonation event occurring, all timing angles are relative to the spark timing; 20deg before spark, at the spark timing (0degs before spark) and 10deg after spark using gas temperatures based on the mass fraction of burned gas@ 1500rev/min WOT (a) Detonation velocity (b) Mach number (c) Unburned gas fraction (d) Unburned zone temperature

Figure 80 shows the detonation behaviour with the detonation being initiated at three different timings; 20deg before spark, at the spark timing (0degs before spark) and 10deg after spark. It can be seen there is a sudden

320

increase in burned temperature at 12deg ATdc, according to the simulation this is because the combustion transitions from predominantly a laminar flame to turbulent flame, the increase in mass flux entering the flame results in a high heat output. Although the burned gas from the detonation will not exhibit the same behaviour as the main deflagration event because a detonation speed is less dependent on entrainment of combustibles and more on the speed of the shock wave, there will be mass and thermal diffusion between the two burned phases from separate combustion mechanisms. By assuming the burned gas temperatures are the same from both combustion sources, we allow for some accountability of the unburned gas of the detonation increasing in temperature to some extent due to increased heat transfer as the primary burned gas increases in temperature. The Mach number relative to the unburned zone reduces with increasing gas temperature as the speed of sound increases.

As expected, the detonation event with the earliest ignition develops gradually in its detonation velocity as initially there is no burned gas from the primary ignition that allows for the detonation reaction front to accelerate due to elevated temperatures. However, once the spark event takes place the detonation speed increases substantially as the end gas temperature is already elevated by the early pre-ignition. Because of the initial propagation velocity being low, the total duration of the detonation event (to consume all of the fuel-air in the plane) is the longest.

For the pre-ignition events that are initiated later, there is a period between 0degATdc and 12degATdc (figure 81) when the burned gas temperature actually begins to reduce as the flame is still in a predominantly laminar mode and the burn rate is very low, the gas will then cool slightly as volume expands with much of the mixture unburned (as can be seen in Figure 81). The result of this, when a simultaneous detonation is included, is that the unburned gas temperature is nominally constant as the lower temperature

321

resulting from thr expansion is compensated by the continued progress of the detonation front providing heat. The temperature and detonation velocity then increase substantially beyond 12degATdc when the flame transitions into its turbulent form.

When the air-fuel mixture is ignited by the spark plug, the flame forms an almost perfect sphere like kernel that propagates as a very thin laminar flame. The flame thickness and length is small compared with the turbulent length scale of the unburned gas domain [156], and thus the surface of the flame is not deformed by hydrodynamic forces so much. As the flame propagates, its front surface wrinkles and stretches due to hydrodynamic forces from the turbulence as well as thermal and species diffusion, both of which are more influential with a larger flame. This increase in flame size allows the turbulence to distort the flame profile increasingly, especially as the TKE increases as the piston accelerated towards mid-expansion stroke. The influence of the turbulence thickens the flame as the reaction zone is entrained further into the unburned zone by local turbulence, the front face of the thick flame exhibits variable behaviour that is characteristic of a turbulent flame. Eventually, the flame has transitioned from a predominantly laminar flame to a predominantly turbulent flame [27][32].

Because the mass of the unburned zone is reducing rapidly due to the detonation front, so too is the unburned zone's cooling contribution on the unburned gas in the vicinity of the flame front (as it is at a lower temperature). It can be seen from the results in Figure 80, that a detonation event will propagate across the cylinder very quickly. For the case where the detonation was initiated at the spark timing the radial mass of air-fuel was consumed by 28deg ATdc, in comparison to the flame speed model predicting the primary flame would have terminated 138deg ATdc for a normal case. In fact, the simulation (Figure 80 (d)) suggests the unburned gas zone ahead of the detonation front itself exceeds the autoignition temperature of IsoOctane

322

when the burned zone is large enough (and so is the heat transfer it provides), meaning micro autoignition events are potentially taking place in the unburned zone itself.

This type of rapid and uncontrolled combustion in general is not observed when testing engines for LSPI according to literature, even mega-Knock cases are not characterised with such a violent and abrupt heat release. The analysis suggests it is very unlikely the pre-ignition is a detonation and is more likely in a slow deflagration regime as simulated by the CFD model in the previous section of a hot particle in an air-fuel mixed environment (chapter 8).

Conventional Knock is a detonation event [32], especially an audible frequency can be detected (suggesting a shock wave). The frequency or its harmonic can be compared with the speed of sound through the medium and the frequency at which it can travel across the bore. However, there is a delay associated with the unburned zone reaching the enthalpy of combustion (autoignition), which will be determined by the compression due to the piston and hot zone expanding, as well as the heat transfer from the flame front. So, generally the autoignition will not impact the combustion until the late stages of the primary flame propagation. A faster turbulent flame velocity can assure the unburned gas zone is consumed before the end gas reaches the autoignition state. This is the type of detonation event that is often observed in gasoline engines.

Although the pre-ignition event is likely a deflagration it will assist in heating up the end gas zone more quickly prior to the spark event, especially if it is a late LSPI event and thus increase the propensity and severity (increase rate of reaction) of knock/Mega Knock after the spark timing.

323
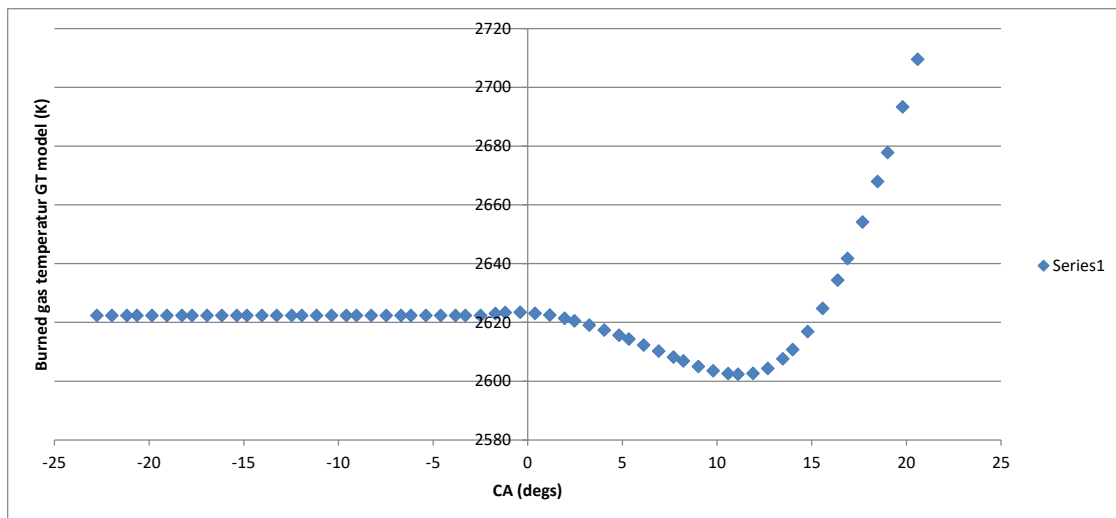
Figure 81 – Burned gas temperature predicted by GT flame speed model @ 1500rev/min WOT

9.4. Impact of water injection on Pre-ignition

This section will discuss the possibility of water injection being used as a solution for mitigating LSPI. Several findings already provide indicators as to the impact of water injection. This includes; phase change investigation, impact of residuals, ignition of droplets and detergents as well as transport from the liner. The benefits of water injection can be summarised as follows:

1. Water injection during the valve overlap period can help scavenge the CO2 from the combustion chamber, reducing the likelihood of a detergent reaction, as this has been shown to require a critical concentration of CO2 (chapter 8).

2. Latent heat transfer due to phase change of the water will cool the air-fuel mixture, reducing the possibility of ignition. It is known from the detergent ignition CFD simulation (section 8.4.6-8.4.7) that a cooler gaseous environment reduces the likelihood of ignition.

3. The higher specific heat capacity of steam can help cool the air-fuel mixture.

4. The presence of steam can displace some of the oxygen, either avoiding or slowing down the detergent or hydrocarbon reactions.

5. Condensation can settle on the liner, mixing with the oil film. This can increase the mass and thickness of the overall film and thus increase the mass of oil transported into the combustion zone. It is known from the study completed in chapter 6 that film thickness plays a major role in that amount of oil that escapes the crevice volume.

9.5. Closure and summary - Impact of water injection, fuel selection and nature of reaction propagation

The chapter investigates the impact of water injection, nature of reaction propagation and influence of fuel composition. As discussed in the literature, several researchers have found LSPI propensity is impacted by fuel selection and can be reduced by water injection.

For the impact of water injection, it was found that the study had already established enough learning to lend to the mechanisms that reduce LSPI. It is known that cooling the mixture will reduce the possibility of the fuel-air ignition. The latent heat transfer during water evaporation and higher specific heat capacity will assist in cooling. The only counter effect of water injection is that the condensation developed in the liner would mix with the oil forming a thicker film and assisting in transport to the combustion chamber. From our research [155] we know that water would itself require a large amount of energy to create radicals (more than air) and contribute to reactions, it is unlikely to play a major role in the early stage of combustion, it is far more conceivable that the effect is related to thermodynamics.

Because LSPI is seen as an issue more so with DI engines rather than PFI, it can be deduced that the impact of fuel is associated more with the spray, fuel-lubricant interaction at the liner. Especially as a fuel sensitivity is not reported to have been observed with highly boosted PFI engines. A Clausius-Clapeyron calculation was performed on the four fuel components that

increased the amount of LSPI from literature. Most of the fuel components will spend significant time in the liquid phase if placed on the cool liner. However, for Toluene and Iso-Octane the phase change characteristics are not too different from other non-responsive components. Some further work could be carried out here, by using molecular dynamics to investigate fuel-lubricant interaction and reactions with various components. Because the phase change response of Ethanol was so much different to other fractions, we can quickly concede that phase change must be a factor, and latent heat transfer is cooling the mixture and thus reducing LSPI. In larger amounts, Ethanol is potentially over cooling the mixture and slowing down the phase change of other fractions, but because of its volatility there is also more hydrocarbon's available in gaseous form present, available for reactions.

The boundary conditions from the GT model were used to simulate a detonation front at various timings when it is plausible a LSPI event may occur, using a quasi-dimensional simulation. It was found that it was extremely unlikely a LSPI event is a detonation as much of the air-fuel mixture will have been consumed by the detonation before the spark event, which is not observed in test. It is more likely the reaction front is a deflagration that warms the end gas and transitions to a detonation after spark ignition.

10. Thesis Conclusions and Further work

This chapter will reflect upon what has been learned through the course of this thesis, how the study has built upon the understanding currently available in literature and finish the chapter by discussing how the current study can be extended by further work.

At this point it is pertinent to refer to the objective and aims laid out in Chapter 1.3. In summary, the objective of this thesis was to establish the main mechanism causing LSPI, and the factors that it is sensitive to. The objectives were to initially conduct a thorough literature survey to understand the observations relating to LSPI from experimentation and scientific explanations that are offered for route mechanisms and trends observed. Because the mechanism takes place at a very small time and space scale, it cannot be observed from testing and thus must be corroborated using numerical methods. Gaps in understanding will be identified and a simulation methodology will be developed to address the gaps.

As part of research a flow diagram developed, representing the most likely series of events that lead up to an LSPI event based on literature. An extensive literature survey was conducted specifically to research the simulation methodologies available. Following this, a simulation process was developed to investigate each of the proposed steps.

Because LSPI is a stochastic phenomenon, it must be sensitive to the spatially and time variable boundary conditions present within a very turbulent environment. As not only must the conditions be such that allow the ignition event to take place, but they must also cause it to take place at the correct timing. It was also found in most cases; the contributors were not interdependent and could be investigated individually. Testing each phenomenon individually also means the response observed is only a result of that aspect, rather than being a combined result of several contributors, potentially leaving us in a scenario which makes it difficult to differentiate between sensitivity to contributors. Similarly, when a design of experiments is conducted assessing the sensitivity to differing boundary conditions, a

coupled model incorporating various contributors would provide a combined response, making it difficult to establish a relationship between the boundary condition and the aspect being investigated. In many cases a single particle approach, where possible an particle that is representative of the population in an engine was assumed, this allowed a precise control on boundary conditions and avoided the need to analyze several entities in an engine domain.

10.1. Conclusions from numerical simulation

Based on the sensitivities noted from literature, care was taken to assure assumptions, initial conditions and environmental conditions were representative of a typical GTDI engine. This was done using; 3D, 1D and 0D simulations. Where possible the models used in the process were validated against test data. This approach proved to be beneficial as many of the findings were aligned with experimental trends found in literature and explained some well-known discrepancies but now with numerical evidence. A reformed theory for the reaction of lubricant detergents is offered based on the findings from the simulation. The remainder of this chapter will delve further into what was found from each numerical experiment.

From literature it is known, LSPI often results in an increase in PM could be due to partial oxidation and cracking of oil or fuel rich pockets. The mass of oil available is unlikely to be sufficient to cause a big change in PM. It is more likely due to slow oxidation prior to spark ignition or due to low temperature autoignition in the end gas zone. More likely due to early slow ignition as this is when the fuel is less likely to be thoroughly mixed with air, and there may reside fuel rich pockets.

10.2. Technical discussion

As discussed in the previous chapter, each aspect of LSPI was investigated in a controlled and efficient way. The technical findings of each investigation are summarized at the end of the end or the relevant sections, a concise summary is offered in the sections below for the convenience of the reader. Novel findings of this thesis are indicated in brackets. An additional but key novelty of this thesis is the simulation process that was developed and the manner in which the diverse methodologies are integrated to provide insight to transport, thermodynamic and chemical behaviour.

Lubricant oil transport and ignition findings:

- The mass of oil that escapes from the crevice volume to the combustion chamber generally reduces with reduces with increasing viscosity of engine oil.
- Most of the oil finds its way to the head or remains in the gaseous domain close to the point when LSPI is generally observed.
- if the viscosity is increased significantly the inter-film shear force becomes much higher than the contact angle stress at the fluid-surface boundary, and the film behaves like a single body with high inertia, resulting in a large mass of oil escaping the crevice volume (novel finding)
- The behaviour of the oil film is greatly affected by wall temperature (viscosity is temperature dependant), as the mass of engine oil escaping the crevice volume reduces with increasing viscosity.
- It was found the full evaporation point became more retarded with longer alkane chain length due to increasing van der waals forces between molecules.
- Including the wet bulb temperature will also retard the ignition timing to some extent.
- The longest chain alkanes that will have the highest rates of reaction and highest rate of heat release
- When a large droplet is introduced, the higher thermal capacitance and thus slower phase change results in a concentration gradient between the liquid

and gas phases. Within the gradient is a thick stoichiometric layer with a high rate of reaction, a high local heat release ensues.

- When a small droplet is introduced, it rapidly evaporates and diffuses across the mixture, the rate of diffusion is faster than the rate of reaction, the local concentration is low resulting in a very slow rate of reaction.

- This explains why ignition due to lubricant hydrocarbons is observed on an RCM but not on engines, because the pilot injection in an RCM is normally a relatively large droplet, whereas an engine shears and releases very small parcels of fluid into the combustion zone (novel finding)

Detergent related findings:

- Magnesium does not react with CO_2 throughout the simulation, irrespective of burned has residual concentration or particle size (novel finding).

- The Ca particle does react with CO_2 but generally reacts during the intake stroke or early part of the compression stroke, when assuming a pre-existing particle from the previous cycle (novel finding).

- The point of reaction as well as the maximum particle temperature and heat release is determined by the particle size and burned gas fraction (novel finding).

- This thesis postulates that the following is most likely sequence of events: fresh oil sprayed onto the liner during the intake stroke. Some CaO and $Ca(OH)_2$ molecule exists in the oil but is protected from the gaseous domain by the hydrocarbons. The lubricant hydrocarbons will vapourise close to the LSPI timing, exposing the $Ca(OH)_2$ and CaO particles to gas. The $Ca(OH)_2$ will relinquish H_2O, resulting in more CaO. The CaO then reacts with CO_2 to release heat at the observed timing (novel finding).

- This thesis challenges the previously held view, of a CaO particle remaining from the previous engine cycle reacted with CO_2 during the compression stroke. The new theory combines the behaviour of the hydrocarbon components and detergent reaction. It is a novel addition to this field of research.

- It is unlikely a hot particle could cause an ignition event with a nominal concentration of CO_2 but given the inhomogeneity inside a combustion

chamber it is possible a particle could be temporarily surrounded by a higher concentration. Far more likely is the effect of direct heat release from the detergent particle into the gaseous domain causing an ignition (novel finding).

10.3. Final Remarks and further work

This research has achieved its original objectives, it has made great strides in understanding the mechanisms and sequence of events that cause LSPI. The simulation process developed can be used by formulators to design lubricants and potentially fuels too. The approach can also be implemented in a full engine combustion model for engine design.

A multi-faceted Physics approach was taken for this study. Validation in its true essence is very difficult to achieve for a phenomenon like LSPI which is very stochastic and non-repeatable. Regardless of this challenge, an effort was made to validate models where test data was available (such as the Reynolds hydrodynamic film solver and 1D predictive combustion model). Where test data was not available, such as single particle models or reactor models, care was taken to assure boundary conditions were derived from validated models, and directional agreement with observations in literature was discussed. In almost all cases very good agreement with literature was found.

The progress made in this research can be extended to use molecular dynamics, ReaxFF or even DFT to understand potential chemical interaction between fuels and lubricants, it would also be useful to simulate surface adsorption onto the detergent particle surface as well as diffusion into its porous structure. If a lubricant component can be developed that blocks the pours of the particle and prevents the gas from reaching the particle's internal surface area, or if a component attaches itself to the surface such that little is exposed to CO2, LSPI could be greatly alleviated. It would be interesting to delve further to understand if there are early stage/low temperature reactions

331

between fuel and oil that is not being captured in this thesis. The physical behaviour investigation could also be extended to investigate the impact of contact angle and surface tension of the fuel spray. The impact of hardware design changes should also be investigated, such as the impact of changes to; crevice volume, piston ring tension, combustion chamber geometry, piston bowl, injector cone angle, improved cooling of valves etc.

There are some factors that could potentially disrupt the findings in this thesis. The predominant possibility being that the Calcium interaction being different to what is assumed in this thesis. This could include surface catalytic effects, impact of porosity and more complex intermediate reactions with oil and fuel hydrocarbons, gases and surfaces. Therefore, these could also be areas to investigate further.

It is felt the simulation process will provide a reliable prediction for hydrodynamic, transport/stress and heat transfer aspects related to LSPI, as the fluid properties come from measured data and simulation practices are well established and validated. The first limitation at this stage is the need to assume the detergent particle is perfectly spherical and not account for its porous nature. The second limitation is the restriction of chemical aspects to what is pre-defined. It is possible there could be chemical interaction between the lubricant and fuel, detergent and fuel, intermediate reactions with gas domain and catalytic behaviour that is currently not being accounted for.

The thesis confirms design changes such as increased piston crevice volume and ring tang loads can help reduce the mass of lubricant entering the combustion chamber. However, these modifications are not absent of disadvantages. The research suggests if a lubricant can be designed such that it has very high boiling point components or surface acting molecules that attach to the detergent surface, then full evaporation may take place after spark ignition, at which point the detergent particle will be exposed to CO_2 but the reaction equilibrium will shift towards the creation of CaO because of the

high end gas temperature, meaning the reaction will be endothermic and LSPI will not occur. This could benefit hybrid vehicle fuel economy. Also, similar to CNG engines, the favoured Hydrogen ICE engine is also prone to LSPI as it also has a very low minimum enthalpy of ignition. Like CNG engines it will be LSPI due to lubricant hydrocarbon combustion rather than detergent. The hydrocarbon related findings in this thesis could benefit Hydrogen ICE designers, the simulation process developed could also be applied to such a case.

11. Bibliography

[1] P.J. O'Rourke, A A Amsden (1987). 'The Tab method for numerical calculation of spray droplet breakup' International Fuels and Lubricants, SAE, Ontario

[2] A B Liu, D Mather, R D Reitz (1993), 'Modelling the effects of drop size and breakup on fuel sprays', International congress and exposition, SAE, Detroit

[3] Wrenick, Scott1, Sutor, Paul1, Pangilinan, Harold2, Schwarz, Ernest E (2005), 'HEAT TRANSFER PROPERTIES OF ENGINE OILS', World Tribology Congress III, Washington DC

[4] A.A. Amsden, P.J. O'Rourke, T.D. Butler (1989), 'KIVA-II A computer program for chemically reactive flows with sprays', Los Almos National laboratory

[5] V. Ya. Basevich, A. A. Belyaev, and S. M. Frolov (2007),The Mechanisms of Oxidation and Combustion of Normal Alkane Hydrocarbons: The Transition from C1– C3 to C4H10, Russian Journal of Physical Chemistry, Khimicheskaya Fizika

[6] FAKHR M. ABU-AWWAD (2004), The Gas-Phase Heats of Formation of *n*-Alkanes as a Function of the Electrostatic Potential Extrema on their Molecular Surfaces, E-journal of Chemistry

[7] Peter Atkins and Julio de Paula, Atkins' Physical Chemistry

[8] T. Morel, C. I. Rackmil, R. Keribar, and M. J. Jennings (1988), Model for Heat Transfer and

Combustion in Spark Ignited Engines and Its Comparison with Experiments, SAE, Ontario IL

[9] P. K. Senecal, K. J. Richards, E. Pomraning, T. Yang and M. Z. Dai, R. M. McDavid, M. A. Patterson, S. Hou and T. Shethaji (2007), A New Parallel Cut-Cell Cartesian CFD Code for Rapid Grid Generation Applied to In-Cylinder Diesel Engine Simulations, SAE, Detroit MI

[10] W. He et al., *Gas Transport in Solid Oxide Fuel Cells*, SpringerBriefs in Energy, DOI 10.1007/978-3-319-09737-4_2

[11] Shuojin Ren, Sage L. Kokjohn, Zhi Wang, Haoye Liu, Buyu Wang, Jianxin Wang (2017), 'A multi component wide distillation fuel (covering gasoline, jet fuel and diesel fuel) mechanism for combustion and PAH prediction', Elsevier Fuel

[12] Yachao Chang, Ming Jia, Yaodong Liu, Yaopeng Li, Maozhao Xie, Hongchao Yin, Application of a Decoupling Methodology for Development of Skeletal Oxidation Mechanisms for Heavy n-Alkanes from n-Octane to n-Hexadecane

[13] Mattias Mayer, Peter Hofmann, John Williams, Danlu Tong (2016), 'Influence of the engine oil on Pre-ignitions at Highly supercharged Direct injection Gasoline Engines'

[14] Gary K. Jacobs, Derrill M. Kerrick, and Kenneth M. Krupka (1981), 'The High-Temperature Heat Capacity of Natural Calcite (CaCO3)', Physics and Chemistry of minerals

[15] Chase, M.W., Jr. (1998, 1-1951), NIST-JANAF Themochemical Tables, Fourth Edition, J. Phys. Chem. Ref. Data, Monograph 9

[16] Mitsuaki Ohtomo, Hiroshi Miyagawa, Makoto Koike, Nozomi Yokoo, Koichi Nakata(2014), 'Pre-Ignition of Gasoline-Air-Mixture Triggered by a Lubricant Oil Droplet', SAE int: J. Fuels & Lubricants

[17] Christoph Dahnz, Kyung-Man Han, Ulrich Spicher, Max Magar, Robert Schießl and Ulrich Maas (2010), 'Investigations on Pre-Ignition in Highly Supercharged SI Engines', SAE

[18] Stefan Palaveev, Max Magar, Heiko Kubach, Robert Schiessl, Ulrich Spicher and Ulrich Maas, 'Premature Flame Initiation in a Turbocharged DISI Engine -Numerical and Experimental Investigations', SAE

[19] Yasuo Moriyoshi, Tatsuya Kuboyama, Koji Morikawa, Toshio Yamada,Yasuo Imai, Koichi Hatamura and Masatoshi Suzuki(2015), 'A Study of Low Speed Preignition Mechanism in Highly Boosted SI Gasoline Engines', SAE

[20] Frances Maron Fraser, Edward J. Prosen (1955), 'Heats of Combustion of Liquid n-Hexadecane, I-Hexadecene, n- Decylbenzene, n-Decylcyclohexane, n-Decylcyclopentane, and the Variation of Heat of Combustion With Chain Length', Journal of Research of the National Bureau of Standards
336

[21] Yao-Dong Liu, Ming Jia, Mao-Zhao Xie,* and Bin Pang (2012), 'Enhancement on a Skeletal Kinetic Model for Primary Reference Fuel Oxidation by Using a Semidecoupling Methodology', Energy & Fuels

[22] Takuo Yoshizaki, Keiya Nishida, and Hiroyuki Hiroyasu (1993), 'Approach to Low NOx and Smoke Emission Engines by Using Phenomenological Simulation', SAE, Detroit MI

[23] Morel, T. and Wahiduzzaman, S., 'Modeling of Diesel Combustion and Emissions', FISITA 1996

[24] J.L. Silveira (ed.), Sustainable Hydrogen Production Processes, Green Energy and Technology (2017),Springer International Publishing Switzerland (2017), DOI 10.1007/978-3-319-41616-8

[25] Thomas Morel and Rifat Keribar, 'A Model for Predicting Spatially and Time Resolved Convective Heat Transfer in Bowl-in-Piston Combustion Chambers' (1985), SAE Detroit

[26] Gamma Technologies, 'Engine performance' manual

[27] John B. Heywood, 'Internal Combustion Engine Fundamentals'

[28] Neal Morgan , Andrew Smallbone , Amit Bhave , Markus Kraft , Roger Cracknell , Gautam Kalghatgi, 'Mapping surrogate gasoline compositions into RON/MON space' (2010), Combustion and flame

[29] 'Influence of Different Fuel Properties and Gasoline - Ethanol Blends on Low-Speed Pre-Ignition in Turbocharged Direct Injection Spark Ignition Engines' (2016), SAE

[30] Patrick Haenel, Henning Kleeberg, Rob de Bruijn, and Dean Tomazic, 'Influence of Ethanol Blends on Low Speed Pre-Ignition in Turbocharged,Direct-Injection Gasoline Engines'(2017), SAE

[31] Michael A. Liberman, 'Introduction to Physics and Chemistry of Combustion'

[32] J. Warnatz, U.Maas, R.W Dibble, 'Combustion – Physical and Chemical Fundamentals, Modelling and Simulation, Experiments, Pollutant formation'

[33] Patrick Smith, John Heywood, and Wai Cheng, 'Effects of Compression Ratio on Spark-Ignited Engine Efficiency (2014)', SAE

[34] J.W.G. Turner, A. Popplewell, R. Patel, T.R. Johnson, N.J. Darnton, S. Richardson, S.W. Bredda, R.J. Tudor, C.I. Bithell, R. Jackson, S.M. Remmert, R.F. Cracknell, J.X. Fernandes, 'Ultra Boost for Economy: Extending the Limits of Extreme Engine Downsizing(2014)', SAE

[35] Jens Ewald, Norbert Peters, 'A Level Set Based Flamelet Model for the Prediction of Combustion in Spark Ignition Engines', Aachen

[36] Hiroyuki Hiroyasu, Toshikazu Kadota, Masataka Arai, 'Development and use of spray combustion modelling to predict Diesel engine efficiency and pollutant emissions' (1983), JSME

[37] George A. Lavoie, 'Correlations of Combustion Data for S. I. Engine Calculations - Laminar Flame Speed, Quench Distance and Global Reaction Rates'(1979), SAE

[38] M. P. HALSTEAD, L. J. KIRSCH, and C. P. QUINN, 'The Autoignition of Hydrocarbon Fuels at High Temperatures and Pressures-Fitting of a Mathematical Model' (1977), Combustion and Flame

[39] P. K. Senecal, E. Pomraning and K. J. Richards, T. E. Briggs, C. Y. Choi, R. M. McDavid and M. A. Patterson, 'Multi-Dimensional Modelling of Direct-Injection Diesel Spray Liquid Length and Flam Lift-off Length using CFD an Parallel Detailed Chemistry' (2003), SAE

[40] Thomas H. Pulliam, David W. Zingg, 'Fundamental Algorithms in Computational Fluid Dynamics', Scientific Computation

[41] H K Versteeg, W Malalasekera, 'An Introduction to Computational Fluid Dynamics – The Finite Volume Method'

[42] A Mahmood, O Nerushev, 'Prediction of Lubricant Performance in an EHL Valvetrain Simulation Using an Equation of State and Detailed Rheology Characterization Approach' (2018), SAE

[43] Yasuo Moriyoshi, Toshio Yamada, Daisuke Tsunoda, Mingzhao Xie, Tatsuya Kuboyama, and Koji Morikawa, 'Numerical Simulation to Understand the Cause and Sequence of LSP I Phenomena and Suggestion of CaO Mechanism in Highly Boosted SI Combustion in Low Speed Range' (2015), SAE

[44] Tatsuya Kuboyama, Yasuo Moriyoshi, and Koji Morikawa, 'Visualization and Analysis of LSPI Mechanism Caused by Oil Droplet, Particle and Deposit in Highly Boosted SI Combustion in Low Speed Range' (2015), SAE

[45] Felt Mounce, 'Development of a Standardized Test to Evaluate the Effect of Gasoline Engine Oil on the Occurrence of Low Speed Pre-Ignition - The Sequence IX Test' (2018), SAE

[46] Alexander Michlberger, Michael Sutton, 'LSPI Durability, a Study of LSPI over the Life of a Vehicle (2018)', SAE

[47] Derek Splitter, Brian Kaul, and James Szybist, Lake Speed, Bradley Zigler and Jon Luecke, 'Fuel-Lubricant Interactions on the Propensity for Stochastic Pre-Ignition (2019)', SAE

[48] Orian Welling, Nick Collings, James Moss, John Williams, 'Impact of Lubricant Composition on Low-speed Pre-Ignition (2014), SAE

[49] E. Distasoa, R. Amirantea, G. Calòa, P. De Palmaa, P. Tamburranoa, R.D. Reitzb, 'Predicting lubricant oil induced pre-ignition phenomena in modern gasoline engines: The reduced GasLube reaction mechanism' (2020), SAE

[50] Andre Swarts, Travis Kostan, and Vickey Kalaskar, 'Combined Effects of Engine and Oil Age on Low Speed Pre-Ignition' (2019), SAE

[51] FREDRIK KÖNIGSSON, 'On combustion in the CNG-Diesel dual fuel engine'(2014), PhD thesis, Royal Institute of Technology, Stockholm

[52] Ian Elliott, Richard Cherpeck, Amir Maria, Theresa Gunawan ,'Alternative Engine Oil Formulating Solutions to Reduce Low Speed Pre-Ignition' (2019), SAE

[53] Abhishek Kar, Andrew Huisjen, Allen Aradi, Jannik Reitz, Asim Iqbal, Karin Haumann, Jennifer Kensler, Ken Hardman, Robert Mainwaring, Sarah Remmert, 'Assessing the Impact of Lubricant and Fuel Composition on LSPI and Emissions in a Turbocharged Gasoline Direct Injection Engine' (2020), SAE

[54] Michael Clifford Kocsis, Thomas Briggs, and Garrett Anderson, 'The Impact of Lubricant Volatility, Viscosity and Detergent Chemistry on Low Speed Pre-Ignition Behavior' (2017), SAE

[55] Eshan Singh and Robert Dibble, 'Mechanism Triggering Pre-Ignition in a Turbo-Charged Engine' (2019), SAE

[56] Eshan Singh, Ponnya Hlaing, Hao Shi, and Robert Dibble, ' Effect of Different Fluids on Injection Strategies to Suppress Pre-Ignition' (2019), SAE

[57] Eric J. Passow, Paras Sethi, Max Maschewske, Jason Bieneman, Kimm Karrip, Paul Truckel, ' An Introduction to How Low Speed Pre Ignition Affects Engine Components' (2017), SAE

[58] Mohammad Ramezani, Priscilla Tremain, Elham Doroodchi and Behdad Moghtaderi, '   Determination of carbonation/calcination reaction kinetics of a limestone sorbent in low CO_2 partial pressures using TGA experiments' (2016), Elsevier

[59] W. van Dam, D. H. Broderick, R. L. Freerks, V. R. Small and W. W. Willis, SAE Transactions, Vol. 106, Section 3: JOURNAL OF ENGINES (1997), pp. 2398-2403

[60] Sadiyah Sabah Chowdhury, Ali Kharazmi, Cyrus Atis, and Harold Schock, 'Three-Dimensional Multi-phase Physics-Based Modeling Methodology to Study Engine Cylinder-kit Assembly Tribology and Design Considerations- Part I' (2020), SAE

[61] Shuyu Sun, Tao Zhang, 'Reservoir Simulations' (2020), ISBN: 978-0-12-820957-8, doi.org/10.1016/C2019-0-02019-5

[62] Sherwood, Pigford, Wilke, 'Mass Transfer', Chemical Engineering series, ISBN 0-07-056692-5

[63]   Abraham, J., Bracco, F.V., and Reitz, R.D., 'Comparisons of Computed and Measured

Premixed Charge Engine Combustion', Combustion and Flame

[64] Adri C. T. van Duin, Siddharth Dasgupta, Francois Lorant and William A. Goddard III, ' A Reactive Force Field for Hydrocarbons', 2001

[65] Harish Hirani, 'Fundamentals of Engineering Tribology with applications', Cambridge University press

[66] Hamrock, 'Fundamentals of Fluid film lubrication', McGraw-Hill series in Mechanical engineering

[67] Lino Guzella, Christopher H. Onder, 'Introduction to modelling and control of internal combustion engine systems' Springer

[68] Bennett and Myers, 'Momentum, Heat and Mass transfer', Chemical Engineering series

[69] Richard Stone, 'Introduction to Internal combustion engines', ISBN 0-333-74013-0

[70] Kristian Ronn, 'Low-speed Pre-ignition and Super-Knock in Spark ignition engines'(2020), master thesis

[71] Converge manual, Converge CFD manual series, Convergent Science

[72] Third year, Heat transfer noted, Dr. Aysar .T. Jarullah,
https://ceng.tu.edu.iq/ched/images/lectures/chem-lec/st3/c2/Lec12.pdf

[73] Yazan A Hussain, 'Reactors', Jordan University of Science and Technology (JUST)

reactors.pdf (just.edu.jo)

[74] Lin Chen, Ren Zhang, Jiaying Pan, Haiqiao Wei, 'Optical study on autoignition and knocking characteristics of dual-fuel engine under CI vs SI combustion modes' (2020), Fuel

[75] D.Bradley, G.T.Kalghatgi, 'Influence of autoignition delay time characteristics of different fuels on pressure waves and knock in reciprocating engines' (2009), Combustion and Flame

[76] Hiroshi Terashima, Mitsuo Koshi, 'Mechanisms of strong pressure wave generation in end-gas autoignition during knocking combustion' (2015), Combustion and Flame

[77] Hiroshi Terashima, Hisashi Nakamura, Akira Matsugi, Mitsuo Koshi, 'Role of low-temperature oxidation in non-uniform end-gas autoignition and strong pressure wave generation' (2021), Combustion and Flame

[78] Peng Dai, Zheng Chen, Xiaohua Gana, Mikhail A.Liberman 'Autoignition and detonation development from a hot spot inside a closed chamber: Effects of end wall reflection' (2021), Proceedings of Combustion institute

[79] Orian Welling, James Moss, John Williams, Nick Collings, 'Measuring the Impact of Engine Oils and Fuels on Low-Speed Pre-Ignition in Downsized Engines' (2014), SAE

[80] Leslie R Rudnick, 'Lubricant Additives Chemistry and applications'(2003), Chapter 4 "Detergents'

[81]Andrew Zdanowicz, Jeffrey Mohr, Jessica Tryner, Kara Gustafson, Bret Windom, Daniel B.Olsen, Gregory Hampson, Anthony J.Marchese , 'End-gas autoignition fraction and flame propagation rate in laser-ignited primary reference fuel mixtures at elevated temperature and pressure' (2021), Combustion and Flame

[82] D.Bradley, G.T.Kalghatgi, M.Golombok, Jinku Yeo, 'Heat release rates due to autoignition, and their relationship to knock intensity in spark ignition engines' (1996), Symposium (International) on Combustion

[83] Diego Bestela, Scott Bayliff, Hui Xu, Anthony Marchese, Daniel Olsena, Bret Windom, 'Investigation of the end-gas autoignition process in natural gas engines and evaluation of the methane number index' (2021), Proceedings of Combustion Institute

[84] Jianfu Zhao, Lei Zhou, Kuangdi Li, Xiaojun Zhang, Jiaying Pan, Rui Chen, Haiqiao Wei, 'Effect of diluent gases on end gas autoignition and combustion modes in a confined space' (2020), Combustion and Flame

[85] Shaoye Jin, Bo Shu, Xiaoyu He, Ravi Fernandes, Liguang Li, 'A study on autoignition characteristics of H_2-O_2 mixtures with diluents of Ar/N_2 in rapid compression machine for argon power cycle engines' (2021), Fuel

[86] Lei Zhou, Kuangdi Li, Jianfu Zhao, Xiaojun Zhang, Haiqiao Wei, 'Experimental observation of end-gas autoignition and developing detonation in a confined space using gasoline fuel' (2020), Combustion and Flame

[87] Xue Gong, Qing Xie, Hua Zhou, Zhuyin Ren, 'Structure and propagation speed of autoignition-assisted flames of jet fuels' (2022), Combustion and Flame

[88] Lin Chen, Jiaying Pan, Haiqiao Wei, Lei Zhou, Jianxiong Hua, 'Numerical analysis of knocking characteristics and heat release under different turbulence intensities in a gasoline engine' (2019), Applied Thermal Engineering

[89] Alireza Valipour Berenjestanaki, Nobuyuki Kawahara, Kazuya Tsuboi, Eiji Tomita, 'End-gas autoignition characteristics of PREMIER combustion in a pilot fuel-ignited dual-fuel biogas engine' (2019), Fuel

[90] James P.Szybist, Derek A.Splitter, 'Impact of engine pressure-temperature trajectory on autoignition for varying fuel properties' (2020), Applications in energy and Combustion Science

[91] Hiroshi Terashima, Yutaka Hanada, Soshi Kawai, 'A localized thickened flame model for simulations of flame propagation and autoignition under elevated pressure conditions' (2021), Proceedings of the Combustion Institute,

[92] Alireza Valipour Berenjestanaki, Nobuyuki Kawahara, Kazuya Tsuboi, Eiji Tomita, 'Performance, emissions and end-gas autoignition characteristics of PREMIER combustion in a pilot fuel-ignited dual-fuel biogas engine with various CO2 ratios' (2021), Fuel

[93] Yu Hao, Qi Chengken, Chen Zheng, 'Effects of flame propagation speed and chamber size on end-gas autoignition' (2017), Proceeding of the Combustion Institute

[94] Dai Peng, Chen Zheng, 'Effects of NOx addition on autoignition and detonation development in DME/air under engine-relevant conditions' (2019), Proceedings of the Combustion institute

[95] Hiroshi Terashima, Akira Matsugi, Mitsuo Koshic, 'End-gas autoignition behaviors under pressure wave disturbance' (2019), Combustion and Flame

[96] Yang Jianting, Hou Zihao, ' Autoignition and combustion wave propagation in a spatial reactivity gradient environment constructed using the shock-converging method' (2021), Combustion and Flame

[97] Dai Peng, Chen Zheng, Gan Xiaohua, 'Autoignition and detonation development induced by a hot spot in fuel-lean and CO2 diluted n-heptane/air mixtures' (2019), Combustion and Flame

[98] Xumin Zhao, Zan Zhu, Zunqing Zheng, Zongyu Yue, Hu Wang, Mingfa Yao, 'Effects of flame propagation speed on knocking and knock-limited combustion in a downsized spark ignition engine' (2021), Fuel

[99] V.Chintala, K.A.Subramanian, 'Experimental investigation of autoignition of hydrogen-air charge in a compression ignition engine under dual-fuel mode' (2017), Energy

[100] Song Cheng, S.Scott Goldsborough, Chiara Saggese, Scott W.Wagnon, William J.Pitz, 'New insights into fuel blending effects: Intermolecular chemical kinetic interactions affecting autoignition times and intermediate-temperature heat release' (2021), Combustion and Flame

[101] Automotive Handbook, Bosch (10th Edition), Wiley

[102] Robert L Norton, 'Design of Machinery'(1999), Second edition, McGraw-Hill series in Mechanical Engineering

[103] BP internal test and research data

[104] Guidance and advice from Dr. Radomir Slavchov

[105] Xinmeng Tang, Edyta Dziemińska, A. Koichi Hayashi, Nobuyuki Tsuboid, 'Numerical investigation of three deflagration-to-detonation transition conditions

related to the velocity of the spontaneous reaction wave' (2021), International Journal of Hydrogen Energy

[106] Bo Zhang, Guangli Xiu, Jian Chen, Shaopeng Yang, 'Detonation and deflagration characteristics of p-Xylene/gaseous hydrocarbon fuels/air mixtures' (2015), Fuel

[107] I.O.Shamshin, M.V.Kazachenko, S.M.Frolov, V. YaBasevich, 'Deflagration-to-detonation transition in stochiometric mixtures of the binary methane–hydrogen fuel with air' (2021), International Journal of Hydrogen Energy

[108] Shengbing Zhou, Hu Ma, Changsheng Zhou, Ning Hu, 'Experimental research on the propagation process of rotating detonation wave with a gaseous hydrocarbon mixture fuel' (2021), Acta Astranautica

[109] Hao-Yang Peng, Wei-Dong Liu, Shi-Jie Liu, Hai-Long Zhang, Si-Yuan Huang, 'The competitive relationship between detonation and deflagration in the inner cylinder-variable continuous rotating detonation combustor' (2020), Aerospace Science and Technology

[110] Mohammad Hosein, Shamsadin Saeid, Javad Khadem, Sobhan Emami, 'Numerical investigation of the mechanism behind the deflagration to detonation transition in homogeneous and inhomogeneous mixtures of H2-air in an obstructed channel' (2021), International Journal of Hydrogen Energy

[111] Ravi Kumar Sharma, 'A violent, episodic vapour cloud explosion assessment: Deflagration-to-detonation transition' (2020), Journal of loss prevention in the process industries

[112] Ruixuan Zhu, Majie Zhao, Huangwei Zhang, 'Numerical simulation of flame acceleration and deflagration-to-detonation transition in ammonia-hydrogen–oxygen mixtures' (2021), International Journal of Hydrogen Energy

[113] Guangyu Wang, Weidong Liu, Shijie Liu, Hailong Zhang, Haoyang Peng, Yunfan Zhou, 'Experimental verification of cylindrical air-breathing continuous rotating detonation engine fueled by non-premixed ethylene' (2021), Acta Astronautica

[114] Xiongbin Jia, Ningbo Zhao, Shizheng Liu, Xiang Chen, Wanli Zhu, Hongtao Zheng, 'Numerical investigation of detonation initiation for low-volatility liquid fuel/air mixtures' (2021), Aerospace Science and Technology

[115] Xiaolong Zhang, Jiyang Yu, Tao Huang, Guangming Jiang, Xianping Zhong, Muhammad Saeed, 'An improved method for hydrogen deflagration to detonation transition prediction under severe accidents in nuclear power plants' (2019), International Journal of Hydrogen energy

[116] Xiang-Yang Liu, Ming-Yi Luan, Yan-Liang Chen, Jian-Ping Wang, 'Propagation behavior of rotating detonation waves with premixed kerosene/air mixtures' (2021), Fuel

[117] Reza Soleimanpour, Hossain Nemati, 'Numerical investigation of deflagration to detonation transition in closed ducts under various working conditions' (2019), Acta Astronautica

[118] Xingkui Yang, Feilong Song, Yun Wu, Yepan Zhong, Shida Xu. 'Investigation of rotating detonation fueled by a methane–hydrogen–carbon dioxide mixture under lean fuel conditions' (2020), International Journal of Hydrogen Energy

[119] Soo-Yeong Cho, Hyun-Jun Kim, Jack J.Yoh, 'Addressing the complex geometric effects on the three-dimensional transition to detonation in hydrocarbon-air mixtures using a parametrized level-set algorithm (2021), International Journal of Hydrogen energy

[120] Camilo Rosas, Scott Davis, Derek Engel, Prankul Middha, Keesvan Wingerden, M.S.Mannan, 'Deflagration to detonation transitions (DDTs): Predicting DDTs in hydrocarbon explosions' (2014), Journal of loss prevention in the process industries

[121] Zhengchuang Zhao, Xiaobin Huang, Haoqiang Sheng, Zhijia Chen, Hong Liu, 'Enhanced low-temperature stable combustion of hydrocarbon with suppressing the Leidenfrost effect' (2022), International journal of Heat and mass transfer

[122] Shane R.Daly, Khang Tran, Kyle E.Niemeyer, William J.Cannella, Christopher L.Hagen, 'Predicting fuel low-temperature combustion performance using Fourier-transform infrared absorption spectra of neat hydrocarbons' (2019), Fuel
350

[123] C.A.J.Leermakers, M.P.B.Musculus, 'In-cylinder soot precursor growth in a low-temperature combustion diesel engine: Laser-induced fluorescence of polycyclic aromatic hydrocarbons' (2015), Proceedings of the Combustion Institute

[124] Thierry LachauxMark, P.B.Musculus, 'In-cylinder unburned hydrocarbon visualization during low-temperature compression-ignition engine combustion using formaldehyde PLIF' (2007), Proceedings of the Combustion Institute

[125] F.Battin-Leclerc, 'Detailed chemical kinetic models for the low-temperature combustion of hydrocarbons with application to gasoline and diesel fuel surrogates' (2008), Progress in Energy and Combustion energy

[126] Shen Wei, Bai Shijie, Wang Kun, Liao Jiyu, Liang Xingyu, 'Simplified modeling combustion chemistry of neat and blended large hydrocarbon fuels with different functional groups' (2021), Combustion and Flame

[127] Hirotoshi Hirai, 'Molecular dynamics simulations for initial formation process of polycyclic aromatic hydrocarbons in n-hexane and cyclohexane combustion' (2021), Chemical Physics

[128] Song Guo, Shuxin Chen, Anwen Zhao, Min Jia, 'Multi-component gaseous alternative model for predicting typical liquid hydrocarbons combustion characteristics' (2020), Safety Science

[129] Xiaoyu He, Qi Wang, Ravi Fernandes, Bo Shu, 'Investigation on the autoignition characteristics of propanol and butanol isomers under diluted lean conditions for stratified low temperature combustion' (2022), Combustion and Flame

[130] Mohammad Zandie, Hoon Kiat Ng, Suyin Gan, Mohd Farid, Muhamad Said, Xinwei Cheng, 'Review of the advances in integrated chemical kinetics-computational fluid dynamics combustion modelling studies of gasoline-biodiesel mixtures' (2022), Transportation Engineering

[131] Julius A.Corrubia, Jonathan M.Capece, Nicholas P.Cernansky, David L.Millera, Russell P.Durrett, Paul M.Najt, 'RON and MON chemical kinetic modeling derived correlations with ignition delay time for gasoline and octane boosting additives' (2020), Combustion and Flame

[132] Alexander Hoth, Christopher P.Kolodziej, 'Effects of knock intensity measurement technique and fuel chemical composition on the research octane number (RON) of FACE gasolines: Part 1 – Lambda and knock characterization' (2021), Fuel

[133] Zhenbiao Zhou, Tanmay Kar, Yi Yang, Michael Brear, Thomas G.Leone, James E.Anderson, Michael H.Shelby, Eric Curtis, Joshua Lacey, 'The significance of octane numbers to drive cycle fuel efficiency' (2021), Fuel

[134] Gurneesh S.Jatana, Derek A.Splitter, Brian Kaul James, P.Szybist, 'Fuel property effects on low-speed pre-ignition' (2018), Fuel

[135] Z. Barbouchi and J. Bessrour, 'Turbulence study in the internal combustion engine' (2009), Journal of Engineering and technology research

[136] Bo Hu, Sam Akehurst, Andrew G.J. Lewis, Pengfei Lu, Darren Millwood, Colin Copeland, Edward Chappell, Andrew De Freitas, James Shawe Dave Burtt, 'Experimental Analysis of the V-Charge Variable Drive Supercharger System on a 1.0 L GTDI Engine' (2017), ImechE Journal of Automobile Engineering

[137] Surface Radiation Absorptivity (engineeringtoolbox.com)

[138] Jorge Plou, Isabel Martínez, Gemma S. Grasa and Ramón, 'Experimental carbonation of CaO in an entrained flow reactor', Reaction chemistry and Engineering journal (2019)

[139] Zhen-shan Li, Fan Fang, Xiao-yu Tang and Ning-sheng Cai, 'Effect of Temperature on the Carbonation Reaction of CaO with CO2', Energy & Fuels (2012)

[140] Nana Wang, Yuchuan Feng, Xin Guo, 'Atomistic mechanisms study of the carbonation reaction of CaO for high temperature CO2 capture', Applied surface science (2020)

[141] G. Grasa, I. Martíneza, M.E. Diego, J.C. Abanades, 'Determination of CaO carbonation kinetics under recarbonation conditions', Energy & Fuels

[142] A.A. Keller, V. Broje, K. Setty, 'Effect of advancing velocity and fluid viscosity on the dynamic contact angle of petroleum hydrocarbons' (2007), Petroleum science and engineering journal

[143] Sandra Turrado, Borja Arias José, Ramon Fernandez and Juan Carlos Abanades, 'Carbonation of Fine CaO Particles in a Drop Tube Reactor'(201*0, I&EC Research

[144] Paul Hellier, Midhat Talibi, Aaron Eveleigh and Nicos Ladommatos, 'An overview of the effects of fuel molecular structure on the combustion and emissions characteristics of compression ignition engines' (2017), ImechE

[145] Ertan Yilmaz, Tian Tian, Victor W. Wong and John B. Heywood, 'The Contribution of Different Oil Consumption Sources to Total Oil Consumption in a Spark Ignition Engine' (2004), SAE

[146] William B. Anderson and Greg H. Guinther, 'Engine Oil Fuel Economy: Benefits and Potential Debits of Low Viscosity Engine Oil' (2019), SAE

[147] Sunil Kumar Pandey, Muralitharan and Ravikrishna, 'Quasi-Dimensional Modelling and Parametric Studies of a Heavy-Duty HCCI Engine' (2011), Journal of combustion

[148] Stefania Falfari, Federico Brusiani, Piero Pelloni, '3D CFD Analysis of the Influence of Some Geometrical Engine Parameters on Small PFI Engine Performances – the Effects on the Tumble Motion and the Mean Turbulent Intensity Distribution' (2014), Energy Procedia

[149] Peter Bechtold, 'Atmospheric Thermodynamics' (2015), EXMWF

[150] Jeremy Manheim, Katherine Wehde, Wan Tang Jeff Zhang, Petr Vozka, Mark Romanczyk, Gozdem Kilaz & Hilkka I. Kenttämaa, 'Identification and Quantitation of Linear Alkanes in Lubricant Base Oils by Using GC×GC/EI TOF Mass Spectrometry' (2019), Journal of The American Society for Mass Spectrometry

[151] Robin Tempelhagen, Andreas Gerlach , Sebastian Benecke, Kevin Klepatz, Hermann Rottengruber, Hermann Rottengruber, 'Investigations for a Trajectory Variation to Improve the Energy Conversion for a Four-Stroke Free-Piston Engine' (2021), Applied sciences

[152] SR Bewsher, M Mohammadpour, H Rahnejat, G Offner and O Knaus, 'An investigation into the oil transport and starvation of piston ring pack' (2018), ImechE

[153] Fabian H. Ruch, Georg Wachtmeister, 'A New Cavitation Algorithm to Support the Interpretation of LIF Measurements of Piston Rings' (2020), SAE

[154] Mitsuhiro Soejima, Yasuo Harigaya, Toshiro Hamatake, Yutaro Wakuri, 'Study on Lubricating Oil Consumption from Evaporation of Oil-Film on Cylinder Wall for Diesel Engine' (2017), SAE

[155] Jayesh Khatri, 'Investigating effects of water injection on SI engines', Chalmers University of Technology

[156] Tarek Echekki, 'Multiscale methods in turbulent combustion: strategies and computational challenges' (2009), Science & Discovery

[157] Keribar, R., Dursunkaya, Z. and Flemming, M.F.*, "An Integrated Model of Ring Pack Performance"*

[158] James A Greenwood, Parmine Putignano, Michele Ciavarella. 'A Greenwood & Williamson theory for line contact'

[159] A. M. Douaud and P. Eyzat, "Four-Octane-Number Method for Predicting the Anti-Knock Behavior of Fuels and Engines", SAE Paper 780080, 1978

[160] D. Franzke, "Beitrag zur Ermittlung eines Klopfkriteriums der ottomotorischen Verbrennung und zur Vorausberechnung der Klopfgrenze", PhD Thesis, Technical University of Munich, 1981

[161] R. Worret, "Zylinderdruckbasierte Detektion und Simulation der Klopfgrenze mit einem verbesserten thermodynamischen Ansatz", PhD Thesis, University of Karlsruhe, 2002

[162] Chiang, C.H., Raju, M.S., and Sirignano, W.A., "Numerical Analysis of a Convecting, Vaporizing Fuel Droplet with Variable Properties," International Journal of Heat and Mass Transfer, 35(5), 1307-1324, 1992. DOI: 10.1016/0017-9310(92)90186-V

[163] Huber, K., Woschni, G., "Investigations on Heat Transfer in Internal Combustion Engines under Low Load and Motoring Conditions," SAE 905018, 1990

[164] Hohenberg, G., "Advanced Approaches for Heat Transfer Calculations," SAE Technical Paper 790825, 1979, doi:10.4271/790825.

12. Appendices

12.1. Appendix 1

```
CaCO3_cp_init = 834; %specific heat capacity, J/kg K

rpm = 1500; %rev/min

time = 1/(6*rpm);%seconds per degree CA

part_rad = 5e-8;%Particle radius, m

part_vol = 4/3*pi*part_rad^3;%particle volume, m3

part_rho = 2710;%particle density, kg/m3

mass = part_vol*part_rho;%particle mass, kg

SA = 4*pi*part_rad^2;% particle surface area, m2

E_remov = HTC*SA*(Temp-Temp_gas)*time;%energy extracted
due to convection, J

conv_dT = E_remov/(CaCO3_cp_init*mass);%Temperature
change, K

Temp = Temp-conv_dT;%New temperature for current time-
step
```

12.2. Appendix II

```matlab
clc

clear

v = 1;




Temp_loc_final = 1200; %Initial temperature, K

Temp_loc_paral = 1200;%Initial temperature, K

CaCO3_cp_init = 834;%Cp, J/kg K



%Initial

part_rad = 6e-08; %Particle radius, m

part_vol = 4/3*pi*part_rad^3;%Particle volume, m3

part_rho = 2710;% particle density, kg/m3

mass = part_vol*part_rho; %particle mass, kg

SA = 4*pi*part_rad^2;%Particle surface area, m2



mols_init_flag = 100;%Initialise flag



mass_react = mass; %Particle mass, kg

MCaCO3 = 0.1;%Molar mass, kg/mol
```

```matlab
mols = mass_react/MCaCO3;%Number of moles

mols_init = mols;

Temp_loc = 1200;

Temp_dumb = 1200;

Temp_loc_plot =1200;


for C_ang=1:360

    w = 1;


CA_interp = […]

part_T = […]

Temp_gas = interp1(CA_interp,part_T,C_ang); %Gas
temperature, K



HTC_interp = […]

HTC = interp1(CA_interp,HTC_interp,C_ang); %HTC, W/m2 K

HTC_mat(C_ang) =HTC;



time_interp = […]

time_t = interp1(CA_interp,time_interp,C_ang);



Pr_interp = […]

Pres = interp1(CA_interp,Pr_interp,C_ang);%Cylinder
pressure, bar
```
359

```matlab
    Temp_loc_net = Temp_loc_plot;



Hf_CaO_stnd = -635.09; %kj/mol

Aj = 49.95403;

Bj = 4.887916;

Cj = -0.352056;

Dj = 0.046187;

Ej = -0.825097;

Fj = -652.9718;

Gj = 92.56096;

Hj = -635.0894;




tj = Temp_loc_net/1000;


Hf_cao_t =Aj*tj+Bj*tj^2/2+Cj*tj^3/3+Dj*tj^4/4-Ej/tj+Fj-
Hj+Hf_CaO_stnd;%kj/mol


Hf_caco3_stand = -1206.9;%kj/mol
```

```
cp_co2 = 37.11;

Hf_CO2_stand = -393.51;%kj/mol

Hf_CO2  = cp_co2*(Temp_loc_net-298)/1000+Hf_CO2_stand;


cp_caco3 = 83.5;

Hf_caco3  = cp_caco3*(Temp_loc_net-
298)/1000+Hf_caco3_stand;

H_react = Hf_caco3-Hf_CO2-Hf_cao_t;%kj/mol




G_CaO_stnd = -604.03; %kj/mol

Ap = 49.95403;

Bp = 4.887916;

Cp = -0.352056;

Dp = 0.046187;

Ep = -0.825097;

Fp = -652.9718;

Gp = 92.56096;

Hp = -635.0894;
```

```
G_cao_t = 3.96794E-09*Temp_loc_net^3 - 3.91162E-
05*Temp_loc_net^2 - 2.90918E-02*Temp_loc_net -
6.33534E+02;


G_test(w) = 3.96794E-09*Temp_loc_net^3 - 3.91162E-
05*Temp_loc_net^2 - 2.90918E-02*Temp_loc_net -
6.33534E+02;


hstand = -1207e3;

sstand = 93;

gstand = -1129.1e3;

cp = 83.5;




h_t = cp*(Temp_loc_net-298);

s_t = cp*log(Temp_loc_net/298);




dG = h_t-Temp_loc_net*s_t;

dG_mat(w) =dG;

dg_ref = dG_mat(1);

dg_diff= dG-dg_ref;

G_caco3 =gstand/1000+dG/1000;
```

362

```
dg_net_mat(w) = (gstand/1000+dG/1000);




G_CO2 = (-1.11957E-06*Temp_loc_net^2 + 3.57779E-
03*Temp_loc_net + 3.93407E+02)*-1;




G_react = G_caco3-G_CO2-G_cao_t;




Greact_mat(w) = G_react;




p_gas = Pres;

pp_CO2 = p_gas*0.005;




R=8.314/1000;




K_equiv = exp(-1*G_react*1000/(R*1000*Temp_loc_net));




R_spec = 287;

rho = p_gas*100000/(R_spec*Temp_gas);
```

```
Cpc = 1.0*rho;




therm_cond_gas = 2.041e-02;

D = therm_cond_gas/(Cpc*1000);

Lc = part_vol/SA;

jd_am = D*pp_CO2*100000/(R*1000*Temp_gas*Lc);


tim_am = mols_init/(jd_am*SA);

Q_iter = jd_am*SA*tim_am*H_react*1000;




Temp_loc_store = Temp_loc_net;




delt_T_part_in  = abs(Q_iter*0.5)/(mass*CaCO3_cp_init);




Tg_loc =
abs(Q_iter*0.5)*Lc/(therm_cond_gas*tim_am*SA)+Temp_gas;

Tg_loc_mat(C_ang) = Tg_loc;
```

```matlab
qo = (delt_T_part_in+Temp_loc_plot-
Tg_loc)*therm_cond_gas*tim_am*SA/Lc



delt_T_end = (abs(Q_iter*0.5)-qo)/(mass*CaCO3_cp_init);

Temp_loc= delt_T_end;

 delt_t_new_mat(C_ang) = delt_T_end+Temp_loc_plot;




K_cap_interp %Equilibrium temperature as for varying
equilibrium constants




T_cap_mat(C_ang) = T_Cap_interp;





if mols/mols_init==0

    E_remov_mols = HTC*SA*(Temp_loc_plot-Temp_gas)*time;

conv_dT_mols = E_remov_mols/(CaCO3_cp_init*mass);

Temp_loc = Temp_loc_plot-conv_dT_mols;



else

Temp_loc = Temp_loc+Temp_loc_plot;



if Temp_loc+Temp_loc_plot>T_Cap_interp;
```

```matlab
    Temp_loc = T_Cap_interp;

else

    Temp_loc = Temp_loc;

end

end




Temp_loc_net_mat(C_ang) = Temp_loc;




rpm = 1500; %rev/min

time = 1/(6*rpm);




Lc = 5*part_vol/SA;




R_spec = 287;

rho = p_gas*100000/(R_spec*Temp_gas);




Cpc = 1.0*rho;
```

```matlab
therm_cond_gas = 2.041e-02;

D = therm_cond_gas/(Cpc*1000);

Lc = part_vol/SA;

jd_am = D*pp_CO2*100000/(R*1000*Temp_gas*Lc);

jtotd = jd_am*SA*time;%mols


if K_equiv/100000>1/(pp_CO2)

    jtotd = jtotd

else

    jtotd =0

end




if mols/mols_init==0

    jtotd=0

else

    jtotd = jtotd

end


jtotd_mat(C_ang) = jtotd;
```

```matlab
mols = mols-jtotd

if mols<0

    mols = 0

else

    mols = mols

end



if mols_init_flag ==0

    mols = 0

else

    mols = mols;

end

mols_init_flag = mols;



mols_mat(C_ang) = mols/mols_init;



Temp_mat(C_ang) = Temp_loc_store;

Temp_gas_mat(C_ang) = Temp_gas;

Pres_mat(C_ang) = Pres;
```

```matlab
E_remov_paral = HTC*SA*(Temp_loc_final-Temp_gas)*time;

conv_dT_paral = E_remov_paral/(CaCO3_cp_init*mass);

Temp_loc_paral = Temp_loc_paral-conv_dT_paral;




pp_CO2_mat(C_ang) = 1/(pp_CO2);

K_equiv_mat(C_ang) = K_equiv/100000;


if K_equiv/100000>1/(pp_CO2)

Temp_loc_plot = max(Temp_loc,Temp_loc_paral);

else

Temp_loc_plot = Temp_loc_paral;

end


if mols/mols_init==0
```

```
        Temp_loc_plot=Temp_loc

else

    Temp_loc_plot = Temp_loc_plot

end




    Temp_loc_final = Temp_loc_plot;








Temp_plot_mat(C_ang) = Temp_loc_plot;


Temp_con_mat(C_ang) = Temp_loc;











    end
```

```matlab
C_ang_mat = 1:360;

figure (1)

plot(Temp_gas_mat)

hold on

plot(Temp_plot_mat(1:343))


hold on

plot(T_cap_mat);

legend('Gas','particle');

xlabel('CA(degs)')

ylabel('Temperature, K')

xlim([0 358])


figure (2)

plot(K_equiv_mat)

hold on

plot(pp_CO2_mat)

xlabel('CA(degs)')

ylabel('1/bar')

legend('Keq(Calcium)','P(CO2)');

xlim([0 358])


figure (3)
```

371

```matlab
scatter(Temp_gas_mat,K_equiv_mat);

xlabel('Temperature(K)')

ylabel('K')


figure (4)

plot(mols_mat)

xlabel('CA(degs)')

ylabel('Fraction of CaO')


xlim([0 358])
```